Derivation of the Properties of Masonry through Micro-Modeling Techniques

PhD DISSERTATION

Doctoral Thesis by
Anastasios Drougkas

Supervised by
Pere Roca Fabregat
Climent Molins i Borrell

Barcelona, April 2015

Universitat Politècnica de Catalunya
Departament d´Enginyeria de la Construcció

Acknowledgments

The research presented in this thesis was carried out at the Department of Construction Engineering of the Polytechnic University of Catalonia. It was directly supervised by Professor Pere Roca and Associate Professor Climent Molins.

Financial support was provided by the Ministerio de Educación y Ciencia through the research project SUBTIS (Study of the Sensitivity of Urban Buildings to Tunneling Induced Settlements, ref. num. BIA2009-13233), the project MICROPAR (Identification of mechanical and strength parameters of structural masonry by experimental methods and numerical micro-modeling, ref num. BIA2012-32234) and the European Regional Development Fund.

I am grateful to my supervisors for their guidance and support throughout the course of this research. I express my gratitude to the staff of the Structural Technology Laboratory and the members of the Department of Construction Engineering.

To my new friends I express my thanks for their encouragement and spirit. They have made my stay in Barcelona an experience to be cherished. To my old friends I express my thanks for their love. They are comrades whom I have; there are no better.

I thank my family for their love and patience. Theirs is all the credit.

Abstract

The aim of this thesis is to present a framework for the application of micro-modeling techniques for the analysis of unreinforced masonry structures.

Finite element analyses of case studies from the literature are carried out in order to establish their capacity to predict the compressive strength of masonry. A critical review of the experimental inventory is carried out in parallel.

An experimental campaign involving masonry materials common in historical structures is presented. A parametric study on the modeling technique and the influence of material properties is also performed based on the finite element framework already presented.

A series of shear wall experiments are simulated using finite element models. The shear tests have been performed under a wide range of vertical prestress levels. The influence of the modeling technique is again investigated.

A micro-mechanical model for the analysis of masonry periodic unit cells is developed and presented, based on a critical analysis of the results of the preceding finite element analyses. The model may be used for the derivation of the linear and nonlinear elastic properties of masonry walls ans pillars of a wide variety of typologies. The results of the model are compared against experimental results, finite element analysis benchmarks and closed form expressions. The model also forms the basis for the development of a closed form expression for the prediction of the compressive strength of masonry.

A complex masonry pillar is tested in compression. Its constituent materials are extensively characterized for the determination of their mechanical properties. The pillar test is simulated using a finite element micro-model for the purpose of highlighting the effect of the properties of its materials on its structural response. An analytical model for the prediction of the compressive strength of multi-leaf masonry is also proposed.

Resumen

El objetivo de esta tesis es presentar un esbozo de aplicación de técnicas de micro-modelado para el análisis de estructuras de fábrica sin refuerzo.

Se han llevado a cabo análisis de elementos finitos de casos prácticos extraídos de la bibliografía para establecer su capacidad de predecir la resistencia a compresión de las estructuras de fábrica. Paralelamente se ha realizado una revisión crítica del inventario experimental.

Se expone una campaña experimental involucrando materiales de fábrica frecuentemente encontrado en estructuras históricas. Así mismo, se realiza un estudio paramétrico de las técnicas de modelado y la influencia de las propiedades de los materiales basado en el esbozo de análisis expuesto previamente.

Se ha simulado por medio de modelos de elementos finitos una serie de experimentos realizados en muros a cortante. Los ensayos a cortante se han realizado bajo la acción de un amplio rango de niveles de pretensado vertical. La influencia de las técnicas de modelado es investigada.

Se desarrolla y expone un modelo micro-mecánico para analizar células de fábrica periódicas, basado en un análisis crítico de los resultados obtenidos en los análisis de elementos finitos previamente realizados. El modelo puede ser usado para la deducción de las propiedades lineales y no lineales de una amplia variedad de tipologías tanto de muros y como de pilares de fábrica. Los resultados del modelo son comparados con resultados experimentales, estándares de comparación de análisis de elementos finitos y ecuaciónes analíticas. El modelo también establece las bases para el desarrollo de una nueva ecuación analítica para la predicción de la resistencia a compresión de estructuras de fábrica.

Se realiza un ensayo de un complejo pilar de fábrica. Los materiales que lo componen son extensamente descritos para la definición de sus propiedades mecánicas. El ensayo del pilar es así mismo simulado por medio de un micro-modelo de elementos finitos con el objetivo de resaltar el efecto de las propiedades de los materiales en el comportamiento estructural. Se expone un modelo analítico para predecir la resistencia a compresión de fábrica de hoja múltiple.

Contents

List of Figures

List of Tables

Notation

Mechanical Properties

E	Young's modulus
f_c	Compressive strength
f_t	Tensile strength
c	Cohesion
ϕ	Friction angle
ν	Poisson's ratio
G_f	Fracture energy
k	Interface stiffness

Material Type Designation Subscripts

u	Unit
m	Mortar
i	Infill
co	Unit/mortar couplet
o	Outer leaf
$i1$	Unit/mortar interface
$i2$	Infill/outer leaf interface
c	Masonry composite

Mechanical Action

F	Force
σ	Normal stress
τ	Shear stress

General Dimensions

L	Length
H	Height
T	Width
A	Area
V	Volume
d	Diameter
h	Characteristic length of finite element
Δ	Interface relative displacement

Body stress and strain

σ_{ii}	Normal stress
σ_{ij}	Shear stress
ε_{ii}	Normal strain
ε_{ij}	Shear strain

Micro-Mechanical Model Component Designation Subscripts

u	Unit (general)
d	Header unit
s	Stretcher unit
b	Bed joint
c	Cross joint
h	Head joint
t	Transversal joint
i	Infill

Micro-Mechanical Model Component Dimensions

l	Length (horizontal direction - x)
h	Height (vertical direction - y)
t	Width (transversal direction - z)
D	Dimension (general)
d	Deformation

General Subscripts

exp	Experimental value
FEM	Finite element method derived value
mm	Value derived from micro-mechanical model
n	Normal component
s	Shear component
max	Maximum value
$flex$	Flexural
0	Initial
r	Residual
cr	Crack
cr,u	Ultimate crack
$c/3$	Proportional limit
c	Unconfined peak
P	Confined peak
u	Unconfined ultimate
U	Confined ultimate
eff	Effective

General Superscripts

I	Mode I failure
II	Mode II failure
c	Compressive failure

Chapter 1

Introduction

1.1 Historical Background

Masonry, defined as the building of structures by the arrangement of units bound together by mortar or laid dry, is the oldest construction methodology still in wide-spread use. The majority of the world's population resides and works in masonry houses, this percentage being very high in underdeveloped and developing countries.

A wide variety of materials has been employed in masonry construction, equally varied for the basic building units and for their binding material. Units may be various types of stone, brick or block. The binding materials used include lime mortar, mud, cement or clay. Additional structural features commonly found in masonry include rubble infills and wooden or metallic tie rods.

In addition to the wide variety of materials used in masonry, owing to its flexibility of application, numerous structural typologies, geometrical interlocking bonds and structural members have been conceived and used. Most commonly, masonry is arranged in wall-type members, including single and multi-leaf walls, with infills, cavities or constructed of solid masonry. Vertical pillars are also common, being composed of stacked or interlocked units or pillars with infill. Masonry arches, vaults, domes and buttresses are other highly specialized and varied members made of masonry, commonly found in major traditional building projects.

While vernacular construction is by far the most extensive, masonry has produced highly regarded works of monumental architecture. It has been extensively used as a building method for the construction of infrastructure works, mainly bridges, aqueducts and gravity dams, characterized by their extremely long resilience and continued use, often since antiquity.

1.2 Use of Masonry in Construction

Due to its long and continued existence as a viable choice for durable construction, the inventory of existing masonry buildings is massive. Furthermore, the number of historically, artistically,

architecturally and culturally important buildings and aggregates made of masonry is extensive. The need to preserve traditional and monumental architecture stems from both practical and cultural considerations. The optimal course of action is for the preservation process to be carried out by way of rational, effective and efficient techniques. In the context of a multi-disciplinary approach this includes the determination of appropriate action using robust analysis and design methods.

Traditional and empirical methods for the design of masonry structures were the norm well after the adoption of more rational analysis and design approaches for industrially produced construction materials, such as reinforced concrete and steel. The preservation of these traditional methods has served well in understanding the design process of, especially, monumental masonry architecture, but has also resulted in the adoption of concepts for masonry materials and composites initially developed for materials with vastly different properties and intended use.

Masonry remains a common structural typology in modern construction. In addition to being a major non-load-bearing element, used as infill panels in reinforced concrete and steel frames, it is commonly used as the main structural system in buildings. Economic and technological limitations in developing countries serves to maintain masonry, such as adobe or rammed earth, a common choice for vernacular architecture.

Masonry presents several features which make it a viable, sustainable choice as a building material. These include water, sound and heat insulation, fire protection, durability, low maintenance cost and aesthetically pleasing appearance. For these reasons, even after having been largely replaced by other load-bearing systems, it remains in use as a secondary element in modern buildings.

Like all structures, masonry buildings, or masonry members used as secondary elements in buildings, run several risks during their life-cycle. These include the risk of injury to individuals, the risk of property damage, including the structure itself, and the loss of use of the building temporarily or permanently. Major sources of these risks include earthquake events, environmental action, fire, improper use and long term loading. Most of the sources of risks mentioned involve the mechanical straining of the main load-bearing and secondary structural members.

Traditional architecture, practically in its entirety, and modern construction, to an important degree, makes use of structurally unreinforced masonry. This fact increases the potential risk to life and property in the case of catastrophic events and accidents. Furthermore, industrial practice and standardization of the material production process and the execution of masonry works has lagged behind its major competitors. Finally, university engineering curricula usually only include courses on the structural analysis of masonry as elective courses or at the postgraduate level.

On the other hand, the structural analysis of masonry has attracted increased research interest in the recent few decades, owing to its close association with sustainable design, the conservation of architectural heritage, the tourism industry and the preservation of culture. The state of the art of structural masonry is especially advancing in the fields of material study, including traditional and innovative materials, structural analysis using advanced specialized methods and intervention techniques. Finally, structural analysis of existing structures for the purpose of ca-

pacity evaluation and design of repair and strengthening interventions is now receiving more focused attention in design codes. The contribution of infill walls in the structural behavior of frame structures is stressed and advanced analysis models are often recommended. The commissioning of intervention projects, ranging from very small to very large in scale and scope, is becoming more common in the construction industry, especially as an alternative to full replacement of an existing building.

1.3 Scope and Goals

A series of subjects will be addressed in this thesis. A number of them deal directly with the application of micro-modeling techniques, while others are related to the conclusions derived from employing them in practical and theoretical problems.

These subjects include:

- The practical implications for analysts in employing micro-modeling techniques for the analysis of masonry, such as the computational cost and its application to various masonry typologies under different loading types.
- The evaluation of the material properties which most strongly influence the compressive strength of masonry composites. The compressive strength, being the main design parameter according to design codes, is by definition possibly the single most important property of masonry.
- The state of modern masonry design codes. In particular concerning their capacity in giving accurate predictions of the compressive strength and elastic moduli of masonry. This issue includes the extent to which these codes take into account the various properties of the individual masonry constituents for these predictions. In the same context, various closed form expressions with the same function may be evaluated as well.
- The application of micro-modeling techniques to existing structures. Given that numerous material parameters need to be determined for a proper micro-modeling analysis, several obstacles are faced when dealing with existing structures.
- Providing detailed insight into the overall behavior and arising failure modes in masonry members. The design and application of materials which improve the mechanical performance of new masonry structures relies on understanding their true role in the composite. This issue is also critical in the design of effective and efficient interventions on masonry buildings.

Based on the treatment of the above subjects, a number of objectives have been pursued. These include:

- The critical analysis of existing numerical modeling techniques.

- The investigation of the influence of specific material parameters on the mechanical properties of masonry composites.
- The development of a micro-mechanical tool for the analysis of masonry structures.
- The proposal of an experimental approach for the testing of materials and assemblages extracted from existing masonry structures and the application of the results in a micro-modeling framework.

1.4 Structure of the Thesis

Chapter 2 presents a broad overview of subjects pertaining to the analysis of masonry structures using micro-modeling techniques. Practical considerations, advantages and disadvantages and application field are discussed. A short overview of the state of material testing and masonry design standards are briefly developed. While each following chapter is accompanied by its individual specialized state of the art, this general introduction serves at highlighting the impetus behind the subjects treated in this thesis.

Chapter 3 presents a modeling framework for the analysis of masonry structures in compression using finite element models. The numerical results are compared to a compiled inventory of experimental data from the literature. Comments on the initiation, development and repetition of damage patterns are presented.

Chapter 4 includes the development of an experimental campaign centered around masonry composed of materials used mostly in traditional architecture. The applicability of the framework presented in Chapter 3 is tested against an experimental campaign developed in a controlled laboratory environment. Parametric studies illustrated several points in the modeling of masonry in compression.

Chapter 5 applies the finite element modeling framework to the simulation of masonry shear wall experiments, in which the simulation of the compressive behavior is critical. Experimental, numerical and closed form expression results are compared. Along with the findings from the two previous chapters, a strong case is made for the use of three-dimensional modeling for the simulation of masonry in compression.

Chapter 6 presents a method of analysis of masonry walls and pillars using micro-mechanical models of periodic unit cells using analytical expressions. Employing detailed micro-modeling techniques, the derivation of the orthotropic elastic properties of masonry composites are calculated with minimal computational cost. The models are based on rational assumptions and idealizations of the behavior of the masonry geometrical components in the composite. Comparison of the model results with experimental data and finite element calculations are favorable.

Chapter 7 expands the elastic analysis model for cells to calculate the nonlinear properties of masonry in compression, tension and shear. The cell models are able to produce good predictions of the compressive strength of various types of masonry and allow for the detailed studying of the behavior of their individual parts. A parametric investigation of the influence of the properties

of the masonry constituent materials on the compressive strength of masonry is conducted. This is of particular importance given that several material parameters with a strong involvement in the phenomena associated with masonry in compression are not given sufficient attention by researchers and practitioners.

Chapter 8 deals with the compressive testing of a complex masonry pillar, the mechanical characterization of its constituent materials and its numerical modeling. It demonstrates the applicability of the finite element framework to the simulation of an existing structure. Furthermore, it serves as an example of micro-modeling of masonry shedding light on the complex failure mode observed in a structural element.

Chapter 9 summarizes and unifies the conclusions reached to in the preceding chapters. Recommendations for future work are also given with the intention of applying the conclusions reached and the tools developed in this thesis for further practical and research purposes.

Chapter 2

State of the Art

2.1 Introduction

2.1.1 Background

Numerical models based on the finite element method consisting exclusively of continuum elements have been applied for the simulation of standard reinforced concrete and steel structures due to the combined effect of the character of the structures as a whole (composition), the shape of individual structural elements normally comprising such structures (form) and the salient features of their behavior in local level (material). Material anisotropy is either essentially absent, as in steel structures, or is attempted to be taken into account in the analysis using simple assumptions and remedied in the actual structure by the use of, for example, reinforcement bars in concrete. Structural elements of ordinary buildings largely fall within the beam-column group, or are approximated as such, for the analysis of which simple geometrical models are mostly sufficient. Global structural forms normally associated with such construction materials consist, to a significant extent, of variants of frames.

Structural analysis for these cases can be fairly accurate without necessitating the use of elaborate computational tools and can be executed successfully with continuum analysis, catering to the finer points of structural behavior by way of adequate material models. This is being mirrored in the widespread application of these structural types, the profound knowledge of, and the continuing intense research on, the behavior of their constituent materials and, finally, on the documentation of this collective knowledge and know-how in design oriented codes.

This has not been the case with masonry structures due to the coincidence of several conditions. Structural elements composed of masonry usually assume shapes whose behavior cannot be adequately approximated by simplified approaches, as is possible in the beam-column element case. The study of the mechanical properties of the constituent materials, both independently of one another and in their interactions in the structure, as well as their behavior in time, has in general lagged behind in depth and extent compared to those on concrete and steel. In fact, many of the material models used for the constituents of masonry are directly borrowed from the selection of models developed specifically for concrete. Finally, the composite behavior of

a masonry structural component or element consisting of materials with intrinsic weakness and brittle behavior in tension further complicates matters, making simplified approaches hardly sufficient.

A discontinuous approach in the structural modeling of masonry, based on the discrete simulation of existing and arising planes of weakness is more appropriate in the effort to achieve accurate and complete results. The adoption of this approach is made attractive by its conceptually sound base, its range of applications in various analysis scenarios and its compliance with localized physical phenomena. It can prove to be a valuable tool in the simulation of all types of structural joints, discontinuities in computational rock mechanics, cracks in quasi-brittle materials, steel-concrete interfaces in reinforced and composite structures, the matrix-aggregate interaction in concrete or in the analysis of discretized continua, to name a few.

2.1.2 Goal of the Micro-Modeling Approach

The micro-modeling of masonry was first implemented by Page several decades ago as means of overcoming the shortcomings of simplified models in their capacity to numerically predict the physical macroscopic phenomena in masonry and their association with dominant failure modes [120]. Taking advantage of the versatility of the finite element method and the extensive practical experience thereon, and infusing it with the concepts derived from damage and fracture mechanics, plasticity theory coupled with nonlinear solution methods, constant increase in computational power and the expansion of the state of the art concerning the mechanics of masonry it has been made possible to create theoretically sound and practical numerical models which reproduce the intrinsic characteristics of the structural behavior of masonry. These approaches derive their characteristics from a consideration of actual physical phenomena and their simulation through both detailed and phenomenological methods.

Among the desirable results of a micro-modeling analysis are the numerical approximation and visualization of damage and collapse mechanisms, the effect which geometrical characteristics such as unit stacking types may have in the response and, in general, the numerical representation of macroscopic phenomena associated with failure in masonry. In essence this means the simulation of the global behavior of a masonry member by independent modeling of its macroscopically discrete constituents.

2.2 Modeling Methods and Element Types

2.2.1 General Aspects

As in most types of finite element analysis requiring more than average structural detailing, the geometrical aspects of masonry micro-modeling, though simple in principle, can be frustrating in practice. It is highly recommended for simple parameterized meshing programs to be developed, as they can be prove to be particularly time and effort saving in the case of even the simplest structural elements, such as single walls.

2.2.2 Level of Detail

Several strategies have been proposed and experimented with concerning the micro-modeling of masonry structures. The main aspect that sets these various approaches apart is the amount of detail incorporated into the geometrical representation of the structure and, therefore, the degree of structural idealization to be applied in the analysis.

In the detailed micro-modeling approach, four basic individual components are simulated: the units in their actual dimensions using continuum elements, the mortar with its actual thickness in the joints using continuum elements, the unit/mortar interface and the potential cracks, both using discontinuous elements, as explained by Lourenço [96]. This configuration constitutes the most detailed representation of the actual structure while, at the same time being the most demanding in terms of model preparation effort and computational time consumption. It does necessitate, however, the least amount of geometrical simplification and, therefore, the least amount of assumptions concerning material behavior. Essentially, this means that a structure can be modeled with a minimum of phenomenological assumptions concerning material properties, provided that the appropriate material models are used.

The simplified micro-model approach introduces an additional degree of homogenization in the masonry. Unit elements dimensions are extended to cover half the width of the mortar joint, thus eliminating the intervening layer of independently modeled mortar and allowed to interact directly with each other through discontinuous elements representing the behavior of the joints. Simplified micro-modeling reduces the geometrical complexity of the model as well as the computational cost significantly without substantial loss of accuracy, thus offering a particularly attractive alternative to detailed micro-modeling when overall knowledge of structural behavior is sought rather than of localized phenomena. It is no surprise that this approach accounts for the majority of studies in the area of masonry micro-modeling analysis. The main drawback of this approach is the necessity for a phenomenological approximation of joint behavior by not accounting for the actual stress state in the mortar or for the Poisson effect generated by the unit/mortar interaction in compression. Illustrated examples of the various types of micro-models are shown in Figure 2.1.

It is possible to further increase the level of detail of a masonry micro-model by introducing additional structural constituents in the model, such as grout, infill and embedded or externally bonded reinforcement bars [13, 69, 128].

2.2.3 Simulation of Units and Mortar

The type of finite elements to be used for the simulation of the units depends on the geometrical configuration of the model. In any case, continuum elements are used for the representation of the units and the mortar.

For two dimensional problems plane stress elements are often used. Examples of applications include studies performed with 4-node quadrilaterals [65], 8-node quadrilaterals [96] and 3-node triangular elements [43, 141]. Geometrical simplicity and regularity of masonry bonds

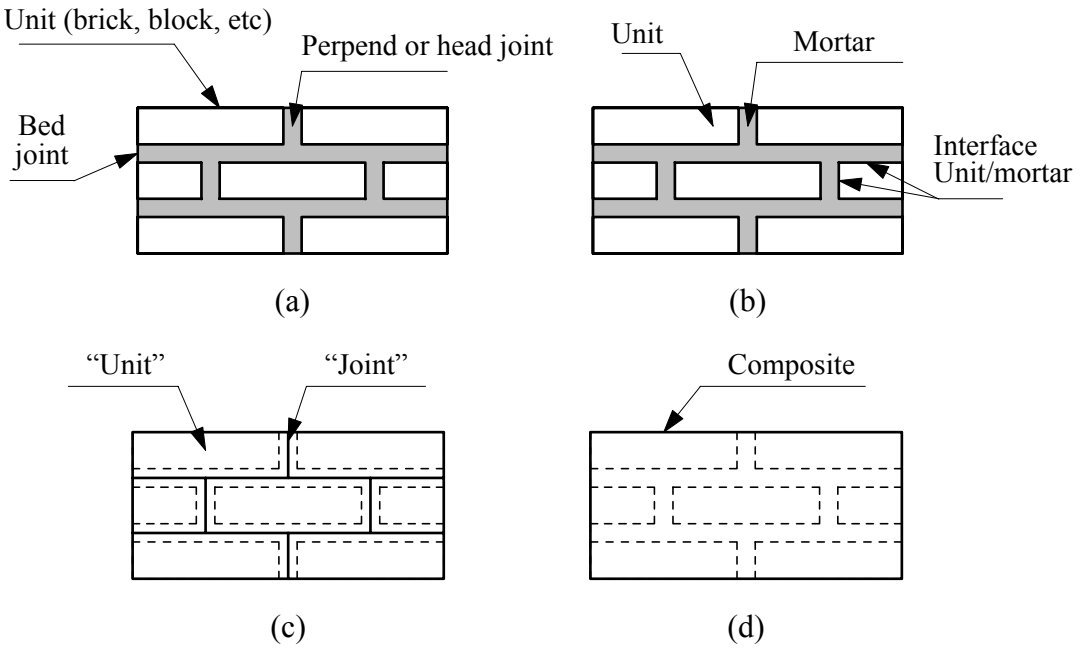

Figure 2.1 Modeling strategies for masonry structures: (a) masonry sample; (b) detailed micro-modeling; (c) simplified micro-modeling; (d) macro-modeling [92].

normally allows for an accurate representation of the structure's geometry using quadrilaterals. The bulk of micro-modeling simulations has been performed on flat wall configurations in two-dimensional problems, which has generally proven to be sufficient for the analysis of masonry walls under in-plane loading. Apart from plane stress analyses, there have been analyses performed using plane strain or generalized plane strain configurations to account for out-of-plane stress effects and to compare these approaches [16].

For three-dimensional analyses 8-node and 20-node brick elements have generally been used [3, 8], along with a small number of studies performed using 6-node wedge elements [108]. Three-dimensional analyses have been performed in both flat wall segments as well as curved geometries [108]. Three-dimensional analysis is arguably the most accurate tool but is far from practical when a parametric investigation or the analysis of a large structure is required. Out-of-plane stresses may be considered by adopting an enhanced plane stress approach with only a fraction of the cost of a full three-dimensional analysis [95].

Units may or may not feature the existence of potential cracks, normally intersecting the unit at mid length. Potential cracks are further explained in the following segment dealing with micro-model discontinuous elements, and the matter is further investigated in the segment concerning material models and their capacity for simulation of failure modes of masonry structures.

2.2.4 Simulation of Joints and Potential Cracks

Given the fact that micro-modeling of masonry was initially conceived and developed as a technique to simulate the effect of joint discontinuities, accurate simulation of the interfaces in masonry is the cornerstone of an accurate micro-model simulation of problems with arising shear and tensile stresses. Therefore, the simulation of masonry joints and potential cracks makes use

of discontinuous elements which through their numerical formulation relate nodal displacements to stresses instead of forces, as is the case for ordinary continuum elements.

Interface elements are used in micro-models in a variety of roles, depending on the desirable level of detail. In detailed micro-models interfaces are used to model the interface (contact) of the units with the mortar, therefore accounting for only part of the composite behavior observed at the joints of masonry. Obviously, this is the most accurate but also most demanding approach currently available; structural idealization is minimized. Additionally, it requires the greatest effort in the mechanical characterization of the materials.

Elements used to prescribe a discontinuity in the stress and strain field of a continuum fall generally into one of two categories: interface elements derived from degenerate continuum elements with an ideally small thickness or interface elements derived from a penalty approach formulation. Penalty approach elements may be of zero thickness, in which instance opposite nodes coincide geometrically, or they may be prescribed with a dummy thickness for easier graphical manipulation. As explained by Hohberg, zero thickness is usually prescribed to interface elements derived from a penalty approach whereas non-zero thickness is given to interface elements derived from continuum elements formulated with the ideally thin layer approach [75]. However, a non-zero physical thickness to penalty formulated interface elements should only be prescribed in the case where strain gradients across the layer are expected. This is not the case in unit/mortar interfaces in detailed micro-models but it could potentially be so in simplified micro-models. Regardless, usually only a global representation of the structural role of the interfaces is required, therefore zero thickness elements are sufficient, which have the additional advantage of being formulated using concepts more attractive from an engineering point of view, such as interface stiffness. The present literature review revealed a distinct prevalence of penalty interface elements with zero thickness regardless of the application type. The derivation of the two main families of interface elements is illustrated in Figure 2.2.

In simplified micro-models interfaces are used to account for the behavior of the joint in its entirety, meaning that interface elements are used to model the complex interaction of the mortar, unit/mortar interface and the portion of the unit involved in the behavior of the joint. This approach is clearly more attractive in terms of computational cost than detailed micro-modeling, but resorts to sacrificing part of the accuracy and completeness of the results. Additionally, this approach, necessitating the approximation of the behavior of the joint, requires the definition of interface element stiffness that does not conform with the values consistent with the penalty approach but rather account for an approximation of the behavior in the vicinity of the mortar joint. This results in quite visible interpenetration of continuum elements and negative interface element volume under compression, [75]. While not strictly making sense in a physical manner, such behavior may be assumed to provide a phenomenological representation of masonry crushing, provided the material properties are appropriately calibrated.

In either of these cases, interface elements can be used to model potential cracks in units. The inclusion of potential cracks serves to simulate the damage in units without resorting to the use of nonlinear constitutive laws in the continuum. This approach may allow for the adoption of a coarser mesh but has been generally replaced by the use of continuum plasticity and damage

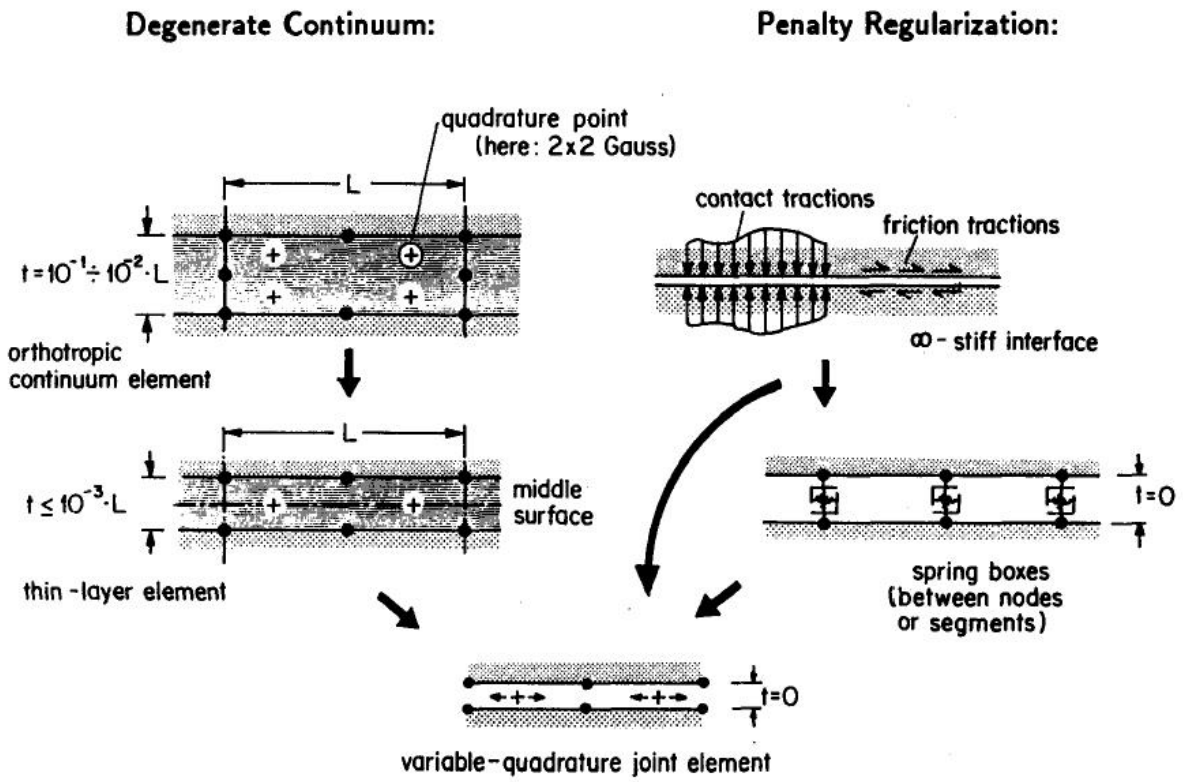

Figure 2.2 Degenerate continuum (left) and penalty method interface elements (right) [75].

models.

For two dimensional problems, discontinuities are modeled with interface elements which simulate the normal and shear interaction between two sides of two different continuum elements. Examples of such elements are 4-node and 6-node structural interface elements [65, 96]. Nodal interfaces have also been used in a number of studies [62, 131], but line interfaces appear to be more attractive from an engineering and conceptual point of view.

In three-dimensional problems, the geometrical formulation principle remains the same, except that interface elements now simulate the interaction between two surfaces of two different continuum elements. Common examples of such elements are 8-node and 16-node structural interface elements [5].

2.2.5 Simulation of Additional Constituents

Masonry structures frequently incorporate additional structural constituents such as grout or other injected materials, reinforcement bars and FRP strips. Their simulation is of particular importance in the cases where they are used as a repair or strengthening measure [83, 128].

Whereas grout used in the construction of hollow masonry can be modeled using the same philosophy as for the interaction between units and mortar, there has been very little research concerning incorporating other materials in micro-modeling analyses. While unreinforced masonry has been extensively investigated using this approach, research on strengthening techniques in

masonry micro-models has lagged behind and presents an attractive field for future research.

2.2.6 Overall Meshing Strategy

The number of elements to be used for the simulation of a single complete masonry unit is a matter of discussion. In the cases where this issue was actively investigated, simplified micro-modeling analyses have exhibited significant mesh insensitivity, always within legitimate margins of mesh coarseness, in terms of capacity, load-displacement curves and even snap-back and snap-through phenomena for nonlinear analyses with linear elastic units and material nonlinearity lumped in the interfaces [96]. This is not, however, necessarily true when smeared cracking concepts are applied in the units, in which case a finer mesh may yield better results as crack bandwidth calculation is dependent on the size of the elements and may also provide increased numerical stability [148].

While the fineness of the mesh as mirrored by the number of elements per masonry unit is not necessarily crucial, the combination of element type with the appropriate interpolation polynomial and integration scheme are important in order to avoid numerical phenomena such as volumetric locking which can significantly lower the accuracy of a nonlinear analysis in terms of capacity assessment. Still, the use of smeared cracking for the units appears to be a parameter that challenges the possible limitations of a given micro-model mesh, and should therefore be used prudently.

The simulation of the mortar in detailed micro-models generally follows the same rules that apply to the units in terms of meshing. However, considering the geometrical peculiarities associated with the existence of mortar modeled with continuum elements (large length to thickness ratio), and the necessity of geometrical consistency of the mesh to accommodate the existence of the interface elements, such an analysis may require a particularly fine mesh in order to avoid continuum elements of inappropriate shape to simulate the mortar which could reduce the accuracy of the results. Local refinement in the mortar joints may be more practical on the condition that mesh conformity is maintained.

In the past, a few progressive mesh refinement methods were proposed in order to account for more accurate simulation of the propagation of yielding [10]. Additionally, analyses were performed with initial local refinements in the mesh in targeted areas of interest in cases where, for instance, concentrated loads were applied [11]. A number of these methods were proposed at a time when computational power was particularly limited compared to modern standards. This fact, coupled with the method's apparent mesh insensitivity under certain conditions renders these techniques largely unnecessary. Nevertheless, the instances in which the nature of the problem at hand may be anticipated with reasonable certainty, the technique of limiting discrete modeling to the areas of interest, while adopting a continuous approach for the remainder of the structure, may yield adequate or even entirely accurate results with reduced computational demands and structural complexity.

Concerning the generation of a micro-model mesh, it is important to use continuum and discontinuum elements based on compatible interpolation. For instance the sides of quadratic

plane stress elements for the units or the mortar should be connected with quadratic interface elements. Incompatibility in that regard could potentially produce erroneous results.

As a final important note, a certain inconsistency in the terminology concerning micro-modeling encountered in the literature should be mentioned. The term micro-model in the available literature includes the previously described detailed and simplified micro-models but also models wherein units and mortar are individually modeled, as in detailed micro-models, but without the inclusion of interface elements between them, thus considering a perfect bond between the constituents. The latter approach is also referred to as the meso-scale approach. In the segment discussing possible application of detailed micro-models to numerical homogenization techniques, a brief comparison between meso and micro approaches is presented.

2.3 Material Models

2.3.1 General Aspects / Simulation of Failure Modes

As the main focus of the micro-modeling approach is the numerical representation of damage and failure, this segment primarily deals with the various nonlinear models that have been used. Nonlinear material behavior is normally taken into account by adopting either a plasticity based approach or a damage based approach.

The appropriateness of a material model should be judged on the basis of its capability to simulate the failure modes associated with masonry structures. The plains of weakness in the composite governed by the existence of mortar joints, coupled with the brittle behavior of the units in tension, produce the following main failure modes: tensile cracking of the joint, shear slipping at the joint, cracking of the unit under direct tension, diagonal tensile cracking of the unit and crushing of the masonry composite. These modes may be simulated for masonry under monotonic or cyclic loading. Additional models simulating creep and shrinkage have also been developed.

2.3.2 Models for Units and Mortar

There is a variety of material models available for the elements comprising the units, as well as the mortar in the case of detailed micro-models.

In its earliest and several of its following incarnations, the micro-modeling approach prescribed a linear elastic behavior for the elements comprising the units, since material nonlinearity was taken into account solely in the interfaces, thus all nonlinear behavior of masonry was lumped at the joints. Apart from elastic linearity, units were approximated considering zero stiffness in tension, thus assuming a brittle behavior with zero tensile strength [148]. Further progress in that regard was achieved when attempts to simulate the actual nonlinear behavior of the units themselves in a masonry composite were made. Initially, two approaches were proposed and subsequently tested.

The first approach relied on the salient feature shared by quasi-brittle materials like clay brick, mortar, ceramics, rock or concrete to fail because of a process of progressive internal crack growth. To simulate this process, a number of material models normally applied to concrete saw use in the modeling of masonry units. Various incarnations of the smeared cracking concept have been used in micro-modeling analyses such as a multi-directional fixed crack model and a total strain model [69]. Smeared cracking had been already applied to simulate diffused cracking in large scale reinforced concrete structures, and given the perceived similar quasi-brittle behavior of masonry units it was extended in masonry analysis. Additionally, several plasticity models have been used, such as the such as the Craft model [3] or others employing the Drucker-Prager [95] or Lubliner criterion [33], which have also been used to model concrete structures. An example of the failure mode obtained from the micro-model of a masonry periodic unit cell and its macroscopic interpretation in the masonry composite is shown in Figure 2.3.

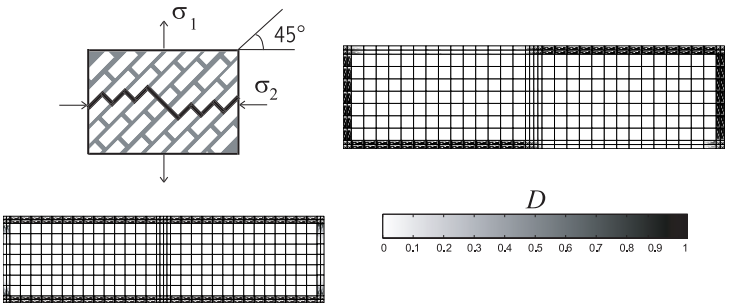

Figure 2.3 Detailed micro-model of periodic unit cell with damage model (left) and associated failure mode in masonry (right) [101].

The second approach involved the interruption of the continuity of otherwise linear elastic units by way of the inclusion of interface elements with dummy stiffness intersecting the units at mid length in order to simulate potential cracks [47]. Potential cracks constitute a legitimate numerical approximation of the tensile failure usually observed in masonry units, which manifests as a localized phenomenon. It has also been shown that this geometrical formulation is capable of predicting the occurrence of continuous linear cracks “jumping” across bed joints from unit to unit [96].

As a further step, masonry units in micro-models have been simulated in a composite manner by the combined application of potential cracks and smeared cracking. Additionally, the pattern of potential cracks incorporated in the units has recently assumed new forms: by discretizing units with triangular elements it is possible to introduce additional diagonal potential cracks within the units, thus physically accounting for one more cracking pattern regularly encountered in units failing under tension [22]. For these cases, numerical instability caused by the large number of nonlinear interfaces could prove to be an issue.

Taking into consideration the nature of cracking failure observed in masonry units, the appropriateness of smeared cracking has been the matter of debate. While particularly suited for the modeling of cracking over large continuous elements, it has been argued that it may not be suitable for the simulation of cracking in a discontinuous geometry characterized by limited areas of smeared crack propagation, whereas potential cracks may be more capable of accurately representing the strongly brittle and localized failure of units in tension. It is arguable that this

shortcoming of smeared cracking could be neutralized in the analysis of periodic masonry cells, where each unit may be several elements across in all directions, thus potentially eliminating problems associated with mesh coarseness.

As far as anisotropic behavior of the units is concerned, which could be caused by the existence of gaps in the case of hollow units, it could be taken into account by way of adoption of an appropriate anisotropic material model in the case of simplified micro-models which do not incorporate a detailed geometrical representation of the units.

The pressure dependent behavior of the mortar is crucial in simulating masonry in compression using detailed micro-models. Since the compressive strength of the masonry is not a prescribed analysis parameter, as in simplified micro-models, accurately simulating the compressive behavior of mortar under multi-axial stress becomes a priority.

2.3.3 Models for Interfaces

The primary purpose of an interface material model is to be able to simulate the failure modes already mentioned and, if possible, be able to unify them in a combined expression. Depending on the adopted level of detail, the interfaces need to be able to simulate a certain number of failure types. Worthy of note is the fact that even though units are often considered as linear elastic, some sort of nonlinearity in the joints is practically always considered.

In general, interface elements should be able to simulate shearing behavior and failure of the unit/mortar interface or of the entire joint. This can be achieved by employing Coulomb friction models normally used in structural interface analysis. Dilatancy may or may not be considered in the analysis, although it is usually ignored in simplified micro-models by prescribing a zero value for the dilatancy angle (shearing in the interface does not produce expansion or contraction), thus assuming a non-associated plasticity formulation [47].

Tensile cracking in the joints is also a salient feature of masonry that should be modeled. Cracking may be brittle or it may present itself with tension softening.

Crushing of the interface to simulate compressive failure in the joints is especially important in the case of simplified micro-models, since mortar, and therefore its interaction with the units, is not individually modeled. It is interesting to note that the compressive failure mode for interface elements was possibly the last failure mode to be modeled. Initially the failure mode was modeled by way of a compressive cap criterion in two dimensions, which was later expanded into three dimensions [91].

In order to simulate the coupling of these failure modes, combined material models within either a plasticity or damage framework have been proposed that account for all three of the major failure types in interfaces. Plasticity based models appear to have seen wider application, as can be deduced from the available literature (e.g. [90, 96, 118]).

A small number of damage and plasticity models have also been proposed for use in interfaces which are appropriate for structures subjected to cyclic loading [119, 139].

While the elastic characteristics to be used for the units can be acquired in a straightforward

manner, the elastic relation between forces and stresses to be used for the interface elements in a simplified micro-model need to be estimated. This requires the definition of both normal and shear stiffness for the interface elements. There have been a number of proposed methods for defining these values, governed by material properties of the constituent materials, the geometric characteristics of the masonry bond, such as unit dimensions and joint thickness, and the overall geometry of the structural element to be analyzed [47, 123, 134]. The interface elements used for the description of potential cracks in units are prescribed a very high dummy stiffness in order for the deformation of the potential crack before failure to be insignificant compared to the deformation of the surrounding continuum and also to suppress element interpenetration [75]. The same approach is adopted in the case of detailed micro-models to model the unit/mortar interface, where shear deformation in the joint is thus entirely due to the shear deformation of the mortar, until shear sliding occurs in the unit/mortar interface.

2.3.4 Combining the Material Models

As long as legitimate assumptions are made concerning the choice of individual models for the materials and the properties associated with them, there does not appear to be any practical incompatibility between them. Accounting for compressive failure in the constitutive laws of the interface is common in simplified micro-modeling and may alleviate the need for this mode to be accounted for in the continuum parts of the model, particularly given the fact that the joints have a compressive strength lower than that of the units. The global failure mode obtained from a micro-model accounting for shear and tensile failure modes in the interfaces is shown in Figure 2.4.

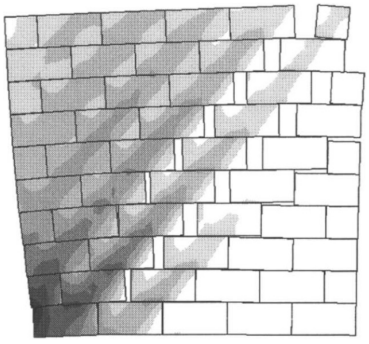

Figure 2.4 Failure mechanism obtained from a simplified micro-model of a masonry shear wall [94].

2.3.5 Reflection on Material Properties for Micro-Models

An accurate micro-model analysis requires extensive knowledge of the mechanical properties of the constituent materials ranging from standard elastic and strength parameters to fracture energies and a variety of other plasticity related values. This is especially true when determining the properties of the unit/mortar interface or of mortar in triaxial state of stress. Acquiring all these values from specimens demands the carrying out of a wide range of experiments, which is not always realistic. Therefore, it is often necessary to adopt methods and material models through

which a number of properties can be indirectly derived or to extract the necessary data from assorted literature in the cases where the property values are more or less standard. Alternatively, it would be advisable to utilize material models which employ a relatively small number of parameters that can be derived through standard testing without sacrificing the accuracy or the completeness of the results.

2.4 Analysis Types

2.4.1 Linear Elastic Analysis

Masonry micro-models are seldom used in linear elastic analysis as it is not generally compatible to the purposes for which it was initially developed. Furthermore, linear elastic analysis fails to simulate the nonlinear intricacies of masonry response to even low levels of stress. However, a small number of linear elastic analyses have been performed for various reasons.

Linear elastic analyses of a continuum model with units and mortar modeled with continuum elements and a simplified micro-model were executed to compare computational effort and results obtained from the two approaches [92]. Through this comparison the efficiency and the accuracy of the simplified micro-model was demonstrated. It is also arguable that this comparison illustrates the computational advantage of simplified over detailed micro-models with a minimal sacrifice in accuracy. The continuum model in question is not a micro-model per se, due to its being analyzed under linear elastic conditions.

Additionally, by adopting values for the maximum allowable tensile and compressive stress, it is possible to make rudimentary safety assessments on masonry structures such as arches. However, by neglecting material nonlinear phenomena, it is debatable whether this approach can yield usable results, especially when compared to results obtained by, for example, nonlinear or limit analysis [93]. Accurate analysis of masonry requires taking its highly nonlinear response into account.

Finally, linear elastic analysis of masonry periodic unit cells using micro-models can be employed in the numerical determination of the elastic properties of masonry composites consisting of components with know elastic properties.

2.4.2 Nonlinear Static Analysis

Up until now, the analysis of masonry micro-models has mostly revolved around a static nonlinear approach using monotonic concentrated loading to predict failure loads and to estimate post-peak response. A relatively large number of examples of such works may be found in the literature [8, 11, 64, 90].

Material nonlinearity lies in the core of the micro-modeling approach. It is not unusual for geometrical nonlinearity to be included in the analysis, although the approach has generally revolved around the development of methods for simulating material nonlinearity and damage.

Nonlinear analysis requires a fair amount of competence in the areas of finite element plasticity and iterative solution techniques if appropriate numerical results are to be obtained. Various iterative solution methods, such as Newton-Raphson, using load or displacement control may be employed. Additionally, arc-length methods in force control have also been used successfully.

2.4.3 Nonlinear Transient and Dynamic Analysis

The long term effects of masonry creep have been investigated by way of nonlinear transient analysis, though the applications involving micro-modeling are very few and present significant numerical challenges [153].

For the types of structures the micro-modeling approach is aimed at, which mainly consist of individual structural elements, modal analysis is largely unnecessary. However, dynamic transient analysis of these structures could prove to be particularly interesting in assessing the risk of earthquake induced damage, though the numerical aspects of it might be discouraging. Attempts at analyzing masonry micro-models have been made, but due to the numerical obstacles posed by this approach, elastic-perfectly plastic material behavior was assumed in order to mediate computation times and to avoid difficulties with convergence. The fact that very few such experimental records are available further compounds the problem of transient dynamic analysis [5, 75, 149]. Modal analysis of entire masonry structures can be quite demanding but research in this area still exists to a limited extent [12].

2.5 Practical Aspects of Micro-Modeling

2.5.1 General

Having acquired a fair amount of familiarity with the theoretical components from which the micro-modeling approach draws, there are still several practical issues to be considered for an analysis. Most of these issues stem from the intrinsic nature of the micro-modeling approach and are thus inherent in practically all such analysis projects. It is possible for some of them to be mediated or even avoided by the appropriate modeling approach. Finally, a few of these issues are worthy of consideration for future developments in the method.

2.5.2 Modeling and Computational Effort

As was mentioned in the segment discussing modeling methods, the geometrical description of the model may present some difficulty and normally demands more involvement than the description of continuum models for similar structures in terms of manual generation or verification of the mesh. It is possible for case specific meshing algorithms to be developed, but producing a generalized algorithm for anything other than simple structural elements may prove to be unrealistic.

Additionally, nonlinear analyses of moderate sized micro-models are usually computationally demanding, even when element types, material models and solution procedures are carefully considered. Currently, the extension of the application field of the method in realistic and practical terms relies to a significant extent on the increase of available computational power.

2.5.3 Parameter Definition and Control

The plasticity and damage models used in nonlinear analysis require the use of a particularly large number of material properties. Apart from the fact that in the case of masonry constituents they are not always readily available, the sheer number of possible combinations of items that may warrant parametric investigation can make tackling such a task unwieldy. Furthermore, model calibration in order to achieve conformity with, for instance, experimental data is one of the challenges posed by this approach and should be limited in the adjustment of the most crucial parameters. However, it could be argued that the potential for an increased scope of a possible parametric investigation serves the attainment of a wider overview and a deeper understanding of the phenomena examined in the analysis: the larger amount of material parameters allows a wider investigation of their effect in the properties of the masonry composite.

During the course of a parametric investigation, it is likely for an indirect determination of several parameters to be necessary, since experimental investigation for the determination of all necessary material properties is unrealistic. Care should be taken in making legitimate and compatible assumptions about unknown parameters, especially those associated with the behavior of the interfaces and the properties governing material plasticity and damage. Nevertheless, the direct determination of as many material properties as possible in integrated experimental-analytical projects should be sought.

The parameter identification method could possibly serve to determine a number of missing parameters numerically by fitting numerical to available experimental data. Such work directly related to calibrating masonry micro-models has been developed [115].

2.5.4 Field of Application

Discontinuous methods, like the micro-modeling approach for masonry, share the characteristic of being computationally demanding while simultaneously limiting structure idealization. This usually renders them ill-suited for large-scale structures. They are, however, the ideal tool for the analysis of small scale structures characterized by strong heterogeneity. This includes masonry structures where the ratio between the structure's overall size and the dimensions of the units is small, such as periodic masonry cells. The relatively narrow focus of the method's application field has resulted in substantial theoretical and practical experience and a considerably large and expanding body of work attempting to scrutinize and unify the finer points of the mechanics of masonry, which still largely elude researchers.

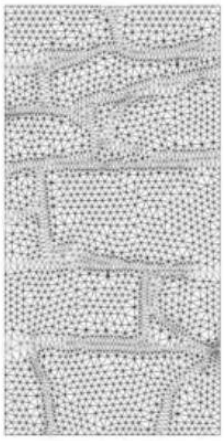

Figure 2.5 Detailed micro-model of irregular stone masonry [13].

2.5.5 Comparison with Other Modern Analysis Methods

Experience has shown that no one analysis method for masonry has a definite advantage over the others for every possible analysis scenario. The variety of continuum and discontinuum methods available for use provides solutions for all practical problems [132]. Micro-modeling cannot currently realistically compete with continuum or macro element methods for the analysis of large scale structures. It is, however, interesting to compare it with other discrete methods for masonry, namely limit analysis, discontinuous deformation analysis and the discrete element method, which may also be referred to as micro-modeling approaches but are not the subject of this review.

Limit analysis and the discrete element method have been used for the analysis of block structures, such as dry stone masonry with a fair amount of success. Analyses performed using these methods are normally done under, among others, the assumption of infinite compressive strength for the blocks, which is legitimate for specific case studies but which cannot be extended to structures made of, for example, adobe or dry brick masonry. Moreover, though there have been efforts in infusing the discrete element method with damage models for the units, micro-modeling based on the finite element method appears to be a more robust and straightforward formulation and also one with a larger body of work supporting it. Nevertheless, in the area of transient dynamic analysis of discontinuous masonry structures the discrete element method is arguably the more attractive choice [48, 87].

2.6 Examples in Engineering Practice

2.6.1 Simulation of Structural Elements

A significant amount of analyses has been carried out with the purpose of testing of masonry elements such as panels or walls of moderate size. These assemblages correspond to individual structural elements which are normally encountered in standard buildings as primary or secondary load bearing elements, namely walls, deep beams and even arches. Wall elements have

been simulated under horizontal loading under the influence of a vertical compression load and also in a diagonal shear configuration similar to the one utilized in diagonal shear testing of panels [128].

Until now, the micro-modeling approach has seen use in various research projects, often accompanying experimental projects or using such experimental data as a frame of reference for model calibration and result verification. The majority of these analyses involved the in-plane behavior of masonry panels under concentrated loading. Static push-over analysis is usually performed, although there have been a few attempts at performing cyclic tests incorporating suitably modified material models.

There have also been a number of numerical investigations on the effect of masonry in the lateral response of confining reinforced concrete frames, in which interface elements were used in the description of the joints in the masonry but also for modeling the interaction between the frame and the infill [9, 107, 141, 146].

The out-of-plane behavior of masonry panels has been also tested recently with this method. Such investigations require three-dimensional models, which can be very demanding from a computational standpoint, a fact which possibly explains the small number of such attempts [98, 160].

A limited amount of research has been performed on masonry arches. The detailed micro-modeling approach in a two-dimensional configuration was adopted for the testing of a new interface element and the investigation included both plain and reinforced structures [62, 134].

Finally, the method has been used as a tool in the homogenization process for the analysis of large scale structures using continuum methods [102]. Additionally, a form of detailed micro-model has been used as a verification tool for the results of masonry homogenization attempts [95, 100, 109].

2.6.2 Simulation of Masonry Tests

Significant work has been performed using numerical models of test specimens, a number of which conforms to the provisions of specific material testing codes on simple masonry prisms. This area is of particular interest because the small size of these specimens, which sets them apart from the study on entire structural elements, implies a much smaller ratio between the size of the structure and the dimension of the units. The coincidence of small specimen size and the requirement for accuracy and detail presses the advantages of the approach over continuum methods while minimizing the effects of its intrinsic shortcomings.

The analysis of the compressive behavior of prisms is a subject of importance; from a design standpoint the compressive strength of masonry is the prime parameter considered, while most of the remainder properties are derived directly from it. The CEN standard test is a common procedure for the determination of the compressive strength of masonry through the testing of wallettes and has been the subject of micro-modeling analysis in the context of verifying the accuracy of the method [95, 131]. Non-standardized tests have been also performed on prisms

for the study of the effect of compressive load eccentricity and the numerical investigation of buckling. Various other concentric and eccentric compression tests on prisms and other small assemblages are also presented in the available literature [3, 23].

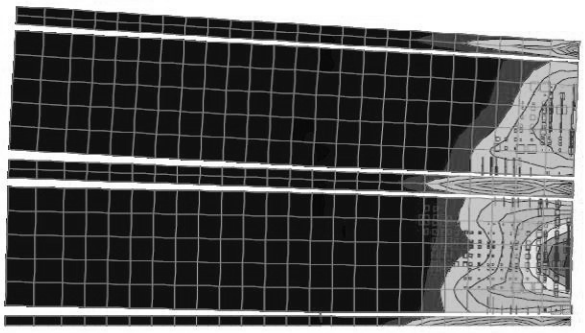

Figure 2.6 Detailed micro-model of eccentrically loaded masonry prism [3].

Similar small assemblages have been incorporated in the simulation of the effects of creep and shrinkage using detailed micro-models with special material models [153].

Overall, it should be stated that the execution of micro-modeling analyses as a complement to experimental investigations of this nature presents an attractive means of expanding upon laboratory results through considered parametric investigation and sensitivity studies. The large number of influencing parameters provides researchers with a wide scope of possible investigation subjects.

2.6.3 Reflection on Application Field

As is made obvious in the preceding segments, the micro-modeling approach is a highly specialized tool with a relatively narrow field of application, considering the scope of theoretical and practical background supporting it. This is a possible explanation for the fact that expansion in the range of problems for which the method is a viable option remains limited. Deviations from this trodden field require robust theoretical support followed by extensive validation and evaluation of practicality.

A major obstacle is posed by the method's computational demands and structural complexity which make it unsuitable for large scale analysis projects and most applications in the construction industry.

2.7 Expanding the Micro-Modeling Approach

2.7.1 Recent Developments

The micro-modeling approach on masonry presents an attractive and challenging field for research as is evident by the most recent developments directly related to the expansion of its

theoretical and practical basis.

Expanding upon the plasticity models developed for the interfaces, the postulation of damage based models followed suit in an effort to more accurately simulate cyclic loading effects. Simultaneously, the existing plasticity models where expanded, or new ones where proposed, for the simulation of cyclic loading, shrinkage and creep as has been mentioned earlier in this chapter.

Interface elements are currently available in many commercial and open finite element software packages. By use of user subroutines, the material models proposed for interface elements can be used for analysis projects. It is noteworthy that a number of software packages offer such models in their built-in material libraries.

The increase in the availability of computational power since the method began gaining notice in the masonry research community led to efforts in modeling structural elements in three-dimensional configurations, thus making it possible to study out-of-plane effects [60, 98]. A number of efforts have been also made in approximating three-dimensional effects in two-dimensional analyses with the employment of a generalized plane strain model without, however, employing interface elements in the meso-scale [103].

Analytical solutions for the stress and strain distribution in periodic unit cells have also been developed over the recent years. The models are formulated based on a discretization of the cell according to the geometric configuration of the units and the mortar, and may thus be seen as a form of micro-modeling of masonry. These models may be used for the derivation of the orthotropic elastic properties of masonry or form the basis for nonlinear multi-scale analysis of large masonry members. Models along these lines have been proposed by Taliercio [143] and Zucchini [162].

2.7.2 Possible Future Objectives

In seeking to expand the theoretical and practical aspects related to the micro-modeling approach, two different but complementary paths could be differentiated: one dealing with more detailed material simulation and one dealing with overall behavior on a structural level, both of which warrant further investigation.

Research on the material level could be focused on the refinement and expansion of the existing material models used in micro-modeling analysis. Even though the models for the interfaces are of primary importance, further compatible continuum models for the units could also be the matter of investigation. Possible examples include the approximation of the Poisson effect and other micro-mechanical phenomena in the interfaces in two-dimensional simplified models and the improvement of nonlinear models capable of simulating cyclic effects. The degree of success in the development of new models is conditioned not only by the governing constitutive laws, but also by the appropriateness of the solution methods employed in their application. Finally, it should be stated that there is a distinct absence of a generally accepted method for determining the appropriate values for the material properties, especially concerning the stiffness parameters for the interface elements, especially in simplified models. This poses an interesting subject for

investigation since it could assist in the establishment of rules of thumb for practical matters, thus making the method more accessible.

Any progress made on the material level should definitely be tested on the structural level as well. However, there are certain areas of interest concerning the expansion of the method that are directly linked to general structural behavior and modeling. Given the fact that the method cannot be realistically applied to expanded structures, discontinuous methods could be used in the same large structure in conjunction with continuum methods, the former used for modeling locations of interest and the latter accounting for the bulk of the building. Additionally, the method could prove useful in the study of certain structural details, such as wall intersections, and the interaction with structural elements of other types, such as those used in strengthening. Finally, there has been very little work done concerning the dynamic transient analysis of masonry micro-models due to numerical difficulties, necessitating the employment of simplified nonlinear models.

In the middle ground between the material level and the structural level lies the area of the simulation of tests on small masonry specimens, as described above. By performing detailed analyses based on standardized tests, or even on devised setups, the method could be used as a virtual laboratory dedicated to the study of masonry. Subjects, such as the behavior of hollow units, the behavior of mortar or the validity of masonry design code provisions could be studied. A closely related potential application is the effort to derive the elastic and strength characteristics of a given masonry type through the detailed analysis of representative volume elements. The capability of numerical models based on the finite element to reliably predict the compressive strength of masonry composites remains an important goal and detailed micro-modeling approaches could investigate this area of interest.

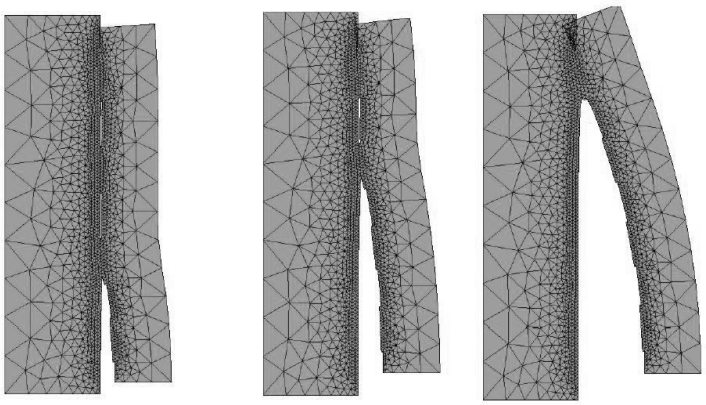

Figure 2.7 Modeling of unit/mortar interaction in shear [27].

So far the application of the method has only tentatively been tried in full three-dimensional analyses due to the high computational costs involved. It is not surprising that most such analyses have been performed under plane stress or plane strain assumptions, the former usually underestimating and the latter overestimating overall capacity. Therefore, considering how out-of-plane effects related to weak mortar confinement, transverse cracking of units and out-of-plane failure of units under high compression appear to be play an important role in masonry behavior, it would be interesting to attempt to investigate such phenomena either through the use of full three-

dimensional analysis or by taking out-of-plane effects into account indirectly. Possible choices for the latter include performing analyses under generalized plane state or enhanced plane strain assumptions, which, while being rough approximations of the actual three-dimensional stress state, have produced interesting results [103].

Finally, the method could be used as a tool in a FEM based nonlinear homogenization or multi-scale approach by simulating the behavior of small masonry cells, instead of performing closed form calculations based on various assumptions. This approach offers the possibility to minimize assumptions on the properties of the materials and their interaction and to simulate the behavior of representative volume elements with increased accuracy. So far, mostly meso-scale models, which assume perfect bond between units and mortar, have been used in FEM based homogenization efforts. Interface modeling could possibly allow for coarser meshes for the analysis of periodic unit cells, since interfaces can account for the discontinuities in the stress and strain fields. The two obvious drawbacks in such an endeavor are the requirement for a very detailed knowledge of the material properties of the constituents, the gathering of which may not be feasible, and the steep computational cost. Currently, it is rather difficult for FEM based homogenization to compete with other methods proposed for that purpose.

2.7.3 Application to Historical Structures

An area of great interest in the structural modeling of masonry is the study of historical masonry structures. Historical structures are often characterized by a lack of geometrical and material regularity, even within a single structural element, the existence of localized damage and the application of structural interventions. Furthermore, localized or diffuse variation in the mechanical properties of materials located in load-bearing elements in historical structures may adversely effect their structural behavior. For these reasons, adopting a strict continuum approach may be highly unsuitable. Therefore, micro-modeling should be considered as a possible analysis tool, for which purpose a number of possible applications for the method are presented.

Historical structures frequently suffer from structural damage in the form of large concentrated cracks. The methods developed for micro-modeling analysis could be utilized in simulating the effect of such cracks in the local and global response. More specifically, micro-modeling could simulate the opening, closing and development of such cracks under monotonic, cyclic or dynamic loading or under the influence of creep. Additionally, it could be of interest to model masonry fatigue in interfaces and applied to arched structures, such as bridges, in order to numerically estimate the remaining service life of historical structures doubling as infrastructure elements.

Multi-leaf and irregular masonry, both of which are extremely common in traditional and monumental architecture, present another possible field of application for the micro-modeling approach. In the case of multi-leaf masonry, the interaction of the wythes with the infill under various loading conditions could be modeled using this approach, in addition to modeling the wythes themselves through a simplified micro-model approach. In the case of irregular masonry, micro-modeling presents a more accurate geometrical definition of the structure able to capture

the structure's behavior with arguably greater accuracy that macroscopic approaches. The experimental and numerical investigation of the compressive behavior of either of the above cases offers a prime area of interest.

The extension of the method into full three-dimensional analysis could be attempted in the analysis of structures and elements of particular typology. Masonry arches and vaults are a possible field of application, although the computational cost may prove to be unwieldy. Furthermore, masonry pillars, being slender elements with relatively small ratios of overall structural dimensions to unit size, could be analyzed in segments with this method. A fact shared by the above mentioned structural types is that they extend the application field normally associated with micro-modeling analyses, which largely consists of shear walls.

Stone block masonry offers another possible field of application. Dry joints could be simulated with simplified micro-modeling methods with potentially less loss of accuracy and completeness of results compared to the analysis of masonry with mortar joints. Modeling of dry joints through interface elements could be formulated with a minimum of assumptions and geometrical and material simplifications, allowing for expansion into the area of cyclic behavior and dynamic response. Micro-modeling can also prove to be an accurate tool in the simulation of stone block masonry featuring stones with damage, such as cracks or missing parts that may affect stability or cause localized separation of elements.

Finally, the study of historical structures concerns the design of structural interventions for repair and strengthening. Micro-modeling could potentially provide a closer look into the effect of such interventions, the design of which is often based on some sort of interfacial interaction as well, on masonry structures as a whole and on the constituent materials. Micro-modeling could provide detailed information on the mediation of particular failure mechanisms, such as the propagation of cracks in the joints, by the application of different intervention techniques.

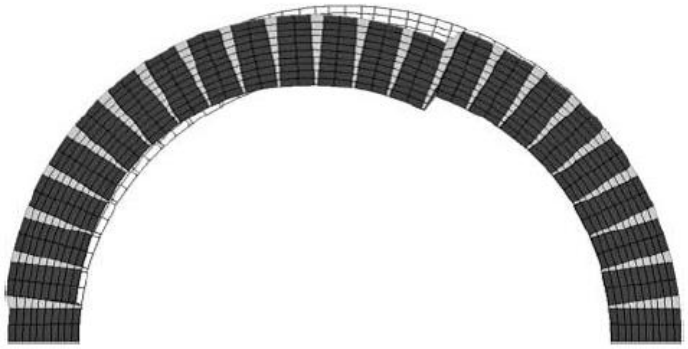

Figure 2.8 Deformed detailed micro-model of FRP reinforced masonry arch [134].

2.8 Mechanical Characterization of Existing Structures' Materials

2.8.1 Introduction

This literature review deals with matters pertaining to coupled mechanical characterization of masonry composites and constituents, The subject of compression is the focus of this review and discusses the matters of the characterization of the units and the mortar accompanying masonry composite tests, the measurements taken during these masonry composite tests and the existing codified provisions for such tests. Mention is given to the range of materials used for the construction of the mortars in masonry.

2.8.2 Testing of Materials and Assemblages

Stack bond masonry in concentric compression has been extensively studied with varied results [3, 20, 28, 64, 68, 71, 76, 78, 81, 106, 114, 119, 130, 136, 155, 159]. The number of concentric compression tests on running or Flemish bond masonry walls with an accompanying adequate characterization of the materials is more limited [25, 131]. The different combinations of materials present researchers with a wide range of possible choices for experimental study. However, reviewing the available inventory of experimental data, one finds a distinct predominance of cement and lime/cement mortars in structural testing. While chemical, curing, mechanical property and sustainability issues of modern pure lime mortars have been extensively studied [32, 84–86], the investigation of their direct structural application has not enjoyed the same attention despite its being extremely common in historical structures.

Measurement of the compressive and flexural strength of units and mortar is well documented and even codified in design guidelines [39, 41, 42]. Further investigation of the research literature and, especially, testing standards reveals a lack of commitment to the measuring of their Young's moduli. Design codes rely solely on the values of the compressive strength of the constituents for the determination of the compressive strength of masonry, which, in turn, is the only parameter for the determination of the masonry Young's modulus [40]. Furthermore, there is a lack of guidelines for the measurement of the Young's modulus of both the units and, especially, the mortar.

Published results on the Young's modulus of units and mortar often do not explain in detail the method used to obtain these results, while other studies present a detailed explanation of such methods alongside their results [78, 106, 114, 119, 159]. In those cases where numerical simulation follows the experiments, these values are measured instead of estimated through empirical means and expressions. This is true for both the materials and the finished masonry.

Measurements of the elastic properties of units are easier to perform and are, therefore, more common. However, compressive tests performed on the unit beds are usually performed on entire units [81, 106, 135]. The dimension ratios do not allow for size effects to be eliminated, thus not allowing for the true uniaxial compressive strength of the material to be measured. By

measuring cylindrical, cubic or cuboid samples extracted from bricks it has been intended to limit or study these size effects or to simply form specimens with appropriate dimensions to facilitate measurements [21, 119].

The issue of the difference between the properties of the mortars in freestanding samples and in the composite remains open. Efforts have been made to measure isolated deformations of the units and the mortar joints in masonry under compression [78, 155]. For other cases, the elastic properties of the mortar in the joints are indirectly deduced by measurements in the units and in the composite [11, 28, 120] or are not measured at all.

2.8.3 Material Characterization and the Prediction of the Compressive Strength of Masonry

Standard material testing practice for masonry constituents is often shaped by demands effected by masonry design codes, which offer closed form expressions for the determination of the compressive strength of masonry. These expressions are often a function of only the compressive strength of the units and the mortar [2, 40]. Being intended for generally application, and in order to be on the safe side from a design perspective, these expressions usually produce conservative results and may not be suitable for particular cases. Furthermore, the underlying theoretical basis may not be entirely compatible with the effects encountered in masonry with highly deformable mortars.

Other closed form expressions have been proposed which rely on the elastic properties of the constituent materials or the tensile strength of the units (e.g. [73, 74, 117]). These expressions have, in theory, a wider applicability spectrum than design code provisions. However, they may produce spurious results for certain combinations of material properties.

Expressions for the prediction of the compressive strength of multi-leaf members rely on a macroscopic determination of the compressive strength of the leaves and a quantification, using numerical parameters, of their interaction under applied compression [57]. Other expressions have a similar theoretical basis, but are mostly used for the determination of the effects of grouting [151, 157].

2.9 Summary and Conclusions

The state of the art of the masonry micro-modeling technique using the finite element method has been investigated in the available related literature. The investigation includes the principles and goals of the method, the theoretical body of work from which it draws and the practical aspects of its application. The most recent developments in the field are presented, along with a number of potential future work subjects which could enhance the practicality and application spectrum of the method as well as its capability to simulate certain aspects of masonry behavior with increased accuracy and completeness. Suggestions are also offered in terms of the coupling of analytical procedures with experimental campaigns for the derivation of mechanical properties

of the constituent materials of masonry, and especially their interaction, most relative to the nature of analysis of structures with interfaces. Finally, several possible applications related to historical structures are presented for consideration.

Masonry analysis through micro-modeling techniques presents a research field which could potentially make significant contributions in understanding the structural behavior of masonry on a structural level as well as from a localized perspective. Either through a phenomenological or a physical approach towards simulating actual masonry behavior, it is possibly the most appropriate tool for the numerical approximation of the intricacies of the structural character of masonry.

Masonry compression tests are of special importance, considering the predominance of the value for the compressive strength in design. Therefore, a fairly large inventory of experimental results is available.

The majority of masonry compression tests which include detailed characterization of the materials is followed by numerical reproductions of these experiments. These have been fairly successful in predicting the compressive strength on a case-by-case basis. This trend, along with the tendency of empirical relations to be inaccurate for a range of combinations, urges towards adopting a stance of detailed material characterization during masonry test campaigns, including the elastic properties of the materials.

Chapter 3

Finite Element Micro-Modeling of Masonry under Compression

3.1 Introduction

Due to the large number of existing buildings composed of masonry structural members such as load bearing walls, the numerical modeling and analysis of masonry structures are receiving at present a growing amount of attention. Masonry buildings are found worldwide and encompass not only a large building stock, still in use, but also valuable architectural heritage.

Given the importance of the seismic action and the potential seismic vulnerability of masonry structures, a significant part of this effort is being devoted to the numerical simulation of masonry failure governed by tension and shear. In particular, the shear failure of masonry walls has been modeled by means of simplified micro-modeling using interface elements to model existing and arising planes of weakness, Lourenço & Rots [96]. Macro-models have also been employed for this purpose, taking into account the orthotropic properties of masonry, Lourenço et al [97], Syrmakezis & Asteris [142] and Pelà et al [126]. Instead, more limited attention has been allocated to the detailed simulation of the masonry response and failure in compression. However, an accurate characterization of the compressive strength of masonry is needed in order to verify the capacity of masonry structures subject to both vertical and horizontal actions, both of which activate compressive struts in masonry members. The main drawback of simplified micro-models and macro-models, which is the assignment of a specified value for the compressive strength of masonry, becomes crucial in such cases.

Several attempts of simulation of the compression behavior of masonry have been undertaken using three-dimensional models with varying purposes and results. This behavior, governed by the interaction of the units and the mortar, may be strongly affected by out-of-plane effects, as analytical models have indicated, Hilsdorf [74]. One of the first numerical attempts involved a set of elastic analyses on hollow concrete masonry under concentric compression, Hamid & Chukwunenye [71]. A similar parametric analysis was conducted to study the influence of elastic properties and joint dimensions on stress distribution and masonry elasticity, Reddy et al [130]. The differences between plane stress, generalized plane strain and three-dimensional modeling

of masonry in terms of strength, elasticity and stress distribution have been discussed, Anthoine [16].

Similar observations have been made using nonlinear models in order to comment on the effects of model geometry on the predicted compressive strength of masonry, Berto et al [24], Barbosa et al [23]. Finally, the general deficiencies of plane models in accurately reproducing the behavior of single- and multi-leaf walls in numerical analyses have also been noted by Milani et al [110, 111]. According the latter authors, three-dimensional effects need to be taken into account for the correct derivation of the failure envelope of masonry under in-plane loads. Additionally, other case studies include the simulation of concentric, Furtmüller & Adam [64], Schlegel [137], Vyas & Reddy [159], and eccentric compression of masonry, Adam et al [3], Brencich et al [28]. Finally, three-dimensional periodic unit cells have been used for the verification of the results of homogenization methods for masonry under triaxial normal and shear stress, Cecchi et al [36], Zucchini & Lourenço [162].

Application of modeling approaches proposed for the study of masonry in compression has been rather narrow in scope, normally extending to only a very small number of experimental cases each. This fact also narrows the capacity for comparison between the results of experiments, empirical expressions and numerical results concerning the compressive strength of differing types of masonry.

The purpose of the modeling strategy presented herein is found in the detailed simulation of the failure of masonry under compressive loading by means of a general approach combining versatility (the ability to analyze a variety of cases regarding geometry and material constituents) and a moderate computer cost. The strategy is based on detailed micro-modeling where specific constitutive equations are used separately for the material constituents (mortar and units) and the unit/mortar interfaces.

The applicability of the method focused on masonry prisms and walls consisting of solid bricks and mortar arranged in stack bond, running bond and Flemish bond walls and in English bond pillars. In principle, this approach can be applied to any type of masonry bond, since geometrical peculiarities are taken into account explicitly in the model geometry. Adopting a detailed micro-modeling approach for the simulation of failure in masonry means that, in principle, geometry and morphology of the structure should not be a limiting factor as long as the phenomena affecting strength, elasticity and failure initiation and development are modeled accurately.

The modeling approach has been tested against existing experimental data, focusing exclusively on case studies where sufficient material characterization has been carried out. In this research, a total of fifty different experiments have been simulated. Micro-modeling requires knowledge of several elastic and strength parameters, many of which are usually not measured in experimental campaigns, the Young's moduli being a case in point. The analyses carried out in this chapter and their comparison with the experimental data may contribute to the enrichment of the inventory of numerical results on the analysis of masonry structures and provide a starting point for further investigation through parametric and sensitivity analyses.

Most of the case studies encountered in the literature and actually adopted for the present

research involve units stronger than the mortars. This leads to compressive failure modes governed by crushing of the mortar under multi-axial compression and cracking of the units under combined compression and tension. The proposed numerical approach can be applied to masonry with typical combinations of materials and structural arrangements, but is especially suited for the analysis of traditional brick masonries composed of lime mortars of low compressive strength. Modern brick masonries, built with cement mortar of a compressive strength close or higher than that of the bricks may require a different approach. The applicability of the method is further discussed in the presentation of the results. The numerical analyses have been performed using the finite element program DIANA [144].

3.2 Material Models

3.2.1 General

The compressive strength of masonry is determined by, among other factors, the properties of its constituent materials. According to empirical expressions, such as the one found in [40], it is estimated by the compressive strength of both the units and the mortar, normally assuming the former is higher than the latter. The resulting strength of the composite lies between the two values, implying that the mortar fails under a stress level higher than its uniaxial compressive strength.

Furthermore, the failure mode commonly encountered in masonry in compression, aside from the crushing of the joints, is vertical cracking of the units, caused by the lateral expansion of the mortar in the joints. Failure at the unit/mortar interface in horizontal, vertical and transversal joints occurs by way of separation under tension, especially in the vertical and transversal joints, and shear slipping.

Therefore, detailed micro-modeling approaches for the simulation of masonry need to be able to model the nonlinear behavior of the units and the mortar in tension leading to cracking and pressure dependent behavior under multi-axial compression. Tensile and shear failure at the unit/mortar interface need to be modeled as well. Thus the failure of the structure in both arising and macroscopically existing planes of weakness needs to be accounted for.

For the present research, the numerical analyses have been performed using a mixed pressure dependent plasticity model in compression and a smeared cracking model in tension, organically combined in a total strain nonlinear model with secant unloading [138, 144]. Therefore, it is possible to simulate all failure modes normally expected to arise in masonry under compression.

Damage due to tensile cracking is modeled using a rotating crack model, in which stress-strain relationships are evaluated in the principal directions of the strain vector. The direction of the cracks may therefore change according to the direction of principal strain. Rotating crack models, initially developed for concrete, have been used in applications involving masonry structures [90, 129].

Shear behavior is explicitly governed by a relationship between shear stress and shear strain,

while six internal damage variables α_k (assembled in the α vector), indicating the ratio of damaged to effective stress, monitor the deterioration of the material, which is non-recoverable.

This constitutive law has been used in numerical simulations for concrete and masonry macro-models. It may be considered an attractive choice for the simulation of masonry since it is capable of modeling its behavior in compression, tension and the interaction of the failure modes.

3.2.2 Tensile Behavior

The stress-strain relationship is elastic until the tensile strength is reached. The expression of the tensile behavior in the post-peak using values for the tensile strength and the tensile fracture energy is accomplished through the use of an exponential softening curve. For the post-peak of the tensile stress-strain relation, the damaged stress is equal to:

$$\sigma(\varepsilon_{cr}) = f_t e^{-\frac{\varepsilon_{cr}}{\varepsilon_{cr,u}}} \tag{3.1}$$

where E is the initial tangent Young's modulus and ε_{cr} is the crack strain and $\varepsilon_{cr,u}$ the ultimate crack strain. To calculate $\varepsilon_{cr,u}$ the softening is rewritten as:

$$\sigma(\varepsilon_{cr}) = f_t y\left(\frac{\varepsilon_{cr}}{\varepsilon_{cr,u}}\right) = f_t y(x) \tag{3.2}$$

According to the definition of the tensile fracture energy:

$$G_f^I = h\int_{\varepsilon_{cr}=0}^{\varepsilon_{cr}=\infty} \sigma(\varepsilon_{cr})\, d\varepsilon_{cr} = f_t h\left(\int_{x=0}^{x=\infty} y(x)\, dx\right)\varepsilon_{cr,u} \tag{3.3}$$

Therefore, the ultimate crack strain is:

$$\varepsilon_{cr,u} = \frac{G_f^I}{f_t h} \tag{3.4}$$

A crack bandwidth equal to a characteristic dimension given by $h = \sqrt[3]{V}$ is adopted, where V is the volume of the finite element. Snap-back is avoided if the absolute initial slope of the softening diagram for the given crack bandwidth is lower than the initial tangent Young's modulus. This holds for:

$$h \leq \frac{G_f^I E}{f_t^2} \tag{3.5}$$

Finally, cracked directions subjected to tension are not affected by the Poisson effect, meaning that such loading does not lead to contraction in the perpendicular directions. Therefore, an orthotropic formulation has been adopted for the Poisson's ratios, which are reduced at the same rate as the secant modulus after cracking [138].

3.2.3 Shear Behavior

Due to the rotating crack approach adopted, the direction of the crack always coincides with that of the maximum principal strain. Therefore, the shear behavior across the crack need not be taken into account.

3.2.4 Compressive Behavior

Uniaxial unconfined compressive behavior is modeled using a parabolic compression curve based on fracture energy [61]. The curve is defined by three characteristic strain values: the strain for which hardening is initiated at one third of the compressive strength, the strain for which maximum stress is reached and the strain for which softening is terminated. For a uniaxial compressive strength f_c and an initial tangent modulus of E, the strain $\varepsilon_{c/3}$, at which one third of the compressive strength has been reached, and is expressed as:

$$\varepsilon_{c/3} = -\frac{1}{3}\frac{f_c}{E} \tag{3.6}$$

The strain ε_c, at which the maximum compressive strength is reached, and is expressed as:

$$\varepsilon_c = -\frac{5}{3}\frac{f_c}{E} = 5\ \varepsilon_{c/3} \tag{3.7}$$

The ultimate strain ε_u, at which the material has terminated its softening in compression, which is expressed as:

$$\varepsilon_u = \varepsilon_c - \frac{3}{2}\frac{G_f^c}{h\ f_c} \tag{3.8}$$

where, in turn, G_f^c is the compressive fracture energy and h is the characteristic element length. In addition to the mesh insensitivity of the model, strain localization and dissipation of the compressive fracture energy is ensured by the geometry of the models themselves given that compressive damage is normally expected to occur in the mortar joints. The parabolic compression curve is defined for strain ε by the piecewise equation:

$$f = \begin{cases} -f_c \frac{1}{3}\frac{\varepsilon}{\varepsilon_{c/3}} & \text{for} \quad \varepsilon_{c/3} < \varepsilon \leq 0 \\ -f_c \frac{1}{3}\left(1+4\left(\frac{\varepsilon-\varepsilon_{c/3}}{\varepsilon_c-\varepsilon_{c/3}}\right)-2\left(\frac{\varepsilon-\varepsilon_{c/3}}{\varepsilon_c-\varepsilon_{c/3}}\right)^2\right) & \text{for} \quad \varepsilon_c < \varepsilon \leq \varepsilon_{c/3} \\ -f_c\left(1-\left(\frac{\varepsilon-\varepsilon_c}{\varepsilon_u-\varepsilon_c}\right)^2\right) & \text{for} \quad \varepsilon_u < \varepsilon \leq \varepsilon_c \\ 0 & \text{for} \quad \varepsilon \leq \varepsilon_u \end{cases} \tag{3.9}$$

Lateral pressure dependence, which accounts for increased strength under confining stress, has been modeled using the four parameter Hsieh-Ting-Chen failure surface [77, 138], which is defined as:

$$f = C1\frac{J_2}{f_c^2} + C2\frac{\sqrt{J_2}}{f_c} + C3\frac{\sigma_1}{f_c} + C4\frac{I_1}{f_c} - 1 = 0 \tag{3.10}$$

where I_1 and J_2 are the stress invariants and σ_1 is the maximum principal stress. The numerical values of the material parameters $C1$, $C2$, $C3$ and $C4$ are determined by four experimental tests: uniaxial compression, uniaxial tension, equal biaxial compression and triaxial compression. All the stresses in the criterion are normalized by the uniaxial compressive strength, implying that the behavior described by the model may be applied to materials of different strength but similar behavior. The stress f_{c3}, a negative stress value which results in compressive failure, is determined by scaling the linear elastic stress vector $\sigma_c = sE\varepsilon_{nst}$ such that equation (3.10) holds, where s is the scaling factor sought, E the tangent Young's modulus and ε_{nst} the principal strain vector. Thus, f_{c3} is defined as the minimum normal stress component of the stress vector. The confined compressive strength is expressed as $f_{cf} = -f_{c3}$ and its ratio to the uniaxial compressive strength is expressed as $f_{cf} = K_\sigma f_c$. The peak strain factor, relating peak to initial strain ($\varepsilon_P = K_\sigma \varepsilon_0$) is equal to the ratio between confined and uniaxial compressive strength.

The peak stress is obtained by taking into account the influence of lateral cracking. This influence on the compressive behavior is modeled using a reduction factor [154]. The reduction factor, denoted as $\beta_{\sigma_{cr}}$, is a function of the average lateral damage variable given by $\alpha_{lat} = \sqrt{\alpha_{l,1}^2 + \alpha_{l,2}^2}$ vector in the two lateral to the compressive load directions, and is calculated by:

$$\beta_{\sigma cr} = \frac{1}{1+K_c} \leq 1 \tag{3.11}$$

where:

$$K_c = 0.27\left(-\frac{\alpha_{\text{lat}}}{\varepsilon_0} - 0.37\right) \tag{3.12}$$

Finally, the peak stress is given by:

$$f_{\text{P}} = \beta_{\sigma_{cr}} \cdot f_{cf} \tag{3.13}$$

The initial strain is given by the equation:

$$\varepsilon_0 = -\frac{n}{n-1}\frac{f_c}{E} \tag{3.14}$$

with:

$$n = 0.80 + \frac{f_{\text{P}}}{17} \tag{3.15}$$

Increase in ductility due to lateral confinement is modeled according to the following stress-strain expression:

$$f = -f_P \left(1 - (1-r)\frac{\varepsilon - \varepsilon_p}{\varepsilon_U - \varepsilon_P}\right) \leq -f_{cr} \tag{3.16}$$

assuming a value for the ultimate strain:

$$\varepsilon_U = \left(\frac{f_P}{f_c}\right)^3 \varepsilon_P \tag{3.17}$$

The residual compressive strength is expressed as:

$$f_{cr} = f_c r \tag{3.18}$$

where:

$$r = 0.1\left(\frac{f_P}{f_c}\right)^3 \tag{3.19}$$

A comparison of the basic parabolic curve for uniaxial compressive loading and its comparison to a curve under lateral compression is presented in Figure 3.1.

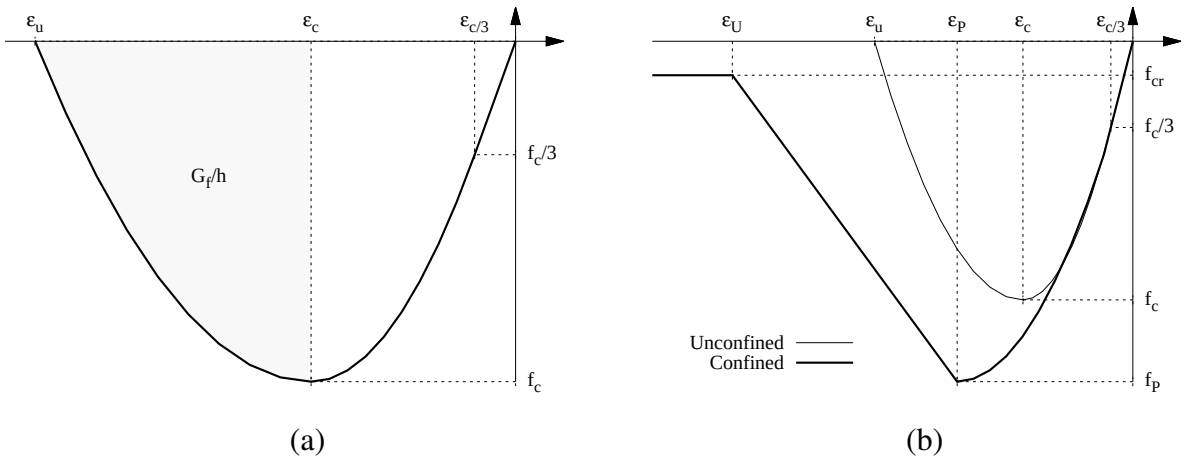

Figure 3.1 (a) Uniaxial compression curve and (b) compression curve under lateral compression load.

3.2.5 Interface Behavior

Unit/mortar interface behavior is described using a discrete cracking model based on a total deformation theory, in which interface tractions are expressed as a function of the total relative displacements [144].

Elastic behavior is assumed until the traction reaches the assigned tensile strength and a brittle behavior is assumed post-peak: normal stiffness is reduced to zero. Therefore, normal tractions t_n are expressed as:

$$t_n = \begin{cases} k_n \Delta_n & \text{if } \Delta_n \leq f_{t,i}/k_n \\ 0 & \text{if } \Delta_n > f_{t,i}/k_n \end{cases} \tag{3.20}$$

where k_n is the normal interface stiffness, $f_{t,i}$ is the interface tensile strength and Δ_n is the interface relative displacement.

It is assumed that shear stiffness reduces to zero after the onset of cracking, by adopting a shear retention factor of zero.

3.3 Modeling

3.3.1 Geometry

A body of work involving detailed modeling of masonry under in-plane loads, in which units and mortar are modeled separately, has been produced [16, 23, 24]. In these cases, the unit/mortar interaction results in out-of-plane stresses which may significantly alter the compressive behavior of the masonry composite. This is especially true in cases where there is significant discrepancy between the elastic characteristics of the two constituent materials, namely the Young's modulus and the Poisson's ratio.

It is appealing from the point of view of computational cost and modeling effort to model wall structures, such as running or Flemish bond masonry using simple plane geometrical models, such as plane stress or plane strain. However, the results obtained demonstrate some patterns of divergence from experimentally observed behavior and obtained compressive strength. In-plane stress analyses the units afford very low confinement to the mortar, while in-plane strain analyses the confinement is excessive. The results of the under- and over-estimation of the effects of unit/mortar interaction in these cases are, expectedly, too low compressive capacity in the former and too high compressive capacity in the latter. The failure modes are also characteristic of these modeling approaches, in plane stress more so than in plane strain, with the former leading to excessive yielding in compression of the weakest material and with the latter usually leading to excessive cracking of the strongest and stiffest. The issue of directly modeling the non-constant geometry of, for example, Flemish bond walls and English bond columns raises further doubts concerning the adequacy of plane methods. Figure 3.2. illustrates various masonry typologies of different degrees of geometrical complexity.

The regular assumptions accompanying plane analysis methods are not sufficient due to the geometrical layout of the masonry composite. The ratio of the thickness of the mortar joints, which is of the order of $10mm$, over the thickness of the masonry, which is of the order of $100mm$, invalidates the plane stress assumption of zero thickness. This dimension ratio results in out-of-plane effects, and stresses, to become locally significant near failure even though the assumption is conceptually sound on a global, structural level. Similarly, the assumption of infinite masonry thickness certainly does not hold globally, though it may be a legitimate simplification for local effects given the usual ratio of masonry thickness to mortar joint thickness. Generalized plane

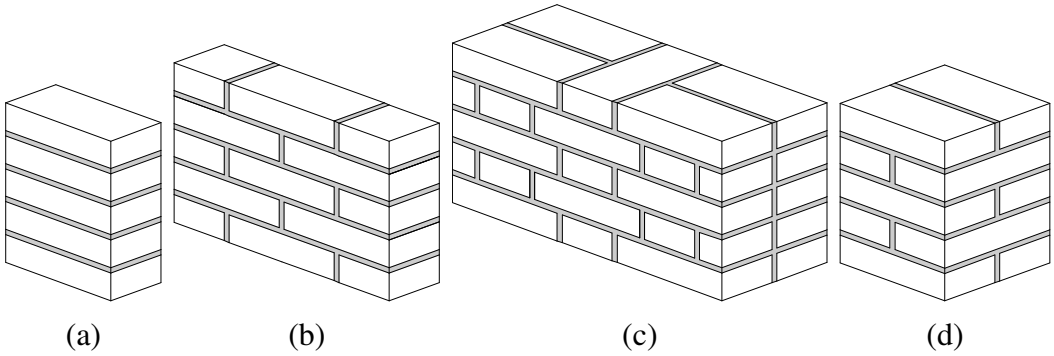

Figure 3.2 Model geometries: (a) stack bond prism, (b) running bond wall, (c) Flemish bond wall and (d) English bond column.

strain, although maintaining some elements of phenomenological modeling, is usually a closer approximation of the actual behavior and leads to better results for the simulation of local failure [95, 103].

Overall, the more homogenous the composite is, implying units and mortar of similar properties, plane stress becomes more accurate, while plane strain becomes more accurate for increasing property disparities between the two material phases. The two plane methods should generally provide accurate results for extreme or particular cases, but their capacity to provide accurate results for intermediate or general cases has not been demonstrated.

Three-dimensional micro-modeling, while computationally the most demanding approach, has been shown to produce the consistently most accurate results in terms of capacity when applied to a large number of different experimental cases. No geometrical assumptions are made and, therefore, out-of-plane effects and stresses are taken into account organically, both on the structural and on the local level, thus allowing the modeling of masonries with a variety of different geometrical textures. Vertical and horizontal compressive strength values obtained using this method fall between those obtained from plane stress and plane strain. Overall, the comparison with available experimental data is favorable compared to that of plane methods. Interestingly, all the above mentioned modeling approaches produce equal initial stiffness in compression for the masonry composite.

Figure 3.3 illustrates examples of three-dimensional models, including the overall layout and the distribution of stress under vertical loading. In this qualitative representation, of the stresses, where the units are less deformable than the mortar, it can be observed that the distribution of all stress components follows a repeating pattern across the surface of the wall. The bed joints are under horizontal confinement, the units are in horizontal tension and the head joints are under lower vertical compression than the units. Shear stresses concentrate in the cross joints and the head joints are in horizontal tension.

In the present work the models are composed of 20-node isoparametric solid elements based on quadratic interpolation and $3 \times 3 \times 3$ Gauss integration scheme [144]. The fineness of the mesh was adjusted accordingly as to include at least two elements along the thickness of each joint. Symmetric loading of symmetric structures allows for three planes of symmetry to be applied, thus greatly reducing the size of the models.

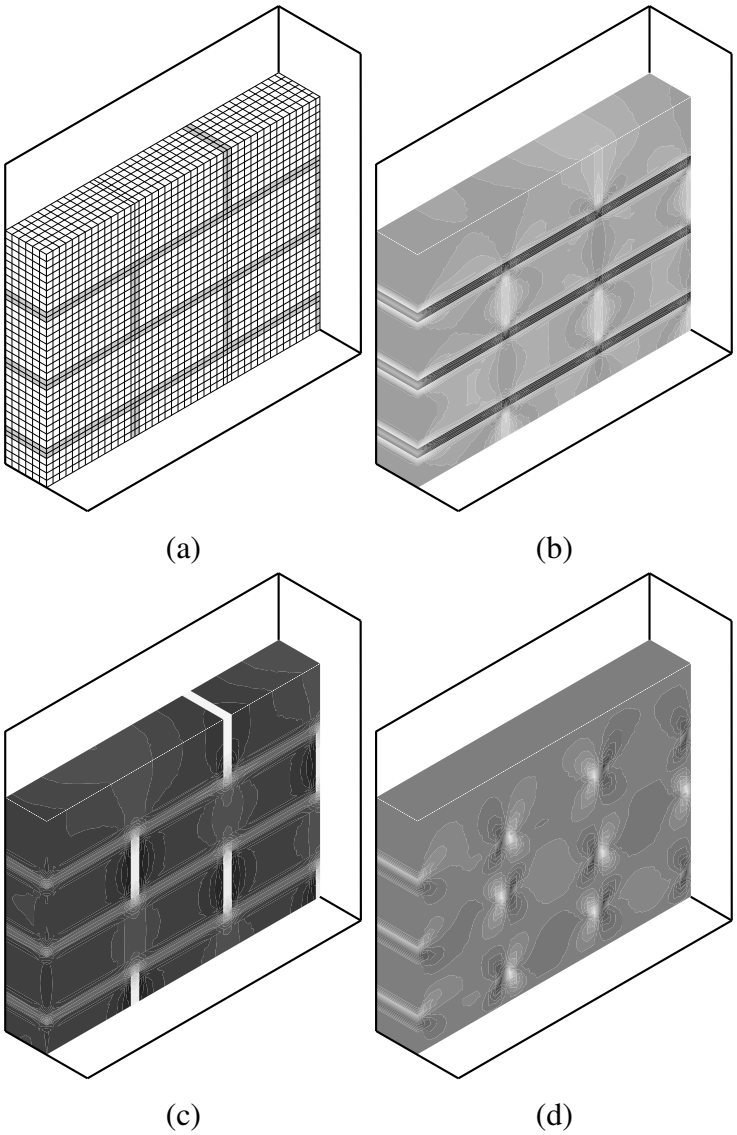

Figure 3.3 Three-dimensional masonry model examples under vertical compressive load with planes of symmetry indicated: (a) finite element mesh, (b) horizontal normal stress, (c) vertical normal stress (d) in-plane shear stress.

The unit/mortar bond was modeled using a discrete cracking law applied on zero thickness $8+8$ node plane quadrilateral interface elements, based on quadratic interpolation and a 4×4 Newton-Cotes integration scheme [144].

3.3.2 Solution Method and Loading

The analysis procedure for the solution of the physically nonlinear problem was the Modified Newton-Raphson method. A Line Search algorithm was used to predict the iterative displacement increment and to speed-up the convergence rate.

The loading was prescribed in displacement control. An energy based convergence criterion was used for the convergence check, since displacement loading reduces the usefulness of the displacement norm criterion and the, mostly, unrestrained lateral expansion of the models

reduces the buildup of internal forces, thus making the force norm less useful. For the convergence criterion a 0.5% energy norm was adopted. When significant interfacial nonlinearities were encountered, the solution method was switched to a Secant-Crisfield method with a 0.1% energy norm, as the Newton-Raphson faced convergence problems in those cases.

The finite element code DIANA, in which the above constitutive laws and element types are implemented, was used for the analyses, employing a parallel direct sparse solver [144].

3.4 Inventory of Experimental Data

3.4.1 Overview

There is a relatively large inventory of existing experimental data on masonry compression. However, the number of cases qualifying for a numerical reproduction using micro-models is fairly limited. The cause of this is the lack of sufficient material characterization. Parametric analysis performed in this research has indicated a clear, if rather strong, influence of the Young's modulus of both units and mortar on the compressive capacity and the failure mode observed. Difficulties in measuring the Young's moduli of small size specimens, coupled with the reliance on empirical expressions for the determination of the strength of the composite based solely on the compressive strength of the two constituents [40], have brought about a lack of motivation for taking adequate measurements of it, especially in the case of mortars, despite observations on the effect of the deformation properties of the masonry constituent materials on the behavior of masonry composites [72, 122, 140]. Tensile strength measurements are also often neglected in unit characterization, even though unit cracking is commonly observed in compression of masonry.

Certainly, there exists a strong correlation between the compressive strength and the Young's modulus or the tensile strength, especially in modern types of units. However, the validity of a direct correlation between the two values is less clear for masonries built with low strength mortars (such as traditional lime mortars) where other factors, such as composition and aging, may affect significantly on the resulting masonry stiffness.

In summary, the available candidate case studies for numerical simulation are few in number and mostly concerning stack bond prisms [3, 8, 28, 56, 64, 68, 76, 81, 104, 106, 119, 124, 128, 130, 137, 156, 159]. Case studies of walls in running bond are not uncommon [68, 105, 120, 131, 156] but tests on walls in Flemish bond are rare [25] while a few suitable examples of English bond pillars were also identified [64, 68]. The vast majority of these cases involve the characterization of clay brick masonry with a few exceptions involving stone block masonry [104, 137] or compressed cement block masonry [159]. All mortars were either cement or lime/cement mortars, with one exception where pure lime mortars were used [56].

The average ratio of Young's modulus to compressive strength is 328 for the units, with values ranging from 14 to 1265. The average for the mortars was 699, with values ranging from 22 to 2094. The average for the masonry was 356, with values ranging from 29 to 1903. The

highest figure corresponds to the only case with a ratio above 1000 while the remaining values, and their average, are much lower than 1000, which is the characteristic value recommended by design codes (e.g. [40]).

3.4.2 Assumed Values

The dimensions, compressive strength and Young's modulus of the units and mortar were reported in all the examined cases, with the exception of one case in which the Young's modulus of the mortar was calculated in this study using the values given for the units and the masonry composite.

In order to perform the analyses of the available case studies, it was necessary to assume values for the missing parameters. The available literature overviewed in the present work offers an adequate amount of information on which to base these assumptions.

The average value of the measured Poisson's ratio in the set of case studies is 0.13 for the units with values ranging from 0.07 to 0.24 while for the mortars it is equal to 0.15 with values ranging from 0.07 to 0.2. In the cases where it was not reported, the Poisson's ratio for the units was chosen as being equal to 0.15 while a value between 0.15 and 0.25 was chosen depending on the type of mortar. In [56, 124] a weak lime mortar was used, so a value of 0.25 was adopted. For [8, 68, 119, 120, 156], for which a cement/lime mortar was used, a value of 0.20 was adopted. In [76, 81] Portland cement mortars were used and a value of 0.15 was used.

The average ratio of tensile to compressive strength for the units was 9% with values ranging from 1.8% to 23.9%. For the mortar the average was 8.2% with values ranging from 5% to 26%. For all the mortars a ratio of 10% was assumed for the missing values. In the case of the units the ratio differed from case to case depending on the material used and the workmanship employed. For [68] and [119] a ratio of 10% was used since they involved wire cut solid clay bricks. The average value of all solid clay bricks in the inventory had an average ratio of 9.3%. This value is similar to the 10% usually assumed for masonry units. In [81] a ratio of 5% was assumed since the campaign was performed using hand molded bricks. This lower percentage was assumed in order to reflect the poorer quality and consistency of hand-made bricks compared to machine molded bricks. In [130] soil-cement blocks were constructed, therefore a 5% ratio was adopted. For [104], which involved granite units, a ratio of 5% was chosen. According to [49] this is a ratio that fits the available experimental data on granites well.

The plasticity and cracking models require values for the compressive and mode-I fracture energies in order to describe the softening behavior of the materials. The current status of the research on these values for clay bricks and, especially, lime mortars is quite limited. Only a small number of the cases in the experimental inventory include values for the compressive and tensile fracture energy of the units and/or the mortar. The values for the fracture energy of the units and the mortar were determined using equations (3.21) and (3.22). The compressive fracture energy of both the units and the mortar was calculated assuming a ductility index parameter of $1mm$, defined as

$$d = G_f^c / f_c \tag{3.21}$$

while the tensile fracture energy was calculated according to the following equation:

$$G_f^I = 0.025\,(2f_t)^2 \tag{3.22}$$

which is based on the equation provided for the calculation of the tensile fracture energy by CEB-FIP Model Code 1990 [34] adjusted to assume a ratio between tensile and compressive strength of 5% and a maximum aggregate size of $8mm$. The wide range of mortar and unit materials used in masonry and the lack of information concerning the values for their fracture energy necessitates the adoption of the above rather conservative values.

Very few of the experimental cases provide any measurement of the unit/mortar interface properties. Furthermore, only a small number of works focused on these properties exists [15, 43] which can hardly be used as a general guideline in a study of this extent. Therefore, representative values had to be assumed. Throughout the cases a tensile strength of $0.2N/mm^2$ was considered, while zero Mode I fracture energy (brittle cracking) and zero shear retention after the formation of the crack were assumed. Prior to failure the bond is considered perfect, therefore a large initial elastic stiffness was considered in the normal and perpendicular directions of the interface, meaning that virtually all deformation in the interface is nonlinear.

The numerical parameters $C1$, $C2$, $C3$ and $C4$ were taken as being equal to 2.0108, 0.9714, 9.1412 and 0.2312 respectively. These values correspond to a tensile strength equal to 10% of the compressive strength, a biaxial compression strength equal to 1.15 times the uniaxial and a compressive strength under biaxial pressure equal to 80% of the compressive strength equal to 4.2 times the uniaxial strength. All four tests necessary for the complete determination of the four parameters are practically never available for mortars used in masonry. This problem is compounded in the case of existing masonry structures, where material sampling for all four tests is very difficult. The problem is less crucial in the case of masonry units, either clay or stone, since the behavior of masonry is not influenced by the pressure dependent behavior of the units in compression. Since the failure mode in tension is governed by the smeared cracking model, the determination of the ratio of tensile to compressive strength is not crucial.

3.5 Results

The cases available for numerical analysis include thirty-one stack bond cases (S), nine running bond masonry cases (R), three Flemish bond masonry cases (F) and seven English bond pillar cases (P) for a total of fifty cases. The cases for each bond type have been sorted and numerically named in ascending order according to their statistical fit with the experimental compressive strength.

The material properties and dimensions for the models were taken as reported in the experimental results and are shown in Tables 3.1 through 3.4. The values assumed as mentioned in the

preceding paragraphs for unknown quantities are displayed in curly brackets. Examples include several Poisson's ratios and values for the tensile strength. The experimentally achieved values, along with the numerical value for the compressive strength, are also shown in the same table.

Table 3.1 Stack bond prism cases. Comparison of experimental and analysis results. Assumed values in curly brackets.

Case	Ref.	E_u $[N/mm^2]$	ν_u [-]	f_{cu} $[N/mm^2]$	f_{tu} $[N/mm^2]$	h_u $[mm]$	l_u $[mm]$	t_u $[mm]$	E_m $[N/mm^2]$	ν_m [-]	f_{cm} $[N/mm^2]$	f_{tm} $[N/mm^2]$	h_m $[mm]$	l_m $[mm]$	t_m $[mm]$	$f_{c,exp}$ $[N/mm^2]$	$f_{c,FEM}$ $[N/mm^2]$	$E_{c,exp}$ $[N/mm^2]$	$E_{c,FEM}$ $[N/mm^2]$
S1	[106]	9900	0.17	44.0	1.79	55	194	89	1750	0.16	6.20	0.62	7.5	-	-	19.70	19.44	-	6456
S2	[56]	4200	0.16	23.0	3.10	45	290	135	125	{0.25}	1.25	0.19	10	-	-	12.03	10.50	600	814
S3	[68]	976	{0.15}	5.7	{0.57}	75	230	105	1500	{0.20}	1.16	{0.12}	12	-	-	1.67	2.21	467	1016
S4	[159]	14500	0.18	11.5	0.71	80	260	120	6450	0.16	3.50	{0.35}	10	-	-	6.15	6.83	-	13017
S5	[68]	3370	{0.15}	23.00	{2.30}	75	230	105	8570	{0.20}	5.14	{0.51}	12	-	-	6.70	7.40	2393	3525
S6	[8]	135	{0.15}	9.3	0.46	52	212	104	795	{0.20}	9.37	{0.94}	10	-	-	7.22	7.94	207	154
S7	[56]	4200	0.16	23.00	3.10	45	290	135	250	{0.25}	1.90	0.40	10	-	-	13.73	14.80	1100	1287
S8	[137]	5500	0.11	12.00	0.90	113	240	175	2770	0.07	4.60	{0.46}	30	-	-	4.68	5.44	4200	4702
S9	[68]	3370	{0.15}	23.00	{2.30}	75	230	105	5450	{0.20}	4.36	{0.44}	12	-	-	7.40	8.17	3135	3628
S10	[68]	976	{0.15}	5.70	{0.57}	75	230	105	238	{0.20}	0.60	{0.06}	12	-	-	1.25	2.17	379	735
S11	[159]	14500	0.18	11.5	0.71	80	260	120	6450	0.16	3.50	{0.35}	7	-	-	6.32	7.35	-	13464
S12	[159]	14500	0.18	11.5	0.71	80	260	120	6450	0.16	3.50	{0.35}	20	-	-	5.01	6.21	-	10400
S13	[3]	2000	0.10	13.8	3.30	55	250	110	1700	0.20	9.20	2.40	10	-	-	14.55	13.26	1936	1950
S14	[64]	7500	0.07	30.0	1.30	65	40	40	220	0.20	1.70	0.10	20	-	-	4.50	3.14	878	1475
S15	[119]	12000	0.20	62.6	{6.26}	45	285	130	4200	{0.20}	6.20	{0.62}	10	-	-	28.60	27.01	10000	9761
S16	[137]	5500	0.11	12.0	0.90	238	252	241	2770	0.07	4.60	{0.46}	12	-	-	8.84	6.91	5517	5330
S17	[156]	16700	0.15	66.0	1.20	52	210	100	2100	0.22	3.00	0.22	13	-	-	11.73	13.77	6800	8294
S18	[106]	9900	0.17	44.0	1.79	55	194	89	8600	0.13	21.00	2.10	7.5	-	-	34.70	36.75	-	9724
S19	[124]	5760	{0.15}	19.8	2.46	55	125	120	5490	{0.20}	2.62	0.35	10	-	-	8.24	10.31	2132	5906
S20	[106]	15000	0.13	58.9	2.74	57	200	98	11600	0.10	31.10	3.11	7.5	-	-	48.20	50.59	-	14593
S21	[68]	976	{0.15}	5.7	{0.57}	75	230	105	8570	{0.20}	5.14	{0.51}	12	-	-	1.83	4.63	365	1098
S22	[106]	15000	0.13	58.9	2.74	57	200	98	8600	0.13	21.00	2.10	7.5	-	-	40.90	44.14	-	13788
S23	[130]	8000	0.08	8.3	{0.42}	100	305	143	6600	0.19	3.45	{0.35}	30	-	-	3.10	6.57	5900	7013
S24	[64]	7500	0.07	30.0	1.30	65	40	40	220	0.20	1.70	0.10	10	-	-	9.33	5.74	1938	2380
S25	[106]	9900	0.17	44.0	1.79	55	194	89	6600	0.14	15.20	1.52	7.5	-	-	27.00	31.32	-	9342
S26	[68]	3370	{0.15}	23.0	{2.30}	75	230	105	7080	{0.20}	8.50	{0.85}	12	-	-	10.00	14.38	3700	3585
S27	[106]	15000	0.13	58.9	2.74	57	200	98	6600	0.14	15.20	1.52	7.5	-	-	32.50	37.12	-	13059
S28	[106]	9900	0.17	44.0	1.79	55	194	89	11600	0.10	31.10	3.11	7.5	-	-	37.70	43.16	-	10633
S29	[81]	5300	{0.15}	17.7	{0.89}	75	230	110	545	{0.15}	3.10	{0.31}	10	-	-	4.00	9.74	2239	3034
S30	[76]	12900	{0.15}	60.0	3.20	36	123	60	9590	{0.15}	12.00	0.97	7	-	-	18.16	24.90	8000	12601
S31	[106]	15000	0.13	58.9	2.74	57	200	98	1750	0.16	6.20	0.62	7.5	-	-	29.90	21.12	-	8063

Table 3.2 Running bond wall cases. Comparison of experimental and analysis results. Assumed values in curly brackets.

Case	Ref.	E_u $[N/mm^2]$	ν_u [-]	f_{cu} $[N/mm^2]$	f_{tu} $[N/mm^2]$	h_u $[mm]$	l_u $[mm]$	t_u $[mm]$	E_m $[N/mm^2]$	ν_m [-]	f_{cm} $[N/mm^2]$	f_{tm} $[N/mm^2]$	h_m $[mm]$	l_m $[mm]$	t_m $[mm]$	$f_{c,exp}$ $[N/mm^2]$	$f_{c,FEM}$ $[N/mm^2]$	$E_{c,exp}$ $[N/mm^2]$	$E_{c,FEM}$ $[N/mm^2]$
R1	[68]	3372	{0.15}	23	{2.30}	75	230	105	5450	{0.20}	4.36	{0.44}	12	12	-	8.20	8.47	5232	3590
R2	[156]	4000	0.13	17	1.00	50	206	96	1650	{0.20}	6.90	{0.69}	12.5	10	-	13.60	14.21	3200	3095
R3	[68]	976	{0.15}	5.7	{0.57}	75	230	105	238	{0.20}	0.60	{0.06}	12	12	-	1.23	1.98	580	717
R4	[68]	976	{0.15}	5.7	{0.57}	75	230	105	1500	{0.20}	1.16	{0.12}	12	12	-	1.55	2.35	735	1033
R5	[68]	3372	{0.15}	23	{2.30}	75	230	105	7083	{0.20}	8.50	{0.85}	12	12	-	12.60	14.40	4824	3702
R6	[68]	3372	{0.15}	23	{2.30}	75	230	105	8568	{0.20}	5.14	{0.51}	12	12	-	9.60	7.24	5024	3782
R7	[120]	6740	0.167	36.52	{1.50}	35	110	50	970	{0.20}	3.20	{0.32}	5	5	-	8.60	11.30	3700	3949
R8	[68]	976	{0.15}	5.7	{0.57}	75	230	105	8568	{0.20}	5.14	{0.51}	12	12	-	1.18	4.46	400	1254
R9	[131]	22000	0.15	61	10.70	30	105	49	8880	0.2	12.30	1.58	5	5	-	30.14	37.81	-	18540

Computational effort remains substantial but not excessive: a single small or medium sized wall may be analyzed in order to obtain the maximum load and part of the post-peak curve in two to three hours using a conventional PC. The attainment of the full post-peak curve may cause computational time to double.

3.5.1 Analysis of Results

With a few exceptions, the modeling strategy produced adequately accurate predictions of the compressive strength throughout the group of cases, which includes a wide range of material combinations. Certain experimental results may be regarded as dubious, such as S29 and S24,

Table 3.3 Flemish bond wall cases. Comparison of experimental and analysis results.

Case	Ref.	E_u $[N/mm^2]$	ν_u [-]	f_{cu} $[N/mm^2]$	f_{tu} $[N/mm^2]$	h_u $[mm]$	l_u $[mm]$	t_u $[mm]$	E_m $[N/mm^2]$	ν_m [-]	f_{cm} $[N/mm^2]$	f_{tm} $[N/mm^2]$	h_m $[mm]$	l_m $[mm]$	t_m $[mm]$	$f_{c,exp}$ $[N/mm^2]$	$f_{c,FEM}$ $[N/mm^2]$	$E_{c,exp}$ $[N/mm^2]$	$E_{c,FEM}$ $[N/mm^2]$
F1	[25]	4865	0.09	26.90	4.90	55	250	120	1180	0.06	3.20	0.90	10	10	10	11.00	4.29	1651	3107
F2	[25]	4865	0.09	26.90	4.90	55	250	120	5650	0.09	12.70	3.90	10	10	10	14.50	16.70	3833	5002
F3	[25]	4865	0.09	26.90	4.90	55	250	120	17760	0.12	95.00	15.70	10	10	10	17.80	29.58	4567	6390

Table 3.4 English bond pillar cases. Comparison of experimental and analysis results. Assumed values in curly brackets.

Case	Ref.	E_u $[N/mm^2]$	ν_u [-]	f_{cu} $[N/mm^2]$	f_{tu} $[N/mm^2]$	h_u $[mm]$	l_u $[mm]$	t_u $[mm]$	E_m $[N/mm^2]$	ν_m [-]	f_{cm} $[N/mm^2]$	f_{tm} $[N/mm^2]$	h_m $[mm]$	l_m $[mm]$	t_m $[mm]$	$f_{c,exp}$ $[N/mm^2]$	$f_{c,FEM}$ $[N/mm^2]$	$E_{c,exp}$ $[N/mm^2]$	$E_{c,FEM}$ $[N/mm^2]$
P1	[68]	3372	{0.15}	23.00	{2.30}	75	230	105	8568	{0.20}	5.14	{0.51}	12	20	20	6.70	6.65	3317	4005
P2	[68]	3372	{0.15}	23.00	{2.30}	75	230	105	5450	{0.20}	4.36	{0.44}	12	20	20	8.70	8.13	3789	3684
P3	[68]	976	{0.15}	5.70	{0.57}	75	230	105	238	{0.20}	0.60	{0.06}	12	20	20	1.46	2.07	377	690
P4	[68]	3372	{0.15}	23.00	{2.30}	75	230	105	7083	{0.20}	8.50	{0.85}	12	20	20	13.60	14.24	3677	3865
P5	[68]	976	{0.15}	5.70	{0.57}	75	230	105	1500	{0.20}	1.16	{0.12}	12	20	20	1.44	2.28	381	1056
P6	[68]	976	{0.15}	5.70	{0.57}	75	230	105	8568	{0.20}	5.14	{0.51}	12	20	20	1.38	4.13	376	1510
P7	[64]	7500	0.07	30.00	1.3	65	290	150	220	0.2	1.70	0.10	10	10	10	5.55	9.12	661	2007

where the compressive strength was too high and too low respectively, considering the strength of the materials and the dimensions reported. Others, such as F3, were executed using extremely strong and stiff mortar and should be seen as outside the intended scope of this modeling approach.

The accuracy of the method regarding the determination of the Young's modulus of masonry is comparably high. However, certain cases such as F1, F2 and F3 exhibited an experimental Young's modulus much lower than what would be expected considering the Young's moduli provided for the constituents.

Figure 3.4 illustrates the relation between numerical and experimental values of the compressive strength, showing a good agreement between the experimental and the numerical results. Throughout all cases the coefficient of determination was 0.969 for the numerical prediction. Similarly, Figure 3.5 illustrates the relation between the numerical and experimental values of the Young's modulus of the masonry composite in vertical compression. Throughout the cases the coefficient of determination was 0.892. The ratios of masonry Young's modulus over the compressive strength are roughly equal to the ones produced by the experimental results.

Concerning the comparison of the numerical and experimental results, certain comments should be made regarding the applicability of the proposed method. As has been previously stated, the method is intended to be applied in cases of units with higher compressive strength and lower deformability than the mortar. All of the examined cases comply with this intention, with the exception of the F3 case, involving a mortar that is three times as strong in compression as the bricks, and the S6 case, in which the two components have equal strength.

Some remarks must be also made with regard to a few experimental measurements that do not comply with the general trend of the full inventory of experimental cases considered. These cases, labeled S6, S21, S23, R8, F3 and P6, are the only ones for which the compressive strength of the composite is lower than that of both constituent materials (mortar and units). This low compressive strength cannot be correctly predicted using this analysis method as can also not be accounted for by usual models for predicting the compressive strength of masonry. Finally, the Poisson's ratio reported for the mortar in the F1 case, a pozzolana-lime mortar with low strength, is very low compared to the average derived from the experimental inventory. A higher value

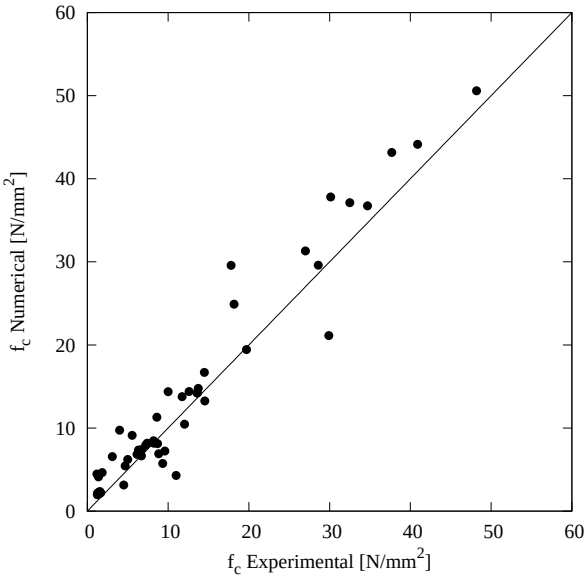

Figure 3.4 Experimental vs. numerical compressive strength. Coefficient of determination $R^2 = 0.969$.

for this parameter, which would increase the amount of confinement on the mortar layers, would result in an increase in the numerically predicted masonry compressive strength. Disregarding the above mentioned cases increases the coefficient of determination for the prediction of compressive strength to 0.976.

The dominant failure mode obtained was a combination of mortar yielding in compression and unit cracking for the majority of the cases. Secondary damage included some initial cracking of the mortar at the unit/mortar interface near the outer faces of the masonry and unit yielding in compression in the case of, comparatively to the units, very strong mortars. The observed failure modes will be discussed in the following paragraphs, with some emphasis on their dependence on material properties.

Great discrepancy between the elastic characteristics of the units and the mortar enhances the confinement afforded on the mortar, resulting in a higher ratio between the masonry compressive strength and the mortar compressive strength. Therefore, the relation between the compressive strength of the constituents and the compressive strength of the composite is partly dependent on the Young's moduli as well, especially in cases where the global failure mode is governed by mortar yielding in compression.

Compressive yielding mainly takes place in the mortar joints. Crushing failure of the mortar, represented numerically by plastic strains, normally initiates near the face of the masonry, where horizontal confinement is lowest, and develops towards the interior of the joint. In the running bond and Flemish bond wall cases, this compressive yielding failure exhibited a repeating pattern across the face of the structure, both in the horizontal and the vertical joints. Lateral expansion of the crushed mortar causes cracking damage in the units at the interface near the free surface of the masonry. The non-uniform development of compressive damage along the depth of the horizontal joints indicates that plane methods, as already discussed, may be inadequate for an accurate description of the phenomenon. The development of mortar yielding is illustrated in

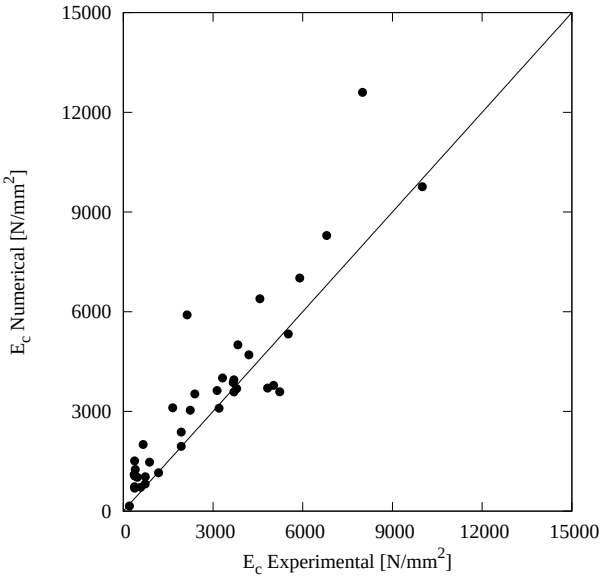

Figure 3.5 Experimental vs. numerical Young's modulus. Coefficient of determination $R^2 = 0.884$.

Figure 3.6, where it is represented by plastic strains.

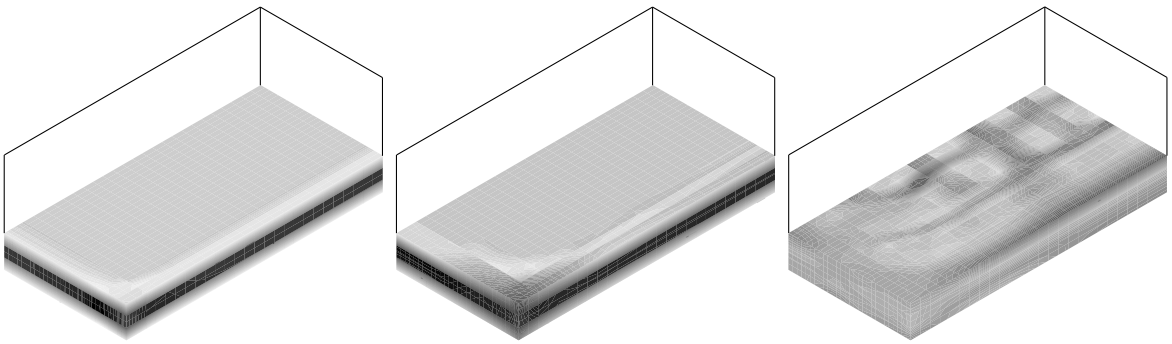

Figure 3.6 Distribution of principal plastic strains in bed joint mortar for case S18 for increasing vertical stress levels: (a) yielding near the edge at the pre-peak range , (b) yielding extended towards the interior of the joint at peak load, (c) yielding of entire joint in the post-peak range.

Compressive yielding of the units to an extent that affects the global failure mode only occurs in cases of very strong mortar. For mortars with compressive strength comparable to or higher than that of the units, compressive yielding of the units may occur in the pre-peak range and initiate overall failure.

Notable compressive yielding of the units may also take place after extensive cracking, covering nearly the entirety of the unit. This only happens far in the post-peak and does not affect the stress-strain curve near the peak.

Cracking damage mainly takes place in the units and the head and transversal joints. The appearance of extensive cracking in the units, represented numerically by crack strains, and its influence on the global failure, are not directly dependent upon the ratio of the Young's moduli. For high ratios, lateral tension on the units increases but the onset of extensive unit cracking may

not necessarily occur before the yielding of the mortar.

The amount of vertical confinement afforded on the mortar and the amount of vertical splitting on the units are directly dependent on the mismatch of elastic properties of the constituent materials. The prevalence of one of the two failure modes over the other depends on both the elastic and inelastic properties.

Overall, the numerically obtained failure mode is chiefly governed by mortar compressive yielding which develops during the hardening of the structure. The compressive strength of the units does not appear to play a direct role in the compressive strength of the composite for the majority of the cases. Unit compressive yielding is not involved in the initiation of failure; conversely, tensile unit strength is more directly involved, especially in the post-peak. Cracking of the units near the unit/mortar interface initiates in the outer surface of the masonry and remains superficial without extending towards the interior of the masonry. The more critical vertical cracks in the units may extend into the interior of the masonry in the post-peak, a further indication that plane analysis methods are inadequate. The development of cracking in the units is illustrated in Figure 3.7.

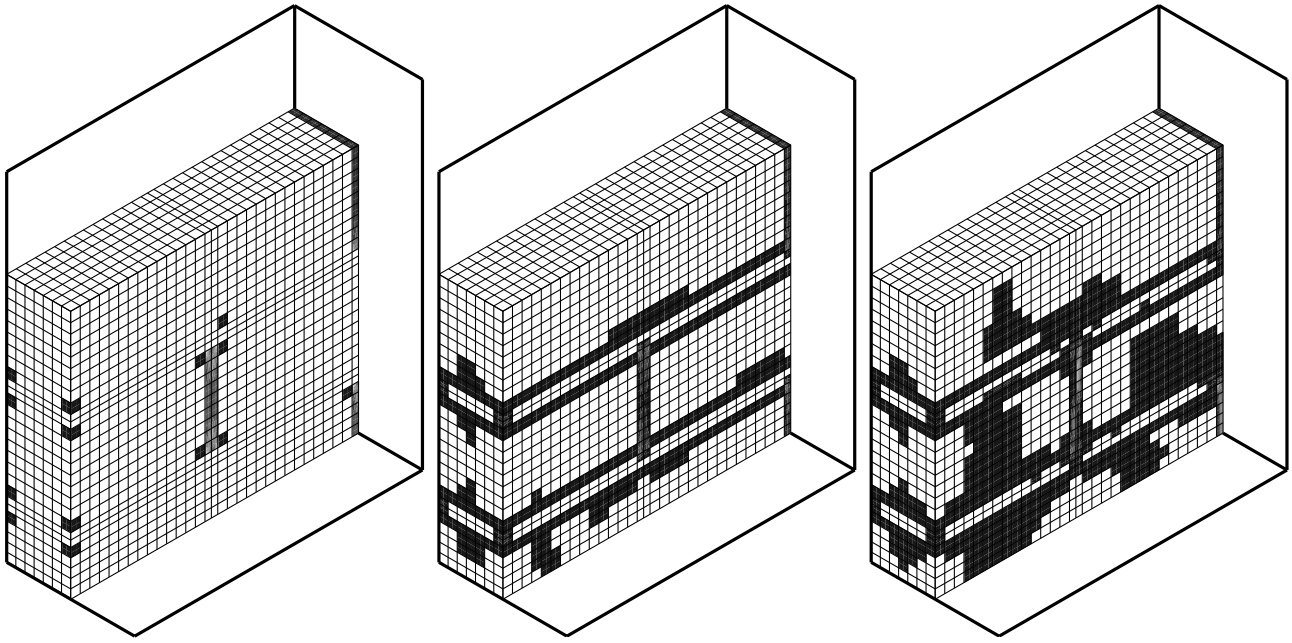

Figure 3.7 Distribution of principal crack strains for case R9 for varying levels of vertical stress: (a) initial cracking in the head joints in the pre-peak range, (b) vertical cracks in the units around the bed joints at the peak load, (c) vertical cracks in the units at the post-peak range.

A comparison of experimentally and numerically derived stress-strain curves is presented in Figure 3.8, covering a wide range of results in terms of compressive strength and elastic stiffness. The graphs show the good agreement obtained between the initial Young's modulus of masonry E_c as measured in the experiments and that predicted by the numerical model. The numerical post-peak curve is usually steeper, as in graphs (c) and (f). This is an indication that the values assumed for the tensile fracture energy of the units and/or the compressive fracture energy of the mortars is low. However, some of the experimental case studies were, indeed, characterized

by such steep softening, a behavior which was well approximated in the numerical model, as shown in graphs (a) and (f).

Concerning the missing material parameters, the absence of values for the tensile strength of the mortar is of very small consequence for the determination of the compressive strength of masonry. However, the tensile strength of the units plays a more substantial role, as demonstrated by the cracking development near and after the load peak. The Poisson's ratio of the mortars with low Young's modulus is also a strong influencing factor as it affects the lateral expansion of the mortar under vertical compression and, therefore, the amount of horizontal confinement afforded to it by the units. It can be thus concluded that the tensile strength of the units and the Poisson's ratio of the mortar are of importance in masonry in compression and their function is linked.

In the majority of cases where a relatively high Poisson's of 0.2 was assumed the model exhibited a tendency to slightly overestimate the compressive strength of masonry. This is especially apparent in the cases from [68], [124] and [120]. A value of 0.15, which is closer to the average of the experimental inventory, would have resulted in a slightly better estimation of the compressive strength of masonry.

For comparison purposes, analyses of the running and Flemish bond cases were performed without taking into account nonlinearities in the interface elements (meso-modeling). The resulting compressive strength was identical to the one obtained from the detailed micro-models, despite the fact that the meso-models could not take into account tensile failure of the interfaces between the units and the head and transverse mortar joints simulated by the micro-models.

Similarly, the influence of tensile strength of the mortar was investigated in the F1 Flemish bond case while at the same time neglecting interface nonlinearities. The existence of both head and transversal mortar joints potentially maximizes the influence of this particular material parameter. Cracking in the mortar occurs very early in the analysis, appearing in all vertical, transversal and horizontal joints. In the former two cases the damage propagates through the entirety of the joint, while in the latter the damage is limited to an area near the surface of the masonry, which is also the first to fail in compression. However, in terms of overall behavior, the strength and the elasticity of the masonry composite are not significantly altered by the modification of the tensile strength of the mortar: using a value of 10% and 1% of the experimentally derived value of the tensile strength of mortar caused a reduction of only 2.1% and 3.6% of the compressive strength of masonry.

The sensitivity of the results on the fineness of the mesh was studied on the S1 experimental case [106]. Three meshes were employed, the defining parameter for refinement being the number of elements along the thickness of the joint. In the main series of numerical analyses performed in this chapter, two elements were used along the thickness of the joint. Two additional meshes were tested: one with a single element and one with three elements along the thickness. The aspect ratio of the resulting finite elements are $1 : 0.93 : 0.92$, $1 : 0.62 : 0.92$ and $1 : 0.41 : 0.92$ for the three cases.

The results are presented in Figure 3.9. While the compressive strength and initial axial stiffness was unaltered, there is a distinct influence of the fineness of the mesh in the post-peak.

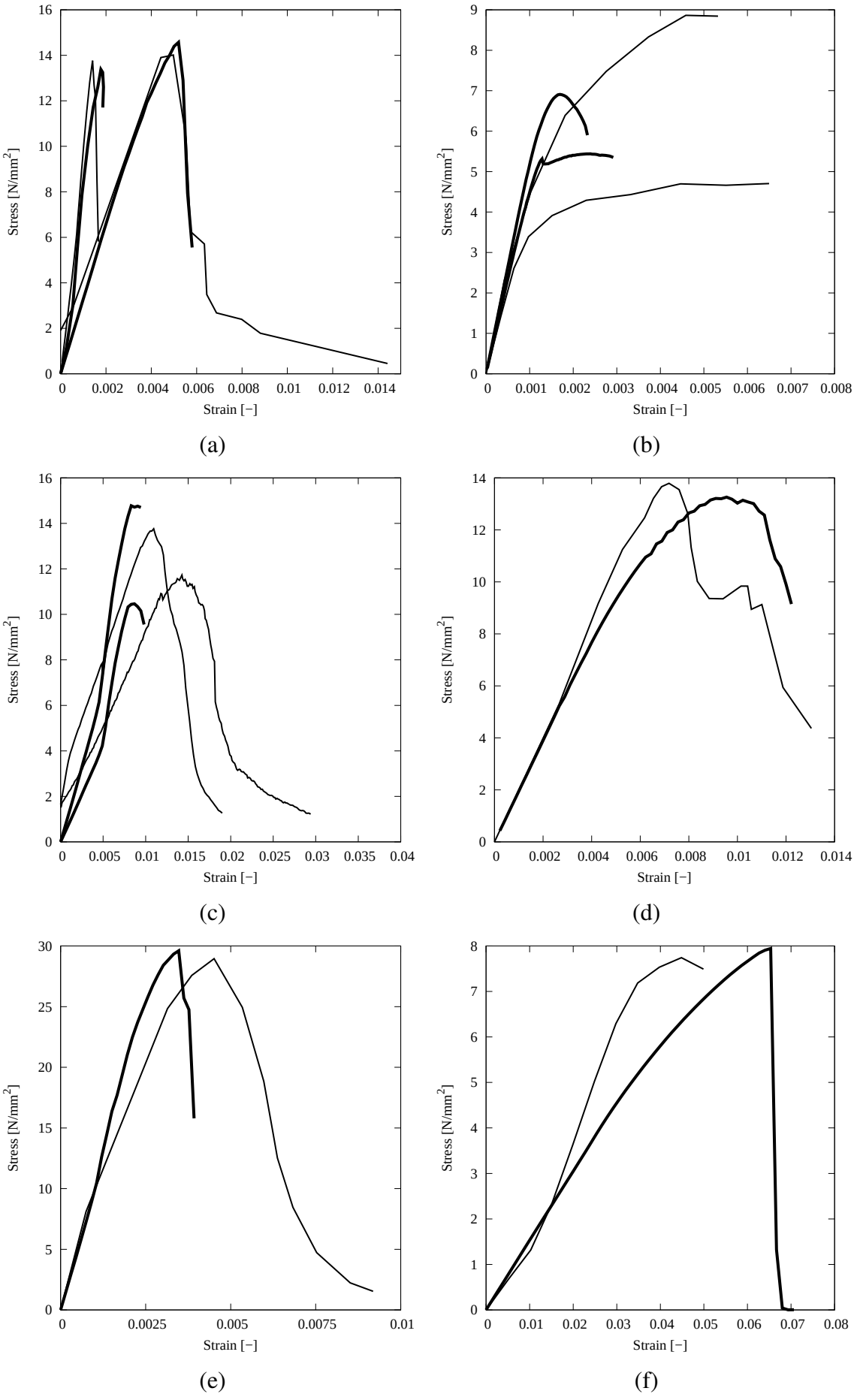

Figure 3.8 Experimental and numerical stress-strain diagram comparison. Numerical curves are shown in tinted lines: (a): S17 & R2 [156], (b): S8 & S16 [137], (c): S2 &S7 [56], (d): S13 [3], (e): S15 [119], (f): S6 [8].

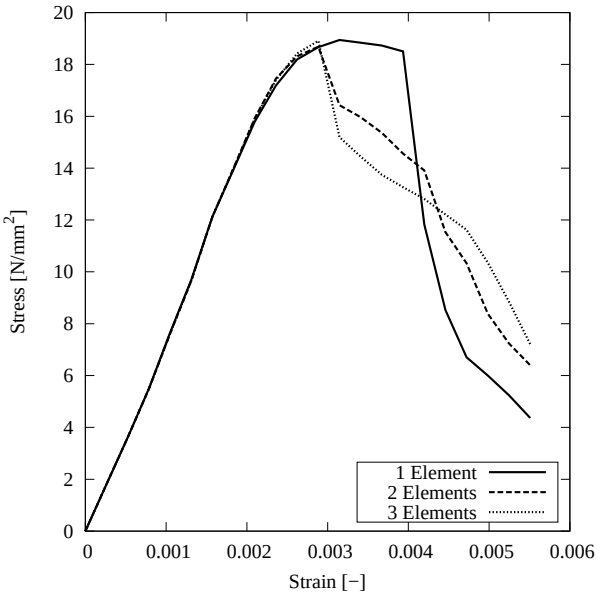

Figure 3.9 Effect of mesh refinement for S1 [106] number of elements long the joint thickness.

The model with a single element across the joint exhibits a more ductile behavior. The results of the two and three element models exhibit similar post-peak behavior.

Overall, mesh refinement only affected the post-peak behavior but not the predicted capacity. The coarser mesh resulted in a more ductile response. Despite the mesh-insensitivity exhibited by fracture energy approaches, the response in the post-peak behavior did not exhibit mesh-insensitivity. Finally, there was very little benefit in using three instead of two element along the thickness of the joint.

3.5.2 Comparison with Closed Form Expressions

The numerical results are compared with a number of closed form and empirical expressions for the prediction of the compressive strength of masonry and its Young's modulus. These analytical expressions are applied to those cases where the masonry materials are completely characterized, with the occasional exception of the value of the tensile strength of the mortar, which does not influence the results for any of the analytical models or for the FEM analyses.

The analytical models proposed by Hilsdorf [74], Khoo & Hendry [82], Francis [63], Ohler [117] and Hendry [73] are used, as well as recommendations by ACI [2] and CEN [40] standards for the characteristic strength of masonry. The Young's modulus of the composite as derived from a simple one-dimensional homogenization method [45] and the CEN European standard are similarly compared to the experimental and numerical results.

The results for the compressive strength and the Young's modulus are summarized in Table 3.5 and Table 3.6 respectively. The numerical model provides the most accurate results overall in terms of compressive strength. The Ohler, Hilsdorf and Francis models follow closely in terms of accuracy while the Hendry and Khoo & Hendry equations appear to provide inaccurate values for several cases. The equations provided by the design codes tend to underestimate

the compressive strength, especially for masonry composites of higher strength, with the values provided by CEN being slightly closer to the experimental results. The FEM model provides, with a few exceptions, results for the Young's modulus very similar to the analytical model. The CEN code tends to greatly overestimate this parameter compared to the experimental results.

Table 3.5 Experimental results vs. numerical and closed form expression results: compressive strength.

Case	Ref.	$f_{c,exp}$	$f_{c,Hilsdorf}$	$f_{c,Francis}$	$f_{c,KhooHendry}$	$f_{c,Ohler}$	$f_{c,Hendry}$	$f_{c,ACI}$	$f_{c,CEN}$	$f_{c,FEM}$
		$[N/mm^2]$								
S1	[106]	19.70	24.54	29.24	19.81	17.63	9.58	11.56	12.22	19.44
S4	[159]	6.15	8.03	9.61	7.16	6.44	3.75	5.05	4.01	6.83
S8	[137]	4.68	7.79	11.36	7.21	6.50	7.93	5.16	4.50	5.44
S11	[137]	6.32	8.56	10.10	7.67	6.94	3.80	5.05	4.01	7.35
S12	[159]	5.01	6.83	8.28	6.18	5.47	3.59	5.05	4.01	6.21
S13	[8]	14.55	11.89	12.44	12.04	11.78	27.94	5.52	6.11	13.26
S14	[64]	4.50	10.96	10.88	7.99	7.12	9.97	8.76	6.34	3.14
S16	[137]	8.84	9.96	11.87	9.46	8.84	8.13	5.16	4.50	6.91
S17	[156]	11.73	15.88	14.52	12.27	10.31	6.04	15.96	13.06	13.77
S18	[106]	34.70	30.59	47.22	29.05	28.46	10.66	11.56	17.62	36.75
S20	[106]	48.20	43.23	59.75	41.25	43.50	21.17	14.54	24.32	50.59
S22	[106]	40.90	39.48	49.90	35.75	35.50	20.03	14.54	21.61	44.14
S24	[64]	9.33	15.33	15.97	10.55	10.08	12.96	8.76	6.34	5.74
S25	[106]	27.00	28.22	39.86	25.75	24.37	10.33	11.56	15.99	31.32
S27	[106]	32.50	37.33	46.29	32.37	30.56	19.53	14.54	19.62	37.12
S28	[106]	37.70	34.72	71.27	34.98	40.74	11.34	11.56	19.83	43.16
S31	[106]	29.90	33.99	39.91	25.71	23.65	18.47	14.54	14.99	21.12
R9	[131]	30.14	47.12	52.33	40.76	39.08	62.29	14.96	18.87	37.81
F1	[25]	11.00	20.24	25.85	16.28	15.77	50.70	8.14	7.10	4.29
F2	[25]	14.50	21.93	27.34	20.99	20.06	55.80	8.14	10.74	16.70
F3	[25]	17.80	36.58	35.23	76.07	-	72.91	8.14	19.64	29.58
P7	[64]	5.55	15.33	15.97	10.55	10.08	12.96	8.76	6.34	9.12

3.6 Conclusions

A systematic numerical simulation of masonry compression tests has been performed on fifty cases with available experimental results using a detailed micro-modeling technique. The main purpose of the simulation has been the validation of the proposed micro-modeling technique for the prediction of the compressive strength and Young's modulus of masonry based on the properties of the constituent materials.

The modeling method, resulting from the application of a combined plasticity and smeared cracking material law in three-dimensional masonry models has been shown capable of producing reliable results in a wide range of combinations of masonry units and mortar. Its accuracy, however, is strongly dependent on sufficient mechanical characterization of the individual materials and should be tested against carefully executed tests on the resulting masonry. Overall, no distinct tendency to over- or underestimate the compressive strength and Young's modulus of the masonry was observed.

The range of applicability of the proposed technique is far greater than that of plane methods (such as plane strain or plane stress applications), as unit/mortar interaction and its out-of-plane effects differ greatly for different ratios of Young's moduli between the materials. Three-

Table 3.6 Experimental results vs. numerical and closed form expression results: compressive strength.

Case	Ref.	$E_{c,exp}$	$E_{c,1D}$	$E_{c,EC6}$	$E_{c,FEM}$
			$[N/mm^2]$		
S1	[106]	-	6351	12221	6456
S4	[159]	-	12734	4014	13017
S8	[137]	4200	4555	4500	4702
S11	[159]	-	13177	4014	13464
S12	[159]	-	11604	4014	10400
S13	[8]	-	1947	6110	1950
S14	[64]	1936	854	6340	1475
S16	[137]	5517	5251	4500	5330
S17	[156]	6800	6986	13055	8294
S18	[106]	-	9724	17622	9724
S20	[106]	-	14506	24315	14593
S22	[106]	-	13805	21613	13788
S24	[64]	1938	1386	6340	2380
S25	[106]	-	9340	15993	9342
S27	[106]	-	13066	19616	13059
S28	[106]	-	10077	19825	10633
S31	[106]	-	7977	14989	8063
R9	[131]	-	18166	18866	18540
F1	[25]	1651	3286	7101	3107
F2	[25]	3833	4971	10738	5002
F3	[25]	4567	6389	19639	6390
P7	[64]	661	1386	6340	2007

dimensional micro-models allow a more accurate and general simulation of the masonry compressive effects due to the more realistic prediction of damage patterns and their development.

In summary, the simulation of phenomena associated with masonry compressive effects using micro-models is much more accurate and of wider applicability when using models of three-dimensional geometry due to the more realistic prediction of damage patterns and their development. Abiding to the principle aims of structural micro-modeling, which include the direct, rather than the phenomenological, simulation of structural behavior and failure, and in an effort to establish a generally applicable modeling approach, three-dimensional micro-modeling appears to be the most promising and advantageous method.

The numerical results have been compared with a number of closed form and empirical expressions for the estimation of the masonry compressive strength and Young's modulus. Compared to the closed form and empirical expression, the numerical model provides far more accurate estimations. In fact, some of the expressions tested provide only fair estimations. A significant discrepancy has been found between the equation proposed by CEN 2005 for the estimation of the Young modulus and the experimental or numerically predicted results. According to the comparison, the equation of CEN 2005 largely overestimates the Young's modulus.

A particular application of the proposed numerical approach can be found in the estimation of masonry average properties based on the knowledge of specific parameters of the material constituents. These properties may be later used as input data for macro-models utilized in the analysis of large structural parts or entire structures.

Chapter 4

Compressive Strength and Elasticity of Pure Lime Mortar Masonry

4.1 Introduction

The compressive strength of masonry is considered by design codes as the main design parameter, on which, additionally, the derivation of its mechanical properties is largely based. For this reason, masonry in concentric compression has been extensively studied. Taking into account the experimental investigations on masonry composites accompanied by a characterization of the masonry constituents, the instances in the literature become fewer in number. A relatively large number of such experimental investigations has been performed on stack bond prisms [23, 64, 68, 71, 76, 81, 106, 114, 119, 124, 130, 136, 156, 159]. Fewer investigations including concentric compression tests on larger members, such as walls in running or Flemish bond or three-leaf samples and columns, have been documented in the literature [14, 17, 25, 26, 29, 51, 58, 59, 67, 113, 116, 121, 131]. These tests are usually monotonic, but cyclic tests have also been performed [116, 119].

The different combinations of materials present researchers with a wide range of possible choices for experimental study. However, reviewing the available inventory of experimental data, one finds a distinct predominance of cement and lime/cement mortars in structural testing. While chemical, curing, mechanical property and sustainability issues of modern pure lime mortars have been extensively studied [26, 32, 50, 53, 84–86], the investigation of their direct structural application has not enjoyed the same attention [46] despite its common use as original material or for restoration purposes in historical structures.

Measurement of the compressive and flexural strength of units and mortar is well documented and even codified in guidelines [39, 40, 42]. However, no comparable effort has been devoted to the characterization of the Young's moduli of the material constituents and the masonry composite. Masonry codes [41] provide empirical relations for the estimation of the masonry Young's modulus using the compressive strength of masonry as the only parameter and hence neglect the important influence of the parameters related to the constituent materials. Regarding experimental procedures, there is a lack of guidelines for the measurement of the Young's modulus

of both the units and the mortar and limited information for the masonry composite.

Published results on the Young's modulus of units and mortar often do not explain in detail the method used to obtain these results. However, a few studies include a detailed explanation of such measurement methods and often make use of the measured moduli in numerical simulations of the experimental processes [106, 114, 119, 124].

Measurements of the mechanical properties of units are easier to perform and are, therefore, more common. However, compressive tests on the unit beds are usually performed on entire units in the direction perpendicular to the unit bed [58, 81, 106]. Due to the dimensions of units, it is foreseeable that this type of tests is significantly affected by both size and shape effects and hence may not be offering a reliable measurement of the uniaxial compressive strength of the material. By measuring cylindrical, cubic or cuboid samples extracted from bricks it has been intended to limit or study these size effects or to simply form specimens with appropriate dimensions to facilitate measurements [21, 51, 119].

The issue of the difference between the properties of the mortars in freestanding samples and in the composite persists due to difficulties in obtaining deformation measurements from both the joints, which are prohibitively thin, and from cast samples due to differences in curing conditions. Efforts have been made to measure isolated deformations of the units and the mortar joints in masonry under compression [51, 156]. For other cases, the elastic properties of the mortar in the joints are indirectly derived by measurements in the units and in the composite [121].

The main objective of the experimental campaign herein presented is to determine the compressive strength and Young's modulus of masonry composed of medium strength solid clay bricks and two types of low strength lime/sand mortar with zero Portland cement content. The intention is to establish whether this particular combination of materials can produce composites of adequate compressive strength and, simultaneously, sufficient deformability so as to be, from a structural perspective, compatible with historical masonry for application in intervention projects.

The tests performed and the measurements taken during their execution have been designed so as to give as much information as possible on both the strength and the deformability characteristics of the constituent materials.

A simulation of the experimental tests using the numerical method developed in the previous chapter is also carried out. The numerical results will be evaluated in terms of the prediction of the compressive strength of masonry and the reproduction of the experimental failure mode. In addition to the basic analyses performed using the material properties as measured or estimated in the campaign, a short parametric investigation is also performed. The objective of this investigation is to evaluate the influence on the compressive strength of masonry of material parameters which were indirectly measured or assumed in the experimental campaign.

4.2 Description of the experimental campaign

For the mechanical characterization of the units, it was preferred to measure the uniaxial compressive strength and the Young's modulus of the material of which they are composed, using appropriate brick cores, rather than measuring the strength of an entire brick in compression. As mentioned above, the latter approach would involve significant size effects in the compression tests. It was also intended to follow a sampling procedure which would allow a large number of testable specimens to be extracted from a single brick. In the case of the application of destructive testing on historical materials this is advantageous for exerting minimum damage and loss of original material in the structure.

The masonry was constructed in stack bond configuration. This geometrical setup allows for a simple way of studying unit/mortar interaction in masonry under concentric compression.

Whenever possible, existing testing standards were consulted in order to compare the parameters in the performed tests and their results against a codified backdrop. It was intended to establish whether the materials and the resulting masonry conform to the application spectrum defined or implied in the corresponding standards.

4.2.1 Units

The units used in the campaign were solid clay bricks with nominal dimensions measuring $290 \times 140 \times 45 mm^3$. The bricks were hand-molded, which resulted in the bricks having smaller actual dimensions and rough, uneven surfaces and, often, slanted heads and faces. The more pronounced scatter in the geometric measurements was obtained for the smaller dimensions of the bricks, namely their height.

The bricks received surface treatment prior to testing. The beds were polished in order to ensure smoothness and planarity and to remove surface fissures and other damage, whereupon the bricks were reduced to a height of roughly $40mm$. Following the surface treatment, cylindrical core samples were extracted from the bricks in the direction perpendicular to the unit bed, numbering six to seven from each unit, with a diameter of $45.25mm$. The height to diameter ratio in the samples was, therefore, roughly 1, which is not ideal for eliminating size effects in compression tests or the confinement afforded on the sample by the loading platen, but provides a significant improvement against the testing of full bricks. Furthermore, the very small height of the bricks, and therefore the very small displacements to be measured, would compound the uncertainty of the measurements. Coring also allows for the influence of local imperfections to be directly measured or even entirely avoided, as internal cracks and voids become visible. Finally, it allows for the clearer overview of the variation of the results, since it may now be decomposed in the variation of the properties between the units as well as in the localized variation of the area from which each sample was extracted. Examples of coring patterns are shown in Figure 4.1. For these reasons, and in order to obtain some understanding of these size effects, the cylindrical samples were tested in single, double and triple stacks. The surface treatment of the unit beds facilitates this configuration.

Figure 4.1 Sample extraction pattern: full bricks and half bricks obtained from flexural test.

The characterization of the tensile strength of the units was done using three-point bending of three complete brick specimens, from which the uniaxial tensile strength may be indirectly determined. There is no EN standard specific to the determination of the tensile or flexural strength of clay units as there are for concrete blocks [40]. Following the aforementioned surface treatment and before testing, the units were placed in a drying oven overnight at a temperature of $105 \pm 5\,^{\circ}\mathrm{C}$ to remove existing moisture and to ensure equal moisture for all samples. The units were left to cool for four hours prior to testing. The testing was performed using a load cell with a $200kN$ capacity in a hinged configuration and displacement measurements were only taken from the load cell readings. The load was applied in force control at a rate of $10N/sec$. The test was performed specifying a central span of $200mm$, as illustrated in Figure 4.2.

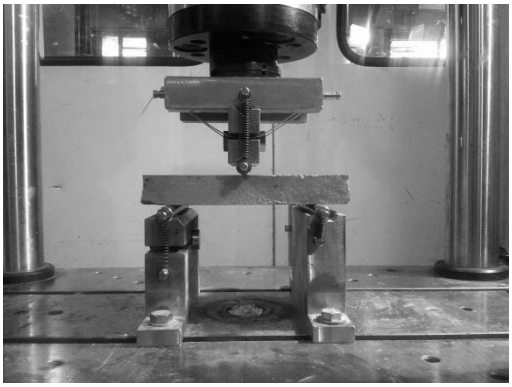

Figure 4.2 Brick flexural test setup.

For the compressive tests on the cylindrical samples, a $200kN$ capacity load cell was used in a hinged configuration. The load was applied in displacement control, in order to record the softening branch with more ease, at a rate of $0.002mm/sec$. Measurements were taken from three LVDTs placed in the perimeter as shown in Figure 4.3, and from the load cell readings. These devices were fixed on the loading plates, as the small height of the cylinders, even when stacked, was not sufficient for the LVDTs to be properly attached directly on them. Overall, eleven single samples, eight double samples and six triple samples were tested for a total of twenty five compression tests. With the exception of one triple sample, the doubles and triples were composed of cores from the same brick.

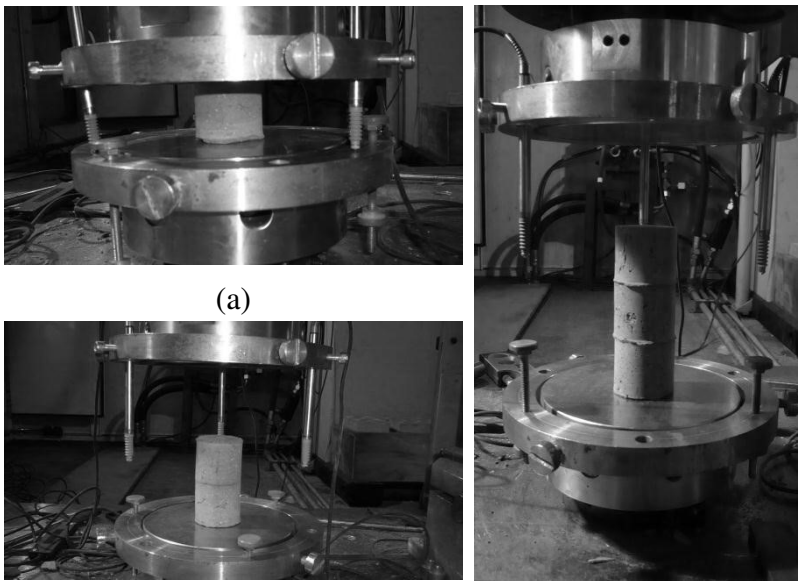

(a) (b) (c)

Figure 4.3 Test and measurement layout for compressive tests on brick cylinders: (a) single, (b) double and (c) triple samples.

4.2.2 Mortar

Two types of mortar were employed in the construction of the masonry: aerial lime mortar (ALM) and hydraulic lime mortar (HLM) combined with fine sand made of crushed limestone and zero Portland cement content. The ALM mortar was produced in putty form obtained from submersion of CL-90 calcium lime in water in a sealed plastic drum and the HLM directly from NHL 3.5 natural hydraulic lime powder. The properties of the sand are presented in Figure 4.4 and Table 4.1. Both mortars were produced in a 1 : 3 lime-to-sand ratio and were hand-mixed using a trowel. The methodology followed in the characterization of the mortars is described in the EN 1015-11 European standard for mortar testing [39], which includes instructions for the preparation and storing of the samples as well as the testing setups and procedures. However, due to the composition of the mortars, it was immediately understood that this standard is mainly applicable to mortars of higher strength. Nevertheless, it may still be, as it indeed has been, consulted as a guideline for planning this and other similar campaigns.

In parallel with the construction of the prisms, mortar was poured and appropriately compacted in steel 3-compartment molds lubricated with mineral oil to prevent adhesion of the mortar to the mold walls. The mortar was poured in two layers, each of which was compacted with 25 strokes of the tamper. In total, 24 prismatic samples measuring at $160 \times 40 \times 40 mm^3$ were prepared for each mortar type. The molds were stored in lab conditions (22.5 °C, 70.2% humidity) and the samples were extracted after 6 days for the aerial lime and 2 days for the hydraulic lime samples, which were subsequently stored in the same lab conditions. The lack of free contact with the air in the faces of the prisms adjacent to the steel walls of the mold, resulting in very slow hardening, made it necessary to allow a longer period of time to pass before unmolding the aerial lime mortar in order to avoid premature deformation and damage to the samples. Inspection of the molds after removal of the mortar prisms did not reveal any sign of adhered

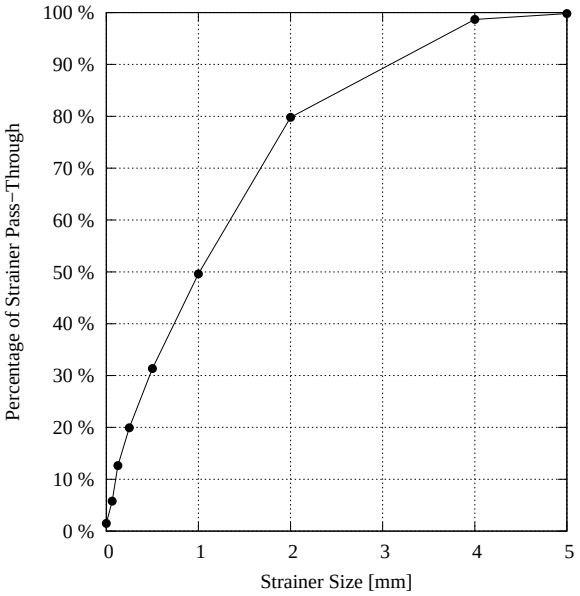

Figure 4.4 Sand granulometry curve.

mortar.

The mortars were subjected to flexural and compressive tests. The mortar prismatic samples were tested in three-point bending and the two resulting halves were tested in compression. A $10kN$ capacity press was used in force control at a rate of $10N/s$ for the bending tests and $50N/s$ for the compression tests, both rates corresponding to the minimum standard specified values. The test setups are shown in Figure 4.5 and the only quantity measured was the force against time. The small dimensions and low strength of the mortars do not allow for accurate displacement measurements to be easily taken. Tests were performed at 14, 28, 42 and 49 days for the ALM and 7, 14, 28 and 49 days for the HLM in order to study the maturation of the mortars.

4.2.3 Masonry Composite

Six masonry wallettes were constructed, three for each mortar type. The EN 1052-1 standard for the determination of the compressive strength of masonry was consulted as a guideline on the preparation of the prisms, the curing and storage, the placement of the measuring instruments and the determination of the loading rate during testing [38]. The masonry wallettes consisted of five bricks and four mortar bed joints of $10mm$ thickness, resulting in overall nominal dimensions equaling $265 \times 140 \times 290mm^3$. The bricks were submerged in water for 30 minutes prior to construction, which took place on a flat surface. For each type of mortar, two prisms were capped on both ends using a $3mm$ thick sulfur-silica sand mortar joint to ensure the flatness of the loading surfaces, while one prism from each mortar case was capped on the top end with the sulfur-silica sand mortar and a $1.5mm$ thick unbonded unreinforced neoprene sheet and with sulfur mortar only on the lower end. Immediately following construction, the prisms were covered with polyethylene sheets for three days in order to prevent premature drying. Subsequently, the masonry was kept in laboratory conditions until it reached an age of 49 days.

Table 4.1 Mortar sand properties.

Sand Grain Size			
Strainer Size [mm]	Weight % Retained	Cumulative Weight % Retained	Weight % Pass
5	0.2	0.2	99.8
4	1.13	1.33	98.67
2	18.86	20.19	79.81
1	30.21	50.4	49.6
0.5	18.24	68.65	31.35
0.25	11.43	80.08	19.92
0.125	7.28	87.36	12.64
0.063	6.87	94.23	5.77
Tray	4.29	98.52	1.48
Sand Properties			
Apparent Density [kg/m^3]			1750
Particle Density [kg/m^3]			2690
% Saturated Porosity			11.3
% Absorption			1.70

The machine used in the compression testing has a static load capacity of $2000kN$. The load cell was set in a hinge configuration to facilitate the adjustment of the load plate with the masonry for uniform load distribution. The load cell was fitted with a short steel profile beam to match the vertical cross section of the prisms. Finally, the masonry was centered between two thick steel plates.

Displacement measurements were taken from 6 LVDTs placed on the masonry, as well as from the readings of the load cell. The LVDTs were placed in such a manner as to measure the vertical deformation of the masonry composite and of an individual unit. The LVDT supports were attached to the masonry using a quick setting adhesive resin. The use of the resin offers good adhesion with minimal disturbance to the surfaces of the units. Placement of the LVDTs often required further surface treatment in the units and the joints in order to properly accommodate their supports and to allow free movement of the instruments. This would not have been necessary in machine-cut bricks.

Due to the irregular heads and faces of the units, the placement of the LVDTs in the exact desired spots was not always possible. For this reason, slight variations of the LVDT setups were attempted, all of which had the same objective. The tests on the aerial lime mortar prisms were performed with a horizontally placed LVDT on the mid height unit. The measured horizontal deformation in the brick may be used in order to determine the Poisson's ratio. Figure 4.6 shows such vertical and horizontal LVDT arrangements on the prisms, while Figure 4.7 presents a schematic view of the two basic LVDT arrangements used.

For the determination of the Young's moduli, and to accommodate the adjustment of the loading platens with the test sample, five initial loading cycles under force control were executed with a final cycle maintained at the maximum load for 1 minute before unloading. The initial cycles were performed with a maximum load of $60kN$ and the final cycle with a load of $90kN$, all

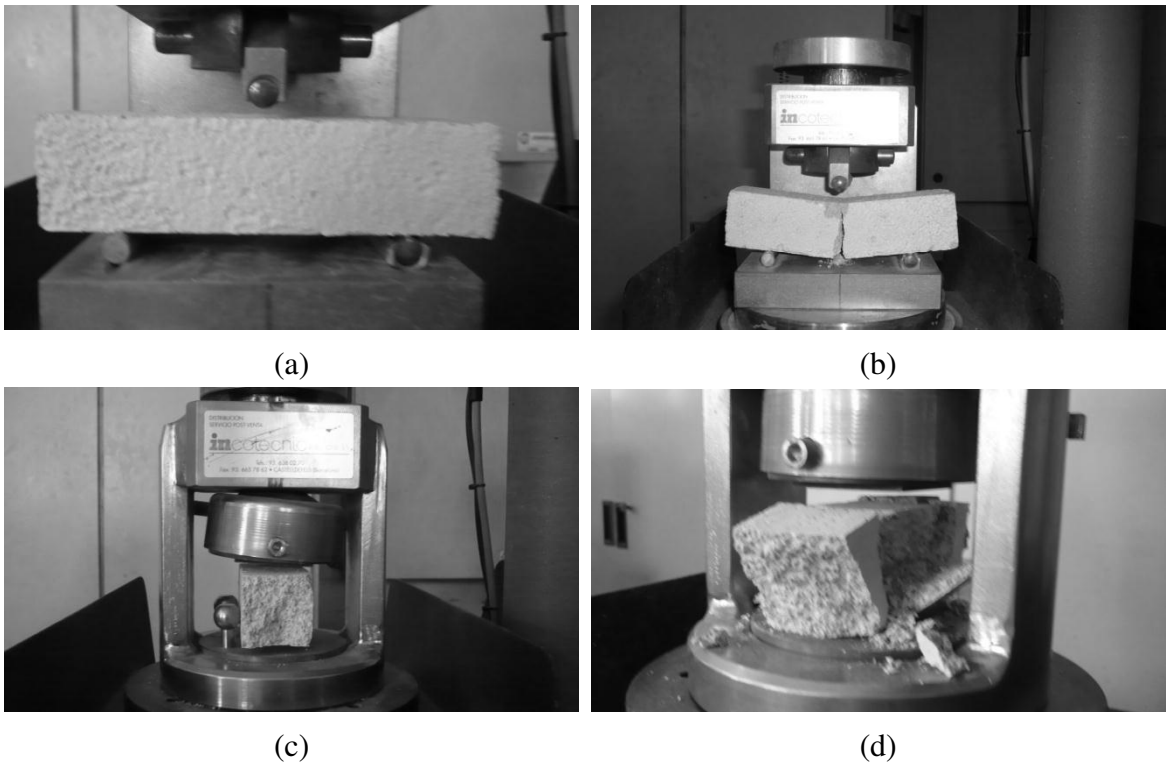

(a) (b)

(c) (d)

Figure 4.5 Mortar testing setup: (a) flexural before and (b) after test, and (b) compression test before and (d) after test.

at a load rate of $400N/s$. The cyclic loading process is based on previous suggested procedures for concrete samples [18] and has been applied on masonry prisms as well [119].

Three values of Young's moduli were measured in the masonry: the initial loading modulus measured in the first loading branch during the cyclic tests, the unloading/reloading modulus in the cyclic tests and the final modulus in the monotonic compression test, which was determined at roughly 40-60% of the compressive strength.

The loading to determine the compressive strength was conducted under displacement control in order to capture the post-peak response of the masonry. The load was applied at a rate of $0.003mm/sec$. The LVDTs were removed from the structure before the peak in order to avoid damage to the equipment, after which point the only displacement measured was that of the stroke of the press. Therefore, information for the Young's modulus could be obtained from this set of tests as well. The test was stopped once the post-peak curve reached roughly 5-10% of the obtained capacity.

Direct measurement of the Young's modulus of the mortars was impractical both on free-standing samples as on the masonry itself. Test samples were required to be of small size, otherwise mortar hardening would not be achieved within a practical time limit, and therefore direct placement of measuring equipment was not possible. As an alternative course of action, the Young's modulus of the mortars may be indirectly determined. This can be achieved following the measurement of the Young's modulus of the units and of the masonry composite by a simple, one-dimensional homogenization process. This process idealizes the masonry composite as a set of linear elastic springs in series. According to this, the Young's modulus of the masonry

(a) (b)

Figure 4.6 Typical layout of LVDTs: (a) vertical layout for displacement measurement in the unit and the composite and (b) horizontal displacement for measurement of the Poisson's ratio.

composite E_c is calculated by the following equation:

$$E_c = \frac{1 + h_m/h_u}{1 + h_m \cdot E_u/(h_u \cdot E_m)} E_u \tag{4.1}$$

where h_m and h_u are the thickness of the mortar bed joint and the height of the units respectively and E_m and E_u are the Young's moduli of the mortar and the units. The model assumes perfect normal and shear bond in the unit/mortar interface as well as neglecting Poisson effects, which do not have a strong influence on vertical masonry stiffness for stack bond prisms.

4.3 Results

4.3.1 Units

The results of the bending tests on the bricks are presented in Table 4.2. Despite the small number of tests, the results were consistent and showed very little scatter. The tensile strength of the brick f_{tu} is derived from the flexural strength f_{flex} by way of equation 4.2, where h is the specimen height [35].

Table 4.2 Unit three-point bending test results.

Sample	Height $[mm]$	Width $[mm]$	f_{flex} $[N/mm^2]$	f_t $[N/mm^2]$
I	39.25	135	7.71	3.39
II	42.00	134	7.06	3.18
III	42.25	134	7.11	3.21
Average	41.17	134.33	7.29	3.26
St. Dev.	1.66	0.58	0.295	0.110
C. o. V.	0.040	0.004	0.040	0.034

$$f_t = \frac{0.06 \cdot h^{0.7}}{1 + 0.06 \cdot h^{0.7}} f_{flex} \tag{4.2}$$

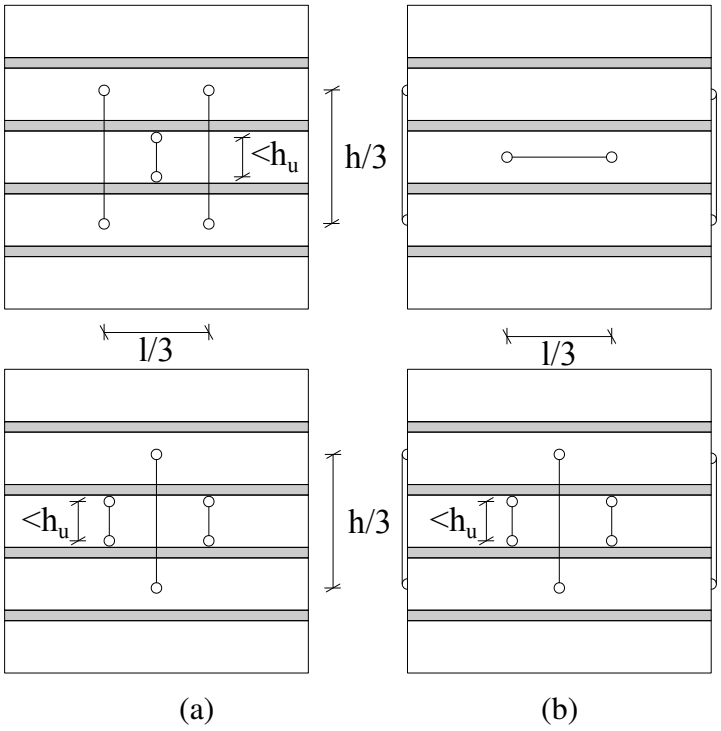

Figure 4.7 Schematic of two LVDT placement arrangements: (a) vertical measurements only (HLM) and (b) vertical and horizontal deformation measurement (ALM), where l is the length of the prism, h is its height and h_u is the height of the unit.

The compressive test results on the brick core samples are presented in two tables. The results and dimensions of the samples, organized according to the number of cylinders in the sample, are presented in Table 4.3. Similarly, Table 4.4 summarizes the same results according to the brick from which the samples were extracted regardless of sample size. This distinction allows to overview the variation of the results according to the parent brick and the sample size. The bricks are again designated by roman numerals (it is reminded that I, II and III where the ones tested in bending) and the extracted samples by ordinary numerals.

Table 4.3 Unit core compression results sorted according to sample size.

Single Samples	Height $[mm]$	f_{cu} $[N/mm^2]$	E_u $[N/mm^2]$	Double Samples	Height $[mm]$	f_{cu} $[N/mm^2]$	E_u $[N/mm^2]$	Triple Samples	Height $[mm]$	f_{cu} $[N/mm^2]$	E_u $[N/mm^2]$
I_1	39.5	28.5	3598	I_2+I_7	79	29.76	3795	IV_3+V_6+IV_1	125.25	22.02	5854
I_3	39.5	31.03	4054	II_2+II_7	85	21.87	4750	IV_4+IV_2+IV_5	124	16.57	5317
I_5	39.5	27.31	3872	II_1+II_4	84.75	23.38	4947	V_3+V_4+V_5	127	26.18	5068
I_6	39.5	22.56	2084	III_1+III_3	85.5	15.39	4389	VI_3+VI_7+VI_1	121.25	27.24	6038
II_3	42.25	21.86	3239	III_2+III_5	85.5	19.17	4801	VII_4+VII_6+VII_1	115	22.01	5394
II_6	42.25	24.41	4544	V_1+V_7	84.5	17.38	4863	VII_5+VII_2+VII_3	113.5	25.21	5730
III_4	42	22.69	2498	VI_2+VI_5	81.25	24.19	5057				
III_6	42.25	20.41	2181	VI_4+VI_6	81.25	19.22	4322				
IV_6	41.25	31.45	4488								
V_2	41.5	16.31	1304								
VII_7	38	26.54	5172								
Average	40.68	24.83	3298		83.34	21.30	4653		121.00	23.21	5567
St. Dev.	1.51	4.64	1258		2.48	4.53	493		5.57	3.90	367
C.oV.	0.037	0.187	0.381		0.030	0.213	0.106		0.046	0.168	0.066

The failure mode of the samples may be seen in Figure 4.8. Vertical and diagonal cracks in

Table 4.4 Unit core compression results sorted according to sampled brick.

Brick	I	II	III	IV	V	VI	VII	Total
No. of tests	5	4	4	2	3	3	3	24
f_{cu} $[N/mm^2]$								
Average	27.83	22.88	19.42	24.01	19.96	23.55	24.59	23.18
St. Dev.	3.261	1.244	3.056	10.519	5.418	4.047	2.328	2.86
C.oV.	0.117	0.054	0.157	0.438	0.271	0.172	0.095	0.123
E_u $[N/mm^2]$								
Average	3481	3535	3467	4903	3745	5139	5432	4243
St. Dev.	798	1552	1319	586	2116	861	281	874
C.oV.	0.229	0.439	0.381	0.12	0.565	0.167	0.052	0.206

the stacked specimens jump across the polished interfaces, indicating good contact between the samples. Continuity of spalling damage was also noticed.

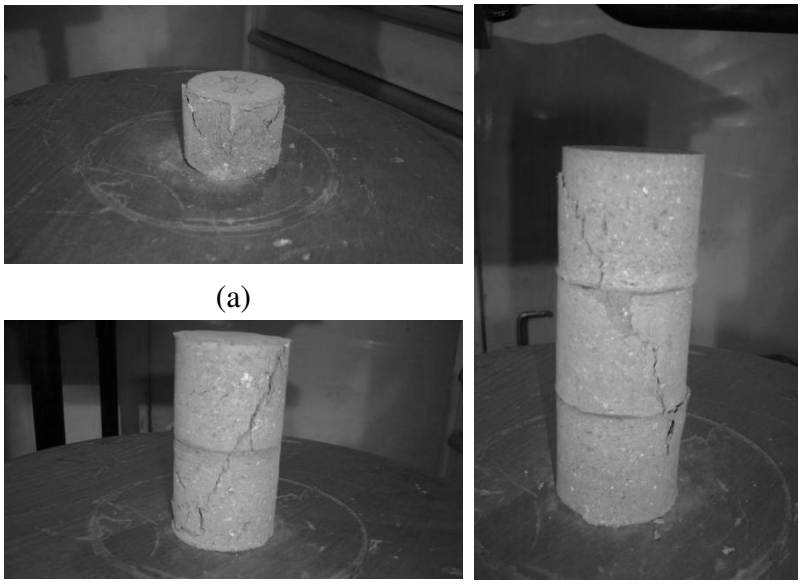

(a) (b) (c)

Figure 4.8 Brick cylinder samples after testing. (a) single, (b) double and (c) triple samples. Continuity of the vertical cracks is visible in the stacked samples.

It was noticed that imperfections such as existing cracks did not have a strong influence on the compressive strength or stiffness of the samples, as compared to undamaged samples from the same brick. However, damage at the base or the top of the samples, mostly due to the coring process, caused a notable reduction of the strength of the samples.

Examining the results of each brick separately, for example bricks II, III and IV, the compressive strength showed a decreasing trend for an increase in sample height. On the contrary, the Young's modulus increased with the specimen height throughout all the cases and on a brick by brick basis, despite the fact that the increase of the height of the specimens, which reduces size effects, and the existence of horizontal joints normally result in a decrease of the axial stiffness. Of further note is the fact that the scatter of the results for the Young's modulus exhibited a marked decrease for an increase in height, even though the number of tests was smaller for larger heights. The scatter of the results on the compressive strength was also the lowest across the triple sample cases.

Moderate variation was discovered in the properties across the bricks, with units VI and VII having a Young's modulus significantly higher than the average and unit I having a compressive strength higher than the average. These trends appear to have been partly influenced by the properties of the individual bricks from which the samples were extracted. For example, half of the triple stacked samples were performed using cores from units VI and VII, which had the highest Young's modulus. Finally, there was no correlation between the flexural strength of the brick and the compressive strength of the samples extracted from it.

4.3.2 Mortars

The evolution of the strength of the two mortars presents a number of differences. This can be attributed to the different maturation process between the binding agents in the two materials considered, aerial and hydraulic lime. Figure 4.9 illustrates the evolution of the compressive and flexural strength of the two mortars [145]. The evolution of these material properties has been idealized using logarithmic curves.

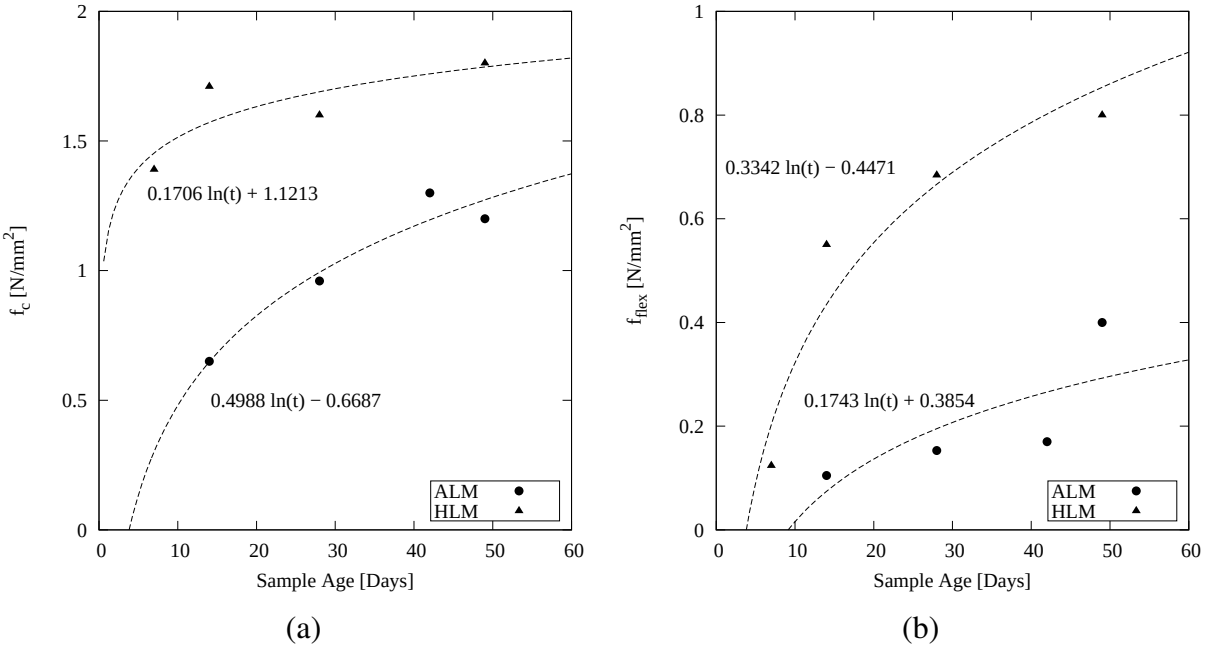

Figure 4.9 Evolution of mortar (a) compressive and (b) flexural strength for standard samples stored in laboratory conditions.

The compressive strength of the ALM exhibited a low initial rate of increase, which tended to decrease after 28 days. At 49 days the rate of increase was low but not zero. The HLM exhibited significant strength at 7 days, compared to the one achieved at 49 days. However, the rate of increase of strength was comparatively low in the remaining period until 49 days. The difference in both cases between the values at 28 and 49 days is significant, however, and should be considered in structural design.

It is unclear whether further maturation of the mortar would result in even higher compressive strength values or how long it would take for a substantial increase. Evaluation of the

tendency lines for the compressive strength seems to indicate that near maximum strength could be reached at 49 days for the HLM, but ALM should be expected to increase further in strength, as is evidenced by practical experience and the obtained development curve. Due to the scatter obtained for the flexural strength of the ALM it is difficult to make a similar estimation, though much higher strength should not be expected. However, the flexural strength of the HLM appears to be increasing significantly even after the 49th day.

The results of the mortar bending tests at 49 days are presented in detail in Table 4.5, where the dispersion of results in the case of the ALM is apparent, whereas the dispersion in the case of the HLM was much smaller. Taking into consideration that the tensile strength of the mortar is not significant in the study of the compressive strength of masonry, especially in stack bond prisms, the scatter of the aerial lime results is of small consequence.

Table 4.5 Mortar flexural strength results at 49 days.

Sample	f_{flex} $[N/mm^2]$	Sample	f_{flex} $[N/mm^2]$
ALM1	0.23	HLM1	0.82
ALM2	0.55	HLM2	0.93
ALM3	0.18	HLM3	0.90
ALM4	0.20	HLM4	0.92
ALM5	0.71	HLM5	0.80
ALM6	0.72	HLM6	0.70
Average	0.43	Average	0.84
St. Dev.	0.235	St. Dev.	0.082
C.oV.	0.545	C.oV.	0.096

The results obtained from the compressive tests at 49 days for both mortar types are presented in detail in Table 4.6. The samples are named after the mortar prisms tested in bending from which they were produced with the added suffix a or b. Once again, only the actuator force in time was measured. As was the case with the unit tests, no distinct relation between flexural and compressive strength of samples from the same prism could be discerned. Overall, the scatter of the results was quite low and much lower than for the bending tests.

According to the EN standard, mortar bending and compressive tests should be performed at an age of 28 days unless retarding agents have been employed in the mix, which was not the case in this campaign. Overviewing the results, it is apparent that the increase in strength in the period between 28 and 49 days is significant compared to, for example, the corresponding increase for concrete or masonry mortars based on Portland cement stored in laboratory conditions.

In addition to the destructive tests on samples stored in the lab, two masonry wallettes were constructed and two sets of standard mortar prismatic samples were stored in an area exposed to the environment. The prismatic samples were used for the standard mortar destructive tests and the wallettes were used for carrying out pin penetration tests on the mortar joints. This minor-destructive technique relates the hardness of a masonry mortar to its compressive strength according to the specifications provided by the manufacturer of the instrument used [80]. The objective of this investigation was to compare the effect of the curing conditions on the com-

Table 4.6 Mortar compression strength results at 49 days.

Sample	f_{flex} $[N/mm^2]$	Sample	f_{flex} $[N/mm^2]$
ALM1a	1.25	HLM1a	1.76
ALM1b	1.27	HLM1b	1.90
ALM2a	1.19	HLM2a	1.98
ALM2b	1.19	HLM2b	2.09
ALM3a	1.32	HLM3a	2.02
ALM3b	1.19	HLM3b	1.72
ALM4a	1.18	HLM4a	1.89
ALM4b	1.18	HLM4b	1.81
ALM5a	1.23	HLM5a	1.93
ALM15b	1.24	HLM5b	1.77
ALM6a	1.21	HLM6a	1.98
ALM6b	1.36	HLM6b	1.98
Average	1.23	Average	1.90
St. Dev.	0.061	St. Dev.	0.080
C.oV.	0.049	C.oV.	0.042

pressive strength of the mortars and to study the development of mortar strength in-situ over an extended period of time.

The development of the compressive strength of the prismatic samples kept in environmental conditions is shown in Figure 4.10a. It is immediately apparent that both mortars obtain a higher compressive strength than the samples stored in lab conditions: 50% higher for the aerial lime mortar and 57% higher for the hydraulic lime mortar at 28 days.

Penetration tests on the wallette mortar joints were performed until an age of 540 days. The determined compressive strength, based on calibrations for extending the pin penetration test results for low strength mortars [145], is illustrated in Figure 4.10b. The development of the compressive strength has been idealized using logarithmic curves, which approximate well its strength development near the end of the testing period.

4.3.3 Masonry

The cyclic loading of the prisms initially performed for each specimen revealed certain aspects of the masonry's response. The initial response in compression is highly nonlinear, as micro-cracks in the unit/mortar interface and voids in the mortar are closed. Unloading, even when only a very small load has been applied, has a far higher elastic modulus than the initial one in compression. The compressive loading modulus eventually becomes equal to the unloading one, provided sufficient load has been applied. This behavior is illustrated in Figure 4.11. Considering this fact, it may be necessary to perform these loading cycles using a higher load in order to get readings of the Young's modulus after the closing of the voids. However, special care must be taken in the case of weak component materials in order to limit the risk of premature damage in

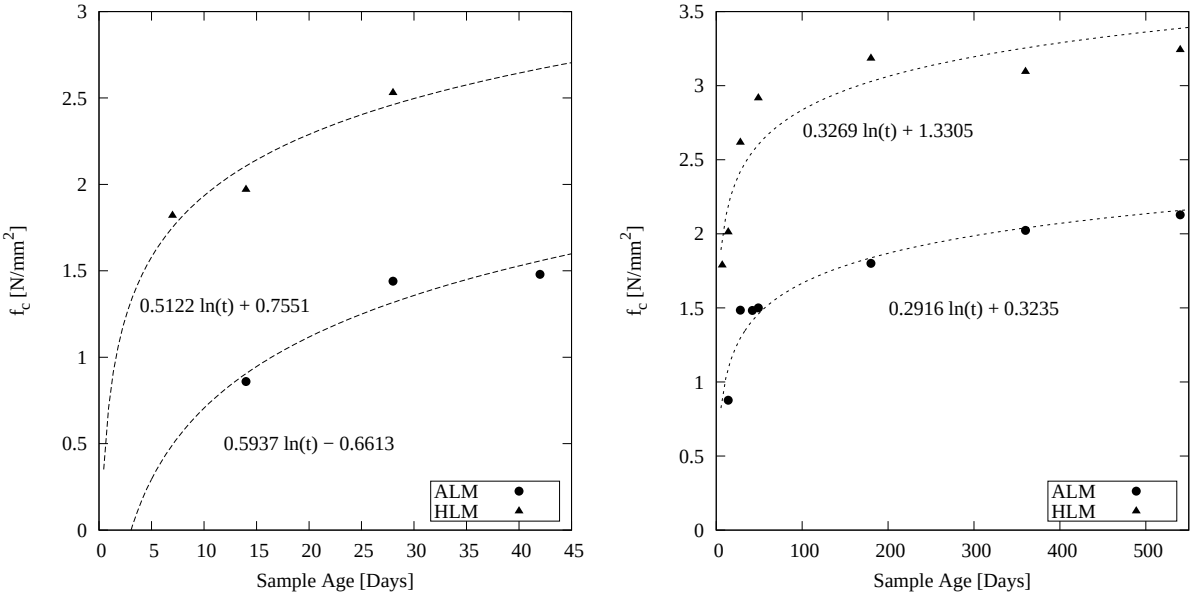

Figure 4.10 Evolution of the compressive strength of mortar stored in environmental conditions: (a) Standard samples and (b) in-situ mortar in wallettes.

the masonry specimen.

Significant agreement was found between the values of the capacity obtained for the two prisms with the sulfur mortar cap (prisms 1 and 3). The stress-displacement diagrams for the ALM masonry prisms are shown in Figure 4.12 and the results are summarized in Table 4.7. The failure mode was similar as well. The first visible cracks were observed at around 70% of the load and they included diagonal cracks originating from near the edges of the top of the prism and were mostly visible on the faces of the units. As cracking progressed, peripheral superficial cracking developed which eventually outlined a mostly crack-free core of masonry with its minimum width at mid height and spreading to the top and base units, which were almost intact. The condition of the ALM masonry at the end of the test is shown in Figure 4.13.

Table 4.7 Masonry compressive strength results for ALM prisms. Neoprene sheet was used for prism 2.

Sample	Height $[mm]$	f_c $[N/mm^2]$	Initial E_c $[N/mm^2]$	Unloading E_c $[N/mm^2]$	Final E_c $[N/mm^2]$
Prism 1	273	12.30	360	2574	488
Prism 2	266	9.68	474	2643	501
Prism 3	265	11.75	-	-	804
Average	268	11.24	417	2609	598
St. Dev.	4.36	1.38	80.61	48.79	178.8
C.o.V.	0.016	0.122	0.193	0.019	0.299
Average (sulfur mortar caps)	-	12.03	-	-	-

The prism with the neoprene sheet as the top compensating layer exhibited a lower strength value and a different failure mode. Whereas the sulfur mortar layer provides a certain degree of confinement on the top and base units, as is demonstrated by the largely undamaged state they

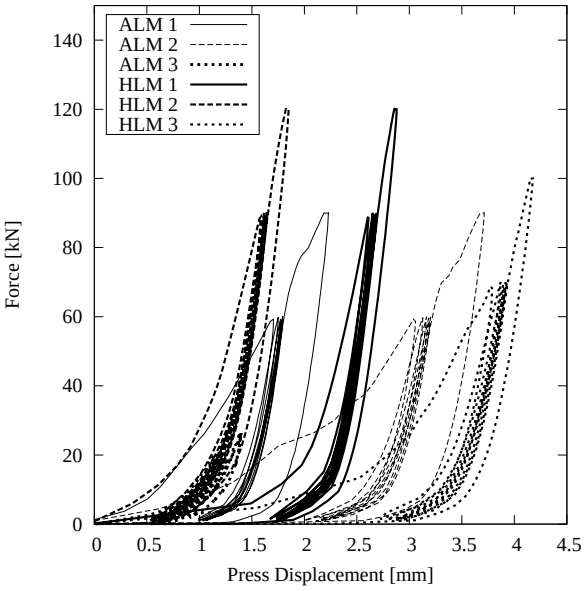

Figure 4.11 Cyclical loading response of masonry prisms.

are in at the end of the test, the neoprene layer affords the opposite effect. The lateral expansion of the sheet causes major vertical cracks at mid length of all the faces of the top unit for a very low load. Further load increase leads to the formation of new vertical cracks, in parallel with the first central crack, as well as to the perimetrical spalling noticed in the sulfur cap cases. At the end of the test the top unit was found to be significantly cracked, while the base unit was once again free from extensive damage.

At the end of the test, the remaining masonry cores were inspected and manipulated and were found to be very fragile, which is to be expected from the fact that the test was continued until a very low level of residual strength. The sulfur mortar caps were also inspected, and, apart from limited damage near the edges of the masonry where the perimetrical spalling had affected the top and base units, they were found to be intact. The neoprene sheet did not show significant damage.

In all three cases the mortar was found to be in a much deteriorated state due to crushing. The smooth post-peak curve appears to indicate that the failure is governed by crushing, which would account for the amount of energy release. Furthermore, examination of the samples after testing revealed that the mortar had no residual strength and even completely lacked integrity, especially near the edges of the masonry. Finally, the detached pieces of brick had hardly any mortar adhering to the beds, indicating either a poor tensile and shear bond or simply complete deterioration of the mortar due to crushing.

It is possible that the carbonation of the mortar near the center of the joints was incomplete due to lack of free contact with the air. In this case, complete carbonation of the entire mass of mortar would require a significant amount of time. This could account for the fragility and instability of the remaining masonry core.

The initial and unloading/reloading Young's moduli of the ALM masonry measured from the cyclic tests were lower and higher respectively than the final value registered in the monotonic

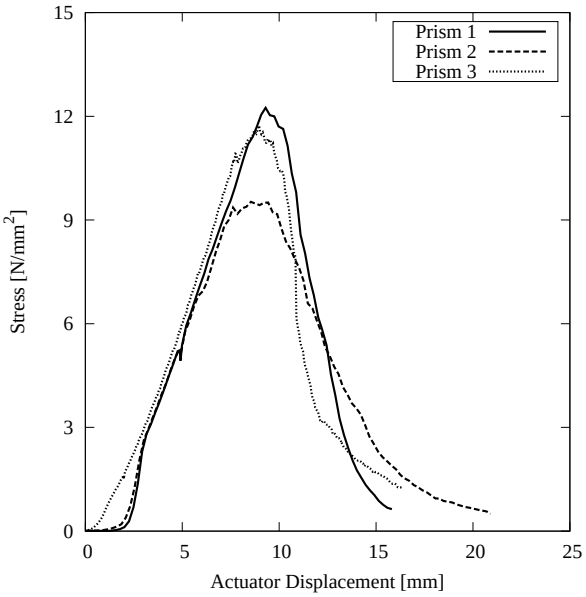

Figure 4.12 Stress displacement diagrams for aerial lime prisms. Neoprene sheet used for prism 2.

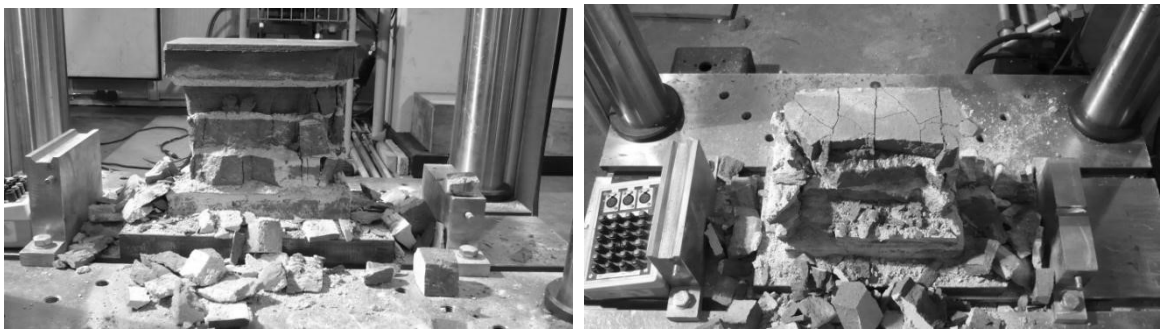

(a) (b)

Figure 4.13 ALM prisms after testing: (a) with sulfur mortar cap and (b) with neoprene sheet.

compression test. The average ratio of the final Young's modulus in the monotonic test over the compressive strength was 53.2.

The HLM prisms exhibited higher capacity and global stiffness and an apparent shift in failure mode. Although the initiation and propagation of cracking was similar to the ALM case, as was the fact that the top and base units remained mostly undamaged, there were a number of noticeable differences. Firstly, the mortar retained its integrity to a higher degree, as was evident by inspection of the mortar masses adhering to the broken off pieces of brick as well as the existence of intact mortar pieces which, after manual manipulation, did not exhibit signs of significant crushing. Furthermore, the mortar in the remaining core was not crushed. Hydraulic lime should not normally experience problems with curing in areas not in free contact with air.

There appeared to be evidence of more extensive unit cracking than in the ALM case. The broken off pieces of brick were generally of smaller size and there was noticeable presence of unit dust, which was not present in the ALM samples. Due to the relatively high compressive strength of the units, it seems unlikely that the unit dust is the result of unit crushing. Overall, the above evidence appears to point towards a more prevalent influence of unit cracking in the

failure mode. The condition of the HLM masonry after the test is shown in Figure 4.15.

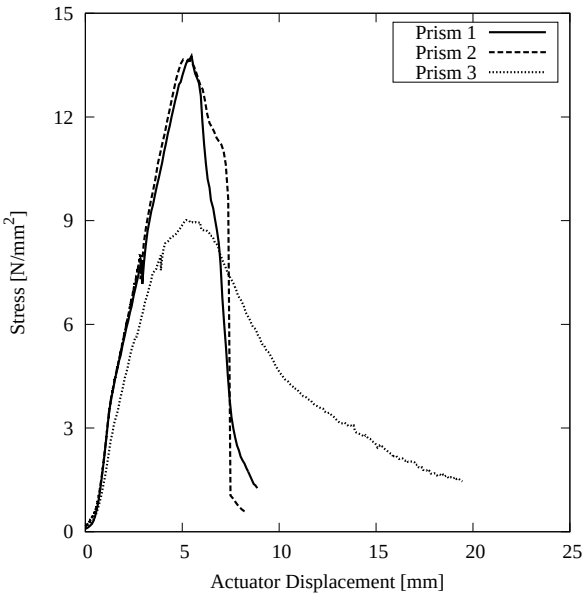

Figure 4.14 Stress displacement diagrams for hydraulic lime prisms. Neoprene sheet used for prism 3.

(a) (b)

Figure 4.15 HLM prisms after testing: (a) with sulfur mortar cap and (b) with neoprene sheet.

The HLM post-peak curves were also of a different overall shape, featuring steep, almost vertical, decline in the resisting force. However, the remaining masonry core was more stable than in the ALM cases and mostly intact due to the better condition the mortar was in at the end of the test. The steeper post-peak curves corroborate the point of higher involvement of cracking in the failure.

The HLM prism with the neoprene cap (prism 3) exhibited a lower compressive strength than the corresponding ALM prism. The failure mode was again similar across both material types, with extensive cracking at the top unit in the HLM case. The neoprene sheet itself was torn at the end of the test, but it could not be determined whether the failure of the sheet was responsible for the reduced apparent capacity of the masonry. The load displacement graphs for the HLM masonry are shown in Figure 4.14.

Both the values of the initial and unloading reloading Young's moduli measured in the cyclic tests were higher than the value recorded during the monotonic compression tests. The average ratio of the final Young's modulus over the compressive strength was 89.81.

The vertical deformation measurements, obtained by means of the LVDTs placed in this direction, are presented in Table 4.7 and Table 4.8. The average value for the Young's modulus of the units measured directly in the masonry considering all six cases was $6031 N/mm^2$, but the coefficient of variation was 1.06. The results from the compressive strength tests on the units should, for all intents and purposes, be considered more reliable for determining the Young's modulus of the units. However, it is worth noting that the average brick Young's modulus measured in the masonry agrees with the one measured in the compressive tests carried out on three stacked samples.

Table 4.8 Masonry compressive strength results for HLM prisms. Neoprene sheet was used for prism 3.

Sample	Height $[mm]$	f_c $[N/mm^2]$	Initial E_c $[N/mm^2]$	Unloading E_c $[N/mm^2]$	Final E_c $[N/mm^2]$
Prism 1	265	13.80	1153	2836	1021
Prism 2	268	13.66	1326	2488	1053
Prism 3	280	9.05	1928	3078	1204
Average	271	12.17	1469	2801	1093
St. Dev.	7.94	2.70	406.81	296.58	97.7
C.o.V.	0.029	0.222	0.277	0.106	0.089
Average (sulfur mortar caps)	-	13.73	-	-	-

Having acquired the values of the Young's modulus for the units and the two masonry composites it is possible, through equation (1), to estimate the Young's modulus of the mortars. The resulting Young's moduli for the ALM and HLM are $125 N/mm^2$ and $225 N/mm^2$ respectively.

The horizontal measurements in the central brick were also successful. The average Poisson's coefficient over the three ALM cases was 0.162. These results could not be based on the cyclic tests but on the monotonic tests for the determination of the masonry strength, as the horizontal deformation in the former proved to be too low to be measured accurately.

The development of the cracks typically observed in the masonry is illustrated in Figure 4.16, where the location and order of appearance of visible crack damage is shown for the two capping methods used. Similar crack development was noted for both ALM and HLM masonry.

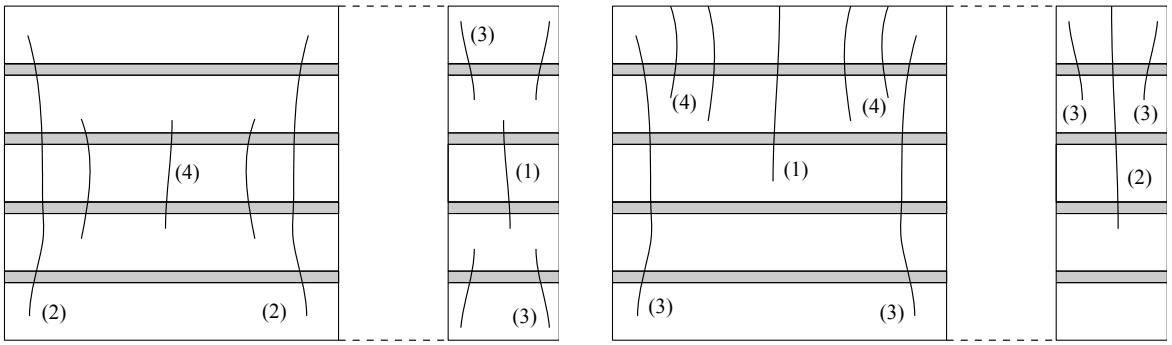

Figure 4.16 Crack development schematic in masonry: front and side view of prisms (a) with sulfur mortar caps and (b) with neoprene top cap, the numbers indicating order of appearance.

For both mortar types, the units and both masonry composites, the ratio between the Young's modulus and the compressive strength was significantly lower than the ratios reported in the literature and particularly lower than the ratios provided as rough estimations in design codes, such as Eurocode 6 [41].

Another major discrepancy between these experimental results and standard design code provisions is in the prediction of the compressive strength of the masonry from that of the two component materials. The Eurocode 6 equation for the characteristic compressive strength of standard masonry composed of clay units and general purpose mortar, such as the ones used in this campaign, reads:

$$f_c = 0.5 {f_{c,u}}^{0.7} {f_{c,m}}^{0.3} \tag{4.3}$$

Equation 4.3 results in a value of $4.7 N/mm^2$ for the aerial lime mortar masonry and $5.4 N/mm^2$ for the hydraulic lime masonry, which are much lower than the experimentally derived values.

In the present experiments, an increase of 50% in the compressive strength of mortar, as the one between the two types of mortar tested, only resulted in a 14% increase in the compressive strength of the composite, considering only the sulfur cap cases. This result is almost entirely consistent with the exponent on the mortar compressive strength which yields an increase of 13% for the composite when the mortar strength increases by 50%. In terms of compressive strength alone, the composite specimens were, in contrast with the mortars, more within the applicability spectrum implied in the EN 1052-1 standard for masonry compression testing.

Throughout all the cases the failure mode remained consistent. It was mostly influenced by the capping method, as was the compressive strength. The two capping materials did not have a significant effect on the global stiffness of the test setup, due to their very low thickness, with slightly lower global stiffness in the neoprene cases, as observed in the readings of the stroke of the actuator. The LVDT readings are, however, independent of the capping, since they were anchored on the masonry and not on the loading plates. The deformation of the composite specimen accounted for almost the entire deformation of the setup.

Concerning the measurement instruments used, the removal of the LVDTs prior to the stress peak may not have been entirely necessary, given the fact that the load is applied in displacement control, thus eliminating the possibility of explosive failure and, therefore, of damage to the instruments. Near the peak the vertical deformation is more uniform, which would allow for better measurements to be obtained.

4.4 Numerical Analysis

4.4.1 Model Description and Initial Results

The numerical simulation of the experiments has been performed using the methodology described in the chapter on finite element micro-modeling of masonry in compression. The prop-

erties used for the analyses is indicated in Table 4.9.

Table 4.9 Constituent material properties for numerical analysis.

	f_c $[N/mm^2]$	f_t $[N/mm^2]$	E $[N/mm^2]$	ν [-]
Units	23.0	3.22	4200	0.16
Aerial Lime Mortar	1.25	0.19	125	0.25
Hydraulic Lime Mortar	1.9	0.37	225	0.25

The three-dimensional mesh used for the analysis, along with the planes of symmetry taken into account, is shown in Figure 4.17a. Since the compressive load direction perpendicular to the unit/mortar interface, perfect bond was considered between the two material phases. Overall, 3213 20-node brick elements were used in the analysis.

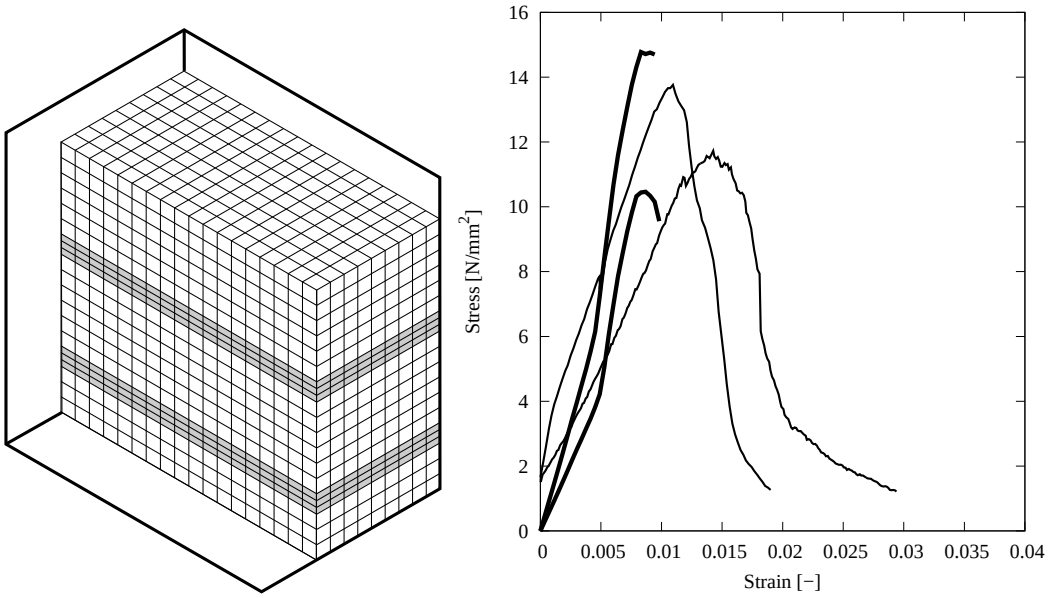

(a) (b)

Figure 4.17 (a) FE mesh used for analysis and (b) Comparison of experimental and numerically derived stress-strain curves for ALM and HLM masonry. FE results in tinted lines.

The stress-strain curves obtained from the analyses are shown in Figure 4.17b and are compared to the curves obtained experimentally. The finite element models obtained a good estimation of the compressive strength of masonry for both cases. The initial elastic stiffness was slightly overestimated, resulting in a peak strain slightly lower than the one registered in the experiments. Additionally, the finite element model of the ALM prism resulted in a more brittle failure mode than the experimentally observed one. The more brittle post-peak behavior observed for the HLM case was more accurately reproduced. The locking behavior obtained in the numerical curves could be the result of the mortar joint behaving as an incompressible layer under a large amount of lateral confinement.

4.4.2 Parametric Investigation

A two-fold parametric investigation has been carried out using numerical modeling. Firstly, the effect of the material properties of the mortar which were not directly measured has been investigated: the Poisson's ratio and the Young's modulus. Secondly, the effect of the finite element model was investigated by comparing the initial analysis results with results obtained from plane stress and plane strain models.

The values of the Young's modulus tested extended from half the original experimentally derived values up to 1000 times the compressive strength of the mortar. This range covers nearly the entirety of the range of values encountered when compiling the inventory of experimental data in the chapter on finite element modeling of masonry in compression. The range of values for the Poisson's ratios tested spanned from 0.15 to 0.3. This range too covers the values encountered in the inventory. While the upper value appears high as an initial value for a lime mortar, it has been experimentally shown that the Poisson's ratio of mortar increases rapidly for an increase in the applied load, starting from very early in the elastic range [106, 114].

The results of the material property parametric investigation are presented graphically in Figure 4.18 and tabulated in Table 4.10. In the figure it is shown that an increase in the Poisson's ratio of the mortar results in an increase in the compressive strength of masonry. Similarly, a decrease in the Young's modulus of the mortar results in an increase of strength as well, especially for high values of the Poisson's ratio of mortar. This behavior is noted for both types of mortar. Increasing the deformability of the mortar increases the confinement afforded to it by the units, resulting, finally, to an increase in the compressive strength of masonry. It is expected, however, though not noticed in these numerical analyses, that an excessive increase in the confinement of the mortar results in excessive horizontal and transversal tension of the bricks under vertical compression. It is therefore demonstrated that very weak mortars coupled with sufficiently rigid and strong units can produce masonry composites with a compressive strength far higher than that predicted by design codes.

A second trend that has been noticed in this parametric investigation is the increase of the Young's modulus of masonry for an increase of the Poisson's ratio of mortar. In the range of Poisson's ratios tested, this increase may be as much as 20% for mortars with low Young's moduli, with the increase being only 5% for mortars with a high Young's modulus.

The effect of modeling strategy on the compressive strength and Young's modulus of masonry is presented in Table 4.11. It is immediately apparent that plane stress models dramatically underestimate the compressive strength of masonry. Three-dimensional models provide the most accurate results and plane strain models tend to overestimate the compressive strength of masonry. Plane strain models result in a Young's modulus for the masonry composite 10% higher than the plane stress models, with three-dimensional models resulting in an intermediate value for both cases.

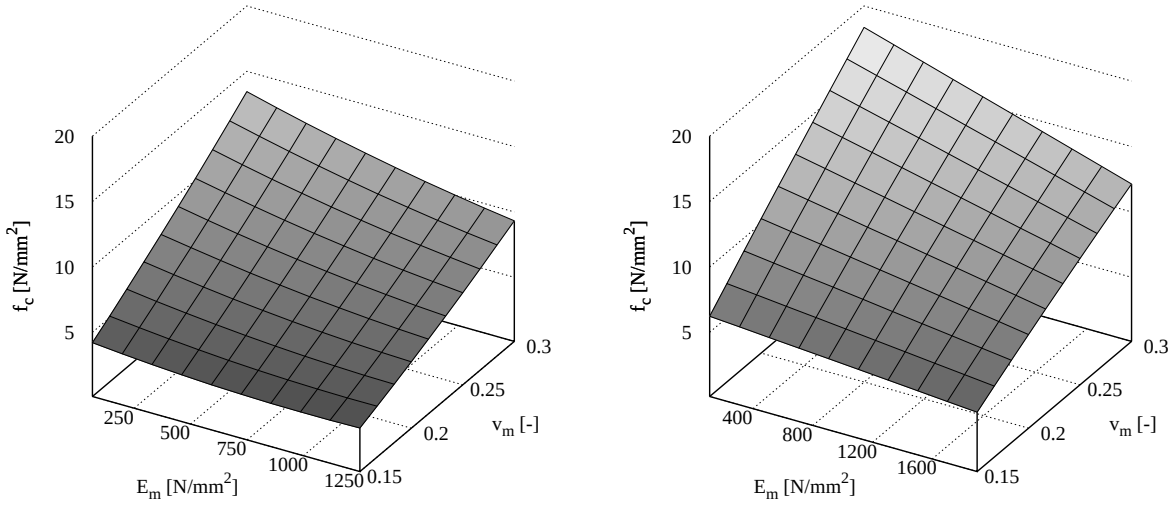

(a) (b)

Figure 4.18 Influence of E_m and ν_m on masonry compressive strength: (a) ALM, (b) HLM.

4.5 Conclusions

In the present work, a series of masonry materials frequently present in historical structures, namely fired clay bricks, aerial calcium mortar and hydraulic calcium mortar, was characterized mechanically. These materials were used in the construction of masonry prisms, which were subsequently tested in compression. A number of conclusions were drawn from these experiments.

Firstly, it has been established that relatively high masonry strength can be consistently achieved using conventional lime mortars and moderately strong units. Specifically, it was possible to achieve masonry strength nearly ten times higher than the compressive strength of the mortar. Additionally, it was observed that a significant amount of energy absorption is possible, especially in failure modes dominated by mortar crushing. In order to achieve this high masonry compressive strength the samples were tested at 49 days instead of the standard 28, a significant increase in the compressive strength of the mortar being registered in the intervening time.

The lime mortars tested in this campaign appear to be situated slightly below the spectrum of mortars covered by the EN 1015-11 standard, as was made apparent not only by their low resulting strength but also by the length of time required for maturity and the very low loading rates necessary for adequately controlled and, therefore, accurate testing.

The resulting masonry composites had a compressive strength much higher than the ones predicted by the EN standard. However, the relative increase in the compressive strength of masonry for an increase in the compressive strength of the mortar was consistent with the increase predicted by the EN standard, even though the prediction was incorrect in terms of absolute values.

Lime mortar specimens present a number of difficulties during experimental testing due to

Table 4.10 Results of parametric investigation: influence of mortar material properties on compressive strength and elasticity of the masonry composite.

	E_m $[N/mm^2]$	ν_m [-]	f_c $[N/mm^2]$	E_c $[N/mm^2]$		E_m $[N/mm^2]$	ν_m [-]	f_c $[N/mm^2]$	E_c $[N/mm^2]$
ALM Masonry	65	0.15	4.2	385	HLM Masonry	110	0.15	6.3	662
		0.20	6.8	402			0.20	10.1	689
		0.25	10.4	429			0.25	15.5	731
		0.30	12.8	471			0.30	17.4	797
	125	0.15	4.2	739		225	0.15	6.2	1185
		0.20	6.6	768			0.20	9.7	1225
		0.25	10.5	814			0.25	14.8	1288
		0.30	13.6	885			0.30	17.8	1383
	625	0.15	3.7	2296		950	0.15	5.5	3131
		0.20	5.6	2342			0.20	8.2	2894
		0.25	8.5	2413			0.25	12.4	2928
		0.30	11.0	2519			0.30	16.0	3009
	1250	0.15	3.5	3126		1900	0.15	5.1	3660
		0.20	5.0	3157			0.20	6.9	3598
		0.25	7.2	3208			0.25	9.7	3627
		0.30	9.4	3285			0.30	12.1	3676

their low strength and curing characteristics. Due to their low strength, it may be inappropriate to use modern testing standards for their characterization. Moreover, and due to the slow curing process experienced by them, only small specimens can be reliably tested, especially for aerial lime mortars. As far as the testing and measuring equipment is concerned, larger specimens, such as cylinders, might provide more accurate measurements of the mechanical properties; however, the proper curing throughout the specimen would not be achieved before a very long time has elapsed.

Employing the coring method for extracting samples from the units, it was possible to obtain sufficient specimens for one bending test and between two and six compressive strength/Young's modulus tests, depending on the number of cores in the compressed stack. Given sufficient brick dimensions, several tests may be performed on a single brick, making the method an interesting choice for historical brick testing.

Boundary conditions during masonry testing, as influenced by the capping method, can have a pronounced effect on the estimation of masonry strength and the obtained failure mode. Sulfur caps provide lateral confinement to the masonry and limit the initiation of failure in the mid-height of the masonry. On the other hand, neoprene caps caused premature failure near the load platen due to excessive lateral expansion of the neoprene sheet.

Numerical modeling of the experiments using micro-models, apart from resulting in an adequate reproduction of the experiments, has highlighted a number of points concerning the influence of the elastic properties of the mortar. Increasing the deformability of the mortar by lowering its Young's modulus and increasing its Poisson's ratio can result in a dramatic in-

Table 4.11 Numerical results from plane stress (PS), three-dimensional (3D) and plane strain (PE) analyses.

		f_c $[N/mm^2]$	E_c $[N/mm^2]$
ALM Masonry	PS	1.49	746
	3D	10.46	814
	PE	11.76	825
HLM Masonry	PS	2.22	1197
	3D	14.77	1287
	PE	15.77	1310

crease in the compressive strength of the masonry composite. The effect of modeling strategy is also noted. Three-dimensional models provide the most accurate results in terms of predicted strength. Underestimation of the confinement of mortar, as is the case when using plane stress models, results in a large underestimation of the compressive strength of masonry. Additionally, overestimation of this effect, as when plane strain models are used, can result in an overestimation of the strength. The effect of the modeling method on the Young's modulus of the masonry composite has been noted, but is not as pronounced.

Chapter 5

Simulation of Wall In-Plane Shear Tests

5.1 Introduction

Unreinforced masonry buildings are common in many seismic prone countries. In most cases they were built before the development of comprehensive research and the proposal of rational engineering procedures for their design. The careful observation of damages and collapses produced by recent earthquakes [127] has shown that the most vulnerable mechanisms are normally the out-of-plane failures of walls, mainly due to presence of insufficient connections between elements and lack of rigid horizontal diaphragms. Once such drawbacks are overcome by introducing appropriate devices able to ensure the box behavior of the building, the shear walls provide to the building the sufficient stability to lateral forces [99]. For this reason, numerous research studies have been devoted to the interpretation of the in-plane failure modes observed in the experimental tests of these structural members. The comprehensive experimental programs available in the literature present both empirical and analytical approaches for the derivation of the strength of masonry shear walls [66, 147, 161]. Nowadays, the advent of sophisticated numerical approaches has produced different strategies for the simulation of the behavior of masonry structures [96, 126, 132]. In this context, it is considered that approaches combining both experimental and numerical studies are necessary to consolidate the existing knowledge and to obtain a better understanding of the complex behavior of masonry shear walls.

The numerical analysis of masonry walls subjected to in-plane shear is a problem often addressed using finite element macro-models. This simplified approach is made necessary by the often insufficient characterization of the mechanical properties of the constituent materials and the need to mitigate computational cost. Analytical expressions may also be employed for the determination of the maximum shear resisted by the walls. Detailed micro-modeling allows for a more in-depth analysis of the failure mode observed in shear walls under varying levels of vertical stress and boundary conditions.

The current state of the art on the numerical simulation of masonry walls subjected to in-plane shear using detailed micro-modeling methods is limited (e.g. [8, 64]). Macro-models and simplified micro-models are far more common, but are faced with the same modeling uncertainties and assumptions necessary to be made for carrying out numerical analyses.

In this chapter, several experimental tests involving masonry shear walls are reproduced using detailed micro-modeling techniques. The experimental campaigns involved several wall geometries and boundary condition types, all of which are considered in the numerical investigation. Furthermore, the effect of the finite element type used on the predicted shear strength of the walls is investigated and discussed in terms of result accuracy and numerical efficiency.

5.2 Case Study

5.2.1 Overview

In the present research, a series of in-plane shear tests on fifteen scale walls, under different levels of vertical stress, was considered [44, 88]. The walls were composed of solid clay bricks and cement mortar arranged in single leaf running bond.

The bricks were scaled to 1:4 of the full brick dimensions and the mortar was produced using M8 mortar with adjusted granulometry for the removal of the larger aggregates. As such, the bricks measured $72.5 \times 12.5 \times 35mm^3$ and the joints were $2.5mm$ thick. The walls were capped using a stiff reinforced concrete beam. The vertical pre-compression and the horizontal load were applied on this beam. The experimental setup for the shear tests is shown in Figure 5.1. The figure illustrates the positioning of the vertical and horizontal presses as well as the LVDTs for measuring vertical and horizontal deformation, the former attached directly to the wall and the latter measuring the movement of the beam.

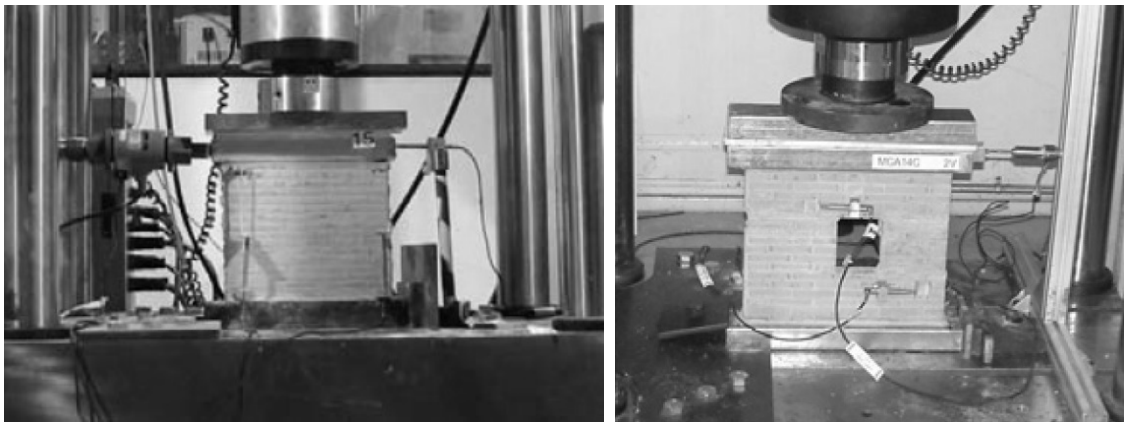

(a) (b)

Figure 5.1 Experimental setup for wall shear tests: (a) main series and (b) walls with openings.

A number of different geometrical layouts were tested, all based on single leaf running bond masonry walls, shown in Figure 5.2. The basic wall was subjected to the widest range of vertical pre-compression levels and consists of sixteen courses in height and four units in length. The remaining typologies were derived from the basic wall by varying the height and length of the structure. These walls were subjected to a single value of vertical stress level. Finally, a wall type with an opening was tested under six levels of vertical stress.

In addition to the different geometrical typologies tested, the basic wall typology was tested under different boundary conditions. One series of tests was performed allowing full freedom of movement to the top bounding beam and one series with a beam restrained against rotation but left free to move vertically.

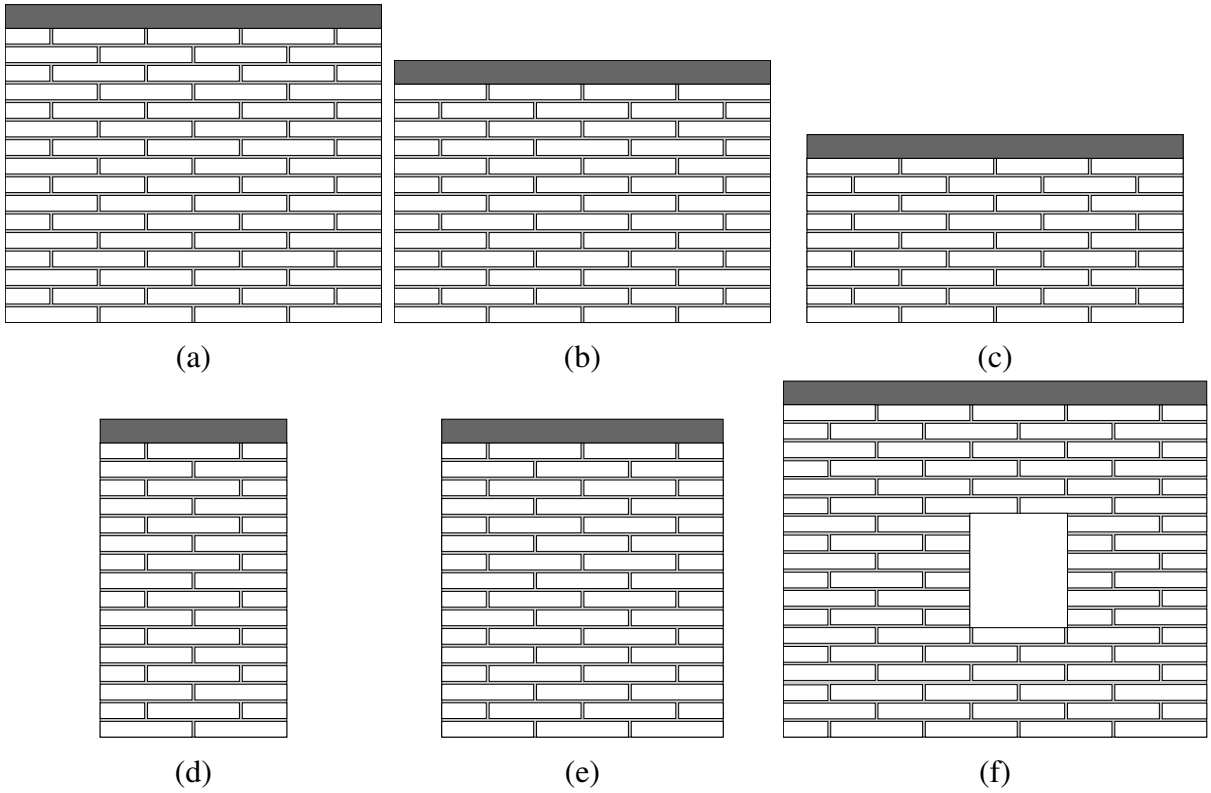

Figure 5.2 Wall types experimentally tested and numerically simulated: (a) basic wall, (b) & (c) with variation in height, (d) & (e) with variation in length and (f) wall with opening.

A single wall was tested for each value of vertical stress in the main series (free and constrained beam), two walls for each of the alternative dimension walls and one for each level of vertical stress for the walls with openings. Despite the use of a single data point for each vertical stress level for most of the series, the continuity of the data sets alleviates the risk of outlying results.

5.2.2 Material Properties

Extensive mechanical characterization has been performed on the units, the mortar and small masonry samples composed of said materials. These properties are presented in Table 5.1. The units and the mortar were tested in compression and three-point-bending. The unit/mortar interface was tested through direct tension of couplets and shear tests on triplets. In the table, the term f_{flex} refers to the flexural strength measured by means of the three-point test. In the absence of direct tests, the uniaxial tensile strength is herein estimated from the flexural strength by using an empirical correlation provided by the Model Code 2010 [35] applied to results obtained from full scale bricks. By applying this correlation, a value of $3.4 N/mm^2$ is obtained for the tensile strength of the solid clay units. The resulting ratio of f_{tu}/f_{cu} is equal to 9.7%, which is deemed

realistic for clay masonry bricks according to the previously studied inventory of experimental results. The same equation has been applied to the mortar, of which standard prismatic samples were produced and tested [41] The obtained tensile strength is $1.36 N/mm^2$. The wallettes were constructed and tested according to the provisions of the relevant CEN standard [38].

Table 5.1 Mechanical properties of materials and small masonry assemblages.

	f_c $[N/mm^2]$	f_{flex} $[N/mm^2]$	E $[N/mm^2]$	ν [-]
Units	35.0	15.2	4080	0.15
Mortar	8.34	3.08	3500	0.20
Prism Vertical	20.2	-	-	-
Wallette Vertical	15.2	-	4370	-
Wallette Horizontal	16.9	-	-	-
	f_t $[N/mm^2]$	c_0 $[N/mm^2]$	φ [-]	
Interface	0.55	0.42	39^0	

The Poisson's ratios of the units were not directly measured, but were rather given standard values. Several observations can be made by examining these experimental results. In particular the influence of the existence of head joints in the behavior of masonry is apparent in the difference between the compressive strength of the running bond wallettes and the stack bond prism in vertical compression. Additionally, the horizontal compressive strength of the running bond wallette was higher than the one in the vertical direction. This fact reveals a good compaction of the mortar in the head joints, to a degree that is often not achieved in brick masonry.

5.2.3 Wall Test Results

All experimental results are summarized in Table 5.2. The results include the Young's modulus of the walls as measured during the application of the vertical stress on the main series of walls (free and constrained).

Comparing the maximum shear stress obtained from the free and constrained beam tests, it is shown that the boundary conditions strongly affect the behavior of the walls under in-plane shear. While for low levels of vertical stress the difference is not acute, the constrained walls reach significantly higher maximum shear for vertical stresses higher than $1 N/mm^2$. Of note is the wide dispersion of the results of the vertical Young's modulus of the walls within each series. The overall average is 36% higher than the Young's modulus measured in the wallette tests, but with a high coefficient of variation of 0.45. The difference in the Young's modulus for different levels of applied stress could be attributable to the compaction of the bed joints under the effect of vertical stress. For higher levels the wall stiffens due to this compaction, while for the highest levels the drop in stiffness could be attributable to the beginning of hardening in compression.

The results of the walls with differing dimensions present a few interesting points for comparison with the main series of results. A decrease in height results in a small increase in maximum

shear. A decrease in length, however, results in a significant decrease of the maximum shear. The walls with the openings tended to produce a slightly lower maximum shear than the main series of walls with a free beam for the same vertical stress.

Table 5.2 Experimental results of vertical compression tests and combined vertical compression and in-plane shear tests on scale walls.

Main Series - Free Beam						Main Series - Constrained Beam					
Sample	Height [mm]	Length	σ	τ_{max}	E_y [N/mm^2]	Sample	Height [mm]	Length	σ	τ_{max}	E_y [N/mm^2]
F_9_V_5	250	300	0.895	0.538	5246	C_3_V_2	250	300	0.286	0.251	4077
F_12_V_6	250	300	1.190	0.646	4143	C_6_V_4	250	300	0.571	0.427	4580
F_15_V_8	250	300	1.486	0.850	3666	C_9_V_5	250	300	0.895	0.518	4854
F_20_V_10	250	300	1.933	1.028	4769	C_15_V_9	250	300	1.486	0.941	3891
F_25_V_12	250	300	2.381	1.180	6515	C_25_V_16	250	300	2.381	1.544	8759
F_28_V_14	250	300	2.681	1.363	9346	C_31_V_17	250	300	2.981	1.705	9801
F_31_V_15	250	300	2.981	1.461	10239	C_40_V_18	250	300	3.867	1.774	10734
F_35_V_15	250	300	3.333	1.454	10874	C_50_V_20	250	300	4.762	2.031	9198
F_40_V_17	250	300	3.867	1.635	8707	C_62_V_27	250	300	5.952	2.584	4715
F_45_V_18	250	300	4.286	1.722	5277	C_75_V_36	250	300	7.143	3.482	5270
F_50_V_18	250	300	4.762	1.737	4643	C_90_V_31	250	300	8.571	3.106	3281
F_56_V_23	250	300	5.357	2.249	4538	C_95_V_30	250	300	9.048	2.864	2836
F_62_V_20	250	300	5.952	1.969	3020	C_105_V_24	250	300	10.000	2.333	2434
F_95_V_18	250	300	9.048	1.737	-	C_115_V_7	250	300	10.952	0.716	-
Different Dimensions						With Window					
Sample	Height [mm]	Length	σ	τ_{max} [N/mm^2]		Sample	Height [mm]	Length	σ	τ_{max} [N/mm^2]	
D_21_V_12	195	300	2.000	1.163		W_1_V_7	270	338	0.645	0.416	
D_21_V_11	135	300	2.000	1.111		W_2_V_13	270	338	1.132	0.649	
D_15_V_5	250	225	2.000	0.732		W_3_V_21	270	338	1.858	1.119	
D_10_V_2	250	150	2.000	0.544		W_4_V_30	270	338	2.540	1.116	
						W_5_V_38	270	338	4.036	1.498	

Examples of the experimentally derived failure modes are shown in Figure 5.3. For the main series of walls for an increase in the vertical stress level the failure mode shifted from a rocking mode dominated by opening of a flexural interface crack, to a shear sliding mode and finally to a diagonal cracking mode accompanied by crushing of the compressed toe.

5.3 Modeling

5.3.1 Finite Element Models

The experimental tests will be simulated using the same modeling strategy presented for the analysis of masonry in compression. With the expectation that correct estimation of the behavior of the masonry composite in compression will be critical in correctly reproducing these experiments and predicting the maximum shear, three-dimensional models will be employed. However, a limited investigation on the effect of the modeling method on the predicted maxi-

(a) (b) (c)

Figure 5.3 Experimental failure modes: (a) main wall series, (b) alternate dimension series and (c) wall with opening.

mum shear has been attempted by simulating a number of these experiments using plane stress and plane strain models of the walls.

The finite element meshes of the shear walls are shown in Figure 5.4. The face of each masonry unit was divided to 32×6 elements. All mortar joints have 2 elements across their thickness. Across the thickness of the wall 6 elements were used. For the main series of walls 101304 20-node solid brick elements were used for the units and the mortar and 26892 16-node interface elements for the unit/mortar interfaces. Since the plane stress and plane strain models used the same overall arrangement of finite elements, 16884 8-node surface and 4482 6-node interface elements were used in those cases.

The vertical load is applied as a uniform stress at the top of the walls, kept constant throughout the analysis. The horizontal load is applied as a uniform displacement at the top, monotonically increasing.

Having already stressed the importance of properly simulating the behavior of masonry in compression in order to predict the shear strength of walls, it was deemed necessary to establish this model's capacity of predicting the compressive strength of this composite. This has been accomplished by simulating the compressive tests on prisms and wallettes using micro-modeling methods. In addition to estimating the accuracy of this method, the influence of the interface nonlinearities on the predicted compressive strength has also been investigated by comparing the results of the detailed micro-model to those of the meso-model. Finally, the results obtained from the full wall models are compared to those of a single periodic unit cell. The prism model has been elaborated as a meso-model, since the compressive load is applied in a direction normal to the unit/mortar interface.

The FE meshes used for the preliminary analyses on the compressive strength of masonry are shown in Figure 5.5. For the prism model 3402 solid elements were used, for the wallette 20886 solid and 3582 interface elements and for the cell 3120 solid and 672 interface elements. The compressive loads were applied as uniform displacements at the compressed face of the model. For the cell model displacement conformity conditions were applied in order to ensure uniform displacement of the faces.

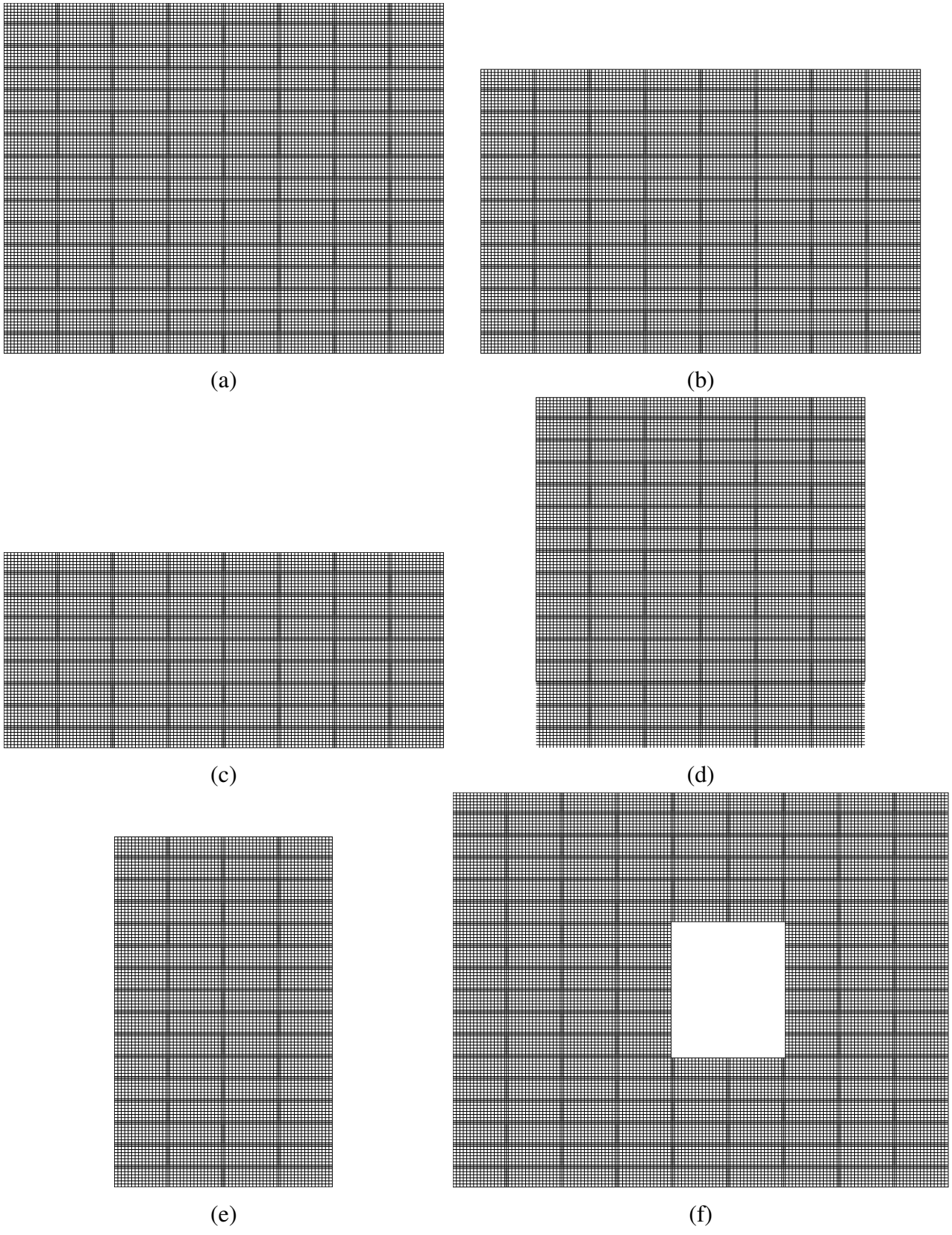

Figure 5.4 Finite element meshes of shear walls: (a) basic wall, (b) & (c) with variation in height, (d) & (e) with variation in length and (f) wall with opening.

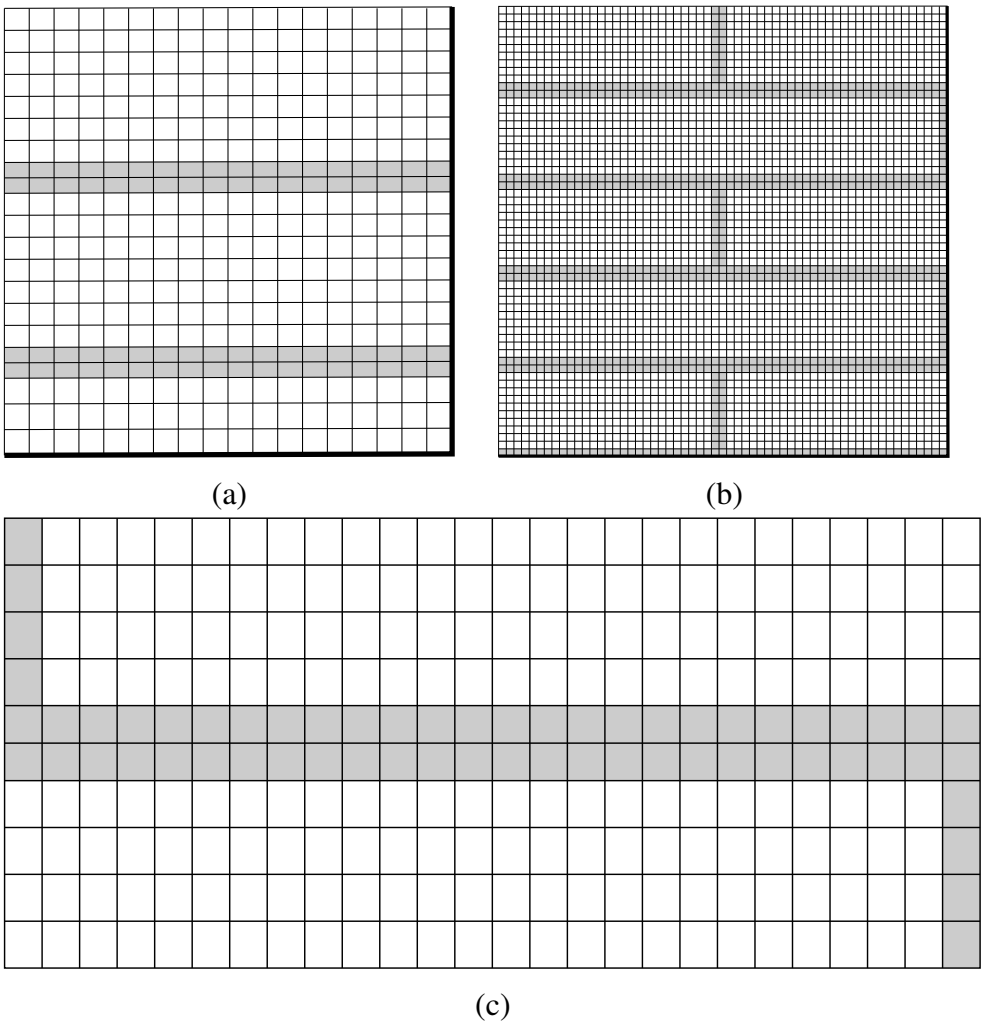

Figure 5.5 Finite element meshes for compressive strength determination: (a) prism, (b) wallette and (c) cell models. Symmetry planes at (a) and (b) shown in tinted lines.

All analysis results are presented in Table 5.3. In terms of the predicted Young's modulus of masonry, the full wallettes and the cells give very similar results. As expected, no difference was registered in the Young's modulus of masonry due to interface nonlinearities. The prism in vertical compression has the highest strength, followed by the wallette in vertical compression and, finally, the wallette in horizontal compression. The influence of the interface nonlinearities on the compressive strength of the wallettes is stronger in the horizontal direction, where a 10% drop in the compressive strength was registered when they are taken into account. For the cell models a 13% drop in the compressive strength was registered in the vertical direction. Despite this relatively small effect on the compressive strength of masonry, interface nonlinearities should be taken into account when investigating the behavior of masonry in tension and shear.

Table 5.3 FE results for masonry in compression: simulation of prism and wallette tests using full models, cell models and with/without interface nonlinearities.

Model	$f_{c,x}$	$E_{c,x}$	$f_{c,y}$	$E_{c,y}$
	$[N/mm^2]$			
Prism	-	-	18.90	3982
Wallette Meso-Model	16.92	3966	16.21	3917
Wallette Micro-Model	15.33	3966	16.08	3917
Cell Meso-Model	15.26	3928	16.9	3982
Cell Micro-Model	14.91	3928	14.74	3982

In general, the FE models give a good approximation of the experimentally derived compressive strength and Young's modulus. The cell models give results similar to the full wallettes. The computational cost for an analysis using the wallette model is significantly higher than for the cell model due to the smaller number of elements of the latter. Therefore, the analysis of masonry walls using cell models for the determination of their compressive strength can be seen as an efficient alternative to full wallette model simulations for the determination of the in-plane failure envelope of the masonry composite.

5.4 Analysis Results

5.4.1 Experimental Results vs. Numerical Analysis

As shown in Figure 5.6, the three-dimensional models are able to reproduce the experimental results fairly accurately. In the case of the unrestrained wall there is nearly complete coincidence of experimental and numerical results for the entire range. In the case of the restrained walls, the radical change of trend in the experimental results for a vertical stress higher than $7.5N/mm^2$ was not registered, although a slight change of trend was indeed noticed for a vertical stress load higher than $8.5N/mm^2$.

The plane stress model, although giving adequate results for low levels of vertical stress, failed to accurately predict the maximum shear for the greatest part of the vertical stress range: the numerical values in this case were greatly underestimated. The low confinement afforded on

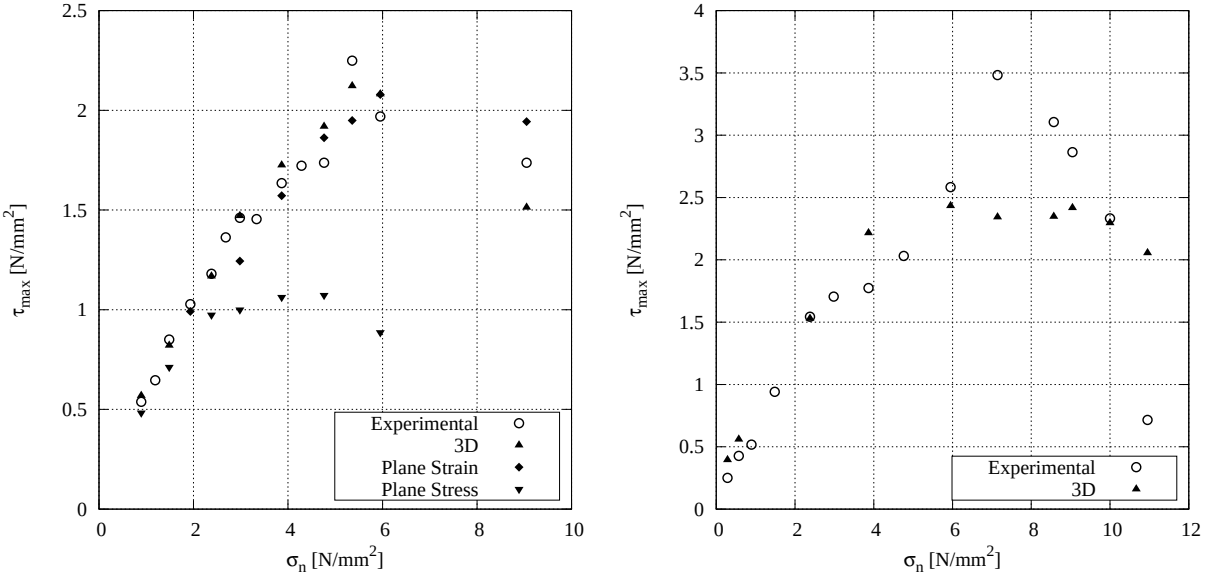

Figure 5.6 Main wall series: comparison of experimental and numerical maximum shear stress: (a) unrestrained top and (b) restrained top cases.

the mortar by the units in the plane stress models did not allow for a vertical pre-stress higher than the uniaxial strength of the mortar to be applied on the walls. The plane strain model, however, provided very adequate results, with values very near those given by the three-dimensional model. For the highest range of the spectrum of vertical pre-stress, the plane strain model tended to slightly overestimate the maximum shear, while the three-dimensional model slightly underestimated it.

It has been already shown that plane strain models tend to provide values for the compressive strength of masonry higher than those of three-dimensional models, while plane stress models usually underestimate it [54]. Three-dimensional models normally provide results between the two plane approaches. In the case of the shear wall experiments here considered, the plane stress models again underestimate the experimental value of the maximum shear. The near coincidence of the results provided by the three-dimensional and plane strain models indicates that in micro-modeling of shear walls the confinement effects in mortar under compression are critical but are not the only decisive factor for correctly predicting the shear capacity of masonry walls.

Overall, unlike the case of masonry under uniaxial compression, plane strain modeling proves practically equal to three-dimensional modeling for the purpose of predicting the capacity of walls in shear, while simultaneously being advantageous in terms of computational efficiency. Plane stress is an adequate choice for a very limited range of the spectrum of vertical stress levels in this particular sample of cases.

Figure 5.7a shows the comparison of the maximum shear between the four walls with alternative dimensions and their numerical simulation. The agreement is good for two of the cases, while some divergence is found for the remaining two. Figure 5.7b shows the comparison of the experimental and numerical results for the series of walls with openings. The maximum

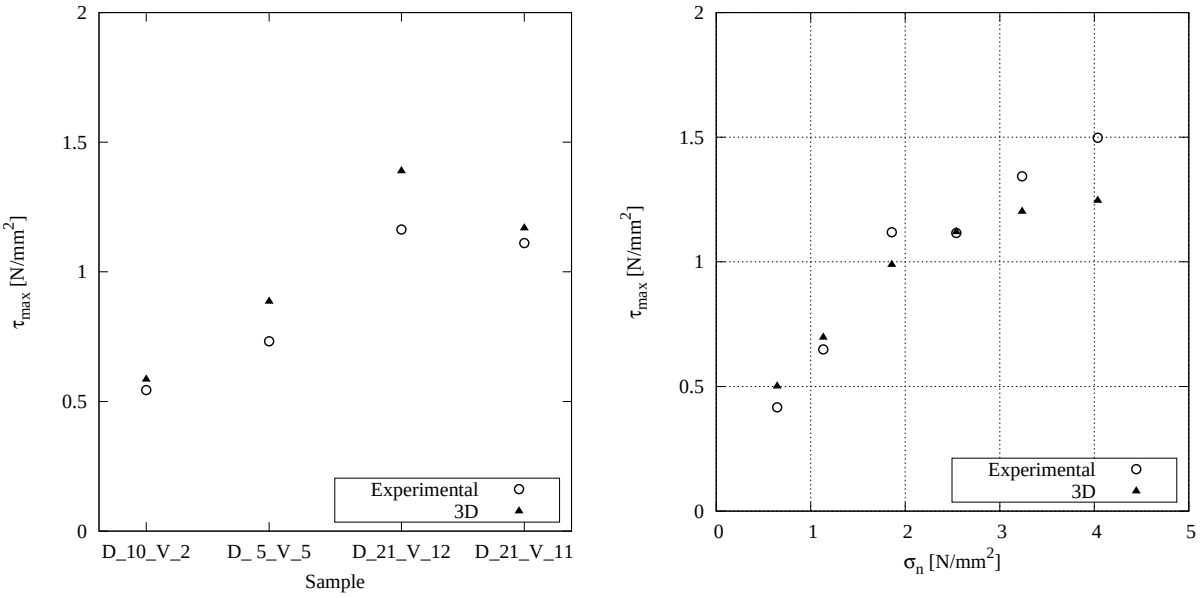

Figure 5.7 Comparison of experimental and numerical results: (a) walls with different dimensions ($\sigma = 2.0N/mm^2$) and (b) walls with opening.

shear predicted by the finite element model is generally in agreement for the greater extent of the range of results, although the numerical model tends to underestimate the value for higher vertical compression levels.

Examining the shear stress-displacement graphs of the main series, a change in the ductility of the response of the walls is noted. For low levels of vertical stress, in which the failure is dominated by a rocking mode, the response is highly ductile. As the vertical stress increases there is a noted drop in ductility. This change of ductility is shown in Figure 5.8, where for low levels of vertical stress the shear reaches a long plateau, whereas brittle behavior is noted for higher levels of vertical stress.

The shift in failure mode is also evident in the deformation and damage patterns obtained numerically for the same series of results. In Figure 5.9a, the rocking failure mode is clearly shown by the opening of the bed joint interface at the lower-most course. Figure 5.9b shows some opening of the bed joint interface in the same location. However, in addition, shear sliding and cracking are also appearing. In Figure 5.9c there is no opening of the bed joint interface and significant cracking takes place at the compressed foot, accompanied by yielding in compression.

5.4.2 Numerical Analysis vs. Closed Form Predictions

The experimental and the finite element analysis results, focusing on the series of walls with unrestrained top, will be compared to the results obtained from closed form expressions and modern masonry design rules. These expressions, proposed for the solution of the same problem, rely on the determination of different material parameters for the masonry composite: its shear, tensile and compressive behavior.

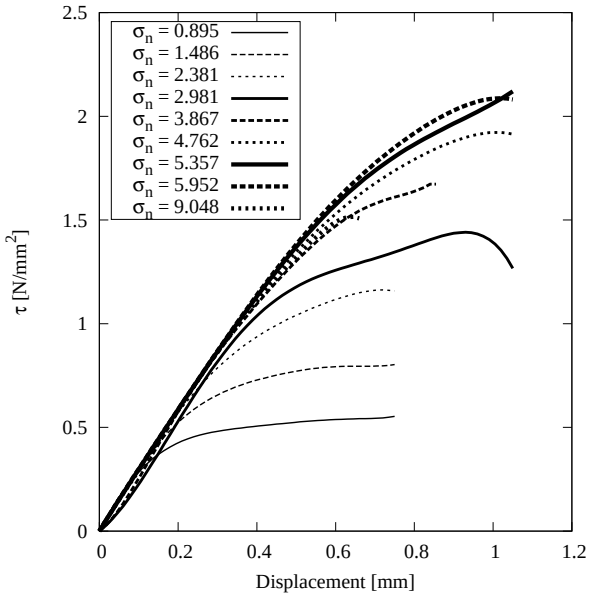

Figure 5.8 Numerically derived stress displacement graphs for main series of walls.

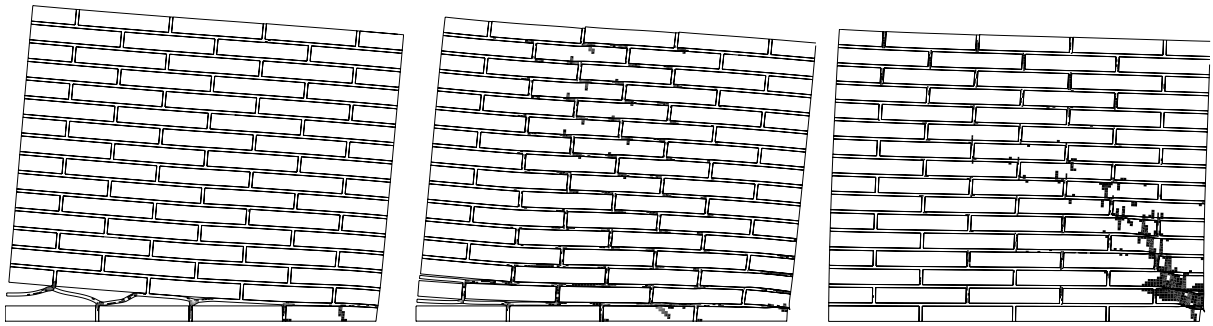

(a) (b) (c)

Figure 5.9 Numerically obtained failure modes: deformation profile and cracking patterns of main series of walls with unrestrained top beam for (a) $\sigma = 0.893 N/mm^2$, (b) $\sigma = 2.981 N/mm^2$ and (c) $\sigma = 9.048 N/mm^2$.

A model based on the Mohr-Coulomb criterion for shear under applied normal stress is proposed by the EN standard for masonry design [40]. The maximum shear is equal to

$$\tau_{max} = c + 0.4\sigma \tag{5.1}$$

where c is the initial shear strength and σ the applied normal stress, taking compressive values as positive. In this standard a value of $0.2 N/mm^2$ may be prescribed for the initial shear strength for this masonry typology, which is not very different from the value of 0.25 determined experimentally. The 0.4 value in the equation corresponds to the tangent of the friction angle as proposed in the standard for masonry in general, which is very different from the value of 0.81 determined in the experiments. In summary, this model is characterized by an apparent disregard of failure types other than shear sliding, which may be encountered in masonry shear walls, and the adoption of empirical values for the initial shear strength of masonry. Furthermore, the expression is not dependent on the dimensions of the studied structural member.

A flexural model for masonry in shear, based on in-plane equilibrium of the shear wall and assuming a plastic distribution of compressive stresses in the compressed toe, has also been formulated, proposed by the Italian Ministry of Infrastructure and Transport [79]. According to this model the maximum shear is equal to

$$\tau_{\max} = \frac{\sigma L}{2H}\left(1 - \frac{\sigma}{0.85 f_c}\right) \tag{5.2}$$

where f_c is the compressive strength of masonry, H is the height of shear wall and L is its length. In this case the compressive strength of masonry will be taken as equal to the average of the compressive strength determined in the running bond wallettes in the vertical and horizontal direction: $16.05 N/mm^2$.

Finally, a model using the tensile strength of the masonry composite has been proposed by Turnšek & Cacovic [147]. It assumes the formation of diagonal cracks in the masonry wall. The dimensions of the wall are not taken into account in the expression. According to this model the maximum shear is equal to

$$\tau_{\max} = f_t \sqrt{1 + \frac{\sigma}{f_t}} \tag{5.3}$$

In this study the tensile strength of masonry f_t will be taken as equal to the tensile strength of the unit/mortar interface. This value corresponds to 3.4% of the compressive strength of the masonry composite. This assumption is deemed reasonable due to the predominantly flexural response of the walls with an unrestrained top, which results in the opening of the bed joints.

The comparison of all the experiments and analysis approaches is shown in Figure 5.10. According to the interaction diagram of applied normal stress vs. maximum shear it becomes apparent that the finite element models produce the most accurate results. Among the three analytical expressions studied the flexural model based on compressive strength produces the most accurate results, being behind in terms of accuracy only to the finite element model. However, due to the formulation used in the model, the shear strength of the wall for zero vertical load is zero as well. The EN standard expression, though based on a nominal friction angle and a prescribed cohesion based on the masonry typology, produces good results in the range of vertical stress between 0.5 and $3 N/mm^2$. Its orientation as a design code makes it reasonably accurate in its intended spectrum of application: vertical stresses higher than $3 N/mm^2$ are unlikely to arise in masonry walls under shear loading. However, its results diverge for higher levels of vertical stress. Finally, the model based on the tensile strength of masonry does not produce consistently satisfactory results for any part of the experimental range. Despite using a low value for the tensile strength (that of the unit/mortar interface) the model overestimates the maximum shear for a range of vertical stress between 0 and $3 N/mm^2$.

Of the three analytical models investigated the one based on the compressive strength of masonry appears to provide the best overall results. This fact highlights the importance of properly modeling and taking into account the compressive strength of masonry in shear walls. Three-dimensional micro-models have already been proven to achieve good results in this regard, hence

their good performance in simulating this series of experiments.

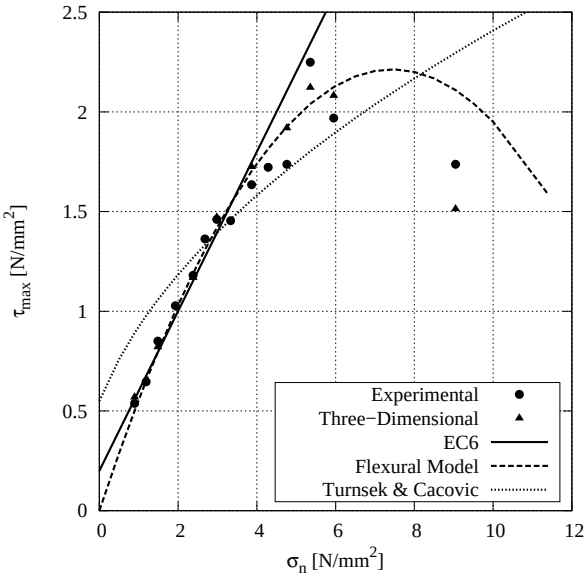

Figure 5.10 Comparison between experimental results, numerical and analytical models predictions: interaction diagrams for applied normal stress vs. maximum shear.

5.5 Conclusions

The analysis of masonry walls subjected to in-plane shear was attempted using detailed micro-models. The resulting maximum shear was for the most part accurately predicted by the models for a wide range of vertical pre-stress levels and different geometrical layouts.

The numerical analysis results proved able to provide far more accurate compared to closed form expressions and design guidelines. While the latter group of methods for predicting the maximum resisting force of shear walls provided good results for low levels of vertical pre-stress, the numerical approach provided more consistently accurate predictions.

The three-dimensional models produced results very similar to the plane strain approach, whereas the plane stress approach greatly underestimated the experimentally derived maximum shear. The equal adequacy of the first two approaches makes plane strain an attractive choice for the analysis of shear walls using detailed micro-modeling as its computational cost is far lower than the cost of full three-dimensional analysis.

The observations concerning the influence of the out-of-plane stresses in masonry under in-plane loading, highlighted by the inadequacy of plane stress models to accurately predict the maximum shear obtained in the experiments, are critical concerning the numerical simulation of such problems. The simulation of the confined mortar in the joints is shown to be important not only in the simulation of masonry under pure compression but under in-plane shear as well.

Concerning the prediction of the compressive strength of masonry using micro-models, significant agreement was found between the results obtained from the analysis of full wallettes

and periodic unit cells, in addition to the results being in good agreement with the experimental findings. The latter models have a much lower computational cost and and may serve as an efficient alternative to full wall models for the determination of the failure envelope of masonry wall structures. Finally, the influence of the nonlinearities of the unit/mortar interface on the compressive strength of masonry was investigated using finite element micro-models and meso-models. Only a small to moderate drop in the predicted compressive strength was found when considering interface nonlinearities.

Chapter 6

Micro-Mechanical Modeling of Masonry - Linear Elastic Analysis

6.1 Introduction

6.1.1 State of the Art

Masonry walls and pillars in buildings constitute a large part of the existing built environment and remain a common structural feature in modern construction, as main load-bearing elements or as secondary features. The composite nature of their structure, which mostly consists of the bonding of units, mortar and infill, makes their structural analysis a not so straightforward subject. The orthotropic behavior of masonry composites composed of largely isotropic materials stems from the complexity of the geometric bond employed in the structural arrangement. Even when the elastic properties of the constituent materials are known, it is difficult to derive the elastic properties of the composite without resorting to sophisticated analysis tools. Furthermore, results for one masonry typology may not be readily suitable for the evaluation of the properties of another. Therefore, the development of simple tools for the derivation of the orthotropic elastic properties of a variety of masonry typologies based on the elastic properties of their constituent materials, while maintaining a single analysis methodology throughout, constitutes a sound framework for the further development of analysis tools based on the detailed micro-modeling approach.

Masonry structures composed of periodically repeating patterns may be simplified in order to facilitate their analysis. In this sense, it is possible to calculate the elastic and strength properties of masonry structures through the analysis of a geometrically repeating part. This part may be further simplified by taking into account symmetry arising from geometrical and loading conditions.

A number of analytical, micro-mechanical and numerical models has been proposed for the analysis of masonry periodic unit cells using a variety of methods. These have been employed for the derivation of the elastic and inelastic properties of masonry composites as a result of the interaction of their two phases: units and mortar. The cells are analyzed considering appropriate

boundary conditions, kinematic compatibilities and stress equilibrium in order to derive the strains and stress state in the cell for different loading conditions. Nonlinear properties may be derived from the iterative solution of the problem under the assumptions of plasticity or damage models for the behavior of the materials in the cell.

Methods for the analysis of masonry cells using micro-mechanical methods have been proposed, mostly focusing on the analysis of stack bond and running bond masonry wall typologies [30, 89, 122]. Finite element representations of masonry unit cells have also been proposed [101] in which the interaction of the two phases, the resulting stress and strains in the cell and the nonlinear behavior of the materials may be accurately represented. This approach has also been adopted for the verification of the accuracy of analytical and micro-mechanical models, such as the ones already described, the production of in-plane strength domain curves for masonry membranes and the execution of two-scale analyses. However, FE calculations may require time for the creation of the models and high computational effort. A comparison of analytical model and FE model results may be found in [37].

A micromechanical approach for the analysis of periodically reinforced composites, according to which a repeating cell of the composite is discretized into sub-cells with different properties and arranged in a regular grid, has been proposed in the past [1]. Equilibrium and compatibility conditions are assembled in a set of closed form expressions and can be solved in a single analysis step for the derivation of, for example, the average elastic properties of the composite. The benefit of this approach is its computational efficiency and relative simplicity. Masonry periodic unit cells, seen as regular arrangements of square or cubic sub-cells with different material properties, can be analyzed using the same approach. This method has been already applied for the analysis of single leaf stack bond and running bond cells [143, 162].

Masonry analyzed in this manner is usually idealized as an infinitely thin or infinitely thick membrane, these assumptions being accordingly equivalent to a plane stress and plane strain approach. However, the existence of transversal joints, gaps or other discontinuities, which result in non-constant geometric structure along the depth of the masonry, render these two approaches fundamentally not accurate. Analysis of the unit cell taking into account these discontinuities must consider the actual finite thickness and actual geometry of the masonry structure.

Computations on cells where the actual finite thickness of the masonry is considered allow a more accurate representation of out-of-plane stresses, which, while only marginally affecting the initial elastic stiffness, may strongly influence the compressive strength of the composite [16]. However, since it is intended to apply the models proposed here in nonlinear analysis, it is deemed necessary to include a realistic representation of the out-of-plane stresses using three-dimensional models for linear elastic analysis as well. With this type of models, the true thickness of the masonry may be easily taken into account in finite element calculations.

Through computations on periodic unit cells it is possible to make fairly accurate predictions of the compressive and tensile strength and the elastic moduli of masonry. Such techniques may be, therefore, used for two-scale modeling of masonry walls [4, 100, 102, 110, 163],

6.1.2 Objectives

The purpose of this chapter is to present a simple micro-mechanical calculation method for the derivation of the elastic characteristics of masonry structures. The method is based on the analysis of masonry periodic unit cells, the smallest repeating geometrical entity representative of the overall masonry geometric pattern, in an attempt to derive masonry composite orthotropic macro-properties from material and geometrical micro-properties. The micro-properties considered are those of the units, the mortar and the infill. Structural members allowing this type of modeling include single- and multi-leaf walls and pillar-like structures. These properties are to be determined for normal and shear loading. The models are formulated based on three-dimensional elasticity in order to include the influence of out-of-plane stresses on the response.

These macro-properties may be used for the analysis of large walls and other structures in full multi-scale models or may be used to provide the information needed for analysis with orthotropic material models, such as the Hill, Rankine-Hill or the Hoffmann criteria. Additionally, periodic unit cells may be used for two-scale analysis of large masonry structures. The computational cost associated with this modeling strategy when combined with FE cells is still relatively high, especially when the analyses are carried out on cells in a three-dimensional configuration. Micro-mechanical models for the analysis of the cells present an advantageous, in terms of computational cost, alternative. Finally, the low computational cost of such models makes the production of large databases of results undemanding.

The verification of the model is performed through a comparison against a FE result benchmark following a parametric investigation. A comparison is also carried out with a range of results from the existing inventory of experimental data.

This study includes the analysis of various masonry wall geometrical typologies: single leaf stack bond, single-leaf running bond, double-leaf Flemish bond and three-leaf walls with a running bond outer leaf. In the last case, the infill constitutes a third material phase, with different mechanical properties from the units and mortar normally considered in such analyses. These masonry typologies, and especially the last three, represent a significant portion of existing and new structures, with the available research focusing primarily, if not entirely, on running rather than Flemish bond structures. Three-leaf walls with rubble infill are also commonly encountered both in large structures and common buildings. Stack bond pillars are commonly used as specimens for experimental investigation, therefore a large body of experimental work exists dealing with their elasticity and strength properties. English bond prisms are similarly used for experimental investigation purposes as well as in structural practice. The study focuses on masonries characterized by units with an elastic stiffness higher than that of the mortar. However, the applicability of the model is examined through an analysis of experimental case studies with a wide range of properties. It has been noted that there is a lack of experimental results concerning the horizontal and transversal Young's moduli, the shear moduli and the Poisson's ratios of masonry in experimental cases which include also a detailed mechanical characterization of the units and mortar. This lack of experimental results has been compensated by using finite element results as benchmark cases.

6.2 Overview of the Models

6.2.1 Derivation of Wall Periodic Unit Cells

The derivation of the periodic unit cell is accomplished through the identification of the repeating pattern in the structure and its subsequent simplification due to symmetry conditions. The four masonry typologies studied, in order of complexity, are stack bond, running bond, Flemish bond and three-leaf masonry with a running bond outer leaf and infill. The derivation patterns for the masonry wall typologies considered in this work are shown in Figure 6.1.

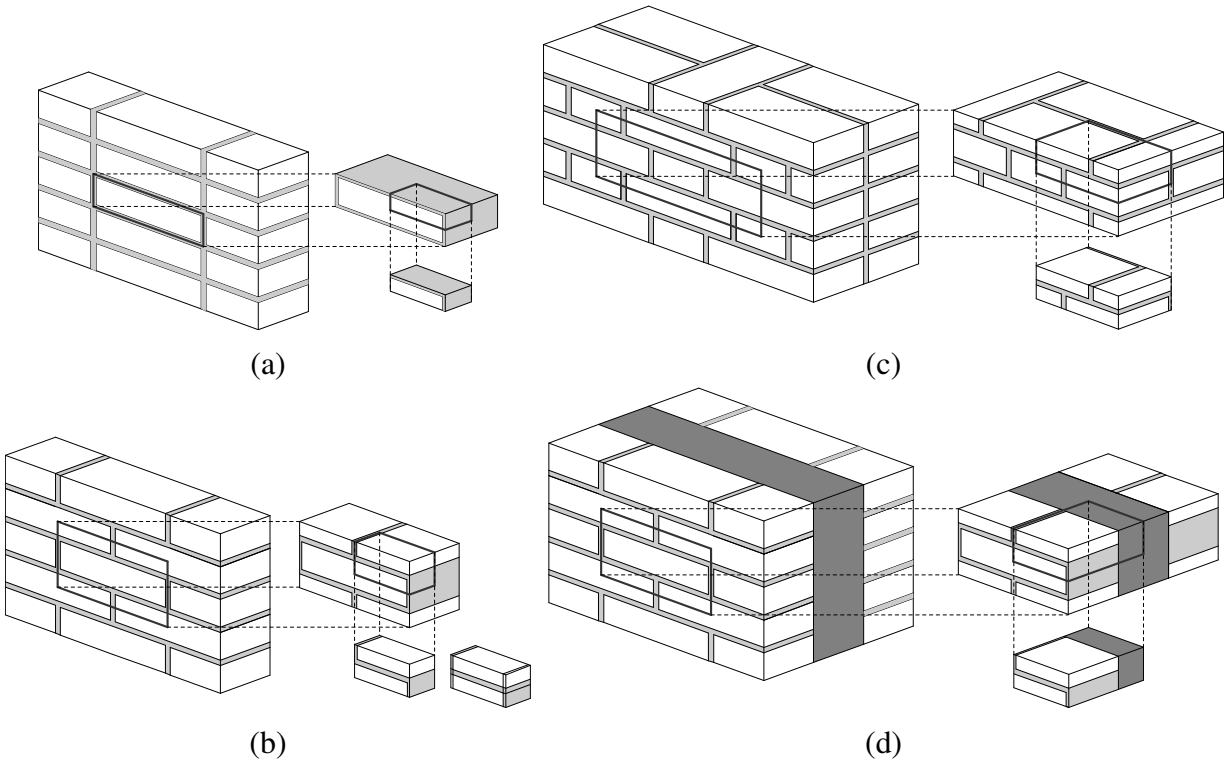

Figure 6.1 Derivation of wall cells: full wall, repeating pattern and cell derived from geometrical symmetry of repeating pattern. (a) Stack bond wall, (b) running bond wall, (c) Flemish bond wall and (d) three-leaf wall with running bond outer leaf.

Stack bond and running bond walls are single leaf structures with no variation of the geometry along the thickness. Flemish bond walls include a thin transversal joint and the units are oriented as either header or stretcher blocks, meaning that for the largest portion of the wall the geometry changes along the thickness. Three-leaf walls are composed of outer leaves of any type and an interior leaf whose thickness may be larger than that of the outer leaves.

Increase in the geometrical complexity of the composite results in an increase in the size of the repeating pattern and, therefore, of the unit cell. In stack bond and running bond masonry the layout of the masonry does not change through the thickness and all units are identically oriented, while in Flemish bond masonry the mid-thickness is characterized by a transversal mortar joint and intersecting header units.

The anisotropic behavior of the masonry composite is the result of the geometrical arrange-

ment of components, which are here considered isotropic, although the orthotropic behavior of bricks may be implemented with only minor alterations in the model. The infill is also considered macroscopically isotropic and is normally more deformable than the outer leaf.

6.2.2 Derivation of Pillar Periodic Unit cells

The periodic unit cells for pillar-like structures are derived similarly to the wall typologies. Two different structural types are considered: stack bond prisms and English bond pillars. The derivation of the cells is shown in Figure 6.2.

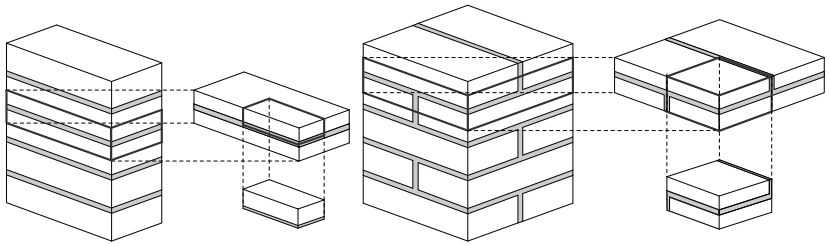

Figure 6.2 Derivation of pillar cells: full wall, repeating pattern and cell derived from geometrical symmetry of repeating pattern. (a) stack bond pillar and, (b) English bond pillar.

6.2.3 Discretization of the Derived Cells

The micro-mechanical model for the analysis of masonry periodic unit cells is based on the discretization of the cell in structural parts, the modeling of their interaction in terms of deformation and stress distribution and equilibrium under external loads. The modeling of the interaction is accomplished using analytical expressions. The equilibrium problem will be primarily solved for three normal stress components, σ_{xx}, σ_{yy} and σ_{zz} and six shear stress components, σ_{xy}, σ_{xz}, σ_{yx}, σ_{yz}, σ_{zx} and σ_{zy} in order to obtain the elastic properties of the cells in the three orthogonal directions dictated by the geometric arrangement of the masonry.

The discretization of the periodic unit cells is done as illustrated in Figure 6.3. It results in each cell being discretized into cuboid parts of units, bed joints, head joints, transversal joints and cross joints. Specifically: the stack bond cell is discretized into one stretcher unit, one bed joint, one head joint and one cross joint part; the running bond cell is discretized into four stretcher unit, one bed, two head and two cross joint parts; the Flemish bond cell is discretized into four header unit, six stretcher unit, three bed joint, four head joint, seven cross joint and six transversal joint parts; the three-leaf cell is discretized similarly to the way the running bond cell with the addition of nine transversal joint parts representing the infill. The stack bond pillar is discretized into a unit part and a mortar part arranged in a layered pattern and the English bond pillar is discretized into four unit parts, one bed joint part two head joint parts and four cross joint parts.

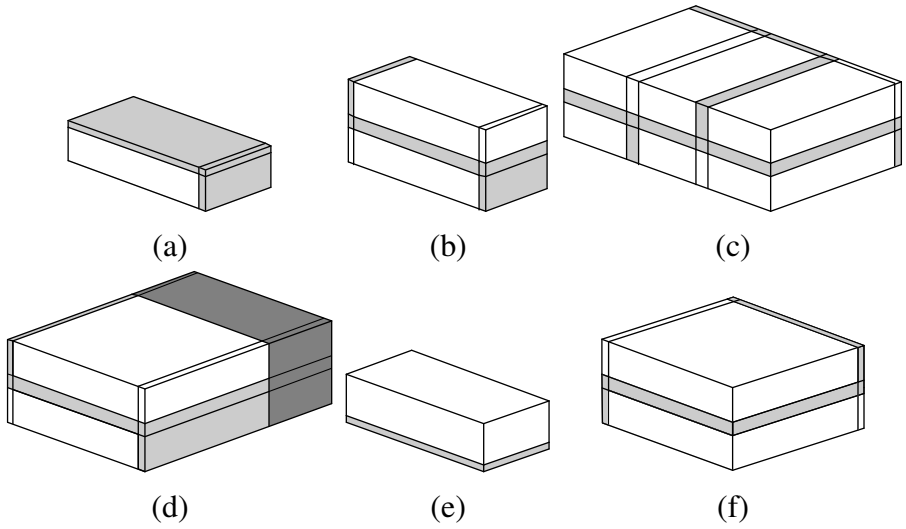

Figure 6.3 Discretization of periodic unit cells: (a) stack bond wall, (b) running bond wall, (c) Flemish bond wall, (d) three-leaf wall, (e) stack bond pillar and (f) English bond pillar.

The orthogonal discretization carried out separates the cell into parts allocated in an orthogonal grid, with each part belonging in one horizontal, one vertical and one transversal strip of cuboid parts. As a result, the stack bond cell is divided into two horizontal, two vertical and two transversal strips, the running bond cell into three horizontal, three vertical and six transversal strips and the Flemish bond cell into six horizontal, ten vertical and fifteen transversal strips. The type of the loading applied on the cell and its orientation compared to the orthogonal grid dictates the assumptions made for the elastic analysis of the cell, which are based on the strains to which each strip is subjected. The proposed discretization of mortar joints and units allows for simplified assumptions in the formulations of the model. The final discretization scheme is shown in Figure 6.3.

6.3 Development of the Micro-Mechanical Model

6.3.1 General Assumptions and Equations

The deformation of the cell faces, and, therefore, the total strain of the cell, depends on the loading applied. Application of normal stress results only in normal global cell strains and the application of shear stress results only in shear global cell strains. This means that under normal stress the total deformation of all strips, or the average strain of each one, is equal in the three principal directions.

Under the application of normal stress, either only normal or both normal and shear stresses may arise in the cuboid parts. In turn, under the application of shear stress, only shear stresses of the same geometrical orientation arise in the cuboid parts. All stresses and strains are assumed constant in the cuboid parts. For linear elastic analysis, the units and the mortar are modeled as three-dimensional isotropic continua. Perfect bond is considered at the unit/mortar interface for the linear elastic computations performed here, so that all deformation of the cell is accounted

for in the units, mortar and infill.

Isotropic linear elasticity stress-strain relations in three dimensions apply for every cuboid component under normal and shear stress. This includes the units, the mortar and the infill. These relations are expressed as:

$$\varepsilon_{ii,n} = \sigma_{ii,n}/E_{\ n} - \nu_n\left(\sigma_{jj,n} + \sigma_{kk,n}\right)/E_n \tag{6.1}$$

$$\varepsilon_{ij,n} = \sigma_{ij,n}\,(1+\nu_n)/E_n \tag{6.2}$$

where the sub-index n refers to the identifier of the cuboid, σ_{ii} and ε_{ii} are the applied normal stress and calculated normal strain along axis i, σ_{ij} and ε_{ij} are the shear stress and strain in plane ij, E_n is the Young's modulus and ν_n is the Poisson's ratio.

When a cuboid with dimensions D_i and D_j is subjected to a shear stress σ_{ij}, leading to a shear strain equal to ε_{ij} in the ij plane, the contribution of the shear deformation of the cuboid d_i^{ij} to its normal deformation in the direction i is taken as being half the displacement at its top due to the shear stress. Therefore, it is defined as

$$d_i^{ij} = \varepsilon_{ij,n}\frac{D_j}{2} \tag{6.3}$$

This assumption, based on the deformation of a rectangular plane body supported at the base and subjected to shear stress at the top, is made in order to take into account the shear deformation of the bed joints in a masonry composite subjected to normal stress in the horizontal direction. The contribution of the shear deformation to the total deformation of the cuboid is essential in running bond and Flemish bond wall masonries under applied horizontal stress. The interlocking pattern in both typologies restricts the normal deformation of the mortar in the bed joint. Not accounting for this deformation in the compatibility relations in the computed cell leads to excessive horizontal stiffness [162].

The three Young's moduli for each cell configuration are calculated by use of the equation

$$E_{c,i} = \sigma_{ii}/\varepsilon_{ii} \tag{6.4}$$

The Poisson's ratios are determined by the equation

$$\nu_{c,ij} = -\varepsilon_{jj}/\varepsilon_{ii} \tag{6.5}$$

The three shear moduli for each cell configuration are calculated by use of the equation:

$$G_{c,ij} = \sigma_{ij}/\left(2\varepsilon_{ij}\right) \tag{6.6}$$

The x, y and z axes in the model correspond to the horizontal, vertical and transversal directions. The transversal direction is normal to the face of the walls and the vertical direction

is parallel to the axis of the pillars. The total strain in each of the three directions and the three resulting planes depends on the type of cell.

The cuboid parts are designated by a set of initials. Throughout all the cases these are: u for units in general, s and d for stretcher and header units respectively where both are present (such as the Flemish bond case), h for head joints, c for cross joints, b for bed joints and t for transversal joints. Infill is designated as i. Dimensions are designated according to their orientation: l corresponds to a horizontal length, h to a vertical height and t to a transversal thickness. The dimension symbols are finally suffixed u, m or i for units, mortar and infill respectively, meaning that h_u is the unit height, h_m is the thickness of the bed joint, l_u is the unit length, l_m is the thickness of the head joint, t_u is the width of the unit, t_m is the thickness of the transversal joint and t_i is the transversal thickness of the infill.

Figure 6.4 illustrates the discretization of the single leaf wall cells along with the naming convention for each component in detail. The discretization of the multi leaf walls is shown in Figure 6.5 and that of the pillars in Figure 6.6.

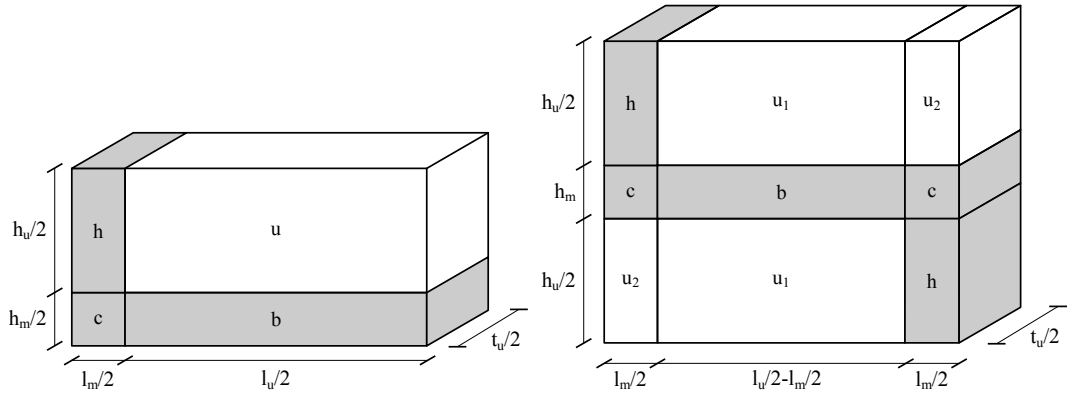

Figure 6.4 Discretization and component designation of single leaf wall periodic unit cells: (a) stack bond and (b) running bond.

Normal stress equilibrium equations are formed according to

$$\sum_n \sigma_{ii,n} A_n - \sigma_{ii} A = 0 \tag{6.7}$$

while shear stress equilibrium equations are formed according to

$$\sum_n \sigma_{ij,n} A_n - \sigma_{ij} A = 0 \tag{6.8}$$

where A is the total cross sectional area of the cell and A_n is the cross sectional area of cuboid n in direction i.

All normal and shear stress equilibriums at the faces or cross sections of the cell assure global equilibrium of internal and external stress. External stresses are averaged over the surface of the cell, meaning that there may exist a mismatch between the external average stress and the stress of an individual cuboid.

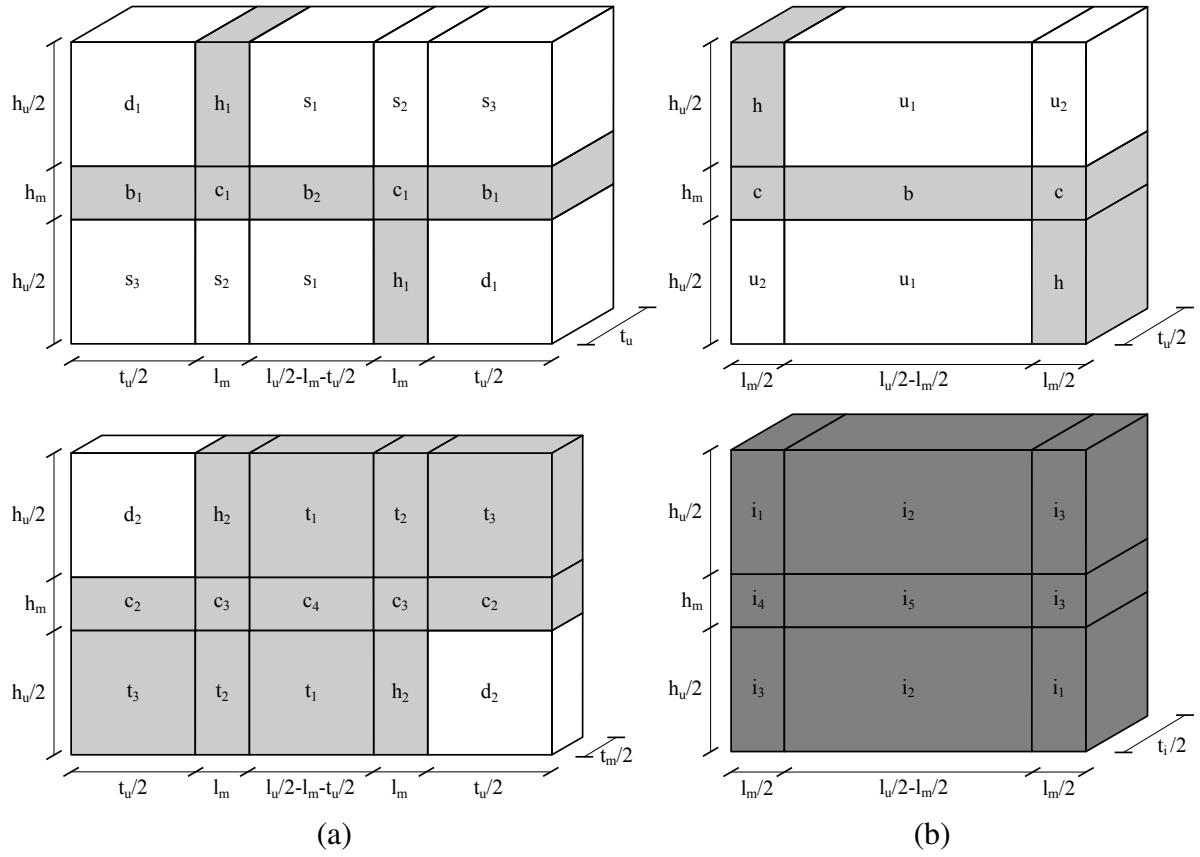

Figure 6.5 Discretization and component designation of multi leaf wall periodic unit cells: (a) Flemish bond and (b) three-leaf wall with running bond outer leaf.

6.3.2 Stack Bond Wall

Due to the simple geometrical layout of the cell, which does not include complex geometrical interlocking of mortar joints and units, shear stress components are disregarded for applied normal stress.

Normal strain conformity is assumed as follows:

$$\begin{aligned} \varepsilon_{zz,h} &= \varepsilon_{zz,u} = \varepsilon_{zz,c} = \varepsilon_{zz,b} \\ \varepsilon_{xx,h} &= \varepsilon_{xx,c} \\ \varepsilon_{xx,u} &= \varepsilon_{xx,b} \\ \varepsilon_{yy,h} &= \varepsilon_{yy,u} \\ \varepsilon_{yy,c} &= \varepsilon_{yy,b} \end{aligned} \tag{6.9}$$

These strain conformity relations assume equal out-of-plane strains for all cuboids and equal in-plane strains for parallel cuboids in a given direction.

Horizontal normal stress equilibrium conditions at the right and left face of the cell are as follows:

$$\begin{aligned} \sigma_{xx}\,(h_u/2 + h_m/2\,) &= \sigma_{xx,u} h_u/2 + \sigma_{xx,b} h_m/2 \\ \sigma_{xx}\,(h_u/2 + h_m/2\,) &= \sigma_{xx,h} h_u/2 + \sigma_{xx,c} h_m/2 \end{aligned} \tag{6.10}$$

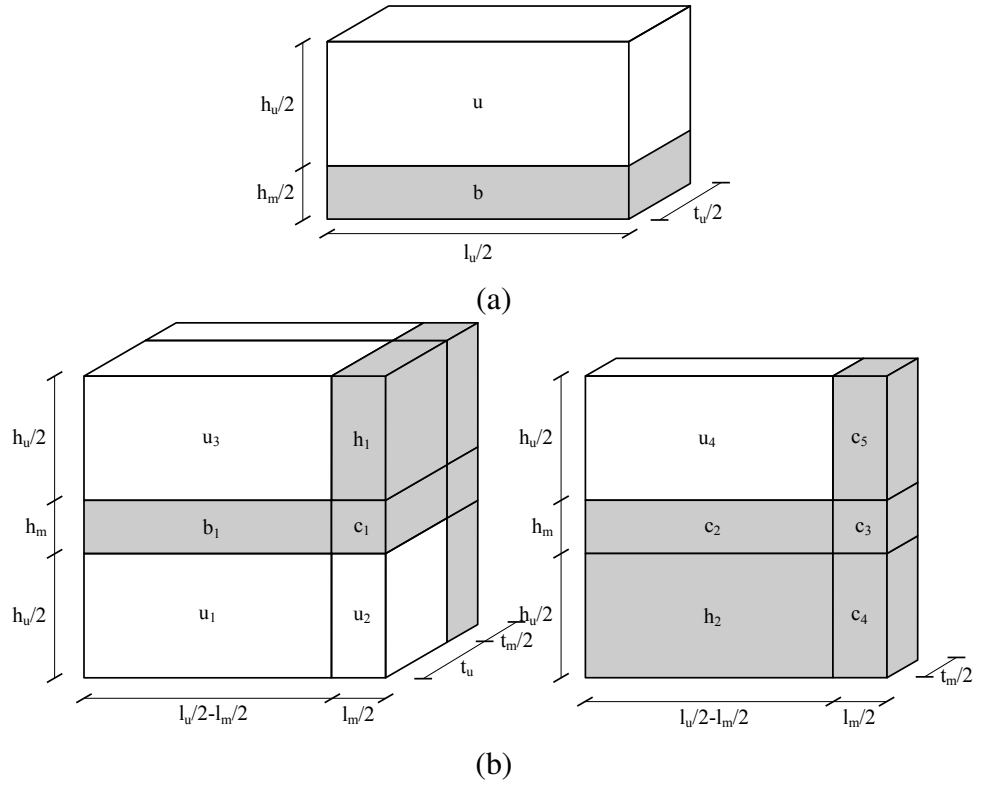

Figure 6.6 Discretization and component designation of pillar periodic unit cells: (a) stack bond pillar and (b) English bond pillar.

Vertical normal stress equilibrium conditions at the top and lower faces of the cell are as follows:

$$\begin{aligned} \sigma_{yy}\,(l_m/2\,+l_u/2\,) &= \sigma_{yy,h} l_m/2\,+\sigma_{yy,u} l_u/2 \\ \sigma_{yy}\,(l_m/2\,+l_u/2\,) &= \sigma_{yy,c} l_m/2\,+\sigma_{yy,b} l_u/2 \end{aligned} \tag{6.11}$$

Transversal normal stress equilibrium at the front face of the cell is as follows:

$$\begin{aligned} &\sigma_{zz}\,(l_m/2\,+l_u/2\,)\,(h_m/2\,+h_u/2\,) = \\ &\sigma_{zz,h} l_m/2\cdot h_u/2\,+\sigma_{zz,u} l_u/2\cdot h_u/2\,+\sigma_{zz,c} l_m/2\cdot h_m/2\,+\sigma_{zz,b} l_u/2\cdot h_m/2 \end{aligned} \tag{6.12}$$

The normal strains of the entire cell along the three axes can be calculated as

$$\begin{aligned} \varepsilon_{xx} &= \left(\varepsilon_{xx,h} l_m/2\,+\varepsilon_{xx,u} l_u/2\,\right)/(l_m/2\,+l_u/2\,) \\ \varepsilon_{yy} &= \left(\varepsilon_{yy,h} h_u/2\,+\varepsilon_{yy,c} h_m/2\,\right)/(h_u/2\,+h_m/2\,) \\ \varepsilon_{zz} &= \varepsilon_{zz,h} \end{aligned} \tag{6.13}$$

For *xy* shear it is assumed that

$$\begin{aligned} \varepsilon_{xy,h} &= \varepsilon_{xy,u} \\ \varepsilon_{xy,c} &= \varepsilon_{xy,b} \end{aligned} \tag{6.14}$$

The shear stress equilibrium conditions at the top and right faces of the cell are as follows:

$$\begin{aligned}\sigma_{xy}\,(l_m/2+l_u/2\ ) &= \sigma_{xy,h}l_m/2+\ \sigma_{xy,u}l_u/2\\ \sigma_{xy}\,(h_u/2+h_m/2\ ) &= \sigma_{xy,u}h_u/2+\ \sigma_{xy,b}h_m/2\end{aligned} \tag{6.15}$$

The cell shear strain can be calculated as

$$\varepsilon_{xy} = \left(\varepsilon_{xy,c}h_m/2\ +\varepsilon_{xy,h}h_u/2\ \right)/(h_m/2\ +h_u/2\ ) \tag{6.16}$$

For xz shear it is assumed that

$$\begin{aligned}\varepsilon_{xz,u} &= \varepsilon_{xz,b}\\ \sigma_{xz,c} &= \sigma_{xz,h} = \sigma_{xz}\end{aligned} \tag{6.17}$$

Shear stress equilibrium at the right face of the cell is as follows:

$$\sigma_{xz}\,(h_m/2\ +h_u/2\ ) = \sigma_{xz,b}h_m/2\ +\sigma_{xz,u}h_u/2 \tag{6.18}$$

The cell shear strain is equal to

$$\varepsilon_{xz} = \left(\varepsilon_{xz,u}l_u/2\ +\varepsilon_{xz,h}l_m/2\ \right)/(l_u/2\ +l_m/2\ ) \tag{6.19}$$

For yz strain it is assumed that

$$\begin{aligned}\varepsilon_{yz,h} &= \varepsilon_{yz,u}\\ \varepsilon_{yz,c} &= \varepsilon_{yz,b}\end{aligned} \tag{6.20}$$

Shear stress equilibrium at the front and top faces of the cell is as follows:

$$\begin{aligned}&\sigma_{yz}\,(l_m/2\ +l_u/2\ )(h_m/2\ +h_u/2\ ) =\\ &\sigma_{yz,h}l_m/2\cdot\ h_u/2\ +\sigma_{yz,u}l_u/2\cdot\ h_u/2\ +\sigma_{yz,c}l_m/2\cdot\ h_m/2\ +\sigma_{yz,b}l_u/2\cdot\ h_m/2\\ &\sigma_{yz}\,(l_m/2+l_u/2\ ) = \sigma_{yz,h}l_m/2+\sigma_{yz,u}l_u/2\end{aligned} \tag{6.21}$$

The cell shear strain is equal to:

$$\varepsilon_{yz} = \left(\varepsilon_{yz,u}h_u/2\ +\varepsilon_{yz,b}h_m/2\ \right)/(h_u/2\ +h_m/2\ ) \tag{6.22}$$

6.3.3 Running Bond Wall

The geometrical interlocking of the units and the mortar requires to take into account the in-plane shear stresses for normal stress loading conditions. Therefore, apart from the three components of normal stress for each cuboid component, the xy shear stress and strains have also been included for the formulation of the system of equations. In turn, the compatibility conditions take

into account the shear deformation of the cuboids for applied loads in the horizontal direction. The resulting shear stresses are negligible for loading in the vertical and transversal directions.

The horizontal normal stress equilibrium conditions at the left face and at a cross section across the middle of the cell are expressed as follows:

$$\begin{aligned} \sigma_{xx}\,(h_m+h_u) &= \sigma_{xx,u2}h_u/2 \;+\sigma_{xx,c}h_m+\sigma_{xx,h}h_u/2 \\ \sigma_{xx}\,(h_m+h_u) &= \sigma_{xx,u1}h_u/2 \;+\sigma_{xx,b}h_m+\sigma_{xx,u1}h_u/2 \end{aligned} \tag{6.23}$$

The vertical normal stress equilibrium conditions at the top face and at a cross section across the middle of the cell are as follows:

$$\begin{aligned} \sigma_{yy}\,(l_m/2\;+l_u/2\;) &= \sigma_{yy,h}l_m/2\;+\sigma_{yy,u1}\,(l_u/2-l_m/2\;)+\sigma_{yy,u2}l_m/2 \\ \sigma_{yy}\,(l_m/2\;+l_u/2\;) &= \sigma_{yy,c}l_m/2\;+\sigma_{yy,b}\,(l_u/2-l_m/2\;)+\sigma_{yy,c}l_m/2 \end{aligned} \tag{6.24}$$

The transversal normal stress equilibrium condition at the front face of the cell is as follows:

$$\begin{aligned} &\sigma_{zz}\,(h_m+h_u)\,(l_u/2\;+l_m/2\;) = \\ &h_u\left(\sigma_{zz,h}l_m/2\;+\sigma_{zz,u1}\,(l_u/2-l_m/2\;)+\sigma_{zz,u2}l_m/2\;\right)+ \\ &h_m\left(2\sigma_{zz,c}l_m/2+\sigma_{zz,b}\,(l_u/2-l_m/2\;)\;\right) \end{aligned} \tag{6.25}$$

The shear stress equilibrium conditions at the top face, at the left face and at a vertical cross section at the middle of the cell are as follows:

$$\begin{aligned} \sigma_{xy,h}l_m/2\;+\sigma_{xy,u1}\,(l_u/2\;-l_m/2\;)+\sigma_{xy,u2}l_m/2\;&=0 \\ \sigma_{xy,h}h_u/2\;+\sigma_{xy,c}h_m+\sigma_{xy,u2}h_u/2\;&=0 \\ \sigma_{xy,u1}h_u/2\;+\sigma_{xy,b1}h_m+\sigma_{xy,u1}h_u/2\;&=0 \end{aligned} \tag{6.26}$$

Deformation compatibility of the cuboids, considering both normal and shear deformation along the horizontal axis and only normal deformation along the vertical and transversal axis, is as follows:

$$\begin{aligned} &\varepsilon_{zz,h}=\varepsilon_{zz,u1}=\varepsilon_{zz,u2}=\varepsilon_{zz,c}=\varepsilon_{zz,b} \\ &\varepsilon_{yy,h}=\varepsilon_{yy,u1} \\ &\varepsilon_{yy,c}=\varepsilon_{yy,b} \\ &\varepsilon_{xx,h}=\varepsilon_{xx,c} \\ &\varepsilon_{xx,u1}=\varepsilon_{xx,b} \end{aligned} \tag{6.27}$$

$$\begin{aligned} &\left(\varepsilon_{xx,h}l_m/2\;+\varepsilon_{xx,u1}\,(l_u/2-l_m/2\;)+\varepsilon_{xx,u2}l_m/2+\left(\varepsilon_{xy,h}+\varepsilon_{xy,u1}+\varepsilon_{xy,u2}\right)h_u/4\;\right)= \\ &\left(2\varepsilon_{xx,c}l_m/2\;+\varepsilon_{xx,b}\,(l_u/2-l_m/2\;)+\left(2\varepsilon_{xy,c}+\varepsilon_{xy,b}\right)h_m/2\;\right) \end{aligned}$$

$$\varepsilon_{yy,h}h_u/2\;+\varepsilon_{yy,c}h_m+\varepsilon_{yy,u2}h_u/2\;=\varepsilon_{yy,u1}h_u/2\;+\varepsilon_{yy,b}h_m+\varepsilon_{yy,u1}h_u/2$$

The following assumptions are made about the normal and shear stress distribution in the cell:

$$\begin{aligned} \sigma_{xx,u1} &= \sigma_{xx,u2} \\ \sigma_{xy,u1} &= \sigma_{xy,h} \end{aligned} \tag{6.28}$$

The normal strains of the entire cell along the three axes are equal to

$$\begin{aligned} \varepsilon_{xx} &= \left(\varepsilon_{xx,h} l_m/2 + \varepsilon_{xx,u1}\left(l_u/2 - l_m/2\right) + \varepsilon_{xx,u2} l_m/2 + \left(\varepsilon_{xy,h} + \varepsilon_{xy,u1} + \varepsilon_{xy,u2}\right) h_u/4\right)/\left(l_m/2 + l_u/2\right) \\ \varepsilon_{yy} &= \left(\varepsilon_{yy,h} h_u/2 + \varepsilon_{yy,c} h_m + \varepsilon_{yy,u2} h_u/2\right)/\left(h_u + h_m\right) \\ \varepsilon_{zz} &= \varepsilon_{zz,h} \end{aligned} \tag{6.29}$$

For xy shear it is assumed that

$$\begin{aligned} \varepsilon_{xy,h} &= \varepsilon_{xy,u1} = \varepsilon_{xy,u2} \\ \varepsilon_{xy,c} &= \varepsilon_{xy,b} \end{aligned} \tag{6.30}$$

The shear stress equilibrium conditions at a horizontal cross section and a vertical cross section at the middle of the cell are as follows:

$$\begin{aligned} \sigma_{xy}\left(l_u/2 + l_m/2\right) &= \sigma_{xy,c} l_m/2 + \sigma_{xy,b}\left(l_u/2 - l_m/2\right) + \sigma_{xy,c} l_m/2 \\ \sigma_{xy}\left(h_u + h_m\right) &= \sigma_{xy,u1} h_u/2 + \sigma_{xy,b} h_m + \sigma_{xy,u1} h_u/2 \end{aligned} \tag{6.31}$$

The cell shear strain is equal to

$$\varepsilon_{xy} = \left(\varepsilon_{xy,h} h_u/2 + \varepsilon_{xy,c} h_m + \varepsilon_{xy,u2} h_u/2\right)/\left(h_u + h_m\right) \tag{6.32}$$

For xz shear it is assumed that

$$\begin{aligned} \varepsilon_{xz,u1} &= \varepsilon_{xz,u2} \\ \varepsilon_{xz,u1} &= \varepsilon_{xz,b} \\ \sigma_{xz,c} &= \sigma_{xz,u2} \end{aligned} \tag{6.33}$$

The stress equilibrium conditions at the front and left face and at a cross section at the center of the cell are as follows:

$$\begin{aligned} &\sigma_{xz}\left(h_m + h_u\right)\left(l_u/2 + l_m/2\right) = \\ &h_u\left(\sigma_{xz,h} l_m/2 + \sigma_{xz,u1}\left(l_u/2 - l_m/2\right) + \sigma_{xz,u2} l_m/2\right) + h_m\left(2\sigma_{xz,c} l_m/2 + \sigma_{xz,b}\left(l_u/2 - l_m/2\right)\right) \end{aligned}$$

$$\begin{aligned} \sigma_{xz}\left(h_m + h_u\right) &= \sigma_{xz,h} h_u/2 + \sigma_{xz,c} h_m + \sigma_{xz,u2} h_u/2 \\ \sigma_{xz}\left(h_m + h_u\right) &= \sigma_{xz,u1} h_u/2 + \sigma_{xz,b} h_m + \sigma_{xz,u1} h_u/2 \end{aligned} \tag{6.34}$$

The cell shear strain is equal to

$$\varepsilon_{xz} = \left(\varepsilon_{xy,h} l_m/2 + \varepsilon_{xy,u1}\left(l_u/2 - l_m/2\right) + \varepsilon_{xy,u2} l_m/2\right)/\left(l_u/2 + l_m/2\right) \tag{6.35}$$

For yz shear it is assumed that

$$\begin{aligned} \varepsilon_{yz,h} &= \varepsilon_{yz,u1} = \varepsilon_{yz,u2} \\ \varepsilon_{yz,c} &= \varepsilon_{yz,b} \end{aligned} \tag{6.36}$$

Shear stress equilibriums at the top and front faces of the cell are as follows:

$$\sigma_{yz}\left(l_u/2 + l_m/2\right) = \sigma_{yz,h} l_m/2 + \sigma_{yz,u1}\left(l_u/2 - l_m/2\right) + \sigma_{yz,u2} l_m/2$$

$$\begin{aligned} &\sigma_{yz}\left(h_m + h_u\right)\left(l_u/2 + l_m/2\right) = \\ &h_u\left(\sigma_{yz,h} l_m/2 + \sigma_{yz,u1}\left(l_u/2 - l_m/2\right) + \sigma_{yz,u2} l_m/2\right) + h_m\left(2\sigma_{yz,c} l_m/2 + \sigma_{yz,b}\left(l_u/2 - l_m/2\right)\right) \end{aligned} \tag{6.37}$$

The cell shear strain is equal to

$$\varepsilon_{yz} = \left(\varepsilon_{yz,h} h_u/2 + \varepsilon_{yz,c} h_m + \varepsilon_{yz,u2} h_u/2\right)/\left(h_u + h_m\right) \tag{6.38}$$

6.3.4 Flemish Bond Wall

As in the running bond cell model, the in-plane shear deformation of the cuboids is taken into account for normal stress loading in the horizontal direction. The transfer of stress across the transversal joint is also taken into account without, however, considering the effects of shear stress in other planes. Additionally, as in the case of the running bond cell, arising shear stresses are negligible for vertical and transversal applied normal stress.

The horizontal normal stress equilibrium conditions at the left face and at two cross sections along the length of the cell are as follows:

$$\begin{aligned} &\sigma_{xx}\left(h_u + h_m\right)\left(t_u + t_m/2\right) = \\ &\left(\sigma_{xx,d1} h_u/2 + \sigma_{xx,b1} h_m + \sigma_{xx,s3} h_u/2\right) t_u + \left(\sigma_{xx,d2} h_u/2 + \sigma_{xx,c2} h_m + \sigma_{xx,t3} h_u/2\right) t_m/2 \end{aligned}$$

$$\begin{aligned} &\sigma_{xx}\left(h_u + h_m\right)\left(t_u + t_m/2\right) = \\ &\left(\sigma_{xx,h1} h_u/2 + \sigma_{xx,c1} h_m + \sigma_{xx,s2} h_u/2\right) t_u + \left(\sigma_{xx,h2} h_u/2 + \sigma_{xx,c3} h_m + \sigma_{xx,t2} h_u/2\right) t_m/2 \end{aligned} \tag{6.39}$$

$$\begin{aligned} &\sigma_{xx}\left(h_u + h_m\right)\left(t_u + t_m/2\right) = \\ &\left(\sigma_{xx,s1} h_u/2 + \sigma_{xx,b2} h_m + \sigma_{xx,s1} h_u/2\right) t_u + \left(\sigma_{xx,t1} h_u/2 + \sigma_{xx,c4} h_m + \sigma_{xx,t1} h_u/2\right) t_m/2 \end{aligned}$$

The vertical normal stress equilibrium conditions at the top face and at a cross section across the middle of the cell are as follows:

$$\begin{aligned}
&\sigma_{yy}\,(t_u+t_m/2\,)\,(t_u/2\,+l_m+l_u/2\,)=\\
&\big(\sigma_{yy,d1}t_u/2\,+\sigma_{yy,h1}l_m+\sigma_{yy,s1}\,(l_u/2\,-l_m-t_u/2\,)+\sigma_{yy,s2}l_m+\sigma_{yy,s3}t_u/2\,\big)\,t_u+\\
&\big(\sigma_{yy,d2}t_u/2\,+\sigma_{yy,h2}l_m+\sigma_{yy,t1}\,(l_u/2\,-l_m-t_u/2\,)+\sigma_{yy,t2}l_m+\sigma_{yy,t3}t_u/2\,\big)\,t_m/2\\
&\sigma_{yy}\,(t_u+t_m/2\,)\,(t_u/2\,+l_m+l_u/2\,)=\\
&\big(\sigma_{yy,b1}t_u/2\,+\sigma_{yy,c1}l_m+\sigma_{yy,b2}\,(l_u/2\,-l_m-t_u/2\,)+\sigma_{yy,c1}l_m+\sigma_{yy,b1}t_u/2\,\big)\,t_u+\\
&\big(\sigma_{yy,c2}t_u/2\,+\sigma_{yy,c3}l_m+\sigma_{yy,c4}\,(l_u/2\,-l_m-t_u/2\,)+\sigma_{yy,c3}l_m+\sigma_{yy,c2}t_u/2\,\big)\,t_m/2
\end{aligned}\tag{6.40}$$

The transversal normal stress equilibrium conditions at the front face and at a cross section across the middle of the cell are as follows:

$$\begin{aligned}
&\sigma_{zz}\,(h_u+h_m)\,(t_u/2\,+l_m+l_u/2\,)=\\
&\big(\sigma_{zz,d1}t_u/2\,+\sigma_{zz,h1}l_m+\sigma_{zz,s1}\,(l_u/2\,-l_m-t_u/2\,)+\sigma_{zz,s2}l_m+\sigma_{zz,s3}t_u/2\,\big)\,h_u+\\
&\big(\sigma_{zz,b1}t_u+2\sigma_{zz,c1}l_m+\sigma_{zz,b2}\,(l_u/2\,-l_m-t_u/2\,)\big)\,h_m\\
&\sigma_{zz}\,(h_u+h_m)\,(t_u/2\,+l_m+l_u/2\,)=\\
&\big(\sigma_{zz,d2}t_u/2\,+\sigma_{zz,h2}l_m+\sigma_{zz,t1}\,(l_u/2\,-l_m-t_u/2\,)+\sigma_{zz,t2}l_m+\sigma_{zz,t3}t_u/2\,\big)\,h_u+\\
&(\sigma_{zz,c2}t_u+2\sigma_{zz,c3}l_m+\sigma_{zz,c4}\,(l_u/2\,-l_m-t_u/2\,))\,h_m
\end{aligned}\tag{6.41}$$

The shear stress equilibrium conditions at the top face, at a horizontal cross section along the middle of the cell, at the left face and at a vertical cross section along the middle of the cell are as follows:

$$\begin{aligned}
&\big(\sigma_{xy,d1}t_u/2\,+\sigma_{xy,h1}l_m+\sigma_{xy,s1}\,(l_u/2\,-l_m-t_u/2\,)+\sigma_{xy,s2}l_m+\sigma_{xy,s3}t_u/2\,\big)\,t_u+\\
&\big(\sigma_{xy,d2}t_u/2\,+\sigma_{xy,h2}l_m+\sigma_{xy,t1}\,(l_u/2\,-l_m-t_u/2\,)+\sigma_{xy,t2}l_m+\sigma_{xy,t3}t_u/2\,\big)\,t_m/2\,=0\\
&\big(\sigma_{xy,b1}t_u/2\,+\sigma_{xy,c1}l_m+\sigma_{xy,b2}\,(l_u/2\,-l_m-t_u/2\,)+\sigma_{xy,c1}l_m+\sigma_{xy,b1}t_u/2\,\big)\,t_u+\\
&\big(\sigma_{xy,c2}t_u/2\,+\sigma_{xy,c3}l_m+\sigma_{xy,c4}\,(l_u/2\,-l_m-t_u/2\,)+\sigma_{xy,c3}l_m+\sigma_{xy,c2}t_u/2\,\big)\,t_m/2\,=0\\
&\big(\sigma_{xy,d1}h_u/2+\sigma_{xy,b1}h_m+\sigma_{xy,s3}h_u/2\big)\,t_u+\big(\sigma_{xy,d2}h_u/2+\sigma_{xy,c2}h_m+\sigma_{xy,t3}h_u/2\big)\,t_m/2\,=0\\
&\big(\sigma_{xx,h1}h_u/2+\sigma_{xx,c1}h_m+\sigma_{xx,s2}h_u/2\big)\,t_u+\big(\sigma_{xx,h2}h_u/2+\sigma_{xx,c3}h_m+\sigma_{xx,t2}h_u/2\big)\,t_m/2\,=0
\end{aligned}\tag{6.42}$$

Deformation compatibility of the cuboids, considering both normal and shear deformation along the horizontal axis and only normal deformation along the vertical and transversal axes, is as follows:

$$
\begin{aligned}
&\varepsilon_{xx,d1}t_u/2 + \varepsilon_{xx,h1}l_m + \varepsilon_{xx,s1}\left(l_u/2 - l_m - t_u/2\right) + \varepsilon_{xx,s2}l_m + \varepsilon_{xx,s3}t_u/2 + \\
&\left(\varepsilon_{xy,d1} + \varepsilon_{xy,h1} + \varepsilon_{xy,s1} + \varepsilon_{xy,s2} + \varepsilon_{xy,s3}\right)h_u/4 = \\
&\varepsilon_{xx,d2}t_u/2 + \varepsilon_{xx,h2}l_m + \varepsilon_{xx,t1}\left(l_u/2 - l_m - t_u/2\right) + \varepsilon_{xx,t2}l_m + \varepsilon_{xx,t3}t_u/2 + \\
&\left(\varepsilon_{xy,d2} + \varepsilon_{xy,h2} + \varepsilon_{xy,t1} + \varepsilon_{xy,t2} + \varepsilon_{xy,t3}\right)h_u/4
\end{aligned}
$$

$$
\begin{aligned}
&\varepsilon_{xx,d1}t_u/2 + \varepsilon_{xx,h1}l_m + \varepsilon_{xx,s1}\left(l_u/2 - l_m - t_u/2\right) + \varepsilon_{xx,s2}l_m + \varepsilon_{xx,s3}t_u/2 + \\
&\left(\varepsilon_{xy,d1} + \varepsilon_{xy,h1} + \varepsilon_{xy,s1} + \varepsilon_{xy,s2} + \varepsilon_{xy,s3}\right)h_u/4 = \\
&\varepsilon_{xx,b1}t_u/2 + \varepsilon_{xx,c1}l_m + \varepsilon_{xx,b2}\left(l_u/2 - l_m - t_u/2\right) + \varepsilon_{xx,c1}l_m + \varepsilon_{xx,b1}t_u/2 + \\
&\left(\varepsilon_{xy,b1} + \varepsilon_{xy,c1} + \varepsilon_{xy,b2} + \varepsilon_{xy,c1} + \varepsilon_{xy,b1}\right)h_m/2
\end{aligned}
$$

$$
\begin{aligned}
&\varepsilon_{xx,d1}t_u/2 + \varepsilon_{xx,h1}l_m + \varepsilon_{xx,s1}\left(l_u/2 - l_m - t_u/2\right) + \varepsilon_{xx,s2}l_m + \varepsilon_{xx,s3}t_u/2 + \\
&\left(\varepsilon_{xy,d1} + \varepsilon_{xy,h1} + \varepsilon_{xy,s1} + \varepsilon_{xy,s2} + \varepsilon_{xy,s3}\right)h_u/4 = \\
&\varepsilon_{xx,c2}t_u/2 + \varepsilon_{xx,c3}l_m + \varepsilon_{xx,c4}\left(l_u/2 - l_m - t_u/2\right) + \varepsilon_{xx,c3}l_m + \varepsilon_{xx,c2}t_u/2 + \\
&\left(\varepsilon_{xy,c2} + \varepsilon_{xy,c3} + \varepsilon_{xy,c4} + \varepsilon_{xy,c3} + \varepsilon_{xy,c2}\right)h_m/2
\end{aligned}
$$

$$
\begin{aligned}
&\varepsilon_{zz,d1}t_u + \varepsilon_{zz,d2}t_m/2 = \varepsilon_{zz,b1}t_u + \varepsilon_{zz,c2}t_m/2 \\
&\varepsilon_{zz,d1}t_u + \varepsilon_{zz,d2}t_m/2 = \varepsilon_{zz,s3}t_u + \varepsilon_{zz,t3}t_m/2 \\
&\varepsilon_{zz,d1}t_u + \varepsilon_{zz,d2}t_m/2 = \varepsilon_{zz,h1}t_u + \varepsilon_{zz,h2}t_m/2 \\
&\varepsilon_{zz,d1}t_u + \varepsilon_{zz,d2}t_m/2 = \varepsilon_{zz,c1}t_u + \varepsilon_{zz,c3}t_m/2 \\
&\varepsilon_{zz,d1}t_u + \varepsilon_{zz,d2}t_m/2 = \varepsilon_{zz,s2}t_u + \varepsilon_{zz,t2}t_m/2 \\
&\varepsilon_{zz,d1}t_u + \varepsilon_{zz,d2}t_m/2 = \varepsilon_{zz,s1}t_u + \varepsilon_{zz,t1}t_m/2 \\
&\varepsilon_{zz,d1}t_u + \varepsilon_{zz,d2}t_m/2 = \varepsilon_{zz,b2}t_u + \varepsilon_{zz,c4}t_m/2 \\
&\varepsilon_{xx,b1} = \varepsilon_{xx,c2} = \varepsilon_{xx,d1} \\
&\varepsilon_{xx,s3} = \varepsilon_{xx,t3} \\
&\varepsilon_{xx,c1} = \varepsilon_{xx,c3} = \varepsilon_{xx,h1} = \varepsilon_{xx,h2} \\
&\varepsilon_{xx,s2} = \varepsilon_{xx,t2} \\
&\varepsilon_{xx,s1} = \varepsilon_{xx,t1} = \varepsilon_{xx,b2} \\
&\varepsilon_{xx,b2} = \varepsilon_{xx,c4} \\
&\varepsilon_{yy,d1} = \varepsilon_{yy,h1} = \varepsilon_{yy,s1} = \varepsilon_{yy,s2} = \varepsilon_{yy,s3} = \varepsilon_{yy,d2} = \varepsilon_{yy,h2} = \varepsilon_{yy,t1} = \varepsilon_{yy,t2} = \varepsilon_{yy,t3} \\
&\varepsilon_{yy,b1} = \varepsilon_{yy,c1} = \varepsilon_{yy,b2} = \varepsilon_{yy,c2} = \varepsilon_{yy,c3} = \varepsilon_{yy,c4} \\
&\varepsilon_{zz,s1} = \varepsilon_{zz,s2} = \varepsilon_{zz,s3} \\
&\varepsilon_{zz,d1} = \varepsilon_{zz,h1} \\
&\varepsilon_{xy,d1} = \varepsilon_{xy,d2} \\
&\varepsilon_{xy,h1} = \varepsilon_{xy,h2} \\
&\varepsilon_{xy,s1} = \varepsilon_{xy,t1} \\
&\varepsilon_{xy,s2} = \varepsilon_{xy,t2} \\
&\varepsilon_{xy,s3} = \varepsilon_{xy,t3} \\
&\varepsilon_{xy,b1} = \varepsilon_{xy,c2} \\
&\varepsilon_{xy,c1} = \varepsilon_{xy,c3}
\end{aligned}
\tag{6.43}
$$

The following assumptions are made about the normal stress distribution in the cell:

$$\begin{aligned}
\sigma_{zz,c1} &= \sigma_{zz,c3} \\
\sigma_{zz,b2} &= \sigma_{zz,c4} \\
\sigma_{zz,d1} &= \sigma_{zz,d2} \\
\sigma_{zz,s1} &= \sigma_{zz,t1} \\
\sigma_{zz,s2} &= \sigma_{zz,t2} \\
\sigma_{zz,s3} &= \sigma_{zz,t3}
\end{aligned} \tag{6.44}$$

This set of equations assumes that the transversal normal stress is equal for the cuboids of the two leaves of masonry, be they unit or mortar. They also, again, lead to equal effective stresses in the different cuboids comprising a single brick. Damaged stresses in nonlinear analysis, however, are different.

The assumptions concerning the shear stresses in the cuboids read:

$$\begin{aligned}
\sigma_{xy,s1} &= \sigma_{xy,s3} = \sigma_{xy,h1} \\
\sigma_{xy,b1} &= \sigma_{xy,b2}
\end{aligned} \tag{6.45}$$

The normal strains of the entire cell along the three axes are equal to:

$$\begin{aligned}
&\varepsilon_{xx} = \\
&\frac{\varepsilon_{xx,d1}t_u/2 + \varepsilon_{xx,h1}l_m + \varepsilon_{xx,s1}(l_u/2 - l_m - t_u/2) + \varepsilon_{xx,s2}l_m + \varepsilon_{xx,s3}t_u/2 + \left(\varepsilon_{xy,d1} + \varepsilon_{xy,h1} + \varepsilon_{xy,s1} + \varepsilon_{xy,s2} + \varepsilon_{xy,s3}\right)h_u/4}{(l_u/2 + l_m + t_u/2)} \\
&\varepsilon_{yy} = \left(\varepsilon_{yy,d1}h_u/2 + \varepsilon_{yy,b1}h_m + \varepsilon_{yy,s3}h_u/2\right)/(h_u + h_m) \\
&\varepsilon_{zz} = \left(\varepsilon_{zz,d1}t_u + \varepsilon_{zz,d2}t_m/2\right)/(t_u + t_m/2)
\end{aligned} \tag{6.46}$$

For xy shear it is assumed that:

$$\begin{aligned}
&\varepsilon_{xy,d1} = \varepsilon_{xy,h1} = \varepsilon_{xy,s1} = \varepsilon_{xy,s2} = \varepsilon_{xy,s3} = \varepsilon_{xy,d2} = \varepsilon_{xy,h2} = \varepsilon_{xy,t1} = \varepsilon_{xy,t2} = \varepsilon_{xy,t3} \\
&\varepsilon_{xy,b1} = \varepsilon_{xy,c1} = \varepsilon_{xy,b2} = \varepsilon_{xy,c2} = \varepsilon_{xy,c3} = \varepsilon_{xy,c4}
\end{aligned} \tag{6.47}$$

The shear stress equilibrium condition at the left face and at a cross-section along the mid height of the cell are as follows:

$$\begin{aligned}
&\sigma_{xy}(t_u + t_m/2)(h_u + h_m) = \\
&\left(\sigma_{xy,d1}h_u/2 + \sigma_{xy,b1}h_m + \sigma_{xy,s3}h_u/2\right)t_u + \left(\sigma_{xy,d2}h_u/2 + \sigma_{xy,c2}h_m + \sigma_{xy,t3}h_u/2\right)t_m/2 \\
&\sigma_{xy}(t_u + t_m/2)(l_u/2 + l_m + t_u/2) = \\
&\left(\sigma_{xy,b1}t_u/2 + \sigma_{xy,c1}l_m + \sigma_{xy,b2}(l_u/2 - l_m - t_u/2) + \sigma_{xy,c1}l_m + \sigma_{xy,b1}t_u/2\right)t_u + \\
&\left(\sigma_{xy,c2}t_u/2 + \sigma_{xy,c3}l_m + \sigma_{xy,c4}(l_u/2 - l_m - t_u/2) + \sigma_{xy,c3}l_m + \sigma_{xy,c2}t_u/2\right)t_m/2
\end{aligned} \tag{6.48}$$

The cell shear strain is equal to

$$\varepsilon_{xy} = \left(\varepsilon_{xy,d1} h_u/2 + \varepsilon_{xy,b1} h_m + \varepsilon_{xy,s3} h_u/2\right)/(h_u + h_m) \tag{6.49}$$

For xz shear it is assumed that

$$\begin{aligned} &\varepsilon_{xz,d1} = \varepsilon_{xz,s1} = \varepsilon_{xz,s2} = \varepsilon_{xz,s3} = \varepsilon_{xz,b1} = \varepsilon_{xz,c1} = \varepsilon_{xz,b2} \\ &\varepsilon_{xz,h2} = \varepsilon_{xz,t1} = \varepsilon_{xz,t2} = \varepsilon_{xz,t3} = \varepsilon_{xz,c2} = \varepsilon_{xz,c3} = \varepsilon_{xz,c4} \end{aligned} \tag{6.50}$$

The shear stress equilibrium conditions at the front face, transversal section at the middle, the left face and a vertical section along the middle of the cell are as follows:

$$\begin{aligned} &\sigma_{xz}\left(l_u/2 + l_m + t_u/2\right)\left(h_u/2 + h_m/2\right) = \\ &\left(\sigma_{xz,d1} t_u/2 + \sigma_{xz,h1} l_m + \sigma_{xz,s1}\left(l_u/2 - l_m - t_u/2\right) + \sigma_{xz,s2} l_m + \sigma_{xz,s3} t_u/2\right) h_u/2 + \\ &\left(\sigma_{xz,b1} t_u/2 + \sigma_{xz,c1} l_m + \sigma_{xz,b2}\left(l_u/2 - l_m - t_u/2\right) + \sigma_{xz,c1} l_m + \sigma_{xz,b1} t_u/2\right) h_m/2 \end{aligned}$$

$$\begin{aligned} &\sigma_{xz}\left(l_u/2 + l_m + t_u/2\right)\left(h_u/2 + h_m/2\right) = \\ &\left(\sigma_{xz,d2} t_u/2 + \sigma_{xz,h2} l_m + \sigma_{xz,t1}\left(l_u/2 - l_m - t_u/2\right) + \sigma_{xz,t2} l_m + \sigma_{xz,t3} t_u/2\right) h_u/2 + \\ &\left(\sigma_{xz,c2} t_u/2 + \sigma_{xz,c3} l_m + \sigma_{xz,c4}\left(l_u/2 - l_m - t_u/2\right) + \sigma_{xz,c3} l_m + \sigma_{xz,c2} t_u/2\right) h_m/2 \end{aligned}$$

$$\begin{aligned} &\sigma_{xz}\left(t_u + t_m/2\right)\left(h_u + h_m\right) = \\ &\left(\sigma_{xz,d1} h_u/2 + \sigma_{xz,b1} h_m + \sigma_{xz,s3} h_u/2\right) t_u + \left(\sigma_{xz,d2} h_u/2 + \sigma_{xz,c2} h_m + \sigma_{xz,t3} h_u/2\right) t_m/2 \end{aligned}$$

$$\begin{aligned} &\sigma_{xz}\left(t_u + t_m/2\right)\left(h_u + h_m\right) = \\ &\left(\sigma_{xz,s1} h_u/2 + \sigma_{xz,b2} h_m + \sigma_{xz,s1} h_u/2\right) t_u + \left(\sigma_{xz,t1} h_u/2 + \sigma_{xz,c4} h_m + \sigma_{xz,t1} h_u/2\right) t_m/2 \end{aligned} \tag{6.51}$$

The cell shear strain is equal to:

$$\varepsilon_{xz} = \frac{\left(\varepsilon_{xz,d1} t_u/2 + \varepsilon_{xz,h1} l_m + \varepsilon_{xz,s1}\left(l_u/2 - l_m - t_u/2\right) + \varepsilon_{xz,s2} l_m + \varepsilon_{xz,s3} t_u/2\right)}{\left(l_u/2 + l_m + t_u/2\right)} \tag{6.52}$$

For yz shear it is assumed that:

$$\begin{aligned} &\varepsilon_{yz,d1} = \varepsilon_{yz,h1} = \varepsilon_{yz,s1} = \varepsilon_{yz,s2} = \varepsilon_{yz,s3} = \varepsilon_{yz,d2} = \varepsilon_{yz,h2} = \varepsilon_{yz,t1} = \varepsilon_{yz,t2} = \varepsilon_{yz,t3} \\ &\varepsilon_{yz,b1} = \varepsilon_{yz,c1} = \varepsilon_{yz,b2} = \varepsilon_{yz,c2} = \varepsilon_{yz,c3} = \varepsilon_{yz,c4} \end{aligned} \tag{6.53}$$

The shear stress equilibrium conditions at the front and top faces of the cell are as follows:

$$\begin{aligned}
&\sigma_{yz}\,(l_u/2\,+l_m+t_u/2\,)\,(h_u+h_m)=\\
&\big(\sigma_{yz,d1}t_u/2\,+\sigma_{yz,h1}l_m+\sigma_{yz,s1}\,(l_u/2\,-l_m-t_u/2\,)+\sigma_{yz,s2}l_m+\sigma_{yz,s3}t_u/2\,\big)\,h_u/2+\\
&\big(\sigma_{yz,b1}t_u/2\,+\sigma_{yz,c1}l_m+\sigma_{yz,s3}\,(l_u/2\,-l_m-t_u/2\,)+\sigma_{yz,c1}l_m+\sigma_{yz,b1}t_u/2\,\big)\,h_m+\\
&\big(\sigma_{yz,b1}t_u/2\,+\sigma_{yz,c1}l_m+\sigma_{yz,s3}\,(l_u/2\,-l_m-t_u/2\,)+\sigma_{yz,c1}l_m+\sigma_{yz,b1}t_u/2\,\big)\,h_u/2\\
&\sigma_{yz}\,(t_u+t_m/2\,)\,(l_u/2\,+l_m+t_u/2\,)=\\
&\big(\sigma_{yz,d1}t_u/2\,+\sigma_{yz,h1}l_m+\sigma_{yz,s1}\,(l_u/2\,-l_m-t_u/2\,)+\sigma_{yz,s2}l_m+\sigma_{yz,s3}t_u/2\,\big)\,t_u+\\
&\big(\sigma_{yz,d2}t_u/2\,+\sigma_{yz,h2}l_m+\sigma_{yz,t1}\,(l_u/2\,-l_m-t_u/2\,)+\sigma_{yz,t2}l_m+\sigma_{yz,t3}t_u/2\,\big)\,t_m/2
\end{aligned}\tag{6.54}$$

The cell shear strain is equal to

$$\varepsilon_{yz}=\big(\varepsilon_{yz,s3}h_u/2\,+\varepsilon_{yz,b1}h_m+\varepsilon_{yz,d1}h_u/2\,\big)/(h_u+h_m)\tag{6.55}$$

6.3.5 Three-Leaf Wall

The three-leaf-model retains the set of assumptions made for the running bond model, which still apply to the outer masonry leaf. A number of further assumptions are made for the infill and the stress equilibrium conditions are modified to accommodate the new geometrical entities.

The horizontal normal stress equilibrium conditions at the left face and at a cross section across the middle of the cell are as follows:

$$\begin{aligned}
&\sigma_{xx}\,(h_m+h_u)\,(t_u+t_i/2\,)=\\
&\big(\sigma_{xx,u2}h_u/2\,+\sigma_{xx,c}h_m+\sigma_{xx,h}h_u/2\,\big)\,t_u+(\sigma_{xx,i3}h_u/2\,+\sigma_{xx,i4}h_m+\sigma_{xx,i1}h_u/2\,)\,t_i/2\\
&\sigma_{xx}\,(h_m+h_u)\,(t_u+t_i/2\,)=\\
&\big(\sigma_{xx,u1}h_u/2\,+\sigma_{xx,b}h_m+\sigma_{xx,u1}h_u/2\,\big)\,t_u+\big(\sigma_{xx,i2}h_u/2\,+\sigma_{xx,i5}h_m+\sigma_{xx,i2}h_u/2\,\big)\,t_i/2
\end{aligned}\tag{6.56}$$

The vertical normal stress equilibrium conditions at the top face and at a cross section across the middle of the cell are as follows:

$$\begin{aligned}
&\sigma_{yy}\,(l_m/2\,+l_u/2\,)\,(t_u+t_i/2\,)=\\
&\big(\sigma_{yy,h}l_m/2\,+\sigma_{yy,u1}\,(l_u/2-l_m/2\,)+\sigma_{yy,u2}l_m/2\,\big)\,t_u+\\
&\big(\sigma_{yy,i1}l_m/2\,+\sigma_{yy,i2}\,(l_u/2-l_m/2\,)+\sigma_{yy,i3}l_m/2\,\big)\,t_i/2\\
&\sigma_{yy}\,(l_m/2\,+l_u/2\,)\,(t_u+t_i/2\,)=\\
&\big(\sigma_{yy,c}l_m/2\,+\sigma_{yy,b}\,(l_u/2-l_m/2\,)+\sigma_{yy,c}l_m/2\,\big)\,t_u+\\
&\big(\sigma_{yy,i4}l_m/2\,+\sigma_{yy,i5}\,(l_u/2-l_m/2\,)+\sigma_{yy,i4}l_m/2\,\big)\,t_i/2
\end{aligned}\tag{6.57}$$

The transversal normal stress equilibrium conditions at the back face of the cell are as follows:

$$\begin{aligned}&\sigma_{zz}\,(h_m+h_u)\,(l_u/2\,+l_m/2\,)=\\&h_u\,(\sigma_{zz,i1}l_m/2\,+\sigma_{zz,i2}\,(l_u/2-l_m/2\,)+\sigma_{zz,i3}l_m/2\,)+h_m\left(2\sigma_{zz,i4}l_m/2+\sigma_{zz,i5}\,(l_u/2-l_m/2\,)\right)\end{aligned} \tag{6.58}$$

Shear stress equilibriums are taken at the left face, a vertical cross section at the middle of the cell and at the top face. These equilibriums lead to the following equations:

$$\begin{aligned}&\left(\sigma_{xy,u2}h_u/2\,+\sigma_{xy,c}h_m+\sigma_{xy,h}h_u/2\,\right)t_u+\left(\sigma_{xy,i3}h_u/2\,+\sigma_{xy,i4}h_m+\sigma_{xy,i1}h_u/2\,\right)t_i/2\,=0\\&\left(\sigma_{xy,u1}h_u/2\,+\sigma_{xy,b}h_m+\sigma_{xy,u1}h_u/2\,\right)t_u+\left(\sigma_{xy,i2}h_u/2\,+\sigma_{xy,i5}h_m+\sigma_{xy,i2}h_u/2\,\right)t_i/2\,=0\\&\left(\sigma_{xy,c}l_m/2\,+\sigma_{xy,b}\,(l_u/2-l_m/2\,)+\sigma_{xy,c}l_m/2\,\right)t_u+\\&\left(\sigma_{xy,i4}l_m/2\,+\sigma_{xy,i5}\,(l_u/2-l_m/2\,)+\sigma_{xy,i4}l_m/2\,\right)t_i/2\,=0\end{aligned} \tag{6.59}$$

Constant normal stress is assumed in the infill, so that

$$\begin{aligned}\sigma_{xx,i1}&=\sigma_{xx,i2}=\sigma_{xx,i3}=\sigma_{xx,i4}=\sigma_{xx,i5}\\\sigma_{yy,i1}&=\sigma_{yy,i2}=\sigma_{yy,i3}=\sigma_{yy,i4}=\sigma_{yy,i5}\\\sigma_{zz,i1}&=\sigma_{zz,i2}=\sigma_{zz,i3}=\sigma_{zz,i4}=\sigma_{zz,i5}\end{aligned} \tag{6.60}$$

The following assumptions are made concerning the shear strains in the infill cuboids

$$\begin{aligned}\varepsilon_{xy,i1}&=\varepsilon_{xy,i2}=\varepsilon_{xy,i3}=\varepsilon_{xy,u1}\\\varepsilon_{xy,i4}&=\varepsilon_{xy,i5}\end{aligned} \tag{6.61}$$

Three additional equations imposing total deformation compatibility are introduced: two in the horizontal direction and one in the vertical. They read as follows:

$$\begin{aligned}&\left(\varepsilon_{xx,h}l_m/2\,+\varepsilon_{xx,u1}\,(l_u/2-l_m/2\,)+\varepsilon_{xx,u2}l_m/2+\left(\varepsilon_{xy,h}+\varepsilon_{xy,u1}+\varepsilon_{xy,u2}\right)h_u/4\,\right)=\\&\left(\varepsilon_{xx,i1}l_m/2\,+\varepsilon_{xx,i2}\,(l_u/2-l_m/2\,)+\varepsilon_{xx,i3}l_m/2\,+\left(\varepsilon_{xy,i1}+\varepsilon_{xy,i2}+\varepsilon_{xy,i3}\right)h_m/2\,\right)\\&\left(\varepsilon_{xx,h}l_m/2\,+\varepsilon_{xx,u1}\,(l_u/2-l_m/2\,)+\varepsilon_{xx,u2}l_m/2+\left(\varepsilon_{xy,h}+\varepsilon_{xy,u1}+\varepsilon_{xy,u2}\right)h_u/4\,\right)=\\&\left(2\varepsilon_{xx,i4}l_m/2\,+\varepsilon_{xx,i5}\,(l_u/2-l_m/2\,)+\left(2\varepsilon_{xy,i4}+\varepsilon_{xy,5}\right)h_m/2\,\right)\\&\varepsilon_{yy,h}h_u/2\,+\varepsilon_{yy,c}h_m+\varepsilon_{yy,u2}h_u/2\,=\varepsilon_{yy,i1}h_u/2\,+\varepsilon_{yy,i4}h_m+\varepsilon_{yy,i3}h_u/2\end{aligned} \tag{6.62}$$

The total cell strain in the horizontal and vertical direction remains the same as in the running bond case, since the total strain is equal in the two leaves. The strain in the transversal direction is now defined as:

$$\varepsilon_{zz}=\left(\varepsilon_{zz,h}t_u+\varepsilon_{zz,i2}t_i/2\,\right)/(t_u+t_i/2\,) \tag{6.63}$$

For *xy* shear the same assumptions as for the running bond cell apply, although several additional assumptions are needed. Based on these assumptions the equilibrium equations are again adjusted.

Constant shear strain is assumed in the infill, so that

$$\sigma_{xy,i1} = \sigma_{xy,i2} = \sigma_{xy,i3} = \sigma_{xy,i4} = \sigma_{xy,i5} \tag{6.64}$$

The shear stress equilibrium conditions at the top face and at a horizontal cross-section across the middle of the cell are expressed as

$$\begin{aligned}
&\sigma_{xy}\,(l_m/2\,+l_u/2\,)\,(t_u+t_i/2\,) = \\
&\big(\sigma_{xy,h}l_m/2\,+\sigma_{xy,u1}\,(l_u/2-l_m/2\,)+\sigma_{xy,u2}l_m/2\,\big)\,t_u+ \\
&\big(\sigma_{xy,i1}l_m/2\,+\sigma_{xy,i2}\,(l_u/2-l_m/2\,)+\sigma_{xy,i3}l_m/2\,\big)\,t_i/2 \\
&\sigma_{xy}\,(l_m/2\,+l_u/2\,)\,(t_u+t_i/2\,) = \\
&\big(\sigma_{xy,c}l_m/2\,+\sigma_{xy,b}\,(l_u/2-l_m/2\,)+\sigma_{xy,c}l_m/2\,\big)\,t_u+ \\
&\big(\sigma_{xy,i4}l_m/2\,+\sigma_{xy,i5}\,(l_u/2-l_m/2\,)+\sigma_{xy,i4}l_m/2\,\big)\,t_i/2
\end{aligned} \tag{6.65}$$

Deformation conformity is assumed between the leaves, leading to

$$\varepsilon_{xy,h1}h_u/2\,+\varepsilon_{xy,c1}h_m+\varepsilon_{xy,u2}h_u/2\,=\varepsilon_{xy,i1}h_u/2\,+\varepsilon_{xy,i4}h_m+\varepsilon_{xy,i3}h_u/2 \tag{6.66}$$

The total shear strain of the cell in the *xy* plane remains unchanged compared to the running bond case.

For *xz* shear the deformation of the cell is dominated by the deformation of the infill. Therefore, the system of equations and the assumptions need to be adjusted.

The shear stress equilibrium conditions at the back of the cell and at a vertical cross-section at the middle of the cell are as follows:

$$\begin{aligned}
&\sigma_{xz}\,(h_m+h_u)\,(l_u/2\,+l_m/2\,) = \\
&h_u\,(\sigma_{xz,i1}l_m/2\,+\sigma_{xz,i2}\,(l_u/2-l_m/2\,)+\sigma_{xz,i3}l_m/2\,)+h_m\,\big(2\sigma_{xz,i4}l_m/2+\sigma_{xz,i5}\,(l_u/2-l_m/2\,)\,\big) \\
&\sigma_{xz}\,(h_m+h_u)\,(t_u+t_i/2\,) = \\
&\big(\sigma_{xz,u1}h_u/2\,+\sigma_{xz,b}h_m+\sigma_{xz,u1}h_u/2\,\big)\,t_u+\big(\sigma_{xz,i2}h_u/2\,+\sigma_{xz,i5}h_m+\sigma_{xz,i2}h_u/2\,\big)\,t_i/2
\end{aligned} \tag{6.67}$$

The stress assumptions read:

$$\sigma_{xz,i1} = \sigma_{xz,i2} = \sigma_{xz,i3} = \sigma_{xz,i4} = \sigma_{xz,i5} \tag{6.68}$$

The strain assumptions read:

$$\varepsilon_{xz,h} = \varepsilon_{xz,u1} = \varepsilon_{xz,u2} = \varepsilon_{xz,c} = \varepsilon_{xz,b} \tag{6.69}$$

The total strain of the cell is defined as:

$$\varepsilon_{xz} = \left(\varepsilon_{xz,h} t_u + \varepsilon_{xz,i1} t_i/2\right)/(t_u + t_i/2) \tag{6.70}$$

For yz shear the deformation of the cell is again dominated by the deformation of the infill when its Young's modulus is low. However, the deformation profile changes for higher values of the Young's modulus of the infill since in this case the deformation of the outer leaf becomes more significant. Overall, the deformation is still dominated by the different stiffness between the outer and inner leaves.

The stress equilibrium conditions at the top, a horizontal cross section at mid height and at the front of the cell are as follows:

$$\begin{aligned}
&\sigma_{yz}(l_m/2 + l_u/2)(t_u + t_i/2) = \\
&\left(\sigma_{yz,h} l_m/2 + \sigma_{yz,u1}(l_u/2 - l_m/2) + \sigma_{yz,u2} l_m/2\right) t_u + \\
&\left(\sigma_{yz,i1} l_m/2 + \sigma_{yz,i2}(l_u/2 - l_m/2) + \sigma_{yz,i3} l_m/2\right) t_i/2 \\
&\\
&\sigma_{yz}(l_m/2 + l_u/2)(t_u + t_i/2) = \\
&\left(\sigma_{yz,c} l_m/2 + \sigma_{yz,b}(l_u/2 - l_m/2) + \sigma_{yz,c} l_m/2\right) t_u + \\
&\left(\sigma_{yz,i4} l_m/2 + \sigma_{yz,i5}(l_u/2 - l_m/2) + \sigma_{yz,i4} l_m/2\right) t_i/2 \\
&\\
&\sigma_{yz}(h_m + h_u)(l_u/2 + l_m/2) = \\
&h_u\left(\sigma_{yz,h} l_m/2 + \sigma_{yz,u1}(l_u/2 - l_m/2) + \sigma_{yz,u2} l_m/2\right) + \\
&h_m\left(2\sigma_{yz,c} l_m/2 + \sigma_{yz,b}(l_u/2 - l_m/2)\right)
\end{aligned} \tag{6.71}$$

The stress assumptions read:

$$\begin{aligned}
\sigma_{yz,i1} &= \sigma_{yz,h} \\
\sigma_{yz,i2} &= \sigma_{yz,u1} \\
\sigma_{yz,i3} &= \sigma_{yz,u2} \\
\sigma_{yz,i4} &= \sigma_{yz,c} \\
\sigma_{yz,i5} &= \sigma_{yz,b}
\end{aligned} \tag{6.72}$$

Deformation conformity conditions read:

$$\begin{aligned}
\varepsilon_{xz,h} t_u + \varepsilon_{xz,t1} t_i/2 &= \varepsilon_{xz,u2} t_u + \varepsilon_{xz,t3} t_i/2 \\
\varepsilon_{xz,h} h_u/2 + \varepsilon_{xz,c} h_m + \varepsilon_{xz,u2} h_u/2 &= \varepsilon_{xz,u1} h_u/2 + \varepsilon_{xz,b} h_m + \varepsilon_{xz,u1} h_u/2
\end{aligned} \tag{6.73}$$

Since deformation conformity is not rigidly imposed, the total strain of the cell is defined according to the geometrical average of the cuboids participating in the total deformation of the cell according to

$$\varepsilon_{yz} = \frac{\left(\left(\varepsilon_{yz,h}t_u+\varepsilon_{yz,i1}t_i/2\right)\frac{l_m}{2}+\left(\varepsilon_{yz,u1}t_u+\varepsilon_{yz,i2}t_i/2\right)\frac{l_u-l_m}{2}+\left(\varepsilon_{yz,u2}t_u+\varepsilon_{yz,i3}t_i/2\right)\frac{l_m}{2}\right)\frac{h_u}{2}+}{(l_u/2+l_m/2)(h_u/2+h_m/2)(t_u+t_i/2)} + \frac{\left(\left(\varepsilon_{yz,c}t_u+\varepsilon_{yz,i4}t_i/2\right)l_m+\left(\varepsilon_{yz,b}t_u+\varepsilon_{yz,i5}t_i/2\right)\frac{l_u-l_m}{2}\right)\frac{h_m}{2}}{(l_u/2+l_m/2)(h_u/2+h_m/2)(t_u+t_i/2)} \tag{6.74}$$

6.3.6 Stack Bond Pillar

For the stack bond pillar model the system of equations developed by Haller for vertical normal stress is used. According to Haller [70], the horizontal and transversal deformation equality of the two components reads:

$$\begin{aligned} \varepsilon_{xx,u} &= \varepsilon_{xx,b} \\ \varepsilon_{zz,u} &= \varepsilon_{zz,b} \end{aligned} \tag{6.75}$$

The horizontal and transversal stress equilibrium reads:

$$\begin{aligned} \sigma_{xx}\left(h_m+h_u\right) &= \sigma_{xx,u}h_u+\sigma_{xx,b}h_m \\ \sigma_{zz}\left(h_m+h_u\right) &= \sigma_{zz,u}h_u+\sigma_{zz,b}h_m \end{aligned} \tag{6.76}$$

The vertical stress equilibrium demands that both components develop vertical stress equal to the external load according to

$$\sigma_{yy,u} = \sigma_{yy,b} = \sigma_{yy} \tag{6.77}$$

The total vertical strain of the cell is

$$\varepsilon_{yy} = \left(\varepsilon_{yy,u}h_u/2+\varepsilon_{yy,b}h_m/2\right)/\left(h_u/2+h_m/2\right) \tag{6.78}$$

6.3.7 English Bond Pillar

Shear stresses in the components are disregarded for applied normal stress. Normal strain conformity in the cell is achieved by assuming

$$\begin{aligned} &\varepsilon_{xx,u1} = \varepsilon_{xx,b1} = \varepsilon_{xx,u3} = \varepsilon_{xx,h2} = \varepsilon_{xx,c2} = \varepsilon_{xx,u4} \\ &\varepsilon_{xx,u2} = \varepsilon_{xx,c1} = \varepsilon_{xx,h1} = \varepsilon_{xx,c4} = \varepsilon_{xx,c3} = \varepsilon_{xx,c5} \\ &\varepsilon_{yy,u3} = \varepsilon_{yy,h1} = \varepsilon_{yy,u4} = \varepsilon_{yy,c5} \\ &\varepsilon_{yy,b1} = \varepsilon_{yy,c1} = \varepsilon_{yy,c2} = \varepsilon_{yy,c3} \\ &\varepsilon_{yy,u2} = \varepsilon_{yy,c4} = \varepsilon_{yy,u1} = \varepsilon_{yy,h2} \\ &\varepsilon_{zz,u2} = \varepsilon_{zz,c1} = \varepsilon_{zz,h1} = \varepsilon_{zz,u1} = \varepsilon_{zz,b1} = \varepsilon_{zz,u3} \\ &\varepsilon_{zz,c4} = \varepsilon_{zz,c3} = \varepsilon_{zz,c5} = \varepsilon_{zz,h2} = \varepsilon_{zz,c2} = \varepsilon_{zz,u4} \end{aligned} \tag{6.79}$$

Normal stress equilibrium in the horizontal, vertical and transversal directions is expressed as

$$
\begin{aligned}
&\sigma_{xx}\,(h_u+h_m)\,(l_u/2\,)=\\
&\big(\sigma_{xx,h1}\,(l_u/2\,-l_m/2\,)+\sigma_{xx,c5}t_m/2\,\big)\,h_u/2+\\
&(\sigma_{xx,c1}\,(l_u/2\,-l_m/2\,)+\sigma_{xx,c3}t_m/2\,)\,h_m+(\sigma_{xx,u2}\,(l_u/2\,-l_m/2\,)+\sigma_{xx,c4}t_m/2)\,h_u/2\\
\\
&\sigma_{xx}\,(h_u+h_m)\,(l_u/2\,)=\\
&(\sigma_{xx,u3}\,(l_u/2\,-l_m/2\,)+\sigma_{xx,u4}t_m/2\,)\,h_u/2+\\
&\big(\sigma_{xx,b1}\,(l_u/2\,-l_m/2\,)+\sigma_{xx,c2}t_m/2\,\big)\,h_m+\big(\sigma_{xx,u1}\,(l_u/2\,-l_m/2\,)+\sigma_{xx,h2}t_m/2\big)\,h_u/2\\
\\
&\sigma_{yy}\,(l_u/2\,)\,(l_u/2\,)=\\
&\big(\sigma_{yy,u3}\,(l_u/2\,-l_m/2\,)+\sigma_{yy,h1}t_m/2\big)\,(l_u/2\,-l_m/2\,)+\big(\sigma_{yy,c5}l_m/2\,+\sigma_{yy,u4}\,(l_u/2\,-l_m/2\,)\big)\,t_m/2\\
\\
&\sigma_{yy}\,(l_u/2\,)\,(l_u/2\,)=\\
&\big(\sigma_{yy,b1}\,(l_u/2\,-l_m/2\,)+\sigma_{yy,c1}t_m/2\big)\,(l_u/2\,-l_m/2\,)+\big(\sigma_{yy,c3}l_m/2\,+\sigma_{yy,c2}\,(l_u/2\,-l_m/2\,)\big)\,t_m/2\\
\\
&\sigma_{yy}\,(l_u/2\,)\,(l_u/2\,)=\\
&\big(\sigma_{yy,u1}\,(l_u/2\,-l_m/2\,)+\sigma_{yy,u2}t_m/2\big)\,(l_u/2\,-l_m/2\,)+\big(\sigma_{yy,c4}l_m/2\,+\sigma_{yy,h2}\,(l_u/2\,-l_m/2\,)\big)\,t_m/2\\
\\
&\sigma_{zz}(h_u+h_m)(l_u/2\,)=\\
&\big(\sigma_{zz,u3}\,(l_u/2\,-l_m/2\,)+\sigma_{zz,h1}l_m/2\,\big)\,h_u/2\,+\big(\sigma_{zz,b1}\,(l_u/2\,-l_m/2\,)+\sigma_{zz,c1}l_m/2\,\big)\,h_m+\\
&(\sigma_{zz,u1}\,(l_u/2\,-l_m/2\,)+\sigma_{zz,u2}l_m/2\,)\,h_u/2\\
\\
&\sigma_{zz}(h_u+h_m)(l_u/2\,)=\\
&\big(\sigma_{zz,u4}\,(l_u/2\,-l_m/2\,)+\sigma_{zz,c5}l_m/2\,\big)\,h_u/2\,+(\sigma_{zz,c2}\,(l_u/2\,-l_m/2\,)+\sigma_{zz,c3}l_m/2\,)\,h_m+\\
&\big(\sigma_{zz,h2}\,(l_u/2\,-l_m/2\,)+\sigma_{zz,c4}l_m/2\,\big)\,h_u/2
\end{aligned}
\tag{6.80}
$$

The total vertical strain of the cell is

$$\varepsilon_{yy}=\big(\varepsilon_{yy,u3}h_u/2\,+\varepsilon_{yy,b1}h_m+\varepsilon_{yy,u1}h_u/2\,\big)/(h_u/2\,+h_m+h_u/2\,) \tag{6.81}$$

6.4 Calculation

For linear elastic analysis the solution from which the elastic moduli of the cell are derived can be accomplished in a single analysis step by solving the linear system of equations derived from the above expressions. The systems need to be solved for the unknown normal stresses, shear stresses (where considered), normal strains and shear strains. For normal stress loading, the unknowns include three normal stresses, three normal strains, one shear stress and one shear strain value for each cuboid. In total, the stack bond wall model consists of 26 unknowns, the running bond wall of 40, for the Flemish bond wall 128, for the three-leaf wall 80, for the stack bond pillar 12 and for the English bond pillar 72. For shear stress loading each cuboid has one shear stress and one shear strain unknown components. The number of unknowns is: 8 for the

stack bond wall, 10 for the running bond wall, 32 for the Flemish bond wall and 20 for the three-leaf wall model.

Overall, obtaining closed form expressions for the stresses and strains in the cuboids, as well as for the elastic moduli of the cells, under conditions of applied normal stress is extremely difficult even for the simple case of stack bond masonry. Expressions for the shear moduli of the cells are far easier to be obtained due to the much smaller number of unknowns. However, the linear systems of equations can be solved with very little effort using simple linear algebra or any basic symbolic math software.

6.5 Verification of the Model

The capacity of the model to predict the elastic properties of masonry cells under normal and shear loading is initially evaluated through a comparison with the results obtained from FE analyses. The meshes used for this verification are shown in Figure 6.7. Apart from the comparison between the results obtained from the proposed model and the FE analyses, it is desirable to compare the two approaches in terms of computational cost.

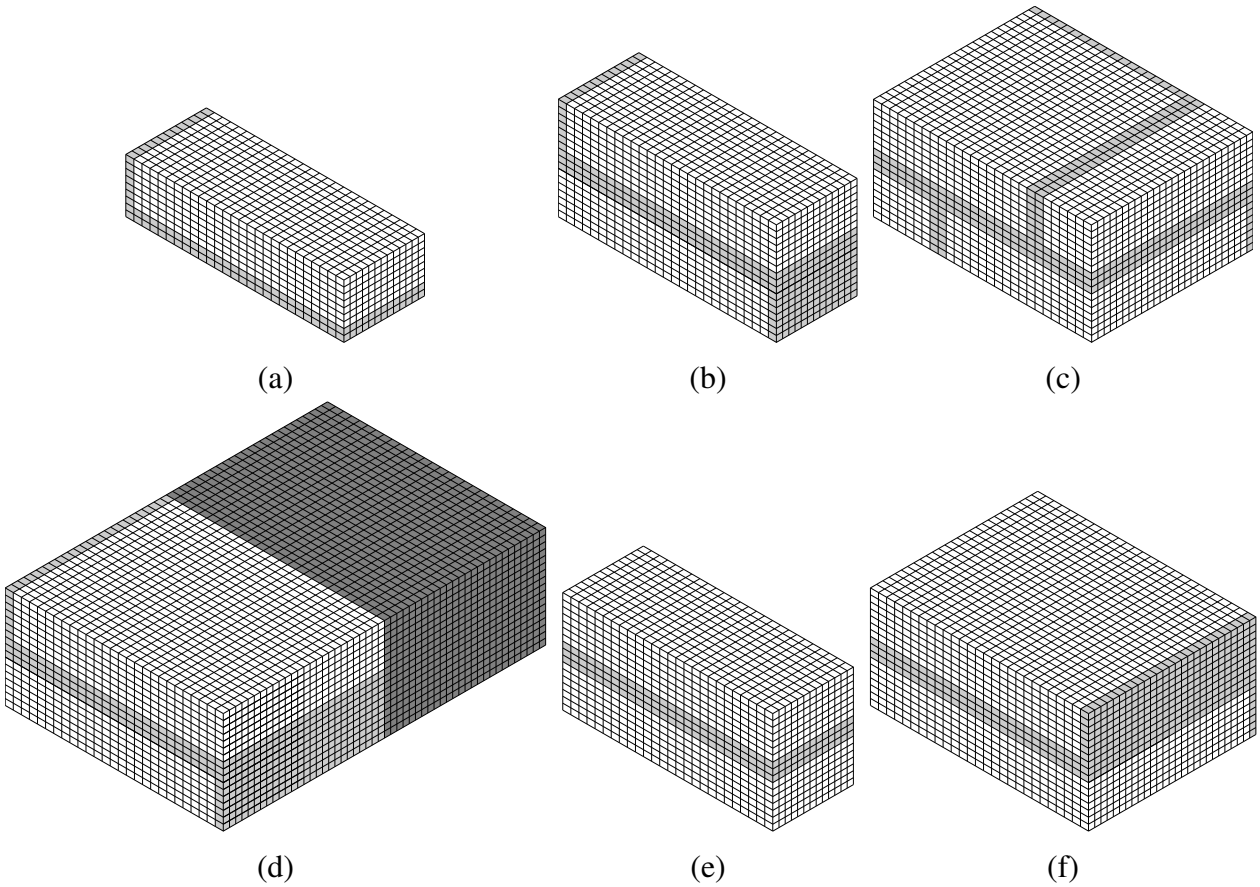

Figure 6.7 Finite element models of wall periodic unit cells: (a) stack bond wall, (b) running bond wall, (c) Flemish bond wall, (d) three-leaf wall, (e) stack bond pillar and (f) English bond pillar cell.

The masonry unit cell is meant to represent a volume of masonry inside an extended composite continuum. Therefore, boundary conditions assuring displacement conformity at the cell

faces need to be applied. Stress distribution in the constituents of the composite is not uniform but rather depends on the relative elasticity parameters of the involved components. The imposed boundary conditions ensure that the distribution of stress in the components is based on strain and deformation compatibility under normal and shear loading.

Periodicity conditions for a cell shown in Figure 6.8a are imposed by tying the displacements of nodes in opposite faces of the FE model. The tyings can be described as keeping the distance between two pairs of nodes equal, specifying a number of controlling nodes $p1$, $p2$, $p3$, $p4$ and $p5$. These controlling nodes also serve to fully describe the deformations necessary for the derivation of the elastic properties of the cell. Therefore the displacement of a node in face $i2$ or $j2$ for the application of a normal stress in the i direction or a shear stress in the ij plane can be derived from the displacement of the node in the opposite face $i1$ or $j1$ and the displacement of node $p1$, $p2$ and $p3$ as follows:

$$d_{i2} = d_{i1} + d_{p2} - d_{p1} \tag{6.82}$$

$$d_{j2} = d_{j1} + d_{p3} - d_{p1} \tag{6.83}$$

where d_{p1}, d_{p2} and d_{p3} are the displacement vectors of nodes $p1$, $p2$ and $p3$ in the ij plane and d_{i1}, d_{i2}, d_{j1} and d_{j2} are the displacement vectors of a node in faces $i1$, $i2$, $j1$ and $j2$ in the ij plane. Equal displacements in the k direction are imposed at the nodes of each of the external faces parallel to the ij plane for both applied normal and shear stress.

The elastic properties of the composite cell may be derived by registered displacements in the above designated controlling nodes, where $d_{pn,i}$ is equal to the displacement of node n in direction i. The total dimension of the cell in each principal direction i (horizontal, vertical and transversal) is designated as D_i. The Young's moduli and the Poisson's ratios of the cell may be calculated from

$$E_{c,i} = \sigma_{ii}/\varepsilon_{ii} = \sigma_{ii}/\left(\frac{d_i}{D_i}\right) = \sigma_{ii}/\left(\frac{d_{p2,i} - d_{p1,i}}{D_i}\right) \tag{6.84}$$

and

$$\begin{aligned} \nu_{c,ij} &= -\varepsilon_{jj}/\varepsilon_{ii} = -\left(\frac{d_j}{D_j}\right)/\left(\frac{d_i}{D_i}\right) = -\left(\frac{d_{p3,j} - d_{p1,j}}{D_j}\right)/\left(\frac{d_{p2,i} - d_{p1,i}}{D_i}\right) \\ \nu_{c,ik} &= -\varepsilon_{kk}/\varepsilon_{ii} = -\left(\frac{d_k}{D_k}\right)/\left(\frac{d_i}{D_i}\right) = -\left(\frac{d_{p5,k} - d_{p4,k}}{D_j}\right)/\left(\frac{d_{p2,i} - d_{p1,i}}{D_i}\right) \end{aligned} \tag{6.85}$$

where d_i, d_j and d_k are relative displacements between two opposing faces, which can be expressed by the difference in displacement of opposing controlling nodes in a given direction.

The shear modulus of the cell is equal to

$$G_{c,ij} = \sigma_{ij}/2\varepsilon_{ij} = \sigma_{ij}/\gamma_{ij} = \sigma_{ij}/\left(\frac{d_{p4,i} - d_{p1,i}}{D_j} + \frac{d_{p4,j} - d_{p1,j}}{D_i}\right) \tag{6.86}$$

The deformation profile of the cell under normal and shear applied stress is shown in Figure 6.8b and 6.8c.

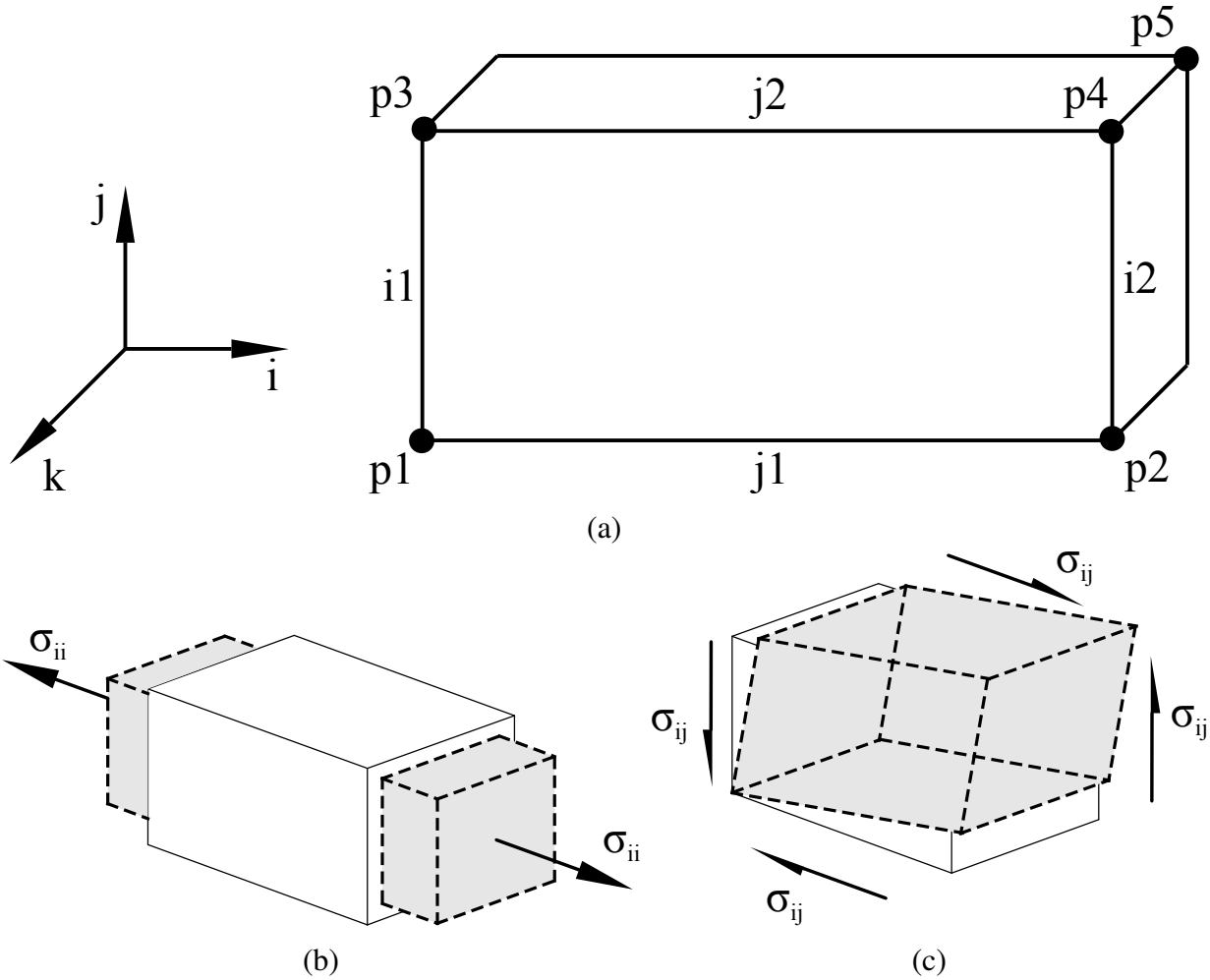

Figure 6.8 (a) FE model faces and nodes for definition of periodicity conditions. (b) Deformation profile of cell under uniaxial normal stress and (c) under pure shear stress.

A parametric investigation is conducted in order to verify the accuracy of the models for a wide range of ratios of unit-to-mortar and mortar-to-infill Young's modulus, as shown in Table 6.1. These properties and dimensions have been applied to all typologies of masonry under study. The parametric investigation of the three-leaf wall is conducted by assuming a ratio of 30 for the unit-to-mortar Young's modulus and altering the Young's modulus of the infill ranging from highly deformable to stiffer than the outer leaf. The wall models have been tested in all normal and shear directions and the pillar models have been tested for vertical loading.

Finally, a comparison is made between the results obtained by the model and experimental results drawn from the existing literature.

Table 6.1 Material properties and dimensions for linear elastic parametric analysis.

E_u $[N/mm^2]$	ν_u $[-]$	E_u $[N/mm^2]$	ν_m $[-]$	E_i $[N/mm^2]$	ν_i $[-]$	h_u $[mm]$	l_u $[mm]$	t_u $[mm]$	h_m $[mm]$	l_m $[mm]$	t_m $[mm]$	t_i $[mm]$
20000	0.15	20, 33, 67, 200, 333, 667, 2000, 3333, 6667, 20000	0.15	7, 11, 22, 67, 111, 222, 667, 2000, 4000, 6667	0.20	52	210	100	10	10	10	150

6.6 Results

6.6.1 Parametric Investigation

The micro-mechanical approach produced elastic results nearly identical to those obtained from FE analysis for all models and for almost the entire range of material properties. The Young's moduli and the Poisson's ratios of the masonry composites were calculated with great accuracy, with the differences being restricted to a number of shear moduli in out-of-plane loading.

The computational cost of the micro-mechanical models is negligible, the results being produced practically instantaneously on an ordinary computer, even for the largest systems of equations. The FE models required a computational time ranging from several seconds to a few minutes for the production of the results. The results of the parametric investigation and their comparison with FEM calculations are illustrated in Figures 6.9 through 6.12.

The comparison of the Young's modulus of walls as calculated by the models, in comparison with the finite element analysis results, is presented in Figure 6.9 for loading in all three orthogonal directions. The comparison for the pillars is shown in Figure 6.10 for loading in the vertical direction only. The models are proven to be very accurate for the determination of the Young's modulus of masonry for all typologies and all directions of loading.

An interesting result is the tendency of the horizontal and vertical Young's modulus of the wall models to be drastically reduced for a reduction in the Young's modulus of the mortar (as is expected due to the existence of the continuous bed joint and the continuous or staggered head joints) while the transversal Young's modulus for stack and running bond walls remains largely unaffected. For high values of the mortar modulus the three Young's moduli are of the same order of magnitude in all models, while for low values the transversal modulus is much higher in the single leaf wall cases. Certain conclusions may be drawn from this observation concerning the applicability of plane analysis methods for stack bond masonry structures. According to the relative deformability in the in-plane and out-of-plane directions, plane stress analysis may provide reasonable results for very rigid mortars and plane strain for very deformable mortars.

The transversal joint in the Flemish bond wall eliminates the distinct higher rigidity in the transversal direction for highly deformable mortars noted in the stack bond and running bond typologies. However, the complex geometry across the thickness of the structure would render the plane stress and plane strain methods of analysis inappropriate by definition.

The elastic stiffness of the infill marginally affects the global stiffness of the three-leaf wall in the vertical and horizontal direction, but greatly affects its stiffness in the transversal direction. The infill acts in a manner similar to that of the continuous bed joint in masonry under vertical load.

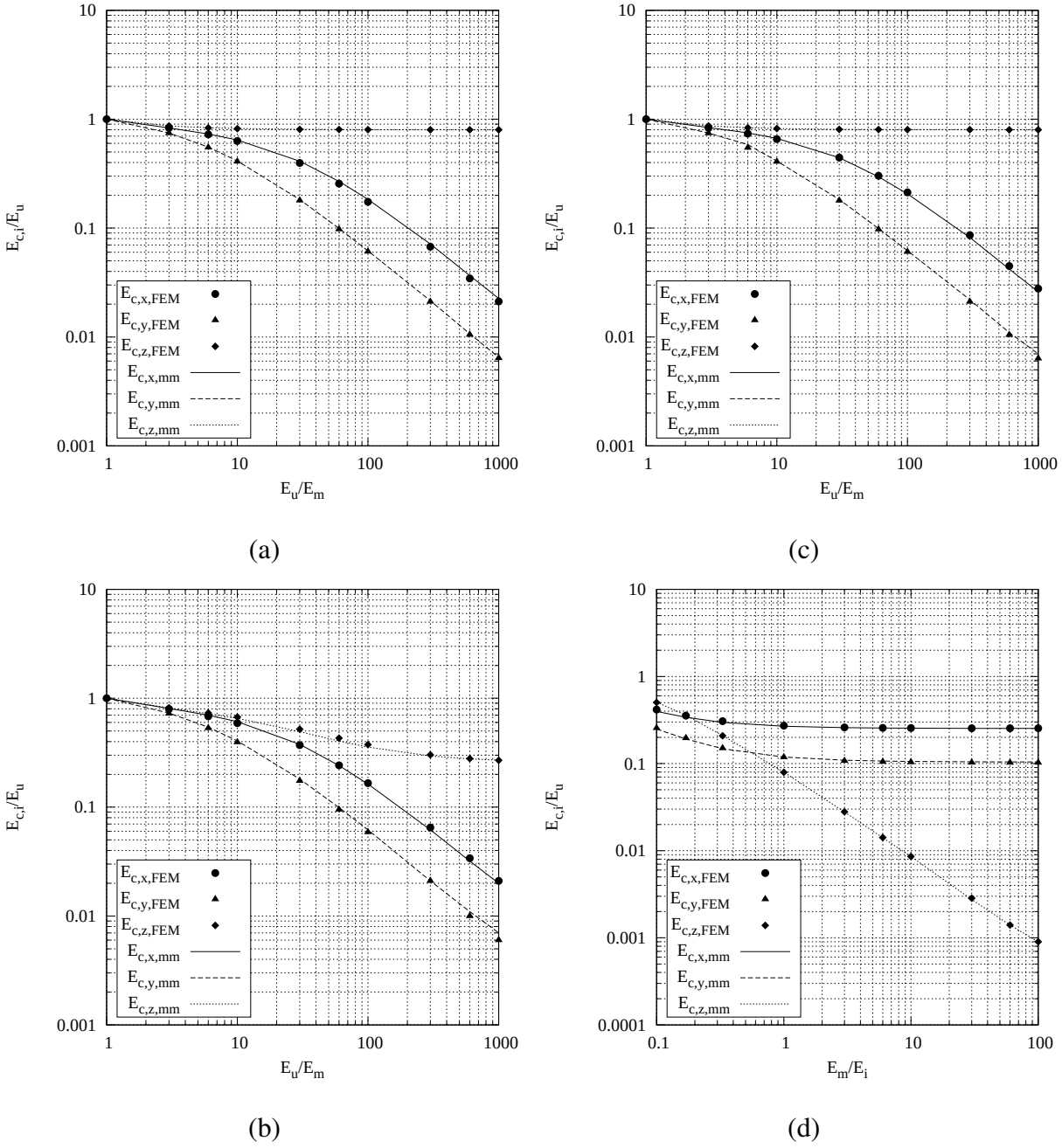

Figure 6.9 Comparison Young's modulus of masonry walls according to micro-mechanical model and FEM results: (a) stack bond, (b) running bond, (c) Flemish bond and (d) three-leaf wall with running bond outer leaf walls.

The micro-mechanical models for the stack bond and English bond pillar, shown in Figure 6.10, produced results identical to the ones obtained from FE analyses. The deformation of the bed joint under vertical loading dominates the response in terms of global elastic stiffness and, as such, the existence of head and cross joints in the English bond pillar case has very small

influence on the final results.

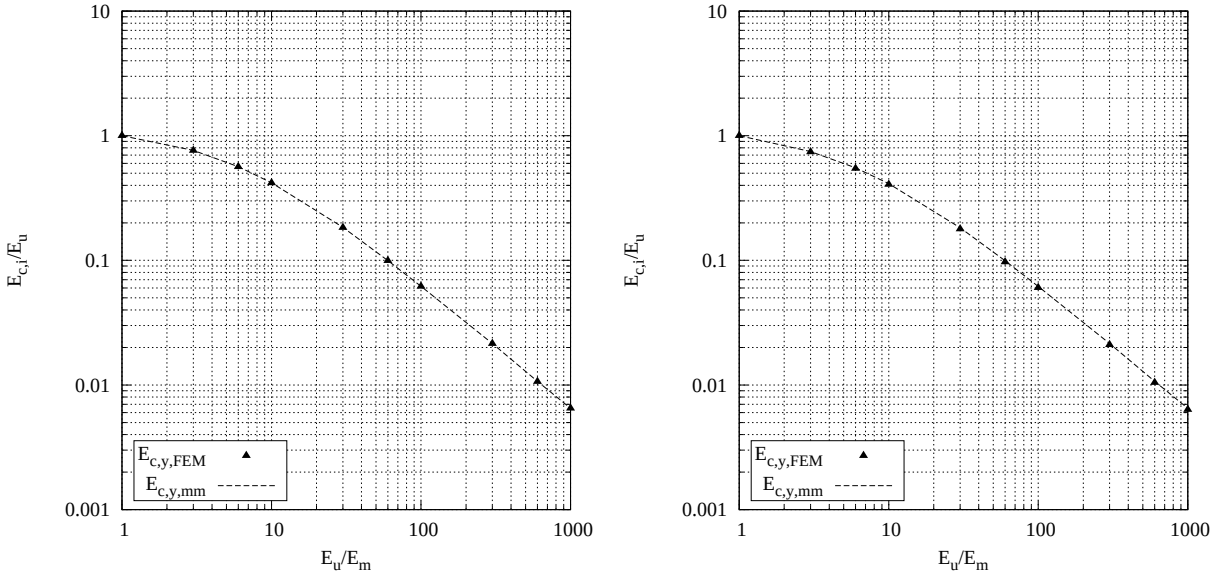

Figure 6.10 Comparison of Young's modulus of masonry pillars according to micro-mechanical model and FEM results: (a) stack bond and (b) English bond pillars.

Figure 6.11 presents the comparison of the micro-mechanically to the numerically derived shear modulus of the wall typologies. Very good agreement is found between the results overall, with the exception of the modulus in the *xz* planne for the running bond model, which is, for $E_u/E_m = 1000$, 18% lower than the numerically derived value.

The effect of the continuous bed joint is apparent in shear in the *xy* and *yz* planes for stack bond, running bond and Flemish bond walls. The shear modulus in those planes is nearly equal for every model investigated. Of interest is the shift in the deformation profile of the three-leaf wall cell under *yz* shear as the Young's modulus of the infill increases. For low values the obtained shear modulus is equal to the modulus in the *xz* plane and for higher values it is equal to the modulus in the *xy* plane. This is due to the deformability of the infill dominating the response when its Young's modulus is low.

The Poisson's ratios derived from the models are presented in Figure 6.12 for the wall models. Overall, the accuracy of the model is very good, with the exception of the $\nu_{c,xy}$ in the stack bond wall case, where the value is slightly underestimated by the model for E_u/E_m greater than 70, and the $\nu_{c,zx}$ in the Flemish bond model, which is slightly overestimated by the model for E_u/E_m greater than 100.

Noteworthy is the fact that the $\nu_{c,zx}$ remains equal to that of the two components (the units and the mortar) regardless of the Young's modulus of the mortar in the single leaf masonry wall cases. The influence of the transversal joint in the Flemish bond wall and of the infill in the three-leaf wall models is shown in Figure 6.12b and 6.12c respectively, with the value noticeably dropping for a decrease of the Young's modulus of the mortar or the infill.

6.6.2 Case Studies

The modeling method has been applied to experimental cases consisting of stack bond, running bond and Flemish bond masonry composites found after an extensive literature review on masonry in compression. The designation of the case studies is the same as the one used in the chapter on finite element modeling of masonry in compression already presented. Only case studies providing experimental values for the Young's modulus of the constituents have been considered. The cases and the analysis results are summarized in Table 6.2 through Table 6.5. The cases selected represent wider range of material properties and dimensions that those considered in the parametric study. In a number of cases the Poisson's ratio is not given in the cited work and, therefore, a nominal value is used. In these cases, the value of the Poisson's ratio is indicated in curly brackets. The average value of the measured Poisson's ratio in the set of case studies is 0.13 for the units with values ranging from 0.07 to 0.24 while for the mortars it is equal to 0.15 with values ranging from 0.07 to 0.2. In the cases where it was not reported, the Poisson's ratio for the units was chosen as being equal to 0.15 while a value between 0.15 and 0.25 was chosen depending on the type of mortar. In [56, 124] a weak lime mortar was used, so a value of 0.25 was adopted. For [8, 68, 119, 120, 156], for which a cement/lime mortar was used, a value of 0.20 was adopted. In [76, 81] Portland cement mortars were used and a value of 0.15 was used.

Again, the case studies have also been analyzed using FE models for the sake of comparison between the analysis methods.

Table 6.2 Stack bond prism cases. Comparison of experimental and analysis results. Assumed values in curly brackets.

Case	Ref.	E_u $[N/mm^2]$	ν_u [-]	h_u $[mm]$	l_u $[mm]$	t_u $[mm]$	E_m $[N/mm^2]$	ν_m [-]	h_m $[mm]$	l_m $[mm]$	t_m $[mm]$	$E_{c,exp}$ $[N/mm^2]$	$E_{c,FEM}$ $[N/mm^2]$	$E_{c,mm}$ $[N/mm^2]$
S2	[56]	4200	0.16	45	290	140	125	{0.25}	10	-	-	600	814	705
S3	[68]	976	{0.15}	75	230	105	1500	{0.20}	12	-	-	467	1016	1025
S5	[68]	3372	{0.15}	75	230	105	8568	{0.20}	12	-	-	2393	3525	3692
S6	[8]	135	{0.15}	52	212	104	795	{0.20}	10	-	-	207	154	154
S7	[56]	4200	0.16	45	290	140	225	{0.25}	10	-	-	1100	1157	1138
S8	[137]	5500	0.11	113	240	175	2765	0.07	30	-	-	4200	4702	4555
S9	[68]	3372	{0.15}	75	230	105	5450	{0.20}	12	-	-	3135	3628	3560
S10	[68]	976	{0.15}	75	230	105	238	{0.20}	12	-	-	379	735	701
S13	[3]	2000	0.1	55	250	110	1700	0.2	10	-	-	1936	1950	1956
S14	[64]	7500	0.07	65	40	40	220	0.2	20	-	-	878	1475	937
S15	[119]	12000	0.2	45	285	130	4200	{0.20}	10	-	-	10000	9761	9110
S16	[137]	5500	0.11	238	252	241	2765	0.07	12	-	-	5517	5330	5250
S17	[156]	16700	0.15	52	210	100	2100	0.22	13	-	-	6800	8294	7486
S19	[124]	5756	{0.15}	55	125	120	5487	{0.25}	10	-	-	2132	5906	5736
S21	[68]	976	{0.15}	75	230	105	8568	{0.20}	12	-	-	365	1098	1137
S23	[130]	8000	0.08	100	305	143	6600	0.19	30	-	-	5900	7013	7687
S24	[64]	7500	0.07	65	40	40	220	0.2	10	-	-	1938	2380	1509
S26	[68]	3372	{0.15}	75	230	105	7083	{0.20}	12	-	-	3700	3585	3641
S29	[81]	5300	{0.15}	75	230	110	545	{0.15}	10	-	-	2239	3034	2679
S30	[76]	12930	{0.15}	36	123	60	9590	{0.15}	7	-	-	8000	12601	12244

The micro-mechanical model gives values nearly identical to the values obtained through FE analysis for the majority of the cases. The comparison with the experimental values shows significant agreement as well, especially for the stack bond pillar and running bond wall cases.

Table 6.3 Running bond wall cases. Comparison of experimental and analysis results. Assumed values in curly brackets.

Case	Ref.	E_u $[N/mm^2]$	ν_u [-]	h_u $[mm]$	l_u $[mm]$	t_u $[mm]$	E_m $[N/mm^2]$	ν_m [-]	h_m $[mm]$	l_m $[mm]$	t_m $[mm]$	$E_{c,exp}$ $[N/mm^2]$	$E_{c,FEM}$ $[N/mm^2]$	$E_{c,mm}$ $[N/mm^2]$
R1	[68]	3372	{0.15}	75	230	105	5450	{0.20}	12	12	-	5232	3590	3660
R2	[156]	4000	0.13	50	206	96	1650	{0.20}	12.5	10	-	3200	3095	3114
R3	[68]	976	{0.15}	75	230	105	238	{0.20}	12	12	-	580	717	685
R4	[68]	976	{0.15}	75	230	105	1500	{0.20}	12	12	-	735	1033	1050
R5	[68]	3372	{0.15}	75	230	105	7083	{0.20}	12	12	-	4824	3702	3825
R6	[68]	3372	{0.15}	75	230	105	8568	{0.20}	12	12	-	5024	3782	3863
R7	[120]	6740	0.167	35	110	50	970	{0.20}	5	5	-	3700	3949	3936
R8	[68]	976	{0.15}	75	230	105	8568	{0.20}	12	12	-	400	1254	1561

Table 6.4 Flemish bond wall cases. Comparison of experimental and analysis results. Assumed values in curly brackets.

Case	Ref.	E_u $[N/mm^2]$	ν_u [-]	h_u $[mm]$	l_u $[mm]$	t_u $[mm]$	E_m $[N/mm^2]$	ν_m [-]	h_m $[mm]$	l_m $[mm]$	t_m $[mm]$	$E_{c,exp}$ $[N/mm^2]$	$E_{c,FEM}$ $[N/mm^2]$	$E_{c,mm}$ $[N/mm^2]$
F1	[25]	4865	0.09	55	250	120	1180	0.06	10	10	10	1651	3107	3178
F2	[25]	4865	0.09	55	250	120	5650	0.09	10	10	10	3833	5002	5025
F3	[25]	4865	0.09	55	250	120	17760	0.12	10	10	10	4567	6390	6547

The largest differences were registered in cases $S2$, $S14$ and $S24$, which are characterized by mortars with a very low Young's modulus for the mortar. The locking effect, as shown in Figure 4.17 may have been involved. The results of the case studies are additionally illustrated in Figure 6.13.

6.7 Conclusions

Models for the derivation of elastic and inelastic properties of masonry composites using micro-mechanical techniques for the analysis of masonry periodic unit cells are presented and tested against results obtained from the analysis of corresponding FE cells and experimental results. The model is capable of simulating the arising normal and shear stresses and strains in the macroscopic components of masonry composites, therefore conforming with the basic principles of detailed micro-modeling.

The results on the elastic properties of several types of masonry composites for a wide range of material combinations are well approximated using an micro-mechanical model based on simple analytical calculations. Using FE calculations as a benchmark, the elastic anisotropic behavior of masonry due to the interaction of isotropic components arranged in various typologies in a periodic structure is well simulated. Additionally, the comparison between the results of the proposed model and the available experimental results is fair, the differences being lower than the experimental scatter.

Finally, the use of micro-mechanical models based on analytical expressions is shown to be very advantageous compared to FE calculations in terms of computational cost and model preparation time. The means required to implement the models for the derivation of the elastic properties of masonry only include simple linear algebra software and can be performed in a

Table 6.5 English bond pillar cases. Comparison of experimental and analysis results.

Case	Ref.	E_u $[N/mm^2]$	ν_u [-]	h_u $[mm]$	l_u $[mm]$	t_u $[mm]$	E_m $[N/mm^2]$	ν_m [-]	h_m $[mm]$	l_m $[mm]$	t_m $[mm]$	$E_{c,exp}$ $[N/mm^2]$	$E_{c,FEM}$ $[N/mm^2]$	$E_{c,mm}$ $[N/mm^2]$
P1	[68]	3372	{0.15}	75	230	105	8568	{0.20}	12	20	20	3317	4005	4157
P2	[68]	3372	{0.15}	75	230	105	5450	{0.20}	12	20	20	3789	3684	3736
P3	[68]	976	{0.15}	75	230	105	238	{0.20}	12	20	20	377	690	663
P4	[68]	3372	{0.15}	75	230	105	7083	{0.20}	12	20	20	3677	3865	3966
P5	[68]	976	{0.15}	75	230	105	1500	{0.20}	12	20	20	381	1056	1070
P6	[68]	976	{0.15}	75	230	105	8568	{0.20}	12	20	20	376	1510	1869
P7	[64]	7500	0.07	65	290	140	220	0.2	10	10	10	661	2007	1500

single analysis step. The extension of the modeling technique herein presented for the nonlinear analysis of masonry walls and the prediction of their nonlinear properties will be presented in the following chapter.

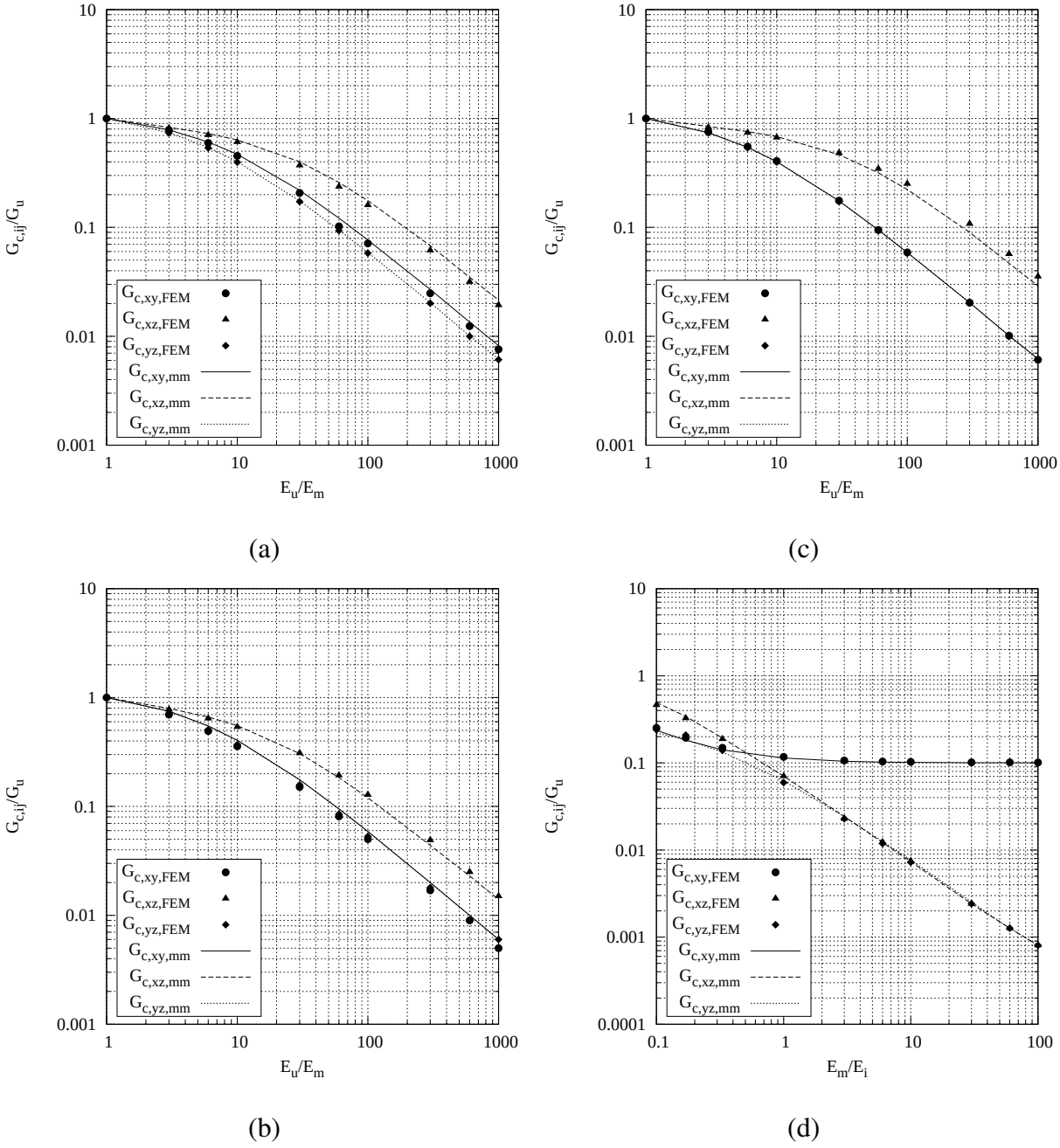

Figure 6.11 Comparison of shear modulus of masonry walls according to micro-mechanical model and FEM results: (a) stack bond, (b) running bond, (c) Flemish bond and (d) three-leaf wall with running bond outer leaf walls.

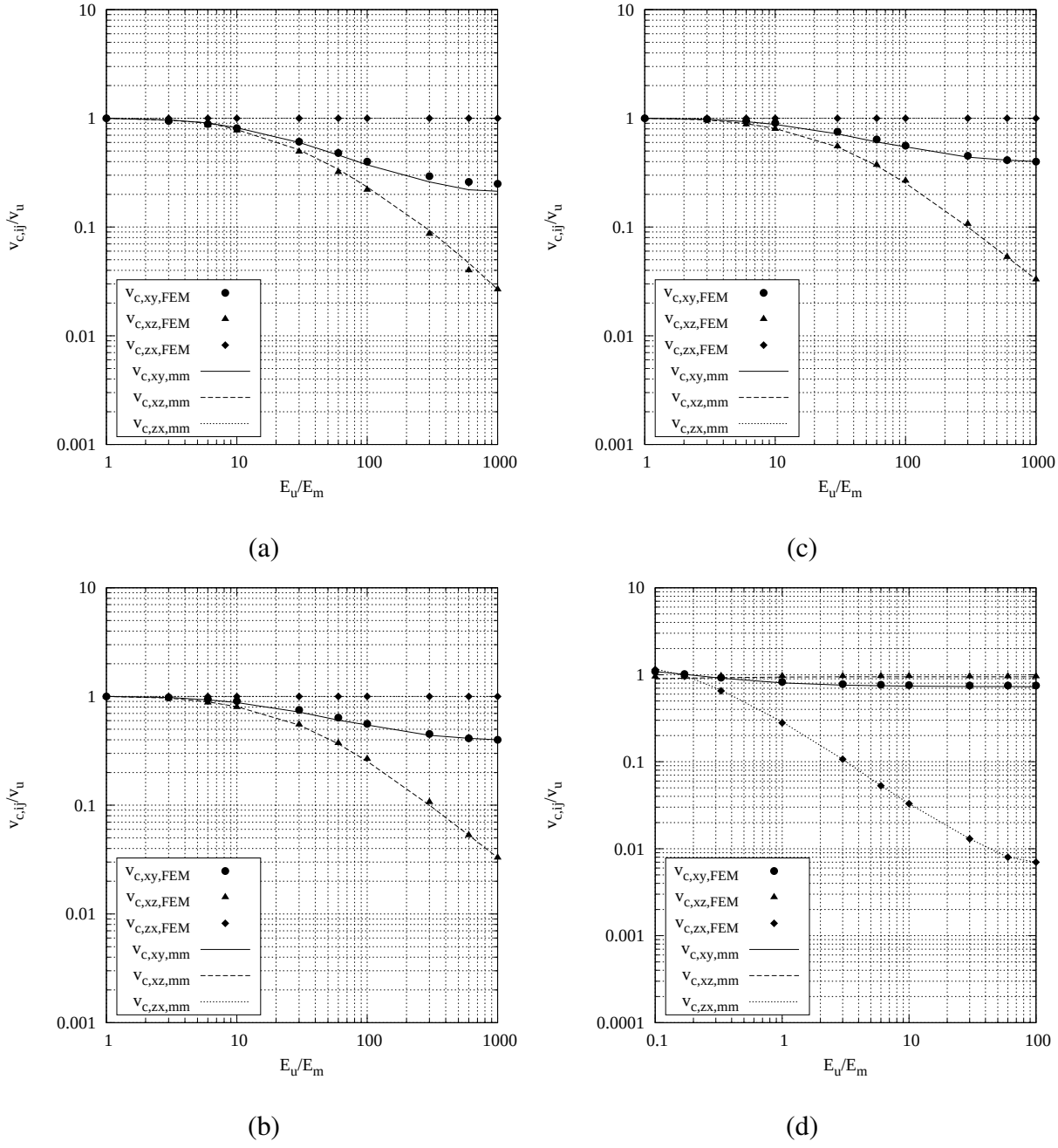

Figure 6.12 Comparison of Poisson's ratio of masonry walls according to micro-mechanical model and FEM results: (a) stack bond, (b) running bond, (c) Flemish bond and (d) three-leaf wall with running bond outer leaf walls.

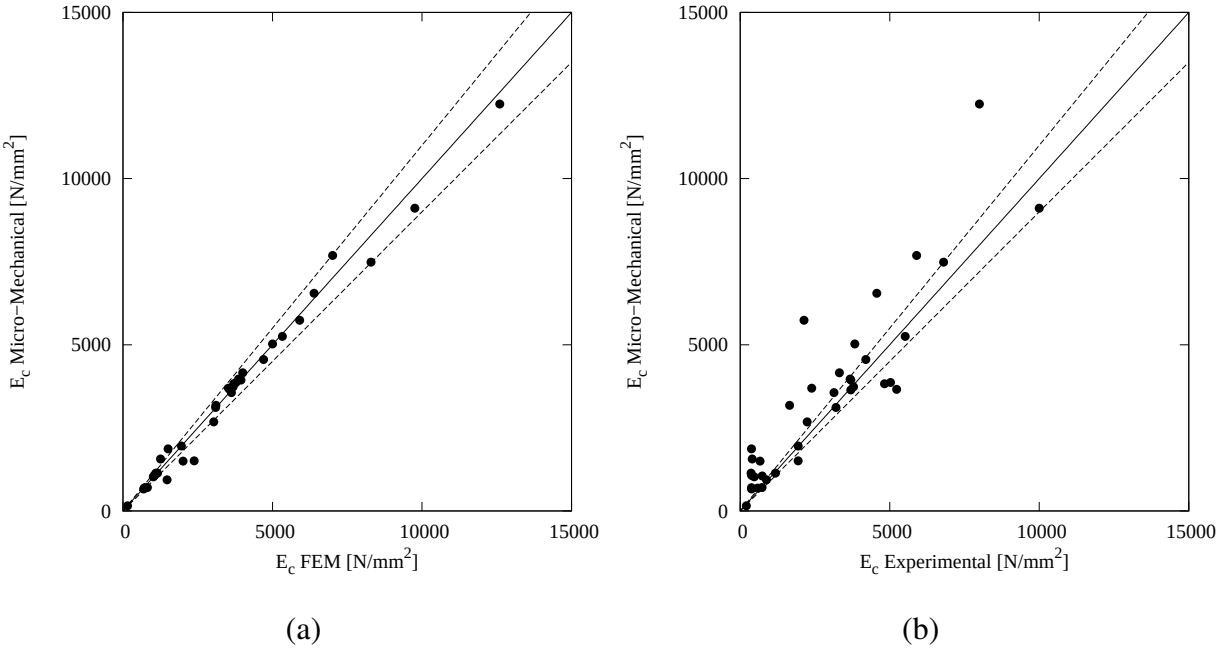

Figure 6.13 Comparison of vertical stiffness according to (a) FEM and micro-mechanical results and (b) experimental and micro-mechanical results. The dotted lines indicate the limits of 10% deviation between the compared values.

Chapter 7

Micro-Mechanical Modeling of Masonry - Nonlinear Analysis

7.1 Introduction

Micro-modeling techniques for the derivation of the orthotropic mechanical properties of masonry composites are a powerful computational tool. They are capable of providing the elastic properties of masonry under normal and shear loads as well as its strength domain under uniaxial and complex loading. The information obtained in terms of strength values, the evolution and propagation of damage in each component and the influence of individual material parameters on the response are highly important for the computational study of masonry structures and can prove to be an incentive for guiding experimental studies on the determination of the critically important mechanical properties of masonry materials.

Being composed of (at least) two macroscopically distinguishable material phases with different mechanical properties, generally arranged in a repeating pattern, masonry structures are a suitable candidate for analysis using periodic unit cells. The analysis of these cells may be performed using finite element computations [24, 103] or analytical expressions [30, 122, 162], in order to derive the distribution of stress and strain in the volume of the cell. While the former is capable of providing accurate results, its use is hindered by potentially high computational cost. The latter choice is attractive due to its very low computational cost, but the validity of the assumptions made in the formulation of the analytical expressions need to be rigorously checked through conceptual reasoning, accurate calculations and comparison with the existing experimental data.

It has been demonstrated that numerical modeling of masonry wall structures under in-plane-loading needs to take into account the out-of-plane stresses [16, 95]. While this necessity is straightforward in the case of multi-leaf walls or of pillars composed of interlocking masonry units, where the accurate representation of the geometry of the structure demands its full three-dimensional modeling, it is essential in the analysis of single leaf structures as well, since three-dimensional effects are a governing factor in the behavior of mortar joints in masonry under compression. While plane stress and plane strain finite element models may present significant

computational cost advantages over full three-dimensional models they tend to under- or over-estimate the confinement effect on mortar in the joints respectively. However, the adoption of three-dimensional finite element models may prove to be very demanding in terms of computational cost.

Several models based on analytical expressions or micro-mechanical approaches have been proposed for various types of masonry. These include early models of stack bond pillars [70] and numerous works on running bond walls [31, 37, 112, 122, 162]. Other types of masonry, such as Flemish bond walls, three-leaf walls with infill and English bond pillars have not been the subject of much investigation.

Detailed micro-modeling requires extensive characterization of the mechanical properties of the masonry units, mortar, infill and interfaces. Due to the large number of parameters involved, coupled with inherent difficulties in determining these parameters from samples extracted from existing structures and with the high scatter that often characterizes them, several of these parameters are routinely given standard values. The study of the sensitivity of the compressive strength of masonry to some of these parameters is an interesting subject for investigation.

Closed form expressions for the determination of the compressive strength of masonry have been proposed based on various analytical formulations [74, 117] and are in use in modern design codes [40]. Many of these expressions have a strong empirical aspect concerning the influence of the material properties of the constituent materials of masonry. Other models in which the majority of the elastic and strength properties of the constituent materials are directly input in the expressions provide unstable results for certain ranges of elastic property combinations [63, 73]. A relatively simple closed form model based on the principles of detailed micro-modeling which overcomes as much as possible empirical assumptions and result instability of other closed form models could be proposed.

A number of objectives is attempted to be tackled through this investigation. A model for computational modeling of masonry wall and pillar structures based on micro-modeling techniques and performed through the analysis of periodic unit cells is proposed. The analysis of the masonry cells is carried out using analytical expressions based on stress equilibrium, strain conformity and rational assumptions concerning the behavior of masonry geometrical components. By coupling with nonlinear constitutive laws these models are intended to be used for the calculation of the nonlinear properties of masonry structures.

The formulation of the models using analytical expressions serves to critically reduce the computational effort required for analysis. Being computationally advantageous to, for example, finite element computations, the models of the cells are appropriate for two-scale analyses of large structures, thus bridging the gap between the accuracy of detailed micro-modeling techniques and the need to investigate the structural behavior of large masonry assemblages.

Several typologies of masonry walls and pillars are treated in this chapter. A number of them, such as stack bond pillars, stack bond walls and running bond walls, have garnered the almost complete attention of researchers so far. The present investigation includes analyses on Flemish bond and three-leaf walls, as well as English bond pillars, which have not received the research attention that their abundance in the built environment would warrant.

The models have been employed in the study of the response of masonry under tensile and, to a more significant extent, compressive loads. The evolution of stress and damage levels in different parts of the masonry has been studied and commented upon. Differences between different masonry typologies under the same loading conditions are also presented.

The models constitute a useful tool for the carrying out of quick but accurate calculations in order for the nonlinear properties of masonry structures to be derived. In addition, they have been here employed in a wide parametric investigation, which, taking advantage of their low computational cost, provides insights on the sensitivity of the compressive strength of masonry to several material and geometrical parameters over a wide spectrum of values.

Finally, a closed form expression for the determination of the compressive strength of masonry is proposed based on the micro-mechanical models investigated. A further simplification of this expression is proposed based on empirical data. A number of experimental case studies on the compressive strength of masonry are compared with the results of the micro-mechanical model and the closed form expressions.

7.2 Nonlinear Analysis

7.2.1 Overview

The framework for the nonlinear analysis of the cells using the micro-mechanical model developed in the previous chapter firstly requires the definition of failure criteria for the components under the different types of action to which they are subjected. Secondly, the simulation of damage when the failure conditions are met are defined. This is accomplished by introducing a set of integrity variables which modify the stresses in the analytical systems of equations so that the "damaged" stresses may be determined. Finally, the analytical systems of equations needs to be solved for the derivation of the stresses and strains in the cuboids.

7.2.2 Failure Criteria

The units, the mortar and the infill are modeled as three-dimensional isotropic continua. Perfect bond is considered at the unit/mortar interface, therefore all deformation of the cell is accounted for in the units and the mortar. The initiation of damage requires the definition of failure criteria in compression, tension and shear.

For the mortar the Hsieh-Ting-Chen failure curve is adopted, while for the units two different failure criteria have been implemented: a Rankine criterion with a compression and a tension cut-off, equal to the uniaxial compression and tensile strength of the unit respectively, and a Mohr-Coulomb criterion. In the former criterion the interaction between tension and compression is disregarded, while in the latter it is taken into account by reducing the compressive strength of the unit when subjected to laterally applied tensile stress. All curves are presented in Figure 7.1.

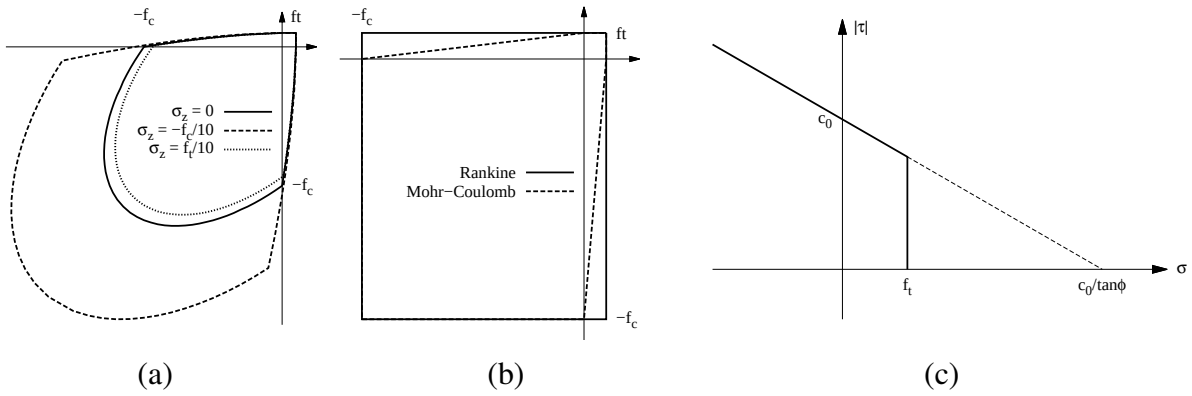

Figure 7.1 Failure curves used for (a) mortar for various levels of out-of-plane stress, (b) units and (c) interfaces.

The Hsieh-Ting-Chen failure surface shape is determined by four material tests: uniaxial compression, uniaxial tension, equibiaxial compression and compression under equibiaxial compression. The mathematical expression of the curve has been presented in equation 3.10. Figure 7.1 illustrates the effect of out-of-plane stresses in the in-plane strength domain of the mortar. Similarly, Figure 7.1 illustrates the effect of lateral tensile stresses on the compressive strength of the unit.

In shear, a Mohr-Coulomb friction failure criterion is adopted, which has the form

$$|\tau| + \sigma \tan \varphi - c = 0 \tag{7.1}$$

where τ is the failure shear stress, φ is the friction angle, σ the applied normal stress and c the cohesion.

7.2.3 Simulation of Damage

Damage in the cuboids due to compression, tension and shear is accomplished by the use of integrity variables. These variables are designated C, T and S for compression, tension and shear respectively and range from 1 to 0. They represent the ratio between the actual stress and the effective stress in the component. A value of 1 signifies that the material is undamaged and a value of 0 signifies that the material is completely softened. The evolution of the integrity variables is a function of the uniaxial strain and, in the case of compressive damage, the lateral compressive stresses.

The determination of these integrity variables requires the description of the hardening and softening behavior of the materials in tension, compression and shear. For tension an exponential softening law based on fracture energy is adopted. According to this assumption, the integrity variables are:

$$T(n) = \begin{cases} 1 & 0 \leq \sigma_{eff}(n) \leq f_t \\ \frac{f_t}{\sigma_{eff}(n)} \exp\left[-\frac{f_t h}{G_f^I}\left(\varepsilon(n) - \frac{f_t}{E}\right)\right] & f_t < \sigma_{eff}(n) \end{cases} \tag{7.2}$$

where f_t is the tensile strength, E is the Young's modulus, G_f^I is the tensile fracture energy, h is the characteristic length and $\varepsilon(n)$ is the total strain. This equation is evaluated in the three principal directions for each cell component and the lowest integrity variable is chosen to represent the isotropic damage.

The failure in tension in the interface may be taken into account by adjusting the tensile properties of the mortar in the chosen direction. For this purpose the tensile strength and fracture energy may be reduced in the horizontal direction for the head joints, the vertical direction for the bed joints and the transversal direction for the transversal joints in order for these parameters to correspond to the mechanical properties of the interface. For the softening of the interface in tension the characteristic length as defined for the mortar joint is adopted.

For compression the integrity variables are:

$$C(n) = \begin{cases} 1 & for \quad 0 < \varepsilon(n) \leq \varepsilon_{c/3} \\ -\frac{f_c}{\sigma_{eff}(n)} \frac{1}{3}\left(1 + 4\left(\frac{\varepsilon(n)-\varepsilon_{c/3}}{\varepsilon_c - \varepsilon_{c/3}}\right) - 2\left(\frac{\varepsilon(n)-\varepsilon_{c/3}}{\varepsilon_c - \varepsilon_{c/3}}\right)^2\right) & for \quad \varepsilon_{c/3} < \varepsilon(n) \leq \varepsilon_c \\ -\frac{f_c}{\sigma_{eff}(n)}\left(1 - \left(\frac{\varepsilon(n)-\varepsilon_c}{\varepsilon_u - \varepsilon_c}\right)^2\right) & for \quad \varepsilon_c < \varepsilon(n) \leq \varepsilon_u \\ 0 & for \quad \varepsilon_u < \varepsilon(n) \end{cases} \tag{7.3}$$

where f_c is the uniaxial compressive strength, $\varepsilon(n)$ the strain and $\sigma_{eff}(n)$ the effective stress. The strain $\varepsilon_{c/3}$, at which one third of the compressive strength is reached, is expressed as:

$$\varepsilon_{c/3} = -\frac{1}{3}\frac{f_c}{E} \tag{7.4}$$

The strain ε_c, at which the maximum compressive strength is reached, is expressed as:

$$\varepsilon_c = -\frac{5}{3}\frac{f_c}{E} = 5\ \varepsilon_{c/3} \tag{7.5}$$

The ultimate strain ε_u, at which the material has terminated its softening in compression, which is expressed as:

$$\varepsilon_u = \varepsilon_c - \frac{3}{2}\frac{G_f^c}{h\ f_c} \tag{7.6}$$

where, in turn, G_f^c is the compressive fracture energy and h is the characteristic element length. The parabolic curve strain and stress values are scaled due to the application of lateral compressive stress according to the ratio between the uniaxial compressive strength and the compressive strength calculated using the Hsieh-Ting-Chen curve.

The values of the compressive strength and the peak and maximum strain are modified according to the lateral effective stress in order to simulate the pressure dependent behavior of the mortar in certain directions. This pressure dependence is taken into account for compression in the vertical direction for the bed joints, the horizontal direction for the head joints and the transversal direction for the transversal joints. As in the case for tension, the compressive integrity variable is evaluated in three directions for each component, the lowest value being the eventual isotropic integrity variable.

The expressions of the integrity variables for shear, assuming a Mohr-Coulomb failure criterion and an exponential softening curve based on fracture energy for the cohesion are:

$$S(n) = \begin{cases} 1 & for \quad \left|\tau_{eff}(n)\right| \leq c_0 - \sigma(n)\tan\varphi_0 \\ \frac{-\sigma(n)\tan\varphi(n)+c(n)}{\left|\tau_{eff}(n)\right|} & for \quad \left|\tau_{eff}(n)\right| > c_0 - \sigma(n)\tan\varphi_0 \end{cases} \tag{7.7}$$

where c_0 is the initial cohesion, $c(n)$ is the cohesion in the load step, $tan\varphi(n)$ the tangent of the friction angle, $\sigma(n)$ and $\tau_{eff}(n)$ the applied normal and effective shear stress. The tangent of the friction angle is assumed to develop according to

$$\tan\varphi(n) = \tan\varphi_0 + (\tan\varphi_r - \tan\varphi_0)\frac{c_0 - c(n)}{c_0} \tag{7.8}$$

where $tan\varphi_0$ and $tan\varphi_r$ are the initial and residual tangents of the friction angle. The cohesion softens exponentially according to

$$c(n) = c_0 \exp\left(-\frac{c_0 h}{G_f^{II}}\left(\varepsilon(n) - \frac{c_0 - \sigma(n)\tan\varphi_0}{2G}\right)\right) \tag{7.9}$$

where G is the shear modulus, G_f^{II} the shear fracture energy, h the characteristic length and $\varepsilon(n)$ the total strain.

As in the case for tension, shear failure of the bed joint interface may be taken into account by assigning the shear strength and fracture energy of the interface to the mortar joint components. Otherwise, the initial frictional characteristics for each component may be derived from its uniaxial compressive and tensile strength.

All integrity variables increase monotonically, meaning that damage recovery is impossible. Reduction of the applied strain in a damaged segment results in the integrity variables to stay constant. Therefore, unloading and reloading take place along the damaged stress-strain path.

The characteristic length required by the laws presented here is calculated differently for each damage type. In tension the characteristic length for cracking in a given direction is taken as being equal to the dimension of the cuboid in that direction. The physical interpretation of this assumption is that the width of the crack band is equal to the length of the cuboid, meaning that a single crack is formed along the length of the cuboid. In compression and shear it is calculated as the cubic root of the volume of the cuboid, an approach usually adopted in finite element modeling using solid elements. The physical meaning of the assumption for the characteristic length

is that all of the material in the cuboid yields and is involved in the softening. Representative hardening and softening curves in compression, tension and shear are presented in Figure 7.2.

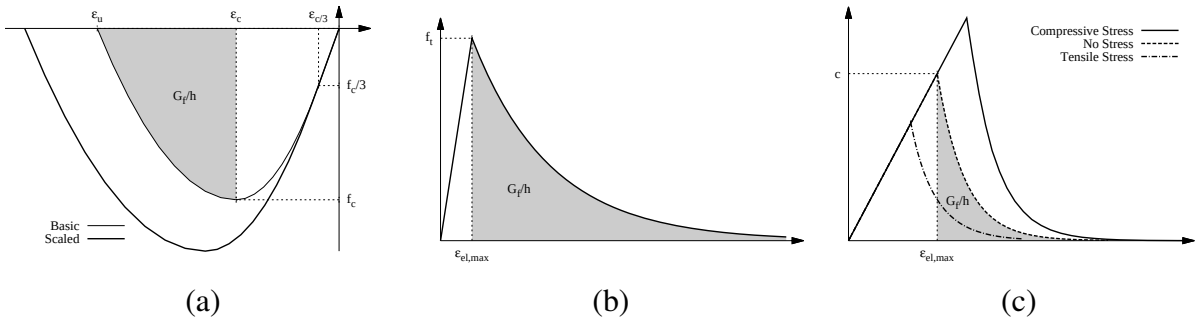

Figure 7.2 Hardening-softening curves for (a) compression: basic and scaled curve for an applied confining stress, (b) tension and (c) shear under varying levels of applied normal stress.

7.2.4 Solution

For linear elastic analysis the solution from which the elastic moduli of the cell are derived can be accomplished in a single analysis step by solving the linear system of equations derived from the stress and strain conformity expressions, as was presented in the previous chapter. The systems need to be solved for the unknown normal stresses, shear stresses (where considered), normal strains and shear strains. To each cuboid correspond three normal stress, three normal strain, one shear stress and one shear strain value for normal stress loading.

Nonlinear elastic analysis requires the modification of these basic systems of equations. Adopting the damage mechanics concepts of damaged and effective (undamaged) stress this can be achieved by the use of integrity variables. The Hooke's law equations remain unchanged, however, since they describe the relation between strain and effective stress.

An isotropic damage concept is adopted, meaning that damage in one direction results in damage and loss of stiffness in all directions. Overall, the actual damaged stress tensor in load step n can be expressed as:

$$\sigma(n) = T(n)\,C(n)\,S(n)\,\sigma_{eff}(n) \tag{7.10}$$

The solution of the system of modified equations is accomplished through the adoption of a multi-variate Newton-Raphson iterative process. As such, the variables in iteration i of each load step are calculated as follows:

$$x^{i+1} = x^{i} - J\left(x^{i}\right)^{-1} F\left(x^{i}\right) \tag{7.11}$$

where x is the vector of variables and J is the Jacobian matrix of the vector of equations. Since the equations are expressed analytically using simple expressions, the Jacobian may also be calculated in closed form. The unknown variables for which the system of equations is solved are the stresses and strains and all the integrity variables for each component. The additional

equations needed to fill out the system of equations are defined as the difference between the integrity variable assumed at the beginning of the iteration and a trial value which is calculated based on the stresses and strains of the component in the iteration. The trial integrity variables are assigned an initial value of 1 at the first iteration of the first load step.

7.3 Results

7.3.1 General Model Behavior

The results produced by the model will be, as a first step, evaluated qualitatively in terms of the behavior in vertical compression and horizontal tension. The preliminary numerical analyses were performed using the material properties and dimensions summarized in Table 7.1. These properties correspond to a masonry composed of strong units, medium strength mortar and low strength, highly deformable infill. The constitutive model for the units was used for the infill as well.

Table 7.1 Material properties and component dimensions for preliminary numerical analysis.

Units	E_u	ν_u	f_{cu}	f_{tu}	
	$[N/mm^2]$	[-]	$[N/mm^2]$	$[N/mm^2]$	
	20000	0.15	50	2.5	
Mortar	E_m	ν_m	f_{cm}	f_m	
	$[N/mm^2]$	[-]	$[N/mm^2]$	$[N/mm^2]$	
	10000	0.15	6	0.6	
Infill	E_i	ν_i	f_{ci}	f_{ti}	
	$[N/mm^2]$	[-]	$[N/mm^2]$	$[N/mm^2]$	
	500	0.2	0.5	0.05	
Interface	f_{tif}	c_0	φ		
	$[N/mm^2]$	$[N/mm^2]$	[-]		
	0.2	0.3	45^0		
Dimensions	l_u	h_u	t_u	l_m, h_m, t_m	t_i
	$[mm]$	$[mm]$	$[mm]$	$[mm]$	$[mm]$
	210	52	100	10	150

Figure 7.3 presents the stress-strain curves obtained by the prism pillar and stack bond, running bond, Flemish bond and three-leaf wall models under horizontal tension and vertical compression. In the horizontal tension case the stack bond wall produced the lowest tensile strength of masonry due to the lack of interlocking between units and mortar. The running and Flemish bond cases produced equal tensile strength of masonry but the latter exhibited a more rapid softening. All stress-strain curves are linear until the peak stress, followed by an exponential softening branch. The softening branch for the three-leaf masonry is divided into two separate branches, as different parts of the masonry yield in tension.

Under vertical compression the prism pillar produced the highest strength, followed closely

by the stack bond and the running bond walls. The softening curve of the running bond wall case was interrupted by an abrupt drop of stress due to tensile damage in the head joint, which has been assigned the properties of the interface. The Flemish bond wall model produced a noticeably lower strength and a steep unloading caused by cracking in the middle of the stretcher unit. The softening curves obtained for the prism pillar, the stack bond wall and the running bond wall are generally characterized by a linear initial part, followed by a parabolic part until after the peak load and followed by a final exponential softening part. Overall, the model is able to produce realistic response curves for both applied tension and compression.

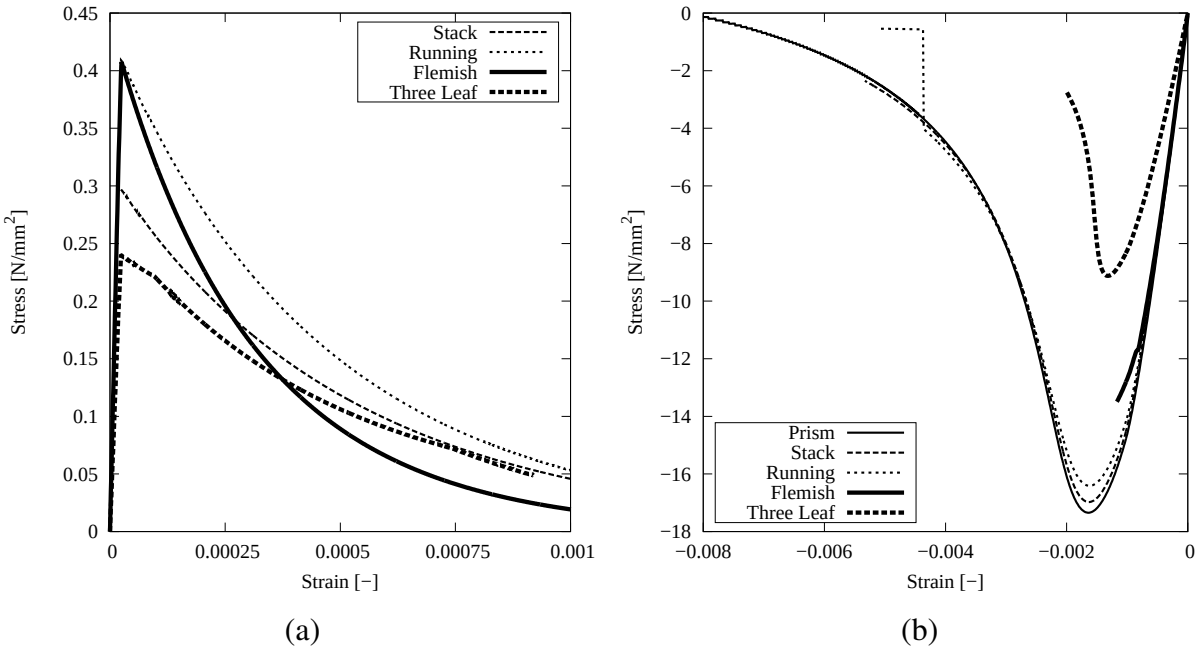

(a) (b)

Figure 7.3 Stress strain curves for two types of loading: (a) horizontal tension and (b) vertical compression.

The progression of damage in a Flemish bond wall cell under vertical loading is presented in Figure 7.4. According to the predictions of the model compressive damage progresses nearly steadily in the cross joint and the bed from near the beginning of the loading. The compressive damage in the bed joint increases rapidly near the peak load. Compressive damage is also registered in the head and transversal joint, though not for low values of vertical stress: due to the lower Young's modulus of the mortar, these joints are less stressed than the neighboring unit cuboids. Tensile damage appears in the last quarter of the loading before the peak and increases rapidly thereafter. This type of damage is registered in the mid part of the stretcher unit in the horizontal direction and in the transversal mortar joints in the transversal direction, the direction in which the interface properties have been assigned. Unlike the running bond wall case, tensile failure in the head joint was not registered.

The progression of normal stresses in the outer and inner masonry leaves will be examined for the three-leaf masonry case. The stresses presented here have been averaged across the components comprising the inner and outer leaf respectively in order to present a global comparison of the stress state between the leaves. It should be noted, in any case, that the average stress in the outer leaf closely approximates that of its units since the volume of masonry accounted for

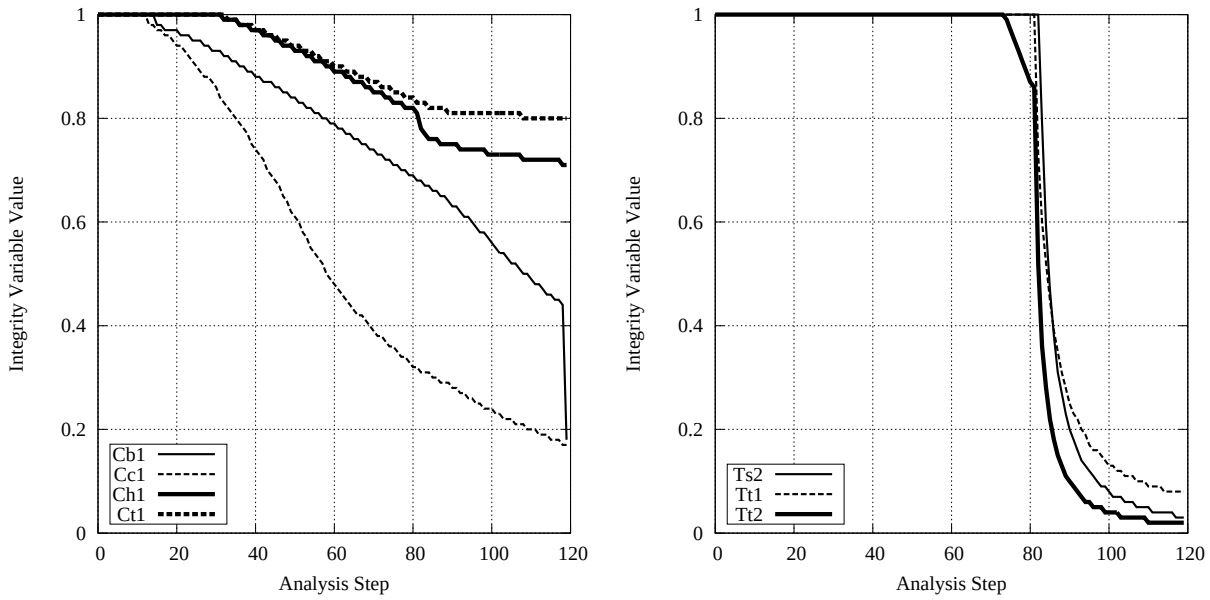

Figure 7.4 Damage progression curves for Flemish bond wall model under vertical compression. (a) Compressive damage: $b1$ stands for a bed joint, $c1$ for a cross joint, $h1$ for a head joint and $t1$ for a transversal joint cuboid. (b) Tensile damage: $s2$ stands for a stretcher unit, and $t1$ and $t2$ for two separate transversal joint cuboids.

by the mortar in the joints is very small. As shown in Figure 7.5, the outer leaf is in horizontal tension when the wall is subjected to vertical compression and the inner leaf is under horizontal compression. Both leaves are under vertical compression. However, given the difference in their Young's modulus, the vertical compressive stresses in the inner leaf are much lower than the ones in the outer leaf. The stress in the outer leaf reaches nearly the compressive capacity of the running bond wall, which may be seen in Figure 7.3, but fails to do so before the compressive yielding of the inner leaf when the vertical stress to which it is subjected reaches its compressive strength.

In all the models tested here the dominating failure type for applied horizontal tension is that of the head joint interface, which constitutes the weakest plane of weakness in this direction. In vertical compression, the response is governed by the compressive yielding of the bed joint mortar, which is in a state of triaxial compression for the properties here chosen.

Finally, the stack bond pillar and the running bond wall models are tested against the experimental case study presented in the chapter on the modeling of masonry shear walls. The models were used for predicting the compressive strength of masonry of vertically loaded stack prisms and horizontally and vertically loaded running bond wallettes. Additionally, the effect of the unit/mortar nonlinearities was again investigated.

As shown in the results presented in Table 7.2, the micro-mechanical models are able to produce results in good agreement with the experimental findings, with the exception of the stack prism, where the model slightly underestimates the compressive strength of masonry. As a second note, the effect of the interface nonlinearities in the vertical compressive strength is

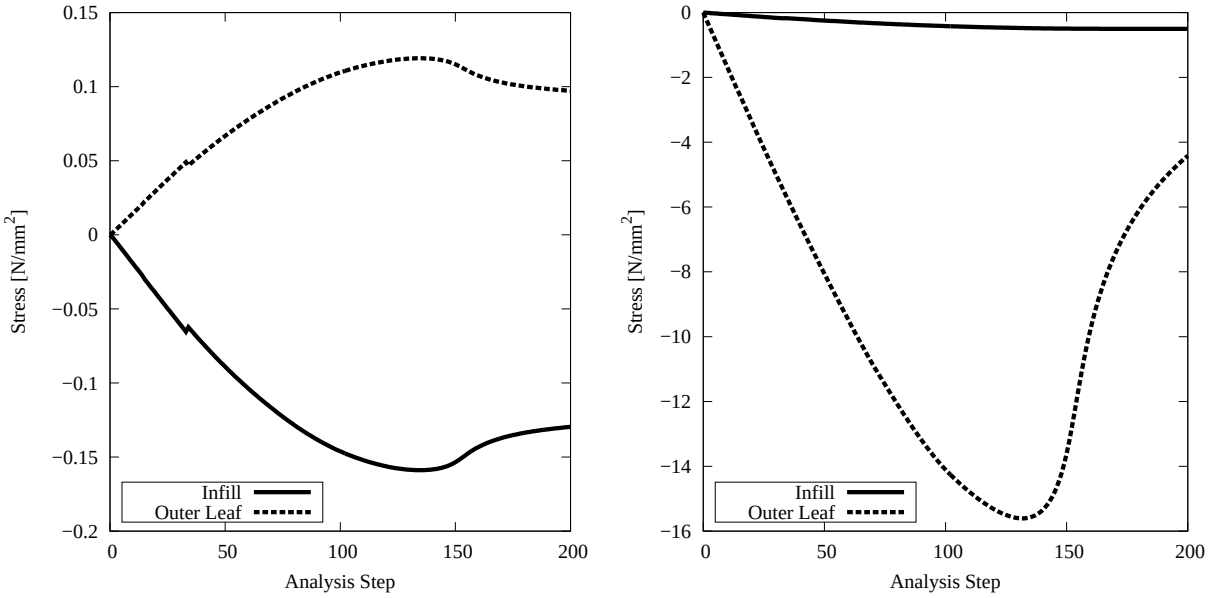

Figure 7.5 Progression of stresses in components of three-leaf wall model under vertical compression: (a) horizontal stress and (b) vertical stress.

Table 7.2 Micro-mechanical model results for the strength and elasticity of masonry wallettes and prisms subjected to compressive loads.

Model	$f_{c,x}$	$E_{c,x}$	$f_{c,y}$	$E_{c,y}$
	$[N/mm^2]$			
Prism	-	-	16.08	3928
Wallette Meso-Model	15.56	3923	15.68	3969
Wallette Micro-Model	14.94	3923	15.62	3969

negligible, while they produce a 4% drop in the predicted compressive strength of masonry in the horizontal direction. Overall, the influence of the nonlinearities of the interfaces on the compressive strength of masonry appears to be low.

7.3.2 Case Studies

A number of experimental case studies were assembled from the relevant literature on masonry under vertical compression. These cases were numerically reproduced using the proposed models in order to predict the compressive strength of masonry. For the sake of comparison, these cases were also simulated using FE models of the full structures. The first eight columns of Table 7.3 summarize the results. The final two columns concern results derived in Section 5 of this chapter. The case studies follow the same naming convention as the one used in the chapter of finite element modeling of masonry under compression.

In Figure 7.6 a comparison is made between the vertical compressive strength as predicted by the FEM and micro-mechanical methods and the one obtained in the experimental case studies.

Table 7.3 Case studies of masonry under vertical compression: comparison between experimental, FEM, closed form, empirical and micro-mechanical model results. The coefficient of determination with the experimental results is also presented.

Case	Ref.	$f_{c,exp}$	$f_{c,Ohler}$	$f_{c,Hilsdorf}$	$f_{c,CEN}$	$f_{c,FEM}$	$f_{c,mm}$	$f_{c,ClosedForm}$	$f_{c,Semi-empirical}$
					$[N/mm^2]$				
S1	[106]	19.70	17.63	24.54	12.22	19.44	18.50	18.98	16.07
S4	[159]	6.15	6.44	8.03	4.01	6.83	3.75	6.91	5.94
S8	[137]	4.68	6.50	7.79	4.50	5.44	6.40	5.08	6.25
S11	[159]	6.32	6.94	8.56	4.01	7.35	3.75	6.98	6.02
S12	[159]	5.01	5.47	6.83	4.01	6.21	3.50	6.67	5.71
S13	[8]	14.55	11.78	11.89	6.11	13.26	13.80	12.62	9.20
S14	[64]	4.50	7.12	10.96	6.34	3.14	10.20	10.34	5.41
S16	[137]	8.84	8.84	9.96	4.50	6.91	6.50	5.13	6.60
S17	[156]	11.73	10.31	15.88	13.06	13.77	8.50	14.90	9.94
S18	[106]	34.70	28.46	30.59	17.62	36.75	34.00	21.00	23.90
S20	[106]	48.20	43.50	43.23	24.32	50.59	45.00	31.10	31.93
S22	[106]	40.90	35.50	39.48	21.61	44.14	42.00	32.52	31.38
S24	[64]	9.33	10.08	15.33	6.34	5.74	10.20	10.42	5.52
S25	[106]	27.00	24.37	28.22	15.99	31.32	29.50	18.64	23.29
S27	[106]	32.50	30.56	37.33	19.62	37.12	37.50	30.16	29.00
S28	[106]	37.70	40.74	34.72	19.83	43.16	35.50	31.10	31.10
S31	[106]	29.90	23.65	33.99	14.99	21.12	24.00	21.77	17.71
R9	[131]	30.14	39.08	47.12	18.87	37.81	25.30	42.27	26.86
F1	[25]	11.00	15.77	20.24	7.10	4.29	4.40	4.24	8.70
F2	[25]	14.50	20.06	21.93	10.74	16.70	16.00	12.70	14.53
F3	[25]	17.80	-	36.58	19.64	29.58	29.00	26.90	26.90
P7	[64]	5.55	10.08	15.33	6.34	9.12	9.84	10.42	4.19
	R^2		0.916	0.912	0.385	0.884	0.906	0.842	0.860

The two numerical methods appear to produce equally good results compared to the experimental values for a wide range of cases. The micro-mechanical model is able to achieve a coefficient of determination with the experimental results of 0.906, which is slightly higher than the 0.884 achieved by the FEM approach. The inability of the otherwise accurate Ohler model to produce results for masonry composed of mortars with a higher compressive strength than the units is noted.

Additionally, the in-plane failure envelope of a running bond periodic unit cell subjected to bilinear stress was produced. Existing biaxial experimental tests on masonry walls for the derivation of the biaxial strength envelopes of the composite are scarce and are not accompanied by sufficient material characterization [120]. The original case study does not include a sufficient characterization of the mechanical properties of the materials. For this reason, the material properties used in a relevant work simulating the same experimental campaign were used instead [33]. The obtained failure envelope and its comparison to the experimental envelope is shown in Figure 7.7. The model overall produces an adequate curve, which approximates well the behavior of the masonry in biaxial tension and vertical compression, but tends to overestimate to a degree the horizontal compressive strength. This could be attributable to inadequate compaction of the mortar in the head joints.

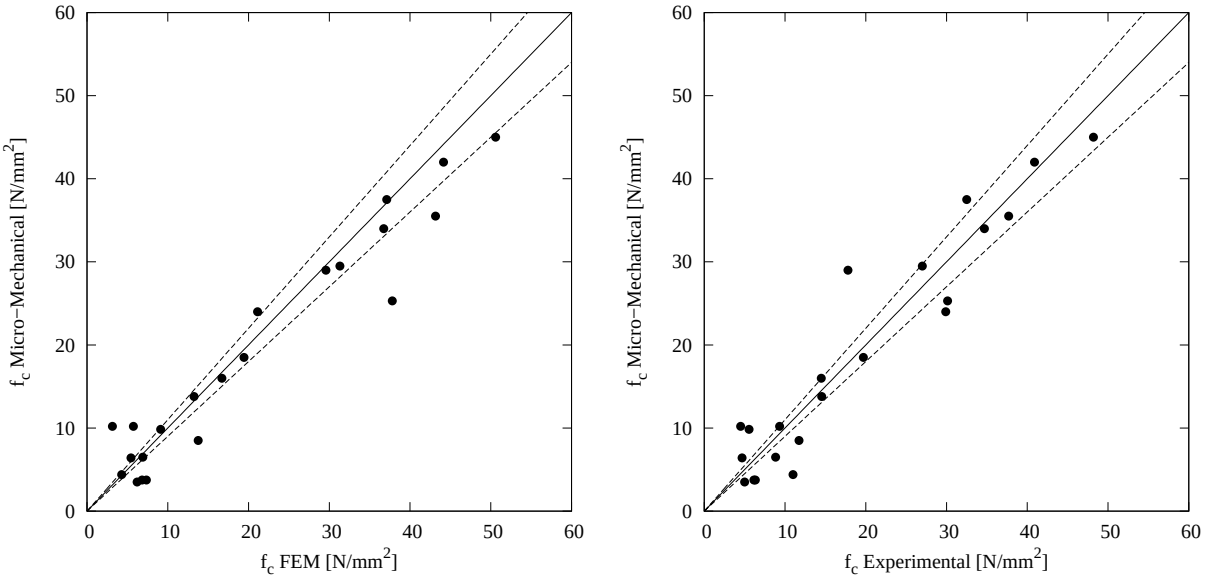

(a) (b)

Figure 7.6 Comparison of vertical compressive strength according to (a) FEM and micro-mechanical results and (b) experimental and micro-mechanical results. Dashed lines indicate 10% difference.

7.4 Parametric Investigation

7.4.1 Overview

A wide parametric investigation was performed, the low computational cost of the method allowing for a very large number of analyses to be performed in a short time. The objective of the investigation was to determine the sensitivity of the predicted vertical compressive strength of masonry, as predicted by the micro-mechanical model, to various material properties and component dimensions. The parameters taken into account for the analyses are summarized in Table 7.4, and represent a very wide, but not unlikely, range of combinations [55]. In total 62208 combinations of material properties and dimensions were considered and were analyzed using the simple stack bond pillar model.

Table 7.4 Material properties and dimensions for nonlinear elastic parametric analysis. "Standard" values in bold.

f_{cu} $[N/mm^2]$	E_u/f_{cu} [-]	ν_u [-]	f_{tu}/f_{cu} [-]	f_{cm} $[N/mm^2]$	E_m/f_{cm} [-]	ν_m [-]	l_u $[mm]$	h_u $[mm]$	t_u $[mm]$	h_m $[mm]$
12.5, 25, 50	75, 150, **300**, 1000	0.05, 0.10, **0.15**	0.01, 0.05, **0.10**, 0.20	1, 5, 10	150, 350, **700**, 1500	0.15, **0.20**, 0.25, 0.30	210	30, **52**, 70	100	5, **10**, 20

Concerning these material properties, the E_u/f_{cu} ratio of 300, f_{tu}/f_{cu} of 0.10, E_m/f_{cm} of 700 are considered "standard values" as are ν_u of 0.15, ν_m of 0.2, h_u of $52mm$ and h_m of $10mm$. The numerical parameters for the Hsieh-Ting-Chen failure curve presented in equation 7.12 are

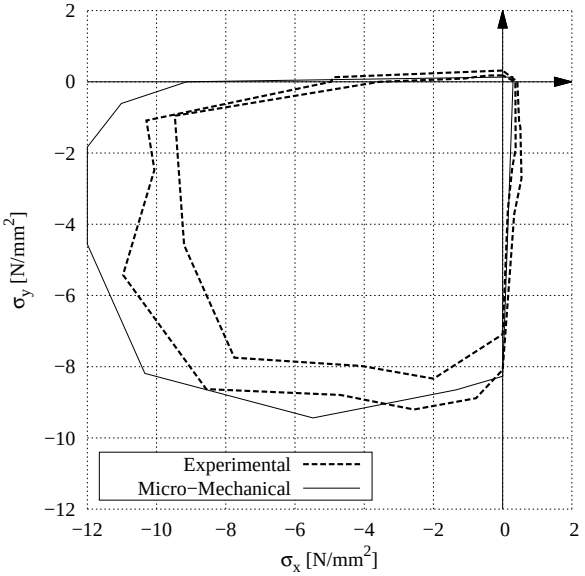

Figure 7.7 In-plane failure envelope for masonry periodic unit cell: comparison of micro-mechanical results with experimental envelope.

also considered "standard"

In addition to the material properties, the influence of the adopted failure surfaces was investigated as well. Two cases were considered for the failure criterion of the units and the mortar alike. For the units the two failure curves presented in Figure 7.1b were used. In the Rankine criterion no interaction is assumed to take place between the applied compressive stress on the unit and the lateral tensile stresses that arise due to unit/mortar interaction. When the Mohr-Coulomb criterion is adopted, the developed tensile stresses reduce the capacity of the unit in compression. The two criteria as implemented in the model are identical in the tension-tension and compression-compression range.

For the mortar the influence of the assumed biaxial and triaxial behavior of the material was investigated. Initially, the standard values proposed in [77] were used, these being the values shown in equation 7.12. These values are obtained by assuming a tensile strength equal to 10% of the compressive strength, a biaxial strength equal to 1.15 times the uniaxial compressive strength and a compressive strength equal to 4.2 times the uniaxial compressive strength under a biaxial confinement equal to 0.8 times the uniaxial strength.

$$f = 2.0108\frac{J_2}{f_c^2} + 0.9714\frac{\sqrt{J_2}}{f_c} + 9.1412\frac{\sigma_1}{f_c} + 0.2312\frac{I_1}{f_c} - 1 = 0 \tag{7.12}$$

A second case with a biaxial strength increase of 10% was assumed, maintaining the same triaxial strength. In that case the derived numerical parameters are shown in equation 7.13. The numerical parameters have not changed substantially by altering the biaxial strength alone.

$$f = 1.9862\frac{J_2}{f_c^2} + 0.8575\frac{\sqrt{J_2}}{f_c} + 9.2816\frac{\sigma_1}{f_c} + 0.1571\frac{I_1}{f_c} - 1 = 0 \tag{7.13}$$

Finally, a case with a compressive strength of 2.6 times the uniaxial strength under a bilateral compression equal to 0.8 times the uniaxial compressive strength was considered. The behavior of masonry under compression is particularly sensitive to the triaxial compressive behavior of the mortar and the behavior of the units under tension. Therefore it was considered desirable to investigate the influence of the adopted material laws on the predicted compressive strength. The numerical parameters derived from these assumptions on the triaxial strength are shown in equation 7.14. Adjusting the triaxial strength of the material has greatly changed the numerical parameters, especially the parameter linked to the J_2 stress invariant and its square root.

$$f = 9.8064\frac{J_2}{f_c^2} - 2.8545\frac{\sqrt{J_2}}{f_c} + 10.7004\frac{\sigma_1}{f_c} + 0.6208\frac{I_1}{f_c} - 1 = 0 \tag{7.14}$$

7.4.2 Results

The large number of results produced by the parametric investigation makes their complete presentation unwieldy. Certain aspects of the parametric investigation results will be presented in a general fashion, while others will be discussed more in-depth.

Assuming the Mohr-Coulomb criterion for the unit failure criterion moderately influenced the results. On average the predicted value for the Mohr-Coulomb curve was 93% that of the Rankine curve, the minimum value being 53% and the maximum being 100%, or equal to the original value.

Decreasing the biaxial strength of the mortar produces results identical to those of the standard case. Given the fact that the failure surface is three-dimensional, this observation is rational.

The change in the triaxial strength results in very noticeable differences in the predicted compressive strength. On average, for a lower triaxial strength the predicted compressive strength of masonry was 60% that of the standard value, with the minimum value being 17% and the maximum being 100%. The influence of the triaxial behavior of the material is therefore shown to be the decisive factor for compression perpendicular to the bed joint as far as the modeling of the behavior of the mortar is concerned.

The results of the model appear to be insensitive to the biaxial strength of the mortar and heavily dependent on its behavior under triaxial compressive strength. This observation raises questions concerning the adequacy of simple biaxial tests on mortars for the full characterization in their behavior in masonry, given its trivial role in the compressive strength of the composite. Triaxial tests appear to be far more relevant.

The results obtained from the analysis using the standard triaxial behavior of mortar and Mohr-Coulomb failure surface for the units were compared to the predictions of the compressive strength of masonry given by a modern masonry design code, the EC6 [40], and two closed form expressions proposed by Ohler [117] and Hilsdorf [74]. The first expression depends only on the compressive strength of the two material components (equation 4.3). The two latter equations additionally depend on the tensile strength of the unit and the height of the unit and of the mortar joint. The Ohler expression reads

$$f_c = f_{cm} + \frac{s f_{cu} - f_{cm}}{1 + \frac{t}{m}\frac{h_m f_{cu}}{h_u f_{tu}}} \tag{7.15}$$

where s and t are parameters describing the failure envelope of the unit and with m being the slope of the failure criterion adopted for the mortar. These parameters are defined according to the specifications presented in Table 7.5. According to the formulation of the model, three values for the compressive strength are calculated and a value is chosen among the three based on its relation to the compressive strength of the unit. Furthermore, it is shown that the model cannot account for masonry composites built using mortars with a compressive strength higher than that of the unit.

Table 7.5 Determination of the s, t and m numerical parameters for Ohler's model.

	$0 < f_c/f_{cu} < 0.33$	$0.33 < f_c/f_{cu} < 0.67$	$0.67 < f_c/f_{cu} < 1.0$	
s	0.662	0.811	1.000	
t	0.662	0.960	2.218	
f_{cm} $[N/mm^2]$	31.6	21.4	15.4	6.4
m	5.3	3.6	2.4	2.1

The Hilsdorf expression reads:

$$f_c = \frac{f_{tu} + \alpha f_{cm}}{f_{tu} + \alpha f_{cu}} \frac{f_{cu}}{U} \tag{7.16}$$

where

$$\alpha = \frac{h_m}{4.1 h_u} \tag{7.17}$$

and U is a safety factor taken as equal to 1.1.

Other closed form expressions have been proposed which are also functions of the elastic properties of the constituent materials but which give divergent solutions for some of the material combinations considered in this study [63, 70, 73].

The comparison is presented in Figure 7.8 in the form of a cumulative frequency distribution graph, the number of individual points being too numerous to illustrate. The graph depicts the distribution of ratios between the micro-mechanical model result and the closed form expressions. All three closed form expressions may give results as much as ten times higher than the micro-mechanical result. In turn, the micro-mechanical model can produce values almost twice as much as the Ohler and Hilsdorf models and more than four times the value given by the EC6 equation. Overall, for the parameters and dimensions considered in this study, the micro-mechanical model of the stack bond prism produces results higher than the closed form expressions more often than it produces lower.

The study of the influence of the material properties of the materials warrants a closer examination. While the number of parameters investigated is prohibitive for a complete overview of the results in the context of this work, the sensitivity of the result to a number of individual

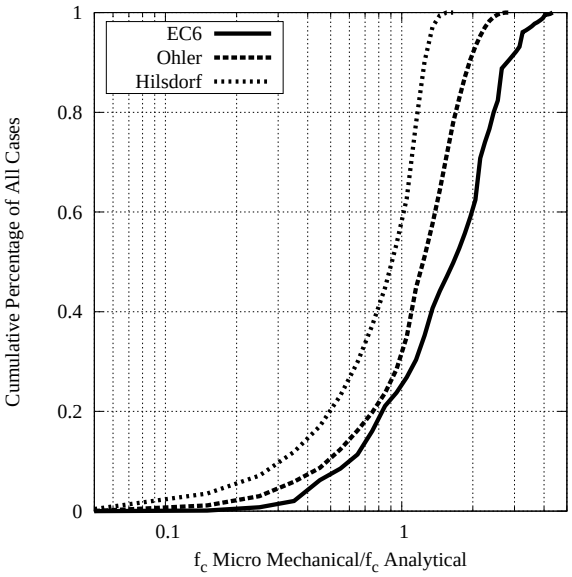

Figure 7.8 Comparison of micro-mechanical results with design code and closed form expression results: cumulative frequency distribution of analytical to micro-mechanical result ratio.

parameters may be easily studied. This sensitivity is investigated by altering a single parameter and keeping the remaining parameters fixed to the already mentioned standard values. Figure 7.9 graphically illustrates the influence of three material properties on the predicted compressive strength of masonry. According to the obtained results, an increase in the Poisson's ratio of mortar can dramatically increase the compressive strength of masonry composed of weak mortar while it may decrease it in the case of strong mortars. An increase of the Young's modulus of the units always results in an increase in the predicted masonry compressive strength. Finally, There appears to be little difference in the predicted compressive strength for units with a tensile higher than 10% their compressive strength, while a moderate decrease is observed for units with a tensile strength equal to 5% their tensile strength.

While understanding the influence of the tensile strength of the units on the compressive strength of masonry is straightforward, a few clarifying comments on the effect of the elastic properties of the materials on the compressive strength of masonry may be necessary, especially given that the closed form expressions used for comparison do not take them into account. The influence of the Poisson's ratio of the mortar on the compressive strength of masonry is logical in the sense that a higher ratio results in an increased tendency of the mortar to laterally expand when subjected to vertical loads. The increased tendency results, in turn, to a higher lateral confinement by the unit. Excessive expansion, however, may lead to premature cracking of the brick and result in a decrease in the compressive strength of masonry, especially in the case of weak units. This effect is illustrated in the discrepancies between Figures 7.9a and 7.9b. The effect of the Young's modulus of the units can be explained along the same lines: a higher value results in smaller lateral deformation of the units and, therefore, an increase in the lateral confinement on the mortar.

The apparent bias of the micro-mechanical model to produce results higher than the Ohler or the EC6 model for the majority of the cases may be explained in light of the influence of the

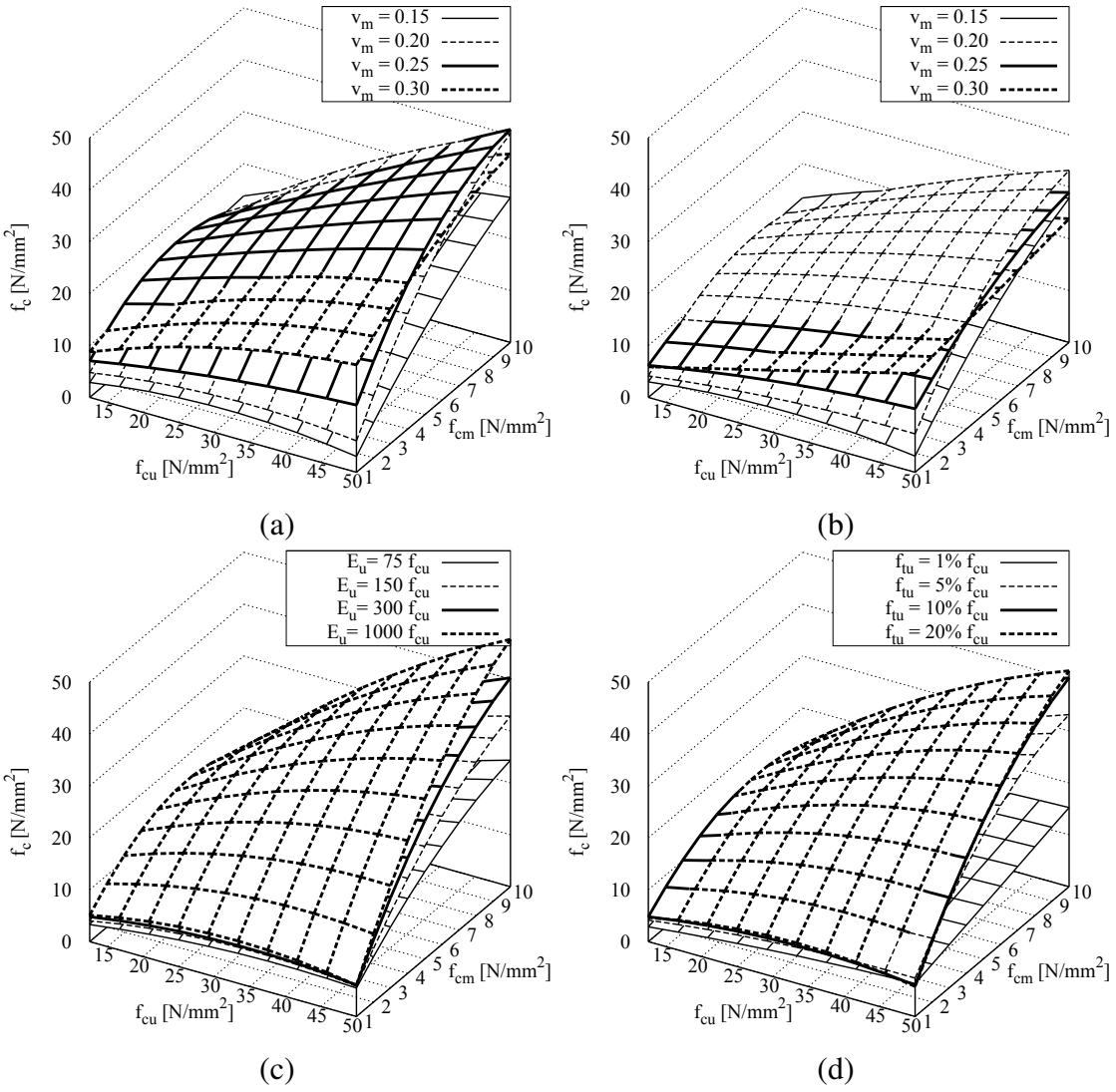

Figure 7.9 Influence of material properties on the compressive strength of masonry: (a) Poisson's ratio of mortar for $f_{tu} = 10\% f_{cu}$, (5) Poisson's ratio of mortar for $f_{tu} = 5\% f_{cu}$, (c) Young's modulus of units and (d) tensile strength of units.

Poisson's ratio of the mortar on the result. For the parametric investigation the values assigned to this parameter generally moved above the average noted for masonry mortars. While mortars may indeed be characterized by lower Poisson's ratios in the linear elastic range, much higher and rapidly increasing values are registered early in the nonlinear range or even before the onset of any noticeable softening in the response of the mortar in compression [106, 114]. Therefore, it was considered appropriate to investigate the effect of this material parameter above the usual range.

7.5 Closed Form Expression

7.5.1 Derivation of the Expression

A new closed form expression taking into account geometrical dimensions, elastic and inelastic properties of the constituent materials is proposed based on the micro-mechanical models examined and the material constitutive laws adopted for analysis. The simple stress distribution obtained from the stack bond pillar model is used for the analysis and a linear response of the materials is assumed until failure. The Mohr-Coulomb failure surface is adopted for the units and the Hsieh-Ting-Chen failure surface is adopted for the mortar. The closed form expression is developed for masonry under compression perpendicular to the bed joint and does not include the influence of head or transversal joints.

The closed form expression serves to create a model for the prediction of the compressive strength of masonry taking into account the interaction of the failure modes most common in masonry under compression but without requiring any computational resources. This expression, while based on simple algebraic equations, takes into account the geometrical and elastic properties of the masonry components and quantifies the unit/mortar interaction in masonry under compression. The range of activated failure modes in the components depends on this quantification.

Four types of failure are identified: failure of the unit in compression (UC), failure of the unit in combined compression/tension (UCT), failure of the mortar in multi-axial compression (MC) and failure of the mortar in combined compression/tension (MCT).

The mortar fails under multi-axial compression (mode MC) when the Hsieh-Ting-Chen criterion, as presented in equation 7.12, is satisfied. It is assumed that for mortar joints under combined compression/tension (MCT) the joint fails for a vertical compression equal to the uniaxial compressive strength of mortar.

According to the stack bond pillar model, the stresses in the components can be analyzed into a vertical stress, equal in the unit and the mortar, the horizontal stress in the mortar and the horizontal stress in the unit. The transversal stresses are equal to the horizontal stresses in either component. The ratio of vertical to horizontal stress in the mortar may be expressed as

$$s_{b1} = \sigma_{m,x}/\sigma_y = \sigma_{m,z}/\sigma_y = \frac{h_u\left(E_m v_u - E_u v_m\right)}{E_u h_u\left(v_m - 1\right) + E_m h_m\left(v_u - 1\right)} \tag{7.18}$$

while in the units as

$$s_{u1} = \sigma_{u,x}/\sigma_y = \sigma_{u,z}/\sigma_y = \frac{h_m\left(E_u v_m - E_m v_u\right)}{E_u h_u\left(v_m - 1\right) + E_m h_m\left(v_u - 1\right)} = -s_{b1}\frac{h_m}{h_u} \tag{7.19}$$

These two parameters depend on the elastic and geometric characteristics of the two materials. When s_{b1} is positive, meaning that simultaneously s_{u1} is negative, the mortar is under triaxial compression and the unit is under vertical compression and horizontal and transversal tension when the masonry is subjected to vertical compression. The higher the value is from

1 the more significant the mismatch of the elastic properties and, therefore, the confining compressive stress on the mortar. In the case of the existence of confining stresses in the mortar, substituting s_{b1} in the Hsieh-Ting-Chen equation a rational function of σ_y is obtained whose root is the vertical compression stress causing MC failure. Further dividing the function by the uniaxial compressive strength of mortar allows for the failure criterion to be expressed in a dimensionless manner.

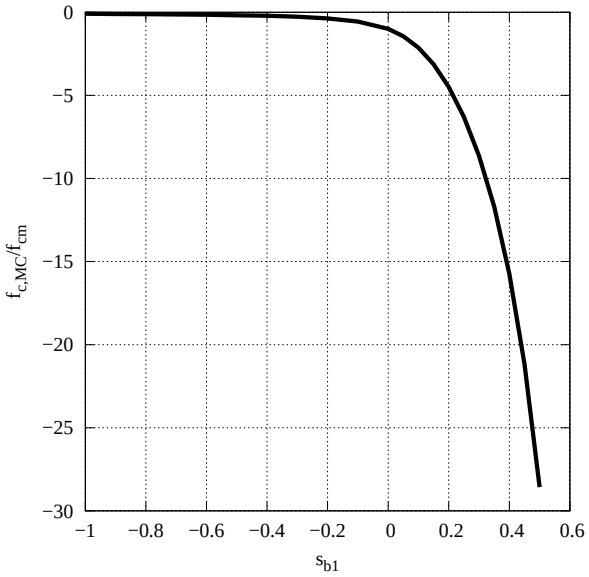

Figure 7.10 Relation between s_{b1} parameter and normalized strength for failure mode MC.

For the standard values of the Hsieh-Ting-Chen criterion the root of the rational function normalized by division with the compressive strength of mortar is plotted in Figure 7.10. For s_{b1} equal to 0 the horizontal and transversal stresses are 0 and the compressive strength of the failure mode is equal to the compressive strength of mortar: the ordinate of the graph is equal to -1. The part of the function with positive abscissae may be approximated nearly perfectly through nonlinear regression analysis by the third order polynomial

$$f_{c,MC}/f_{cm} = -228.83 \times {s_{b1}}^3 + 34.20 \times {s_{b1}}^2 - 14.51 \times s_{b1} - 1 \tag{7.20}$$

thus allowing for a closed form expression of the failure stress of mortar, which here is a negative value, under confinement to be obtained. It is not considered necessary to approximate the part of the graph with negative abscissae since the triaxial behavior of mortar is not critical for that range of values. The numerical parameters of the polynomial depend on the numerical parameters of the Hsieh-Ting-Chen criterion.

Failure mode UC is obtained when the vertical compressive stress equals the compressive strength of the unit:

$$f_{c,UC} = -f_{cu} \tag{7.21}$$

Failure mode UCT is obtained when

$$-\frac{f_{c,UCT}}{f_{cu}}+\frac{\sigma_{u,x}}{f_{tu}}=1 \tag{7.22}$$

Substituting s_{b1} in this equation and solving for the vertical failure stress one obtains

$$f_{c,UCT}=\frac{-1}{\frac{1}{f_{cu}}+\frac{s_{b1}h_m}{f_{tu}h_u}} \tag{7.23}$$

For negative values of s_{b1} the unit is under triaxial compression and the mortar under vertical compression and horizontal and transversal tension when the masonry is subjected to a vertical compressive load. This corresponds to masonries composed of very stiff and strong mortar. In this case the tensile failure of the mortar is disregarded, as is the triaxial behavior of brick, and the failure of the masonry is governed by the crushing of the weaker of the two materials in compression.

Summing up the failure modes, it may be stated that the (negative) compressive strength of masonry is equal to

$$f_c=\begin{cases}\max\left(-f_{cm},-f_{cu}\right) & for \quad s_{b1}\leq 0\\ \max\left(f_{c,MC},-f_{cu},f_{c,UCT}\right) & for \quad s_{b1}\geq 0\end{cases} \tag{7.24}$$

In summary, the model quantifies the mismatch of elastic properties between the units and the mortar through the calculation of s_{b1}. The failure mode activated depends on whether this value is positive. For negative values, the unit is in triaxial confinement. It is assumed that the mortar in the joint is not affected by lateral tension. For $s_{b1}=0$ (no lateral stresses arise in the mortar and the unit) the two branches of the piecewise equation converge. For $s_{b1}\leq 0$ the masonry fails due to uniaxial failure of either the mortar or the units, whichever has the lowest compressive strength. For $s_{b1}>0$ the mortar is in triaxial compression and the unit in uniaxial compression and bilateral tension. In this case the masonry will fail either due to crushing of the mortar, crushing of the unit or cracking of the unit.

7.5.2 Derivation of a Semi-Empirical Expression

The closed form analytical expression may be turned into a semi-empirical expression, in which the only parameters considered are the compressive strength of the units and the mortar and the height of the unit and mortar layers. In order to reach this semi-empirical expression the tensile strength of the units and the elastic properties of the units and the mortar are given representative values. These values have been estimated according to the review of the large number of case studies presented in chapter 3 and are presented in Table 7.6.

In the absence of detailed material characterization, the semi-empirical expression attempts to supply the same results as the closed form expression developed in this chapter (or other similar expressions from the literature) but relying only on the compressive strength of the components and their geometry. The theoretical background behind the closed form expression and the semi-empirical expression is identical.

Table 7.6 General material parameters adopted for semi-empirical model for the prediction of the compressive strength of masonry.

E_u	ν_u	f_{tu}	E_m	ν_m
$300 \times f_{cu}$	0.15	$0.10 \times f_{cu}$	$700 \times f_{cm}$	0.20

7.5.3 Results

The results obtained from the closed form expression and the semi-empirical model are shown in absolute values at the last two columns of Table 7.3. A coefficient of determination of 0.842 between the closed form analytical and experimental values is achieved. The coefficient of determination is increased to 0.860 for the semi-empirical expression. No general tendency to under- or overestimate the compressive strength was noted throughout the series of experimental results. The results of both the closed form analytical and the semi empirical model are illustrated in Figure 7.11a, as compared to the experimental results. Additionally, Figure 7.12 illustrates the comparison of the closed form and semi-empirical expression to the micro-mechanical model for the parametric investigation cases using again a cumulative curve.

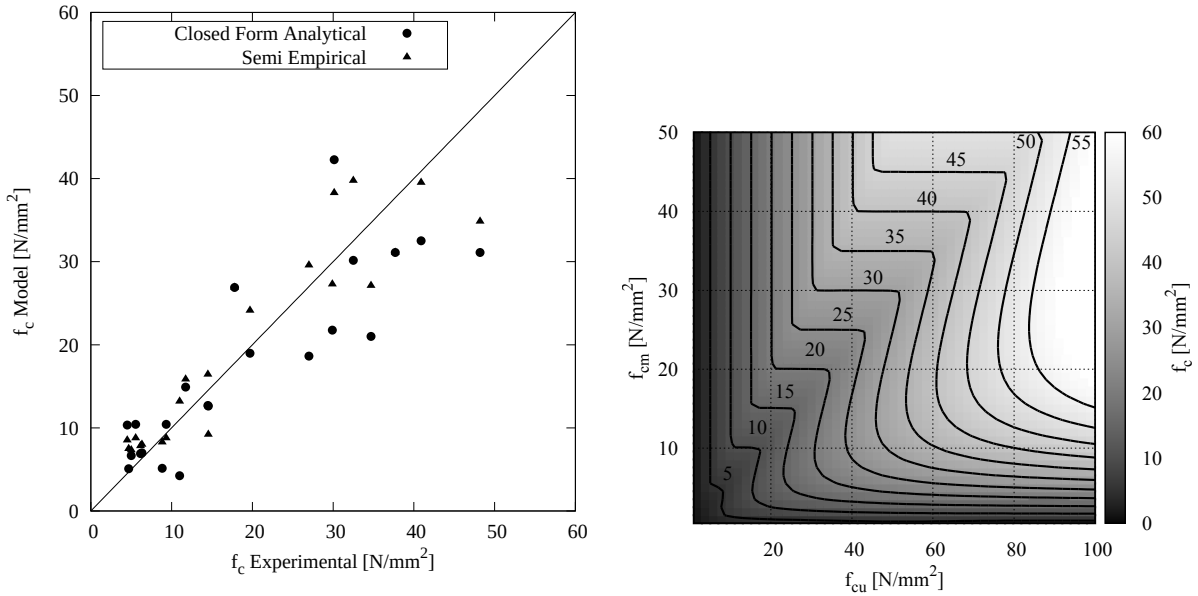

(a) (b)

Figure 7.11 (a) Comparison of closed form analytical and semi empirical models for the prediction of the compressive strength of masonry with experimental results. (b) Contour plot of semi-empirical expression results as a function of the compressive strength of the units and the mortar.

Figure 7.11b presents a contour plot of the results obtained from the semi-empirical expression for a wide range of combinations of units and mortars of varying strengths. The compressive strength iso-lines illustrate the interaction of the failure modes in masonry under compression. The complexity of the contours does not allow for a simple regression model to approximate well the obtained curve. Direct application of the equation 7.24 is preferable.

The correlation between the closed form and the semi-empirical model is good, as is their

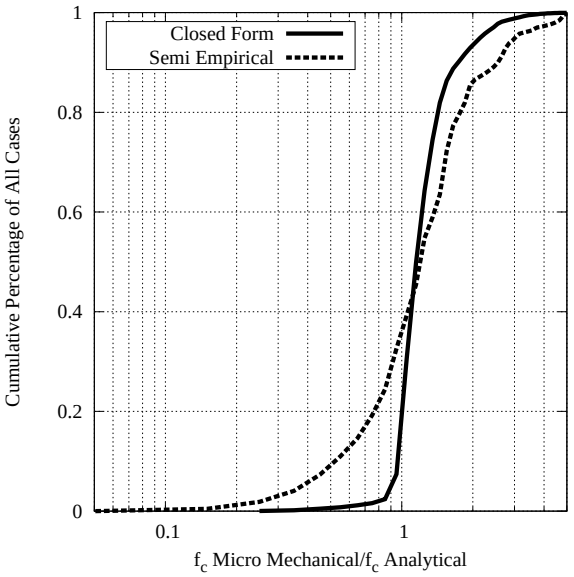

Figure 7.12 Comparison of micro-mechanical results with closed form expression and semi-empirical model results: cumulative frequency distribution of micro-mechanical to analytical model result ratio.

correlation with the experimental results here investigated. The derived semi-empirical model, while not as accurate as other similar proposed models, such as [117], is more inclusive in terms of application scope and is more straightforward in its application.

Neither of the two proposed models produces diverging values, regardless of the combination of material properties. The adequacy of these models may also be evaluated through a comparison with the micro-mechanical model results using the parametric result database as a benchmark. Comparing, again the results obtained using cumulative curves, it is shown that the closed form expression is able to produce good results, with large over- and underestimations accounting for a small percentage of the results. The semi-empirical expression is less accurate in that regard, but it is comparable to the Ohler model.

7.6 Conclusions

A series of masonry models based on the analysis of periodic unit cells has been developed and used for the prediction of the tensile and compressive strength of masonry using micro-modeling techniques. The cells are analyzed according to closed form expressions for the determination of the stress distribution in the cell coupled with an iterative nonlinear solution method for the implementation of damage laws in the analysis.

The models are capable of making good predictions of the compressive strength of various types of masonry pillar and wall structures. Several of the typologies investigated have received very little attention in the existing literature. The computational cost for these analyses is very low, thus forming the basis for the extension of the application of these models to two-scale analysis of large masonry members.

The parametric study conducted using these models has revealed a dependence of the compressive strength of masonry to material parameters usually not taken into account in structural design and often ignored in the mechanical characterization of masonry composites and materials, such as the Poisson's ratio of the mortar. Furthermore, the study of the three-dimensional pressure-dependent behavior of the mortar, as opposed to merely its biaxial strength, appears to be crucial for its use in computational modeling of masonry.

Two closed form expressions for the prediction of the compressive strength of masonry are proposed, based on the aforementioned micro-mechanical models: a closed form adaptation of an micro-mechanical model fully based on detailed micro-modeling and a semi-empirical adaptation relying on the compressive strength of the units and the mortar and their height in the composite. Both approaches produce adequate results.

Chapter 8

Mechanical Characterization and Modeling of a Masonry Pillar

8.1 Introduction

Compression tests on masonry pillars, especially ones extracted from historical structures, are quite rare, but a number of them can be encountered in the existing literature, even if they deal with reproductions of historical building pillars [6, 7, 14, 17, 151, 158]. The opportunity to perform such a test on an original pillar arose during investigation and restoration of a building in the Hospital Sant Pau complex in Barcelona. This particular test, as well as a number of other material tests which have been performed in parallel, is aimed towards investigating the global structural behavior of the pillar and the properties of its constituent materials. The outcome of these tests are of special importance in addressing the concerns of structural designers involved in the intervention projects being carried out in the complex. The mechanical characterization of the materials and members encountered in the buildings of the hospital is a crucial parameter in the estimation of their structural capacity against the prescribed design loads.

Given the fact that the structural typology and materials found in this building are encountered in several other parts of the hospital complex, the conclusions reached in this campaign may prove useful, at least as a first estimation, concerning the structural behavior and capacity of pillars in this and other buildings.

Micro-modeling techniques may be employed in the investigation of the structural behavior of the pillar. In addition to detailed micro-modeling techniques, even simple models may provide critical information concerning the structural behavior of masonry elements with distinct geometrical characteristics.

For proper application of micro-modeling and analytical techniques extensive mechanical characterization of the individual masonry materials is required. The mechanical properties of the masonry materials used in the construction of masonry samples and walls may be easily characterized during execution of the works: fresh mortar can be sampled, molded and finally subjected to standard or non-standard testing.

Standard unit mechanical testing involves, primarily, the subjection of entire units to uniaxial stress in compressive tests and, secondarily, the subjection of the units to three-point bending.

In the case of existing structures these experimental procedures present a number of difficulties. Mortar may normally only be extracted from the joints, thus making the carrying out of most standard mechanical tests impossible. Extraction of full units is possible, if somewhat difficult if full unit samples are to be extracted. However, the results of compressive tests performed on full units are not entirely appropriate for determining the uniaxial strength of the material comprising the units, which would be the desirable value for a micro-model. Furthermore, three-point bending tests usually exhibit high scatter of the results.

One final issue is that of efficient use of the available material for the carrying out of destructive tests. As many tests as possible should be performed on the available material. An example of this approach is the portioning of bricks for the carrying out of several compression or splitting tests from a single unit.

The experimental methodology described in this chapter presents a sampling and testing framework that attempts to address, as best as possible, the highlighted problems. The procedures detailed here focus on destructive and minor-destructive tests, but a combination with non-destructive tests could enhance the applicability of the method and the range of mechanical properties it is able to characterize. It is primarily envisaged as a methodology for masonry composed of solid bricks made of, for example, clay or adobe. The application of this methodology to the identification of the component mechanical properties of a brick masonry complex structural member is also presented and discussed.

The list of properties measured in this methodology are: the compressive strength, Young's modulus, Poisson's ratio and tensile strength of the units, the compressive strength, Young's modulus, Poisson's ratio and tensile strength of the infill, the compressive strength and Young's modulus of masonry couplets and triplets and the compressive strength of the mortar. These properties are essential for the determination of the compressive behavior of the masonry composite but are also of interest for a variety of analysis purposes. Other properties that may be measured using the samples produced with this methodology include the tensile strength, cohesion and friction angle of the unit/mortar interface and the compressive and tensile fracture energy of the units and mortar. Knowledge of these properties is not crucial for the modeling of the compressive strength of masonry, and thus these tests were not performed in the present research, but are still of interest for the analysis of masonry structures.

Having obtained the mechanical properties of the constituent materials comprising the pillar, a finite element simulation of the compressive test on the pillar is carried out using detailed micro-modeling techniques. Analytical models based on the structural behavior of the pillar's macroscopic structural features are also carried out. The results of the simulation are compared with the experimental findings in terms of predicted strength, elastic stiffness, failure mode and post-peak behavior. The effect of the macroscopic damage on the pillar is investigated as well.

8.2 Historical Information on the Building Complex

The Hospital de Sant Pau building complex was commissioned in 1901 as a replacement of the older facilities located at the historical center of Barcelona. The Catalan modernist architect Lluís Domènech i Montaner was commissioned for designing and supervising the execution of the works, which stretched from 1901 to 1930. The supervision of the works was assumed by his son, Pere Domènech i Roura, after 1920, when the second phase of the construction of the complex was initiated. It was under his supervision that the building in question was completed in a more moderate modernist style.

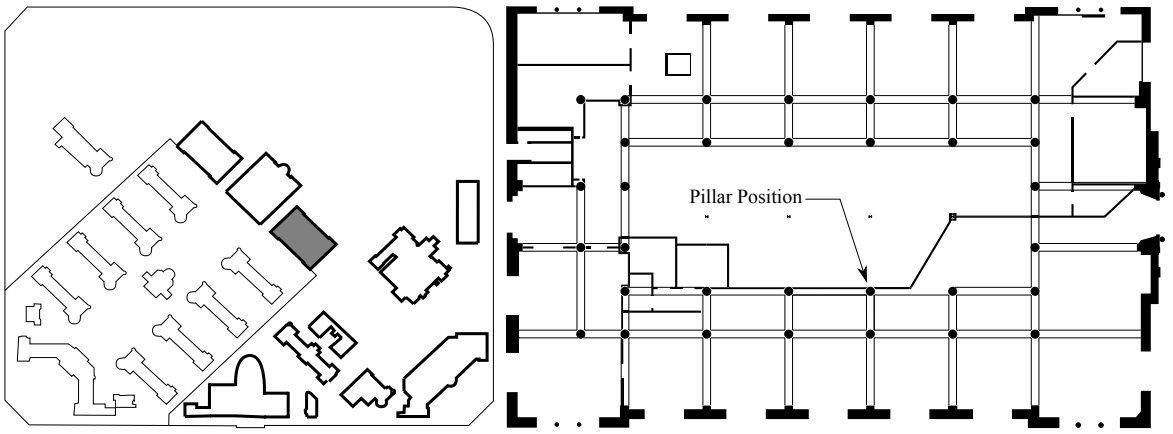

Figure 8.1 (a) Location of the building inside the hospital complex. Buildings of the first phase in regular lines, of the second phase in tinted lines, with the toxicomania building grayed out. (b) Position of the pillar inside the building (ground floor plan).

The project received significant support and funding. Innovative materials and structural techniques were employed, which included sophisticated masonry vaulting systems, extensive use of structural iron and cement based mortar. The building complex consists of individual buildings (pavilions) which kept the administrative and various medical functions each in its own space. The arrangement of the pavilions in the complex is shown in Figure 8.1a.

Due to shifting and increasing operational and administration needs of the hospital, several pavilions underwent functional changes. Additionally, structural interventions, mostly in the form of the addition of secondary elements or load bearing steel and timber beams or partition walls, were carried out.

The entire complex constitutes an important landmark in Catalan Modernista architecture. It was awarded UNESCO World Heritage Site status in 1997. This has increased the visibility of and the public interest in the complex.

In 2008, shortly before the relocation of all medical facilities to a new neighboring building, the master plan for the structural restoration of the complex was compiled, the execution of which began the following year. The execution of the plan, as of 2014, has been almost entirely completed and includes strengthening and complete replacement of members. However, limited investigation has been carried out on the mechanical properties of structural members and their

constituent materials.

8.3 Inspection and Preparation of the Pillar

8.3.1 Overview

The cylindrical pillar was initially located on the ground floor of the two-storey toxicomania department building in the location indicated in Figure 8.1b. In its initial state, the building, originally housing the kitchen facilities, was composed of a central nave and lateral aisles. At some point in the structure's history, steel profile columns were added at the center of the nave as additional supports for the expansion of the first floor. The arrangement of the pillars in the ground floor is a regular grid of similar masonry pillars and steel supporting columns. Therefore, the tributary area supported by the pillar, as defined after the addition of the steel columns, is a rectangular $4.67m \times 3.34m$ area.

The pillar supports a system of brick masonry arches and vaults. Before the beginning of intervention works, a slender masonry wall partition intersected the pillar. This wall was subsequently removed.

Following the removal of a large portion of the pillar, it was placed in a protective steel jacket padded with a neoprene sheet in order to facilitate moving and to avoid damage during transportation.

The total height of the sample was $1600mm$ and had a diameter of $600mm$. A portion with a height of $1000mm$ was decided to be tested in compression and the remainder to be removed for sample extraction and further material testing. The removal and sectioning of the $600mm$ portion of the pillar was performed using a diamond thread. Limitations of the available space between the load surfaces in the testing machine did not allow for a sample of a larger height to be tested.

The central part of the pillar is composed of solid clay bricks and mortar. Its base is a solid stone foot and it is capped by a solid stone capital. The outer structure of the pillar resembles a Flemish bond arrangement of the bricks. Slight variations of the externally visible dimensions of the bricks and the mortar joints are encountered. Being composed of 42 brick courses, the portion of the pillar composed of brick and mortar masonry has a total height of roughly $3m$. Taken as arc lengths at the perimeter, the "stretcher" bricks have an average length of roughly $280mm$, the "header" bricks $90mm$ and the "head" joints have a thickness of $5mm$. The width of the stretcher bricks, which roughly corresponds to the outer leaf of the pillar, is $140mm$. The full circumference of the pillar is composed of 5 "stretcher" and 5 "header" bricks. The bed joints have a thickness of $7.5mm$ and the bricks have a height of $60mm$. The portion of pillar tested was composed of 16 brick courses and 15 bed joints (Figure 8.2).

While the exterior structure presents complete regularity of the Flemish bond pattern, inspection of the cross sections, made visible by the diamond thread cuts, revealed a somewhat irregular internal structure, in which the "header" bricks are but a few centimeters thick. The

"stretcher" bricks have more regular internal dimensions. The infill of the pillar is composed of 5 bricks of moderate dimensions and smaller brick fragments resembling a rubble masonry structure. The mortar, however, appears well compacted, although several voids were found.

The center of the pillar is vertically traversed by a drainage pipe with an external diameter of 90mm. The pipe appeared heavily corroded. The gross cross sectional area of the pillar is 282743mm^2 and the net area, due to the central opening to accommodate the drainage pipe is 276382mm^2, only 2.25% smaller than the gross area.

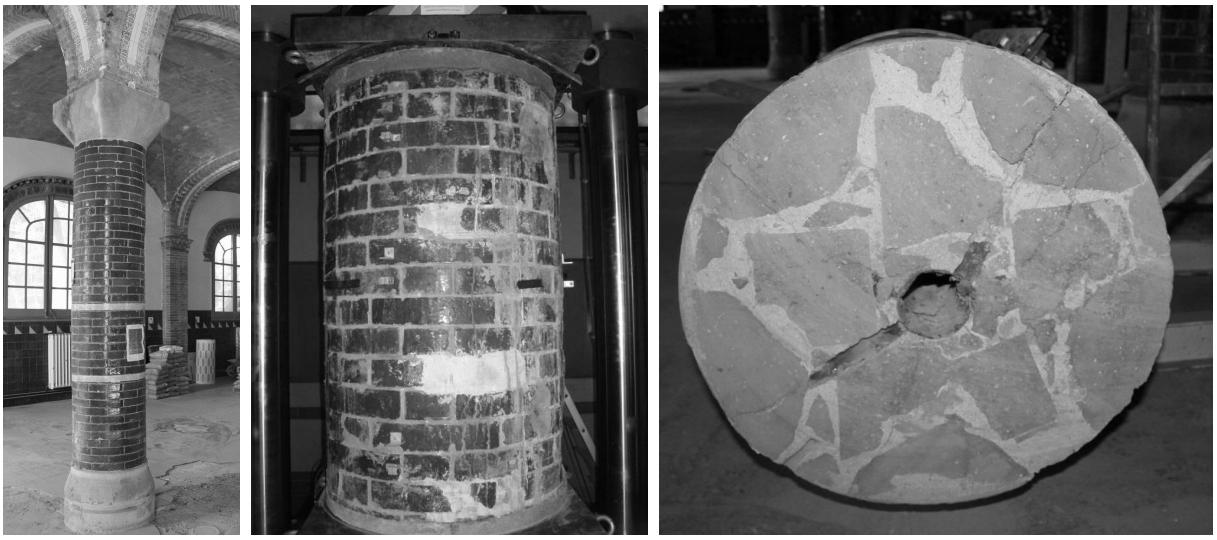

(a) (b) (c)

Figure 8.2 (a) Image of structural layout of pillars, (b) its external and (c) its cross sectional geometry.

8.3.2 Inspection

Visual inspection of the exterior surface of the pillar and the cross sections (Figure 8.3) also revealed several structural defects in the bricks, local loss of material caused by what appears to be anchored timber elements, a large spalling area near the base, significant corrosion of the drainage pipe located at the center of the pillar and, most importantly, three distinct vertical cracks running along the entire height of the specimen and separating it in three segments. Whether these vertical cracks are a result of the pipe corrosion, large sustained vertical loads or the structural interaction with the masonry walls with which it was in prolonged contact is unclear, although one of the cracks extended radially from a large vertical opening of the pipe. It is also not clear whether the steel profile columns were added as a remedy to this cracking. Additionally, while the exterior is composed of bricks of apparently the same type, several different types of bricks were identified in the interior, being recognized by a different color and cut texture.

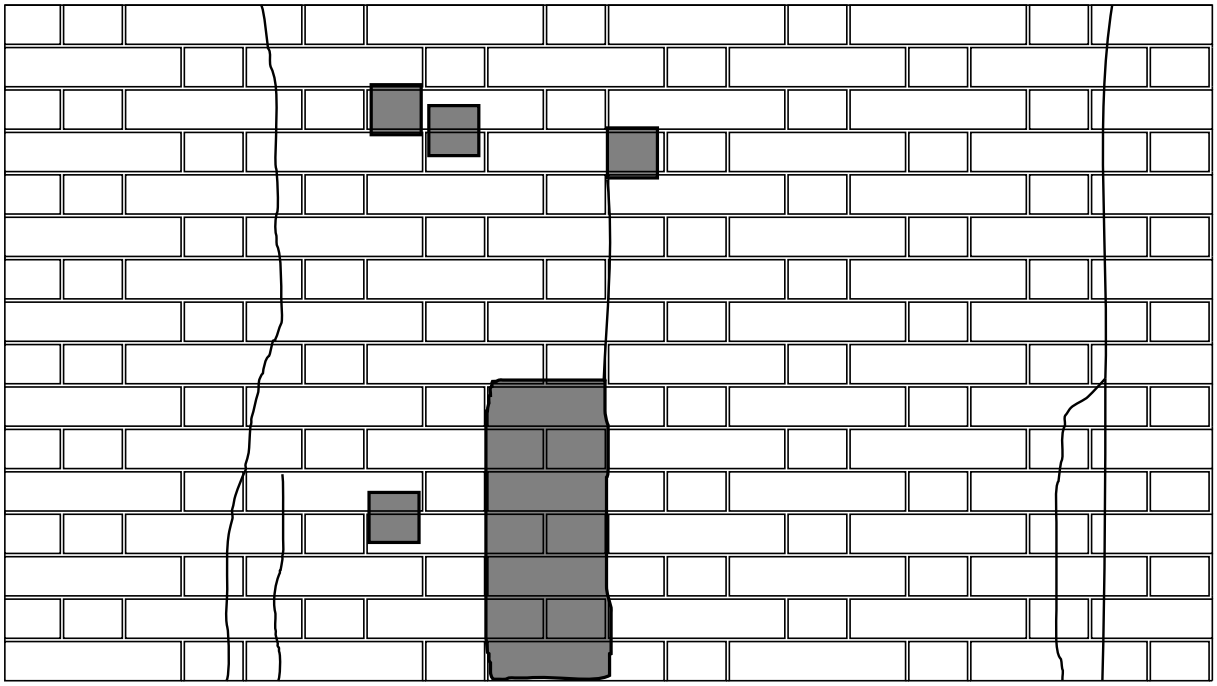

Figure 8.3 Survey of existing damage on masonry pillar. Large vertical cracks and spalling area near the base are visible.

8.3.3 Preparation

The bounding sections at the base and the top, which would serve as the load surfaces in the compression test, were rough and non-parallel. In order to overcome these defects so that good contact could be established with the load plates and in order to avoid premature localized damage during the test, high strength concrete caps were cast directly on the load surfaces. Additionally, 5 mm thick neoprene sheets were applied between the concrete caps and the load plates.

The final configuration is shown in Figure 8.2b.

8.4 Loading and Instrumentation

A large number of several types of instruments were used for the monitoring of the compression test. Given the rather uncommon nature of the test and the lack of an extensive literature on the subject, it was deemed necessary to attempt to gather as much information as possible. Given the large size, the irregular composition and damaged state of the structure, global measurements of vertical and horizontal deformation were deemed appropriate. However, properly arranged local measurements were not ruled out and may in fact provide insight into the global behavior of the structure.

The global axial stiffness of the pillar was measured using three transducers measuring the vertical displacement along a large portion of the height of the pillar: L1, L2 and L3. These transducers were placed one each on every part created by the three large vertical cracks. Therefore, they are not symmetrically distributed on the surface of the pillar. The instruments were

attached using small diameter pins attached in drilled holes.

Local vertical displacements were measured using 9 displacement transducers. These were arranged on three height levels and aligned horizontally where possible: T1, T2 and T3 near the top; M1, M2 and M3 at mid-height; B1, B2 and B3 near the base of the pillar. The purpose of this arrangement was the measurement of variation in local stiffness according to the position along the height of the pillar. A representative measurement length including two half bricks and one bed joint was adopted. These instruments were too attached on the surface of the pillar using pins.

Four displacement transducers were used to measure horizontal movement in four points along the perimeter at the mid height of the pillar. These points were located at 90^0 angle intervals and their measurements could be used to approximate the global radial expansion of the pillar under concentric compression. These instruments were fixed on a perimetric aluminum frame and oriented in a direction normal to the surface of the pillar.

Three strain gauges were used in alignment with the long vertical LVDTs. They were attached to the outer surfaces of three intact bricks using an adhesive resin. The intended purpose of the strain gauges was the measurement of the deformation of a single brick in order to estimate its modulus of elasticity.

The arrangement of the instruments is shown in Figure 8.4, along with the existing damage documented through visual inspection. The distribution of the large vertical cracks and the location of the spalling area divide the pillar in three uneven segments: one part consisting of roughly half the pillar and two parts consisting of roughly a quarter of the pillar each. This fact, along with the superficial damage, dictated the arrangement of the instrumentation.

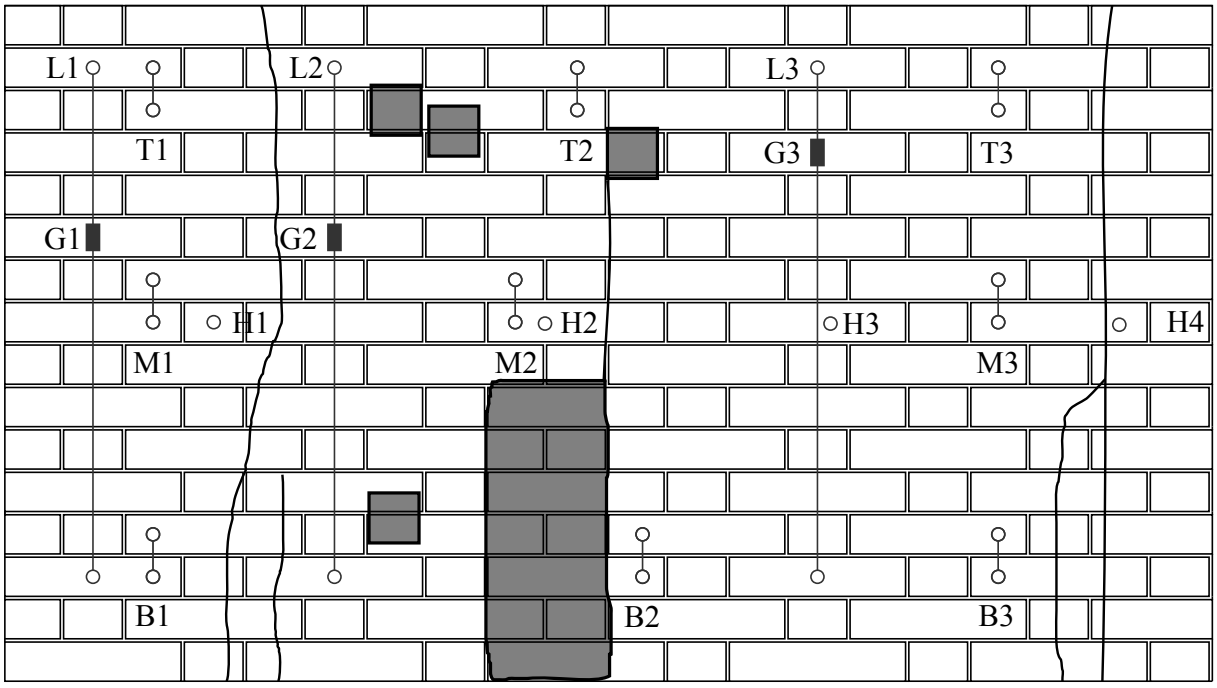

Figure 8.4 Instrument placement on pillar. L: large vertical transducers, H: small horizontal transducers, T, M & B: small vertical transducers at the top, middle and base, G: strain gauges.

Several load cycles were performed during the test. These consisted of two applications of $200kN$ at a load and unload rate of $0.2mm/min$ with the maximum load being maintained for 5 minutes. An application of $400kN$ at a rate of $0.3mm/min$ followed, the maximum load again maintained for 5 minutes. Subsequently, a load of $400kN$ at a rate of $0.5mm/min$ was again applied, held for 5 minutes at the maximum, and, finally, a steady load rate of $0.2mm/min$ was applied until failure of the pillar. Following attainment of the peak the pillar was unloaded by lifting the load cell.

Due to the height/diameter ratio of the pillar, equal to roughly 1.6, failure due to buckling can be ruled out. The monolithic behavior of the pillar, however, cannot be easily ascertained due to the presence of large vertical cracks which may, in effect, split the pillar in three independent parts. The concrete caps may assist in preventing or mitigating such a mode of response, but collapse should be governed by both local material failure and global failure mechanisms.

8.5 Pillar Test Results

The peak force attained was $1694kN$, corresponding to $6.0N/mm^2$ of compressive stress taking into account the gross area of the pillar. The Young's modulus of the pillar at 50% of the maximum load was $6075N/mm^2$. Throughout the application of the load and before the attainment of the maximum force, the variation of the Young's modulus was very small, owing to the good compaction of the concrete used in the joints. The force-axial strain response curve, the strain having been calculated from the displacement measured at the large vertical transducers, is presented in Figure 8.5a. Considering that the aspect ratio of height to diameter of the pillar is lower than 2, which is deemed optimal for compressive testing, signifies that the actual compressive strength of the pillars may be even lower. The fact that the pillars in the actual structure are roughly 3 meters in height compounds the problem of comparing the compressive strength obtained in the experiment to that of the original pillars remaining in the building.

Figure 8.5b illustrates the strain measurements from gauges G1, G2 and G3. According to these readings, the Young's modulus is equal to $7320N/mm^2$. Given the irregular structure of the pillar and the very short measurement length, this value only serves as an indicative measurement of the Young's modulus of the pillar. Furthermore, it is not certain that the stress in the brick is equal to the average vertical stress at the pillar, therefore it should not be considered indicative of the Young's modulus of the brick either.

The progression of damage was visually monitored during the test. At a load of $1000kN$ the large preexisting vertical cracks had expanded into the concrete caps and new vertical cracks had appeared on the surface. It is assumed that the preexisting cracks exhibited further opening. Near the maximum load, limited superficial spalling of bricks was registered, while the already large spalling area near the base had degraded, but not significantly.

Localized damage in the joints, such as vertical cracks in the head joints or crushed mortar in the bed joints was not noticed at close visual inspection. Furthermore, superficial damage in the bricks was mostly limited to "header" bricks, which are only a few centimeters thick at most

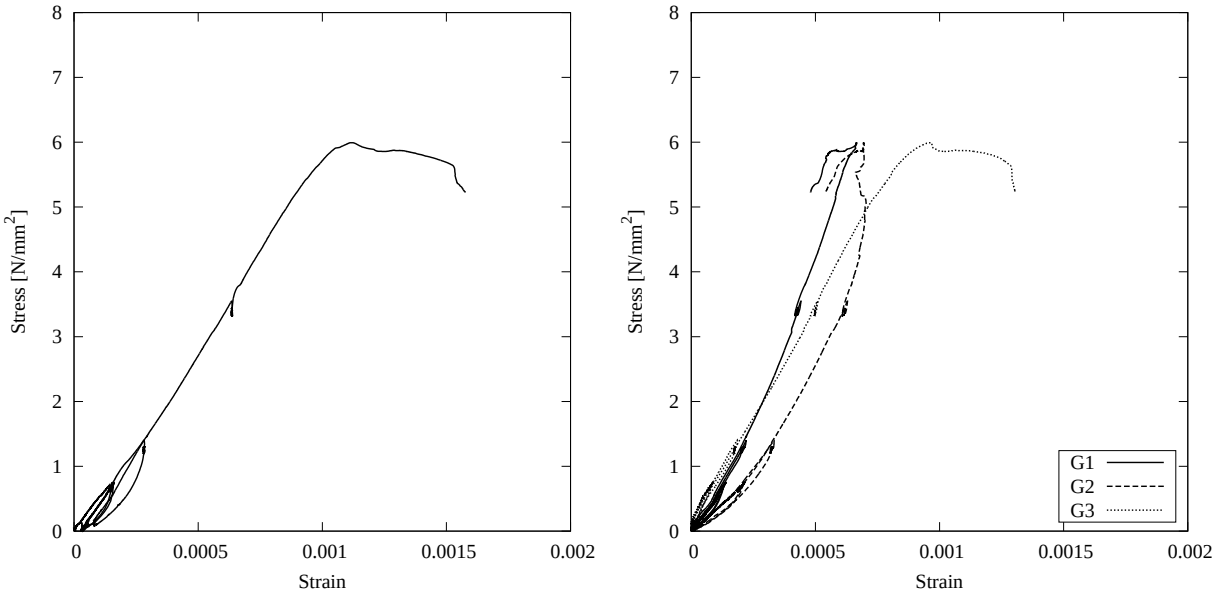

Figure 8.5 Stress-axial strain curves: (a) transducers and (b) strain gauges.

points. Crushed material was not found to have fallen from the pillar in any significant amount from either the bricks or the joints. No cracks or other damage appears to have originated from the pins used for the anchoring of the measurement instruments. The concrete caps also did not appear to bear significant damage except near the edges. Removal of the concrete caps also revealed that no localized damage had been caused near the load surfaces.

This global failure appears to have developed mostly along the preexisting vertical cracks and resulted in separation of the three pillar segments. The new damage identified at the end of the test, along with the preexisting damage, is shown in Figure 8.6. It is clearly indicated that most new vertical cracks originated near the anchor points of the old timber elements. These too extended to the concrete caps. No evidence of crushing damage was discovered externally in neither the bricks nor the joints and new vertical cracks were limited in number and expanse.

Whereas global axial stiffness, defined as the average stiffness derived from the large vertical transducers, was steady until failure, different values of stiffness were registered in each of the three masonry segments. Transducer L2 in particular showed a much smaller stiffness than L1 and L3, especially for low loads and for loads near failure, as can be seen in Figure 8.7. The L2 transducer was placed near the large spalling area which may account for this behavior.

Another discrepancy was found in the behavior registered at different heights by the small vertical transducers, which is also illustrated in Figure 8.7. The base transducers recorded a clearly nonlinear response near the peak, the middle transducers recorded an almost elastic unloading after the peak, as did top transducers following a sudden expansion after the unloading process started. At 50% of the maximum load the top transducers registered a stiffness of $13511 N/mm^2$, the middle transducers $9196 N/mm^2$ and the base transducers $6111 N/mm^2$. However, the transducers at each level did not register the same stiffness, especially at the top part, where the maximum stiffness was $20252 N/mm^2$ and the minimum was $7883 N/mm^2$ at the

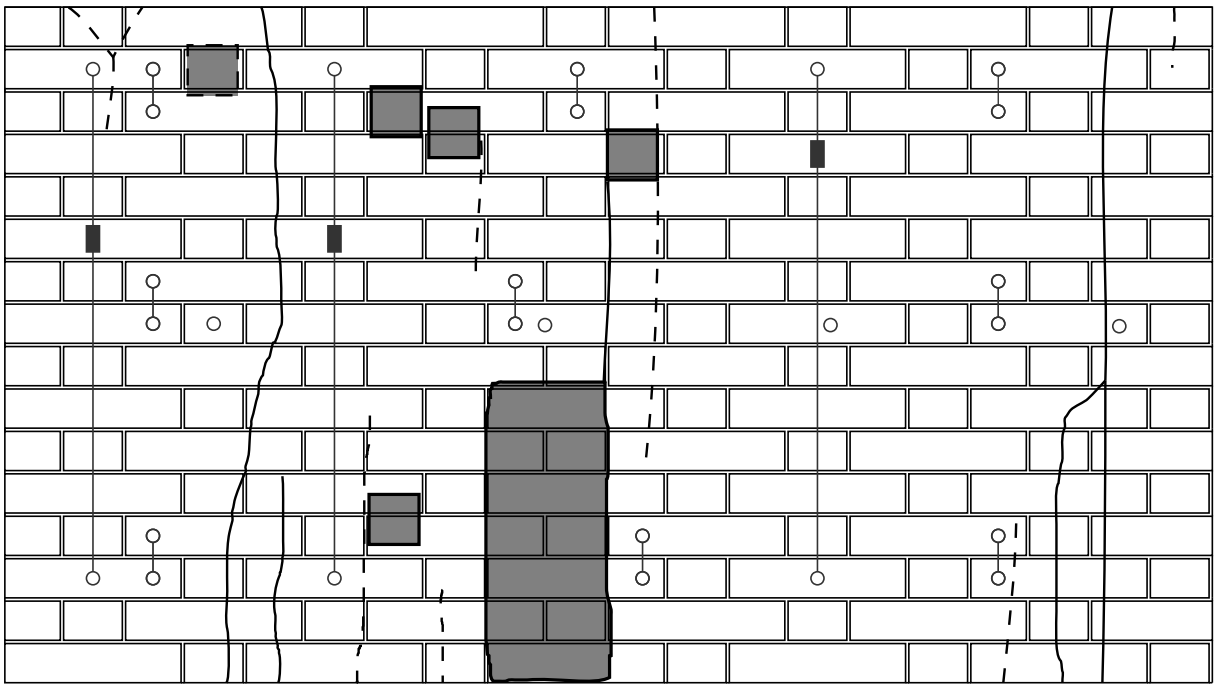

Figure 8.6 Preexisting (solid lines) and new (dashed lines) damage at the end of the test.

T3 and T1 positions respectively. The variation was much smaller for the other two levels.

Horizontal expansion was uneven in the two directions designated by transducers H1-H3 and H2-H4, as shown in Figure 8.8. Generally, the displacements were much larger in the H1-H3 direction. Considering the total radial expansion as the average produced by the two directions, the Poisson's ratio of the pillar reaches the value of 0.50 before 50% of the maximum load. The initial ratio for a load level of $300kN$ is 0.22.

8.6 Sampling Methodology

8.6.1 Overview

The sampling methodology is based on the extraction of vertical cylindrical samples from the masonry. These samples may be used for the formation of cylindrical masonry couplets (two units and one intermediate mortar joint) and cylindrical infill samples. The former samples may be used for the extraction of cylindrical brick samples and thin mortar layer samples. All of these samples can be used for various types of destructive testing.

Extraction of masonry samples through drilling is only marginally disturbing to the masonry when performed with a sufficiently low spinning and advance velocity. The small size and regularity of the extracted samples alleviates the problems that may arise from attempting to extract entire units, which may crack during removal.

Vertical coring requires access to the top of masonry members. This can be achieved in window openings, parapets or other members to which access can be achieved during strengthening, reconstruction or demolition works. In the special, but common, case of single leaf walls, hor-

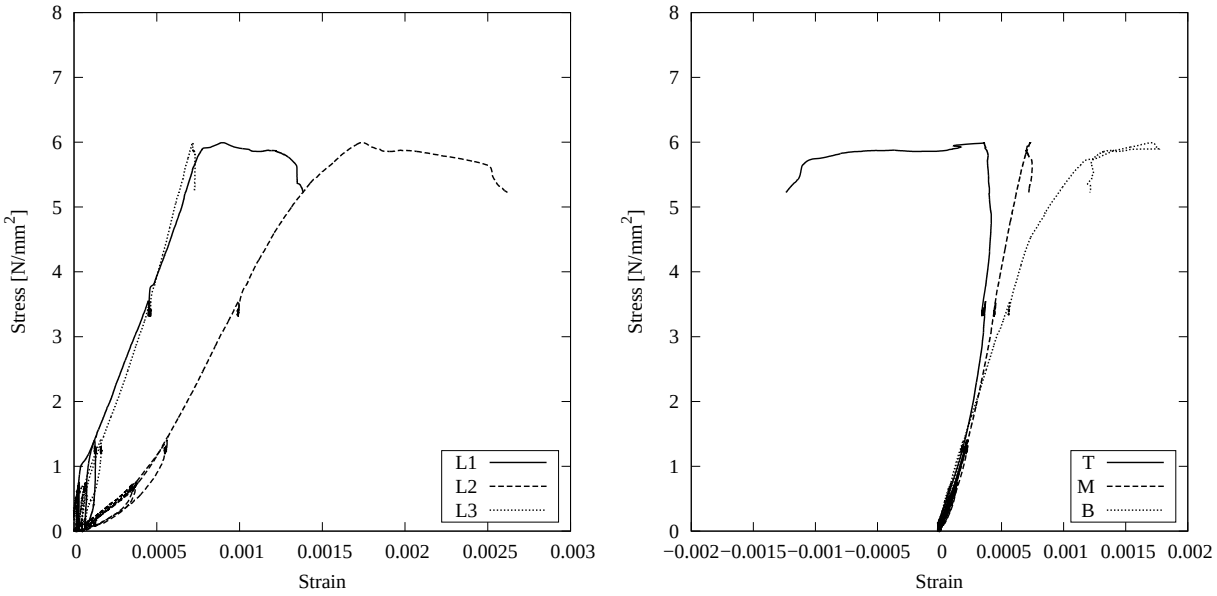

Figure 8.7 (a) Force-displacement curves: (a) L1, L2 and L3 transducers and (b) average of top, middle and base transducers.

izontal cores are arguably easier to extract. However, the interpretation of the results obtained from this type of samples is more challenging. Vertical cores allow for an easier differentiation of the behavior of the constituent materials of masonry.

8.6.2 Application

In the present case study a 600*mm* high portion of the tested pillar was available for sampling. To facilitate the extraction of vertical cores, the pillar was cut into two segments using a diamond thread. The two segments were roughly 5 courses high, and thus sufficiently small for the extraction of the specimens. An additional portion with a height of 1000*mm* was also available, originating from an adjacent pillar. This particular pillar was composed of the same materials and the same overall arrangement of clearly distinct outer and inner leaf, but the exterior pattern was that of a running bond typology. This too was cut to three 5 course segments for further extraction of samples.

Several vertical cores were extracted from each segment. The pillar and the extraction pattern may be seen in Figure 8.9. The cores from the exterior part were extracted so as to produce cylinders composed of full brick and mortar strata. Cylinders were also extracted from the irregular infill. A 75*mm* diameter drill was used for the coring. The infill samples were extracted from both the Flemish bond and the running bond pillar and the couplet and triplet samples were extracted from the running bond pillar alone, since the larger overlapping area of the latter allows for a larger diameter drill to be used for the extraction. Couplets were also extracted from the outer part of the Flemish bond pillar using a 45*mm* diameter drill. The smaller diameter was necessarily used due to the smaller overlap of the bricks in that pillar. These couplet samples

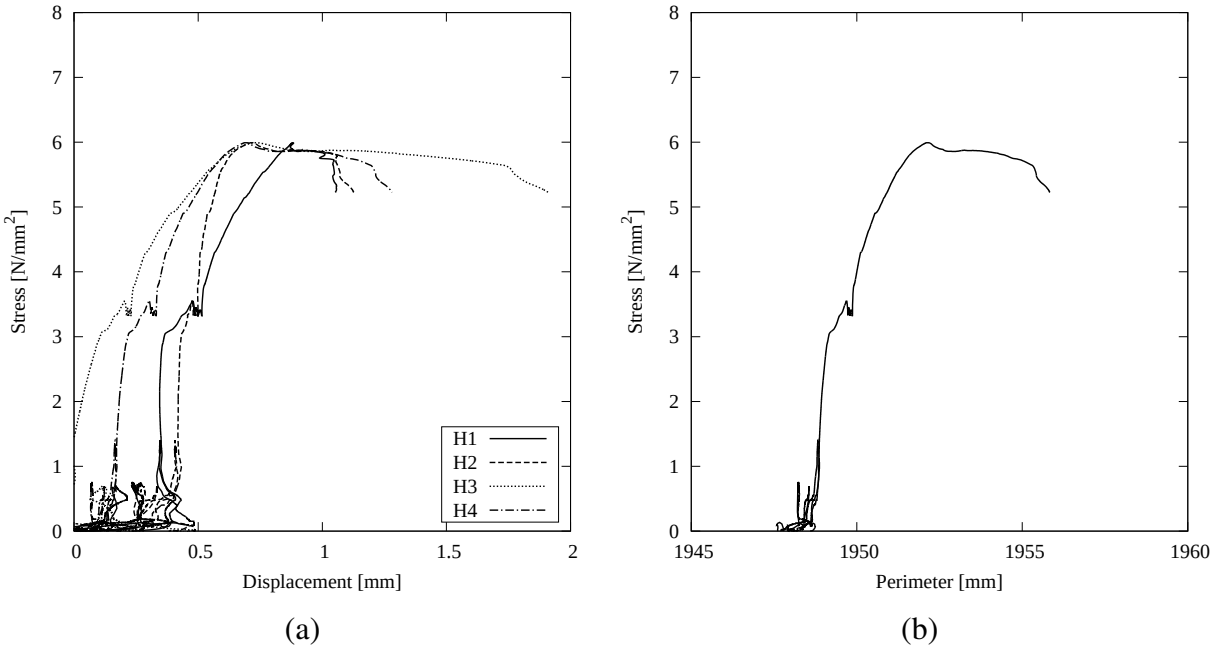

Figure 8.8 (a) Horizontal transducer readings and (b) mid height perimeter change history.

were not used in this campaign, though.

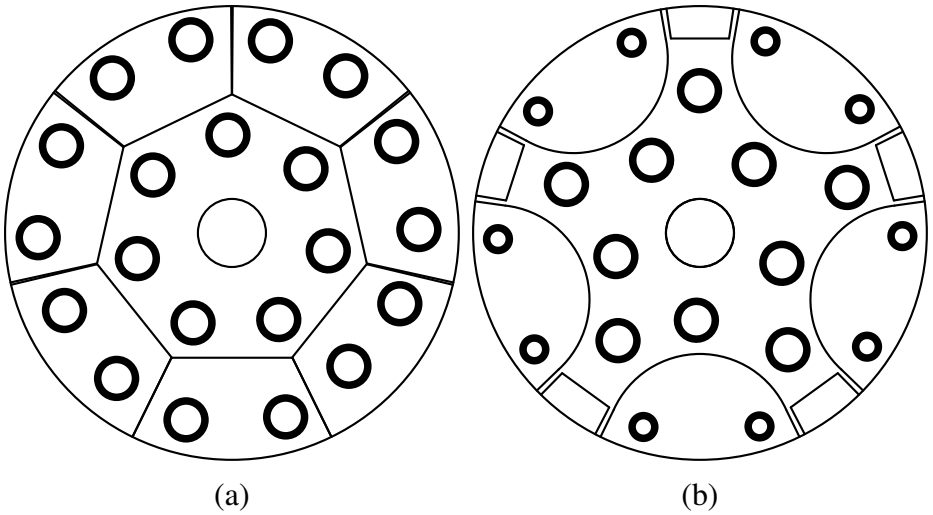

Figure 8.9 Schematic of sample extraction patterns from pillar cross sections: (a) Running bond pillar and (b) Flemish bond pillar.

A large number of cylindrical samples was produced, from which several couplets and triplets were obtained. Cylindrical samples of bricks were obtained by sawing from the long cylinders. A large number of loose mortar samples was also obtained. These samples were for the most part from the infill and from cavities in the exterior part which were filled in the pouring process of the concrete during construction. Intact mortar samples from the joints were also produced, despite the very small thickness of the mortar joints and the strong adherence of the cement to the units. This was accomplished by way of removing the brick part of the couplets using a saw.

8.7 Testing of Units

8.7.1 Compression Test

The cylindrical samples of brick with a diameter of 75.4*mm* obtained from the coring process may be used, following some preparation, for compressive testing. Brick testing standards [42] are oriented towards the testing of entire units. While such standards may be consulted as far as sample preparation and loading are concerned, certain modifications are necessary if the uniaxial compressive strength of the material is to be determined. Furthermore, it would have been particularly difficult to obtain full brick specimens from the column in this particular case study due to the strong unit/mortar bond.

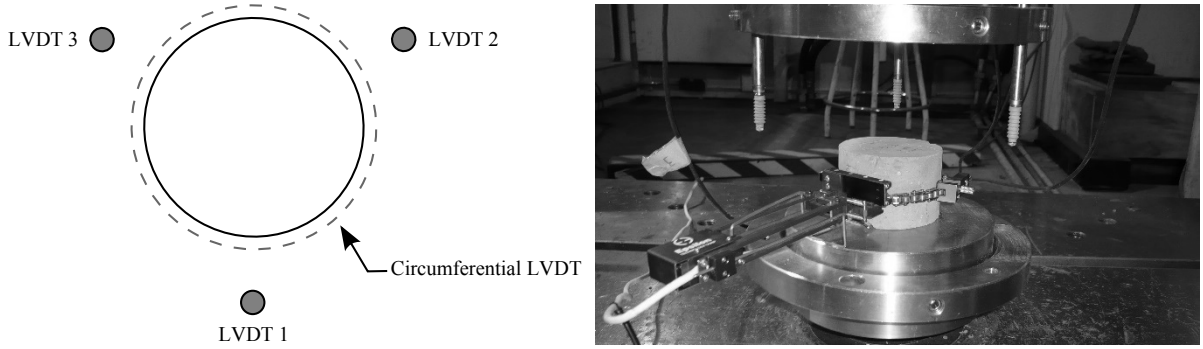

Figure 8.10 Test setup for brick cylinder compression: (a) plan view schematic and (b) actual setup.

Prior to testing, the load surfaces of the cylindrical samples were polished until smooth and parallel. Following the polishing, the samples were of height to diameter ratio smaller than 1 : 1, which is less than optimal for compressive tests but still better more appropriate for the purpose of the test than testing of an entire brick. The test setup, shown in Figure 8.10, consists of three LVDTs for the measurement of the vertical deformation of the sample and a circumferential LVDT for measuring the change in the diameter of the sample. The load was applied in displacement control at a rate of $0.005mm/sec$.

The test results are presented in Table 8.1 and the obtained stress-strain graphs are shown in Figure 8.11. The circumferential LVDT did not function correctly for sample UC_1, while the strength of sample UC_4 exceeded the capacity of the load cell used and is considered an out-lier. The Poisson's ratio was calculated by dividing the circumferential strain by the absolute axial strain. Correction factors were applied to the results according to the EN standard for the determination of the compressive strength of bricks and can also be seen in the table.

8.7.2 Splitting Test

The cylindrical shape of the unit samples and the difficulty in obtaining full brick samples makes the splitting test in place of, for example, the three point bending test for the indirect determination of the tensile strength of the units a viable choice. The length to diameter dimension ratio

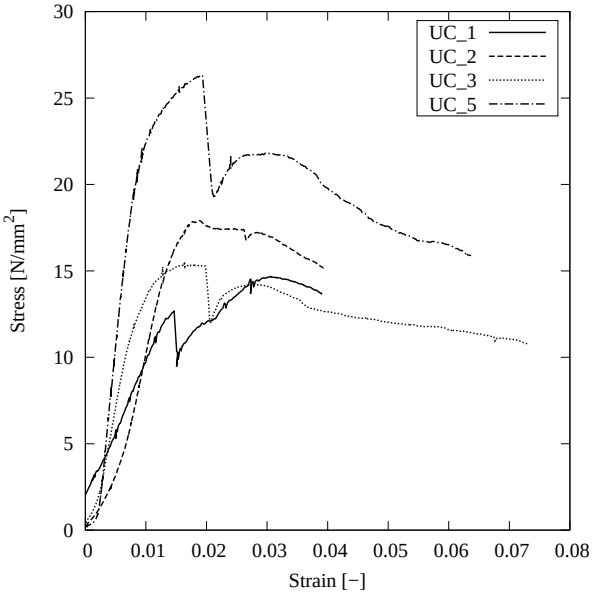

Figure 8.11 Brick compression stress vs. strain graphs.

Table 8.1 Unit compression test results on 75.4*mm* diameter cylinders. Coefficient of variation in parentheses.

Sample	Height $[mm]$	Height/Diameter [-]	Correction Factor [-]	F_{max} $[kN]$	f_{cu} $[N/mm^2]$	E_u $[N/mm^2]$	ν_u [-]
UC_1	50.0	0.663	0.85	65.6	12.5	820	-
UC_2	50.0	0.663	0.85	79.9	15.2	3411	0.032
UC_3	50.3	0.667	0.85	70.4	13.4	1725	0.117
UC_4	40.4	0.536	0.75	-	-	3200	0.201
UC_5	38.7	0.513	0.75	77.8	14.8	3285	0.243
Average	45.9	0.609		73.4	14.0 (0.086)	2488 (0.465)	0.148 (0.635)

of the samples is still an issue, being lower than 1 : 1. Size effects present during splitting tests may be alleviated through the use of sufficiently narrow plywood strips for the application of the splitting force [133]. The diameter of the samples dictated that a plywood strip of 6*mm* in width be used, or 8% of the specimen diameter. The height of the strip was 4*mm*, running across the entire length of each sample. In addition to concentrating the splitting force and alleviating the size effects involved, the plywood strips also assist in overcoming any surface irregularities of the units.

The results of the splitting tests are presented in Table 8.2. Overall, the desirable failure mode of a single splitting crack was achieved. Secondary cracks were formed after the peak load. Typical response graphs of the samples are shown in Figure 8.13. While the scatter of the results in terms of the derived tensile strength is only moderate, the response of the samples in the post-peak is not entirely consistent across the samples. The formation of secondary cracks results in the attainment of secondary load peaks and stress plateaus.

The tensile strength of the unit was derived from the splitting force according to the equation:

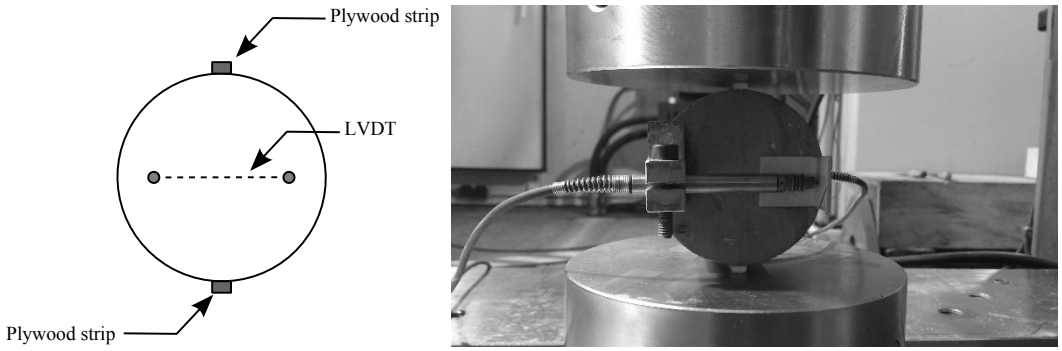

Figure 8.12 Test setup for brick cylinder splitting: (a) schematic and (b) actual setup.

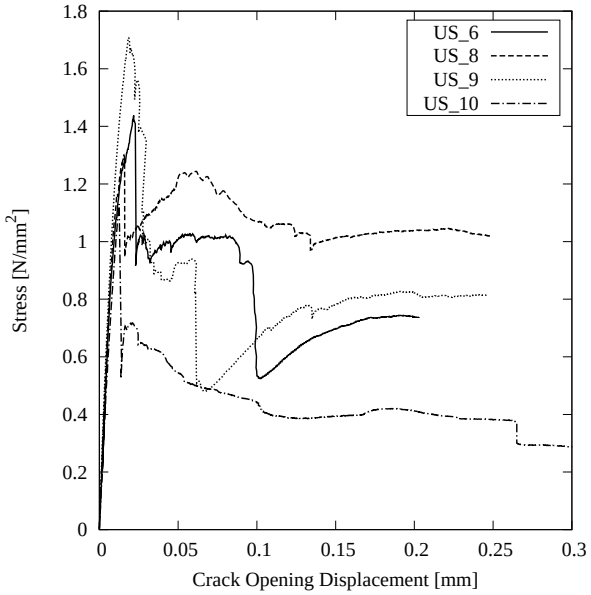

Figure 8.13 Brick splitting stress vs. crack opening displacement graphs.

$$f_{tu} = \frac{2F}{\pi L d} \tag{8.1}$$

where F is the splitting force, L is the specimen length and d the diameter. The loading was applied using crack opening displacement control. A very low rate was of $0.00003 mm/sec$ used initially, followed by an increased rate of $0.00015 mm/sec$ after reaching the load peak.

According to the obtained results, the ratio of the compressive over the tensile strength of the brick is 13.1%. This percentage is slightly higher than the average obtained in the inventory of experimental results already presented in the chapter of finite element modeling of masonry under compression, but well within the limits observed.

Table 8.2 Unit splitting test results on 75.4*mm* diameter cylinders. Coefficient of variation in parentheses.

Sample	Length [*mm*]	Length/Diameter [-]	F_{max} [*kN*]	f_{tu} [N/mm^2]
US_1	46.8	0.621	14.95	2.70
US_2	49.3	0.654	10.42	1.79
US_3	43.8	0.581	11.92	2.30
US_4	40.9	0.542	9.67	2.00
US_5	40.8	0.541	6.61	1.37
US_6	51.8	0.687	9.34	1.52
US_7	52	0.690	12.86	2.09
US_8	49.7	0.659	8.15	1.39
US_9	53.3	0.707	12.29	1.95
US_10	51.4	0.681	7.64	1.26
Average	44.32	0.636	10.39	1.84 (0.228)

8.8 Testing of Unit/Mortar Couplets

8.8.1 Compression Test

The compression test on unit/mortar couplets is meant to provide a mesoscopic measurement of the strength and Young's modulus of the outer leaves of the masonry pillar. It should not be considered a representative measurement of the compressive strength of the masonry composite or even of the outer leaf of the pillar.

The test setup was similar to the one used for the compressive testing of the units and is shown in Figure 8.14a. The main difference is the absence of a circumferential LVDT. The load was applied in displacement control at a rate of $0.001mm/sec$. A total of six samples were tested. Samples CC_1, CC_2 and CC_3 were tested monotonically and samples CC_4, CC_5 and CC_6 were subjected to 5 cycles of cyclic loading ranging from $5kN$ to $25kN$.

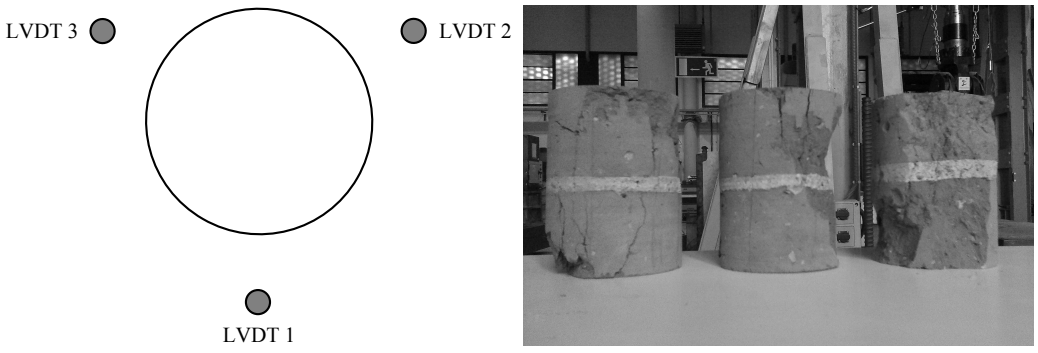

Figure 8.14 (a) Test setup for schematic for unit/mortar couplet compression and (b) couplets after testing.

The results are presented in Table 8.3. No correction factor was applied in this group of results. The average compressive strength was slightly lower than the compressive strength of the bricks as defined before the application of the correction factors on the latter tests. This fact suggests that the failure of the couplets in compression is primarily governed by the compressive

failure of the units. The average Young's modulus of the couplets was higher than the average value for the units. Three values, however, were lower than the average unit Young's modulus. The typical failure mode of the samples is shown in Figure 8.14b.

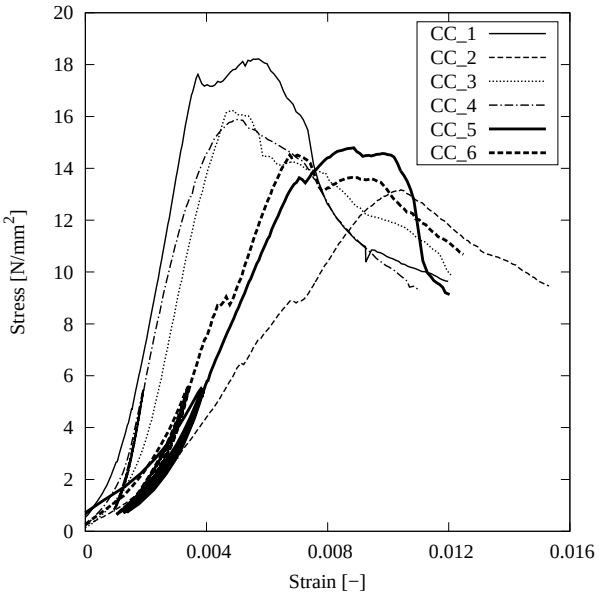

Figure 8.15 Couplet compression stress vs. strain graphs.

Overall, the compressive strength of the samples did not exhibit significant scatter. The Young's modulus, however, presented a coefficient of variation of 49%. Whereas the samples subjected to monotonic loading had equal compressive strength to the ones tested cyclically, the latter group of samples exhibited a Young's modulus lower by 25% on average but with lower result dispersion.

With an average sample height of 102.5*mm*, the samples have an average aspect ratio of 1.36. According to ASTM C42/C42M - 13 standard for the extraction and testing of extracted concrete cores, this ratio requires the adjustment of the obtained compressive strength by multiplication with a factor of 0.96 [19]. This may only be used as a very general estimation of the aspect ratio effects on the compressive strength of the masonry couplets, due to them being a very different material from concrete. It does, however, indicate that this aspect ratio has only a marginal effect on the compressive strength. It has been, therefore, decided not to adjust the obtained compressive strength of the couplets.

8.9 Testing of Infill

8.9.1 Compression Test

As in the case of the unit/mortar couplets, these tests are meant to provide a macroscopic measurement of the strength and elasticity of the infill in compression. The same is true for the splitting tests which are described in the following section.

Table 8.3 Unit/mortar couplet compression test results on 75.4*mm* diameter cylinders. Coefficient of variation in parentheses.

Sample	Height $[mm]$	F_{max} $[kN]$	f_{cco} $[N/mm^2]$	E_{co} $[N/mm^2]$
CC_1	103.0	82.6	18.5	6092
CC_2	102.0	58.9	13.2	1512
CC_3	102.0	72.8	16.3	4836
CC_4	103.0	71.0	15.9	4721
CC_5	103.0	67.9	15.2	2299
CC_6	102.0	66.1	14.8	2466
Average	102.5		15.7 (0.112)	3654 (0.494)

(a) (b)

Figure 8.16 Test setup for infill testing: (a) compression test and (b) splitting test.

Infill cylindrical samples were shaped out of long vertical cores so as to have a height to diameter dimension ratio of 2 : 1, which is adequate for compression tests. The load surfaces of the samples could not be polished without breaking the specimens. For this reason, the samples were capped using a thin sulfur mortar layer. Three vertical LVDTs were placed on an externally fixed module and a circumferential LVDT was placed at mid height (Figure 8.16).

The results are presented in Table 8.4. The obtained values exhibited a dispersion higher than that achieved for the units or the unit/mortar couplets. Additionally, a very low value of $7N/mm^2$ was registered for one of the samples. Also of note is the high Young's modulus of the infill, which is higher than that of the unit/mortar couplets, even though the compressive strength was noticeably lower. The high percentage of cement mortar in the infill could account for this high stiffness. Additionally, the obtained Poisson's ratio is lower than the values typically encountered in clay bricks and cement mortar. A possible explanation is the high percentage of voids in the volume of the infill samples, which act as macroscopically observable pores in the medium. Finally, the post-peak behavior was scattered as well, with two of the samples exhibiting a very brittle response.

8.9.2 Splitting Test

The splitting tests were performed with the same philosophy as in the case of the compressive tests. The overall setup was similar to the one used in the unit splitting tests. The same plywood

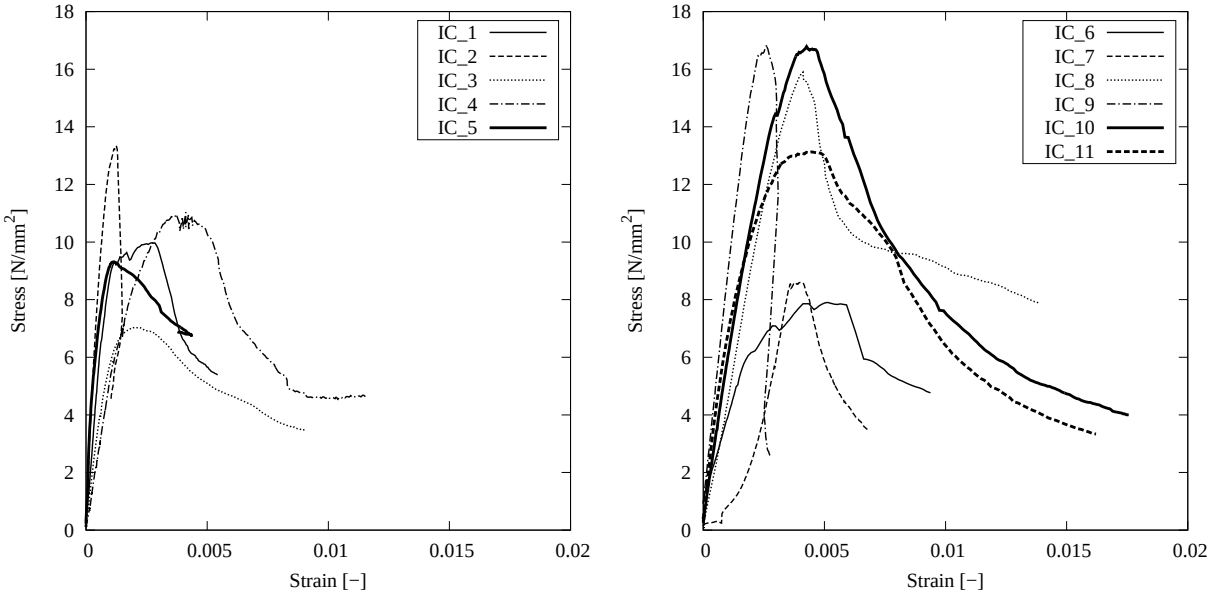

Figure 8.17 Infill compression stress vs. strain graphs: (a) Flemish bond pillar infill and (b) running bond pillar infill.

strips were employed, even though the dimension ratios were adequate for the elimination of size effects, and a load rate of $250 N/sec$ was employed. Only Flemish bond pillar infill samples were subjected to this test. The test results are presented in Table 8.5. The failure mode achieved was again a splitting of the specimens originating from the strips.

8.10 Testing of Mortar

8.10.1 Non-Destructive Testing

The mortar was subjected to optical microscopic inspection and XRD tests. The optical microscopy revealed a well compacted and cohesive mortar containing small size aggregates and the XRD analysis revealed that the binder is in fact Portland cement. The use of Portland cement is common in the pillars of the Sant Pau building complex. It was meant to provide increased strength to the pillars, which were meant to bear high compressive loads and to speed up the construction process. Common lime mortar, however, was used in other structural members, such as walls, which are subjected to lower and more distributed loads.

8.10.2 Minor-Destructive Testing

The mortar joints were also subjected to pin penetration tests, which allow for an indirect estimation of the compressive strength [80, 145]. Two sets of penetration tests were performed: one in-situ on an adjacent running bond pillar and one on the Flemish bond pillar at hand. In the latter case the tests were performed at three height areas: near the base, near the center and near

Table 8.4 Infill compression test results for Flemish and running bond pillars on 75.4*mm* diameter cylinders. Coefficient of variation in parentheses.

Sample	Height [*mm*]	F_{max} [*kN*]	f_{ci} [N/mm^2]	E_i [N/mm^2]	ν_i [-]
IC_1	146.6	44.65	10.0	10579	0.077
IC_2	144.4	59.38	13.3	13888	0.126
IC_3	146.8	31.26	7.0	5241	0.130
IC_4	136.9	50.01	11.2	8621	0.182
IC_5	143.3	42.86	9.6	16702	0.013
Average	143.6		10.2 (0.225)	11006 (0.406)	0.106 (0.566)
IC_6	146.9	35.27	7.9	2819	-
IC_7	149.5	38.40	8.6	3890	-
IC_8	134.0	70.99	15.9	10610	-
IC_9	147.1	75.46	16.9	7926	-
IC_10	147.3	75.01	16.8	5668	-
IC_11	142	58.94	13.2	9990	-
Average	144.5		13.2 (0.311)	6817 (0.471)	-

Table 8.5 Infill splitting test results on 75.4*mm* diameter cylinders. Coefficient of variation in parentheses.

Sample	Length [*mm*]	F_{max} [*kN*]	f_{ti} [N/mm^2]
IS_1	146.78	21.45	1.23
IS_2	151.15	24.72	1.28
IS_3	142.58	18.63	1.10
IS_4	132.16	25.16	1.61
IS_5	113.22	27.38	2.04
IS_6	128.30	23.13	1.52
Average	135.70		1.48 (0.230)

the top.

The results of the penetration tests are presented in Table 8.6. The difference found between the values obtained from the bed and the head joints was 10%, with the bed joints exhibiting the higher value. However, disregarding the zero value from the head joints, the two sets produce equal compressive strengths. Additionally, the average values obtained from the two pillars were: $25.8N/mm^2$ for the running bond pillar and $29.8N/mm^2$ for the Flemish bond pillar, which was tested in compression. However, a more noticeable difference was registered between the different heights in the tested pillar: the values at the top are the highest, being 22% higher than the ones measured at mid-height. The top part in the test sample corresponds to the lower part of the pillar as it was situated in the structure, but it was flipped in the lab during the construction of the concrete caps. Segmental pouring of the mortar at the level of every bed joint during the vertical erection of the pillar could account for this difference, considering the lower execution standards and less advanced concrete technology at the time of construction.

The results of the penetration test exhibited little scatter with only a single outlier measurement. Among the advantages of the testing method employed are the limited interference with the integrity of the structure and its speedy execution. It is still desirable, however, to have a

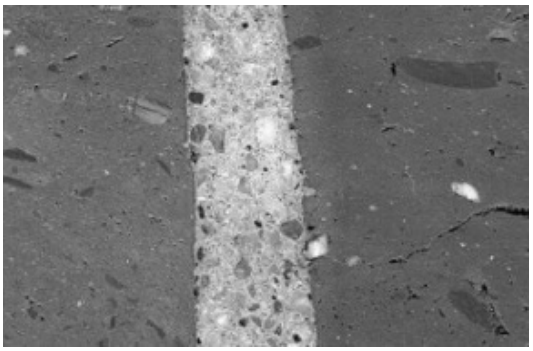

Figure 8.18 Detail of mortar joint cross section.

Table 8.6 Penetration test results.

	Penetration [mm]	f_{cm} [N/mm^2]
Bed Joints	5.055	23.1
	4.470	25.4
	1.168	37.3
	4.039	26.7
	5.334	22.2
	4.521	24.9
	2.997	30.4
	3.886	27.2
Average		27.2
Head Joints	3.988	27.2
	10.947	0.0
	5.055	23.1
	1.930	34.6
	4.953	23.5
	4.420	25.4
	2.743	31.3
	3.175	30.0
Average		24.4
Base	3.302	29.5
	4.115	26.7
	1.829	35
	4.140	26.7
Average		29.5
Middle	3.759	27.7
	3.962	27.2
	5.410	22.2
	3.861	27.7
Average		26.2
Top	2.540	32.3
	2.565	32.3
	2.083	34.1
	1.651	35.5
Average		33.6

complete idea on the compressive strength of the mortar, which is possible to be achieved using destructive testing on extracted samples.

8.10.3 Destructive Testing

During cutting of the column with the diamond thread, a large number of cubic mortar samples was obtained. This material originated mostly from the infill or from loose masses of mortar used to fill cavities in the outer brick leaf of the pillar. They were of varying size, several being cubic samples of 30mm in length. These were subjected to compressive testing.

Additionally, a large number of mortar layer samples was extracted from the bed joints of masonry couplets and triplets. The small thickness of these samples makes standard compressive testing unwieldy. Therefore, these samples were subjected to compressive double punch tests.

Both of the mentioned groups of samples are characterized by a high degree of shape and size irregularity and imperfections due to existing damage or foreign material inclusions. Therefore, the interpretation of the obtained results is challenging. Additionally, rather than belonging to clearly discrete groups of a given thickness, the mortar layer samples covered a range of thicknesses between 6*mm* and 20*mm*.

The mortar cubic samples were cut using a circular saw. They were tested after application of a thin gypsum layer on both load surfaces in order to overcome surface irregularities and to ensure full contact between the samples and the load plates. The load was applied in displacement control at a rate of $0.015mm/s$ using a hinged load plate. The cubic samples were cut in such a manner so as to have the maximum dimensions allowed by the loose mortar from which they originated. This process resulted in, as for the layer samples, a collection of samples with varying dimensions.

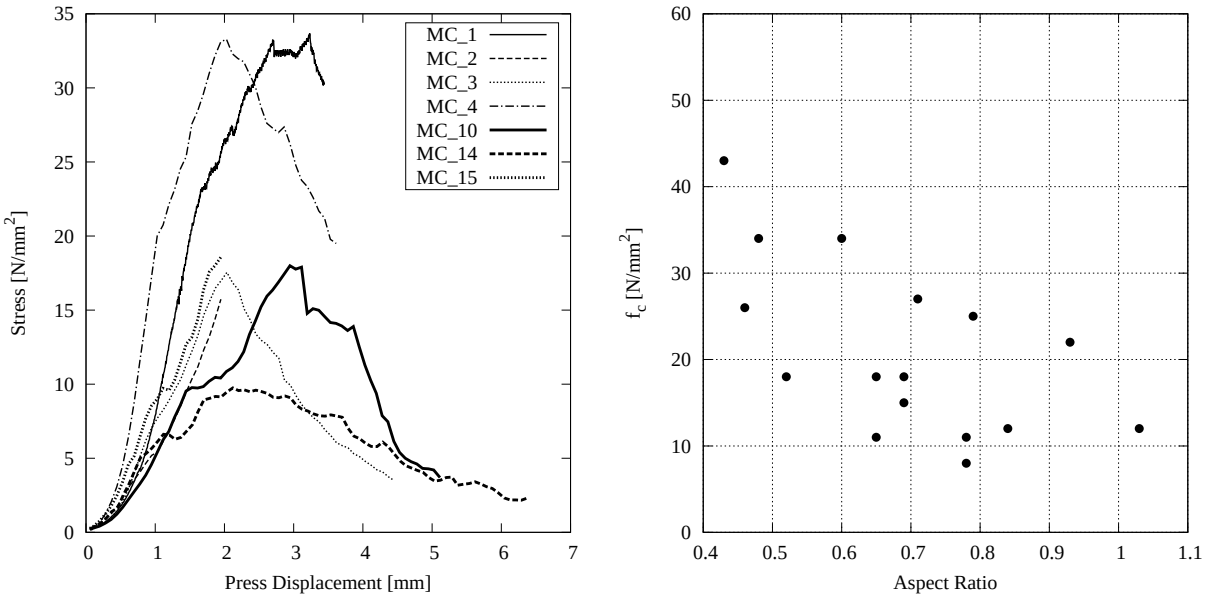

Figure 8.19 (a) Cubic mortar samples compression stress vs. press displacement graphs and (b) compressive strength vs. sample aspect ratio.

The results of the compression tests on the cubic samples are detailed in Table 8.7, while the stress displacement diagrams obtained from the tests are presented in Figure 8.19a. In the results table L1 and L2 represent the length of the two edges of the cubic mortar samples, which when multiplied produce the nominal area of each sample. The actual area is restricted by the length of the load plates of the testing machine, which is 40*mm*. The aspect ratio is defined as the ratio between the height and the minimum edge length of the sample. The compressive strength has been calculated by dividing the maximum force by the actual sample area and in turn dividing by a correction factor relating the compressive strength of a sample with an a standard sample with an aspect ratio different from 1. This factor is calculated as proposed by Drdácký for cement mortar samples with varying aspects ratios [52] according to the expression

$$f_{cm} = F_{\max}/(H/L)^{-1.065} \tag{8.2}$$

where H is the sample thickness and L its length.

Table 8.7 Cubic mortar samples compression results. Coefficient of variation in parentheses.

Sample	L1 [mm]	L2 [mm]	Nominal Area [mm^2]	Actual Area [mm^2]	Thickness [mm]	Aspect Ratio [-]	Correction Factor [-]	F_{max} [kN]	f_{cm} [N/mm^2]
MC_1	36	40	1679	1460	19.6	0.544	1.911	49.17	17.6
MC_2	30	35	1050	1050	21.0	0.701	1.460	18.51	12.1
MC_3	37	40	2014	1540	31.4	0.849	1.191	27.01	14.7
MC_4	33	40	1374	1340	22.2	0.672	1.527	45.05	22.0
MC_5	29	35	988	988	24.9	0.859	1.176	24.68	21.2
MC_6	40	40	1680	1600	17.5	0.438	2.408	68.20	17.7
MC_7	37	38	1406	1406	17.3	0.467	2.251	35.92	11.4
MC_8	37	40	1501	1501	25.3	0.682	1.502	17.19	7.6
MC_9	22	35	776	776	20.1	0.914	1.101	20.57	24.1
MC_10	28	39	1112	1112	28.3	1.009	0.990	13.32	12.1
MC_11	33	40	1374	1340	29.0	0.879	1.148	10.53	6.8
MC_12	38	32	914	914	28.2	1.007	0.992	20.46	22.6
MC_13	29	35	1015	1015	24.9	0.859	1.176	11.08	9.3
MC_14	27	39	1112	1112	17.5	0.647	1.59	19.88	11.3
MC_15	31	33	1056	1056	33.6	1.083	0.909	12.84	13.2
MC_16	26	30	770	770	19.2	0.738	1.381	11.30	10.6
Average									14.9 (0.377)

Nearly all samples had an aspect ratio of well below 1, the value considered adequate for mortar compression tests. Even the samples with an aspect ratio near to 1 did not have the dimensions prescribed in masonry mortar testing codes, which are oriented towards the testing of mortars produced in molds [41]. The relation of compressive strength vs. the aspect ratio obtained in the tests is shown in Figure 8.19b. Despite the scatter of the results, a trend of decrease of the compressive strength for an increase of the aspect ratio is evident. Considering all the results an average value of $14.9 N/mm^2$ is obtained, with a coefficient of variation of 0.377. The average value obtained is 50% lower than the one estimated from the minor-destructive tests already presented. Given that the mortar cubes were originally located mostly in the infill and not the joints, a difference between the results is expected due to the mortar in the infill not being as well compacted as the one in the bed joints.

Several sets of recommendations have been compiled for the carrying out of double punch tests on mortar layers [26, 79] and a number of applications has been recorded in the literature [125, 150]. The mortar layer samples in this campaign were subjected to displacement control loading at a rate of $0.015 mm/sec$. Gypsum layers were again placed on the load surfaces of the samples. The gypsum layers were $1-2mm$ thick. A $20mm$ diameter punch was used for the tests employing a hinged setup for the punch heads (Figure 8.20). Two families of samples were produced and tested: one composed of samples with a circular shape and a diameter of $75mm$, which were extracted from the couplets without further processing, and one composed of samples with a square shape and an edge length of $55mm$, which were produced by sawing

(a) (b)

Figure 8.20 Test setup for (a) mortar layer double punch test and (b) mortar cubic sample compression test.

extracted circular samples.

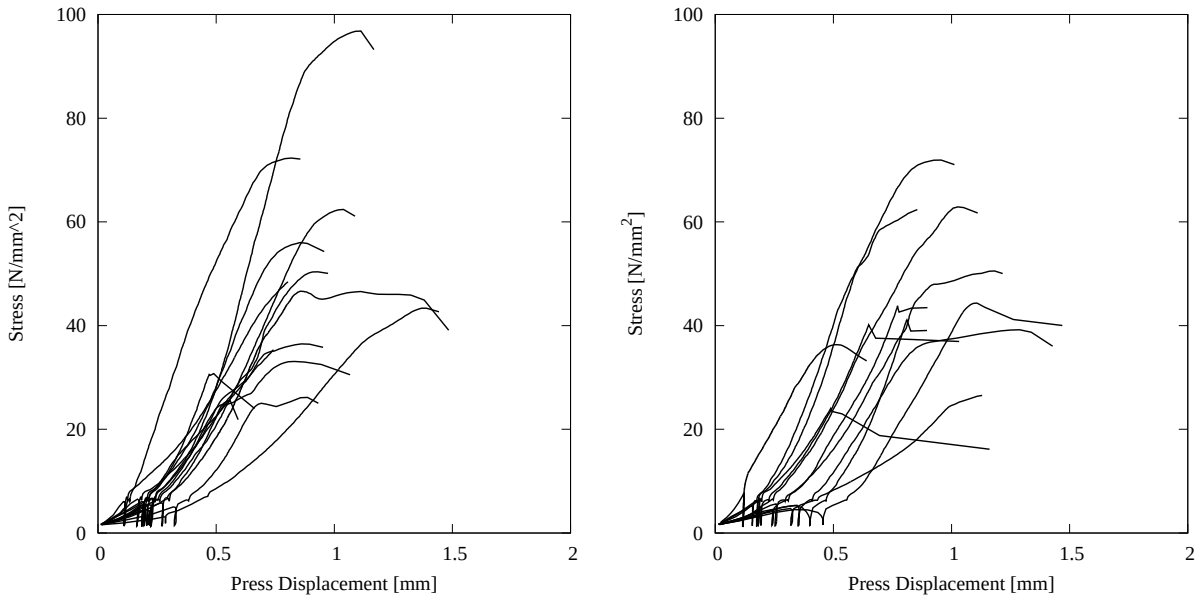

(a) (b)

Figure 8.21 Mortar layer samples compression stress vs. press displacement graphs: (a) square samples and (b) circular samples.

The summary of the results is given in Table 8.8. Both sample families produced roughly the same average compressive strength, although again with a high standard deviation, owed mostly to the wide range of sample thicknesses in the tests. A number of outliers were identified, such as SL_6 and SL_9 among the square samples, having a compressive strength far above the trend, and CL_2, CL_8 and CL_11 for the same reason among the circular samples.

The influence of the sample thickness on the compressive strength is shown in Figure 8.22, which include the already mentioned outliers. The square samples exhibited a trend of reduction of the compressive strength for an increase in the thickness. A similar trend was visible for the

Table 8.8 Mortar layer double punch test results using 20*mm* diameter punch. Coefficient of variation in parentheses.

Square Sample	Thickness $[mm]$	F_{max} $[kN]$	f_{cm} $[N/mm^2]$	Circular Sample	Thickness $[mm]$	F_{max} $[kN]$	f_{cm} $[N/mm^2]$
SL_1	8.1	14.63	46.6	CL_1	6.2	11.40	36.3
SL_2	8.3	15.23	48.5	CL_2	7.4	19.63	62.5
SL_3	6.2	11.15	35.5	CL_3	8.1	12.31	39.2
SL_4	9.4	17.58	56.0	CL_4	8.3	13.94	44.4
SL_5	10.7	11.46	36.5	CL_5	9.4	13.78	43.9
SL_6	9.6	30.43	96.9	CL_6	9.6	7.60	24.2
SL_7	9.8	15.83	50.4	CL_7	9.8	12.91	41.1
SL_8	19.4	8.04	25.6	CL_8	10.7	22.61	72.0
SL_9	7.4	22.73	72.4	CL_9	10.7	15.01	47.8
SL_10	10.7	10.39	33.1	CL_10	10.9	12.65	40.3
SL_11	15.4	9.64	30.7	CL_11	11.0	19.78	63.0
SL_12	10.9	13.63	43.4	CL_12	14.2	8.32	26.5
SL_13	11.0	19.59	62.4				
SL_14	14.2	8.26	26.3				
Average			47.4 (0.416)	Average			45.1 (0.319)

circular samples, with the exception of two results that did not match the overall trend. The larger size of the circular samples, and, therefore, the larger amount of material surrounding the punch area, produce a stronger lateral confinement on the cross section of material under compression. Therefore, size effects due to sample thickness are not as pronounced as in the square sample case.

The results obtained from the double punch test produce results for the compressive strength of the mortar that are much higher than those estimated by the minor-destructive testing and from the compressive tests on the mortar cubic samples. For the interpretation of the results the recommendations made by the International Union of Railways [79] have been consulted. According to these recommendations the compressive strength of the mortar is evaluated from samples of a thickness of $10-25mm$. Considering these values from the present group of samples, excluding the outliers, an average compressive strength of $40N/mm^2$ is obtained for the cement mortar. A very proximate value of $42N/mm^2$ is obtained when considering the samples with a thickness lower than $10mm$ as well. The former value is 25% higher than the value obtained from the nondestructive tests and 50% higher than the tests on the mortar cubes, the latter being a difference higher than that between the mortar cubic samples and the layer samples.

The higher strength achieved by the double punch test compared to the cubic samples may be attributed to several factors apart from the quality and origin of the samples themselves. The small surface of the punch limits the effect of sample imperfection and damage. Furthermore, it is easier to achieve good contact between the load plates and the samples, the use of gypsum layers notwithstanding.

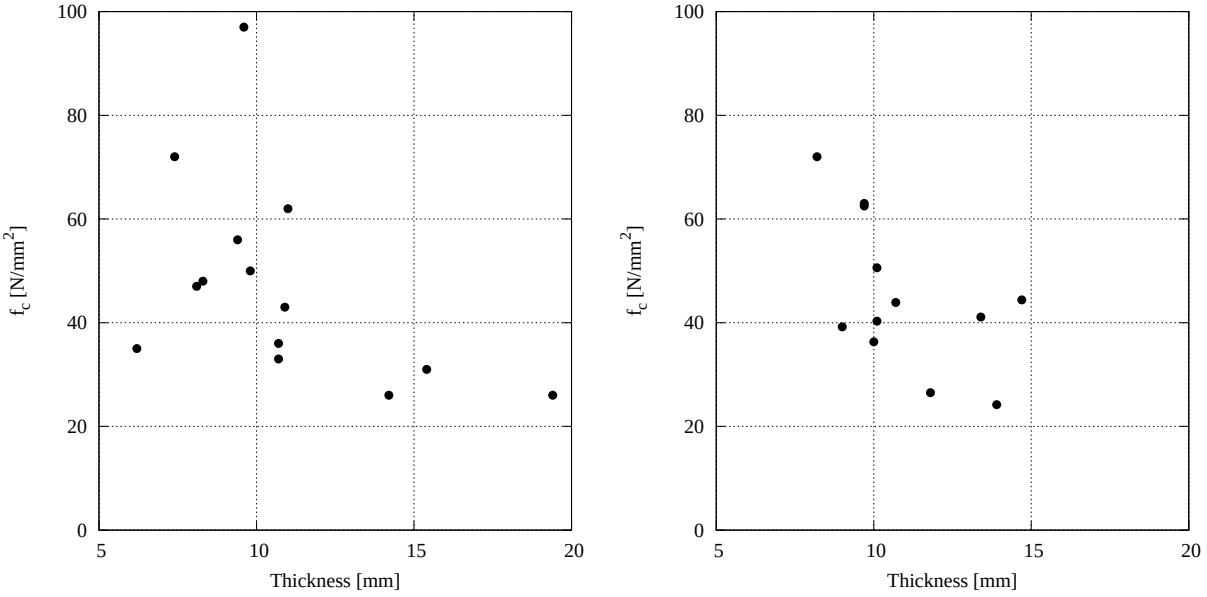

Figure 8.22 Compressive strength vs. sample thickness: (a) square samples and (b) circular samples.

8.11 Discussion on the Results

The extraction of material samples using core drilling on an existing structure allows the acquisition of test specimens of equal size for most tests. This includes unit and infill samples for compressive and tensile testing, couplet samples for compressive testing and mortar layer samples for double punch testing. The uniformity of the test specimens for each category of testing is beneficial for the carrying out of the tests themselves and for the interpretation of the results.

Wide scatter was registered concerning the Young's modulus of the components. On the other hand, their compressive and the tensile strength results were less scattered, although the compressive strength of the infill also exhibited moderate scatter.

The two sets of double punching tests for the mortars produced proximate results, despite the differences in the sample shape. Additionally, the mortar layer samples are relatively easy to produce from couplets and triplets and the only varying dimension is the thickness. In regular structures this dimension ought to not vary very widely. In addition, this thickness is the only parameter used as a basis for the interpretation of the results obtained. The application of a thin gypsum layer, which can be performed very easily, alleviates many of the problems faced by load surface roughness and non-parallel orientation. On the other hand, obtaining cubic samples was painstaking and resulted in samples with widely varying sizes. Control of the regularity and planarity of the load surfaces was difficult, even with the application of gypsum layers. Finally, despite its ease of execution, the penetration tests are limited to evaluating the mortar near the surface of the structure. Overall, the double punch test on mortar layers appears to be the optimal solution for an accurate measurement of the compressive strength of mortar in an existing structure.

According to the material test results, all the material components (units, mortar and infill)

had a compressive strength higher than that of the entire pillar. Even the lowest compressive strength registered in the material tests was higher than the compressive strength of the pillar. The interaction of the materials, the complex geometrical interlocking, irregularities in geometry and material properties and the existence of macroscopic damage appear to have a strong effect on the compressive capacity of the pillar.

The effect of the scatter of the compressive strength of the infill samples is compounded when studying the macroscopic behavior of the infill as a whole. It may be assumed that areas of low strength are present in the infill, which would lower the global compressive strength of the infill part. Size effects lowering the apparent strength of the infill in comparison to the small samples extracted and tested may also be involved. Of further note is the brittle behavior of parts of the infill noted in the testing of the samples which could detrimentally influence its global response. The differences in stiffness noted at different parts of the pillar during the compressive test on the full structure constitute evidence of the varying properties of the materials involved.

The mechanical properties of the unit/mortar interface were not investigated in this study. While its behavior in the pillar structure under concentric compressive loading is not expected to play a major role, a methodology may be proposed for the determination of the mechanical properties of the unit/mortar interface. Given that unit/mortar couplets may be extracted from masonry walls using the same coring process employed here, it is an investigation worth undertaking. Bond wrench tests on unit/mortar couplets can be executed with limited effort on samples such as the ones tested in compression, thus characterizing the tensile strength of the interface. Additionally, unit/mortar couplets and triplets can be employed for shear testing for the determination of the frictional properties of the interface. This potentially requires more arduous sample preparation and complicated testing setups due to the small size of the samples.

8.12 Numerical Model

8.12.1 Overview

Following the extensive material characterization described carried out and presented, a numerical simulation of the compression test of the full pillar was carried out. A finite element model based on detailed micro-modeling approach was developed. The individual parts of the model are shown in Figure 8.23, along with a horizontal cross section of the pillar. Based on previous studies that indicate that the existence of interface nonlinearities between units and mortar do not affect the obtained compressive strength of masonry [55], only an interface between the outer leaf and the infill was considered.

Overall, 36400 20-node brick and 15-node wedge solid elements were used for the continuum parts and 4032 16-node interface elements for the interface between the two leaves. The lead pipe was not considered in the model as it is assumed that its corroded state does not allow it any significant load bearing capacity.

Planes of symmetry were used to reduce the size of the model. Firstly, a horizontal plane

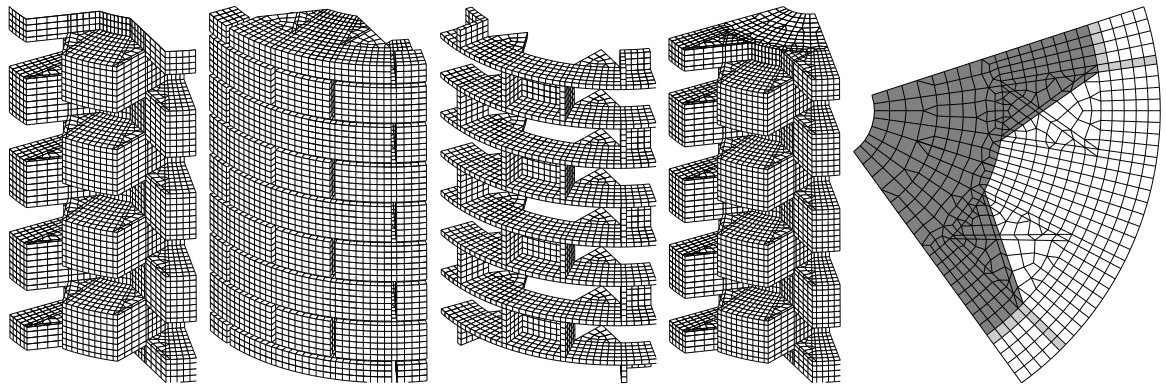

Figure 8.23 Finite element model of pillar: (a) interfaces between outer leaf and infill, (b) units, (c) mortar, (d) infill and (e) cross section of the pillar, with units, mortar and infill shown.

was used at the mid height of the pillar. Secondly, one-fifth of the cross section of the pillar was used, since the entire cross section is composed of five repetitions of the same circular sector. Appropriate boundary conditions were applied on all planes of symmetry considered. Half the pillar along the height was modeled. A single vertical plane of symmetry was considered. Concerning the lateral boundary conditions, two cases were considered: one of an undamaged pillar, for which both lateral sections were constrained and one with only a single lateral section constrained. The latter case was conceived in order to attempt and simulate the effect of the large vertical cracks in the masonry pillar, which nearly separate the pillar in three independent parts.

The mechanical properties of the material components as determined in the experiments were used for the analysis. The properties of the infill were determined taking into account the results of the infill cylinders extracted from the Flemish bond pillar alone. Conventional values were used for unknown material properties. For the Young's modulus of the mortar a value equal to 700 times the compressive strength was used, while a value of 0.20 was used for the Poisson's ratio. The tensile strength of the mortar was taken as equal to 10% of its compressive strength. Similarly, the interface was given mechanical properties in tension and shear equal to values encountered in the relevant literature [152]. All properties used for the analyses are presented in Table 8.9. The values for the tensile fracture energy of all materials and the compressive fracture energy of the mortar were determined according to the suggestions presented in the chapter on finite element micro-modeling. The compressive fracture energy of the units, the infill and the couplet was adjusted in order to fit the experimental curves. The compression curves of the units, mortar and infill according to the material parameters applied are illustrated in Figure 8.25a.

While head and transversal joints commonly suffer from poor mortar compaction, or at the very least poor compaction compared to the bed joints, which are further compacted by the self weight of the member and the applied vertical loads, the same properties were used for the bed, head and transversal mortar joints. The penetration test results presented indicate that the mortar in the head joints has roughly the same compressive strength as the mortar in the bed joints. It was, therefore, decided to use the same mortar properties throughout the model.

The model was subjected to a monotonic vertical displacement applied uniformly at the

Table 8.9 Mechanical properties for numerical analysis of the pillar.

	f_c	f_t	E	ν	G_f^c	G_f^I
	$[N/mm^2]$			[-]	$[N/mm]$	
Units	14	1.5	2500	0.15	10	0.053
Mortar	40	4.0	28000	0.20	40	0.107
Infill	10	1.3	11000	0.10	1	0.049
Couplet	16	-	3500	-	16	-
	f_t	c_0	φ	G_f^I	G_f^{II}	
	$[N/mm^2]$		[-]	$[N/mm^2]$		
Interface	0.2	0.25	45^0	0.012	0.025	

top. This leads to a non-uniform stress distribution between the outer leaf and the infill. The overall vertical elastic stiffness of the former is higher than that of the latter, resulting in a higher concentration of vertical stress in the infill.

8.12.2 Results

A preliminary linear elastic analysis was performed in order to evaluate the distribution of stress in the pillar when subjected to a uniform vertical displacement load. A qualitative depiction of the distribution of the minimum principal stress is shown in Figure 8.24, where a darker color represents a lower minimum principal stress, therefore a higher compressive stress level. The highest values are developed in the head joints and in the infill, especially near the central area of the column and near the interlocking with the units. A decrease of the compressive stress is noted in the infill near the contact area with the transversal mortar joint, which is situated between two large stretcher brick units. In the area of the units the highest vertical compression levels are registered in their central part.

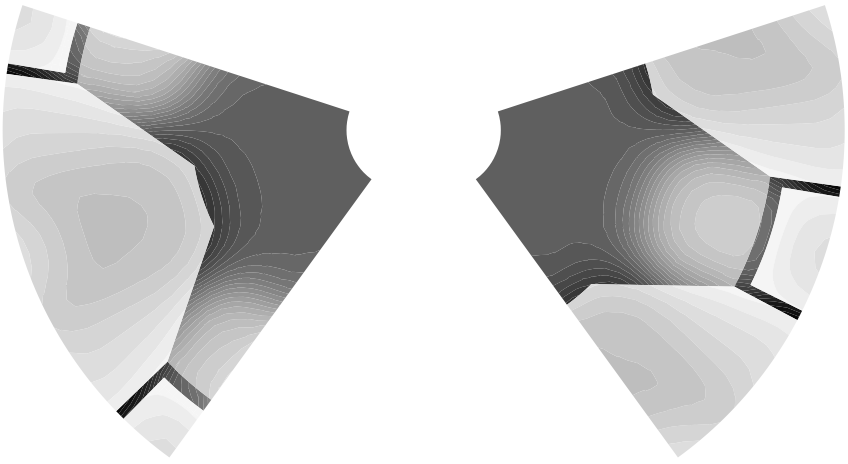

Figure 8.24 Minimum principal stress in pillar cross sections for application of a uniform vertical displacement. A darker shade of grey indicates a higher compressive stress.

In addition to the finite element modeling, a simple analytical macroscopic model may be employed in order for the behavior of the pillar in vertical compression to be better understood. The model is based on the assumption that under vertical compression the outer leaf and the

infill function in perfect composite behavior and, therefore, are subjected to the same strain. Disregarding tensile damage to the components, the effect of existing damage and the lateral expansion of the leaves when yielding in compression the behavior of the pillar can be idealized by assuming that a part of the cross section behaves like the outer leaf, a part of it as the infill and a final part as the central void that does not bear any stress.

For the infill, the same behavior is assumed as in the finite element modeling. The outer leaf is assumed to behave as the couplet. The global stress is calculated as the weighted average of the components, contributing according to their cross section size compared to the gross cross section of the pillar.

By assuming that 35% of the cross section to behave as the infill, 62% as the outer leaf and 2% as voids and summing the contribution of each part to the global stress in the cross section, the curve shown at Figure 8.25b is obtained. The initial elastic stiffness is identical to the experimentally derived value. The global compressive stress reaches a local maximum of $7.7N/mm^2$ before reaching a secondary peak of $9.3N/mm^2$ at the strain coinciding with the peak stress of the outer leaf.

The initial local maximum is remarkably close to the experimentally derived value, despite the simplicity of the model. Several parameters not considered in this analysis could serve to reduce the maximum stress. These include the existing damage and imperfections in the pillar, tensile damage in the components, the interaction of the components after the onset of compressive damage and the non-perfect bond between the outer leaf and the infill. However, the same overall conclusion is reached as highlighted in the linear elastic results of the finite element model: the combined effect of low strength, high stiffness and brittle post-peak behavior of the infill may be detrimental to the global response of the pillar in compression.

Other analytical models for the prediction of the compressive strength of three-leaf masonry have been proposed, mostly for the purpose of estimating the strength increase in injected members [151, 157]. The model proposed by Egermann and Nuewald-Burg in particular could potentially be applied in this case [57]. It is based on the compressive strength and the volume of the two leaves, the compressive strength of the wall being

$$f_c = \left(\frac{V_o}{V_w}\right)\theta_o f_{co} + \left(\frac{V_i}{V_w}\right)\theta_i f_{ci} \tag{8.3}$$

V_o, V_i and V_w are the total volumes of the outer leaf, the infill and the member. The factors θ_i and θ_o are constants which represent the interaction of the leaves. The former is equal to or larger than 1 and indicates the increase in the compressive strength of the infill due to confinement. The latter is equal to or lower than 1 and indicates the decrease in the strength of the outer leaf due to the expansion of the infill. Both factors, in addition to being empirical, describe an interaction process between an outer leaf much stronger and stiff than the infill. The expression may, therefore, be considered ill-suited to the present case. It does however offer a qualitative insight on the fact that failure of one component influences the bearing capacity of the other. Under this light, it seems unlikely that the secondary peak registered in Figure 8.25b may be indeed encountered in practice.

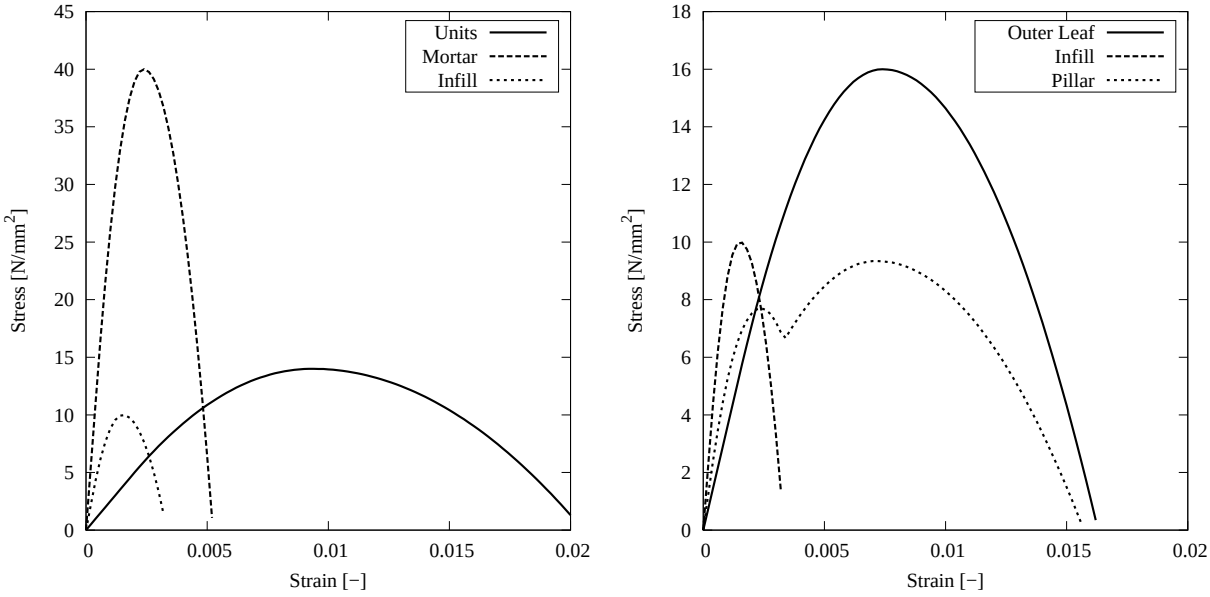

(a) (b)

Figure 8.25 (a) Curves for materials in compression used for finite element modeling and (b) curves in compression for components used for analytical modeling.

In the present case, a value of 1 will be assumed for the θ_i factor: the high stiffness of the infill does not allow it to be confined by the external leaf. For the θ_o factor a value of 0.67 will be assumed, as specified in [57], representing the decrease in the strength of the outer leaf due to bending caused by lateral expansion of the infill. With these assumptions, the model produces a value of $9.85N/mm^2$. This value is considerably higher than the value obtained from the experiment.

The finite element model of the intact pillar produces a maximum compressive stress equal to $8.4N/mm^2$, which is 30% higher than the experimental value. The model of the cracked pillar produces a compressive strength of $7.6N/mm^2$, which is noticeably lower than the former analysis result and closer to the experimental value. The moderate difference may be attributed to the existing damage and irregularities existing in the structure and absent in the model. The Young's modulus obtained from the numerical analysis is equal to the experimentally derived value. The initial Poisson's ratio, as defined by the change of diameter at the mid-height of the pillar, was 0.22, which is higher than the Poisson's ratio of any of the constituent materials but equal to the initial Poisson's ratio measured in the experiment. The vertical stress has been calculated on the gross circular cross section including the gap in the middle of the pillar.

Several observations can be made concerning the failure mode obtained from the numerical model, especially for purposes of comparison with the experimentally derived mode. Very limited hardening was noted in the numerically obtained force-strain diagram, a behavior similar to the one observed in the experiment, as shown in Figure 8.26, although the beginning of the softening of the response was not as abrupt as in the case of the experiment.

The infill exhibited significant compressive yielding, which is to be expected given its higher Young's modulus and lower compressive strength compared to the outer leaf. Additionally,

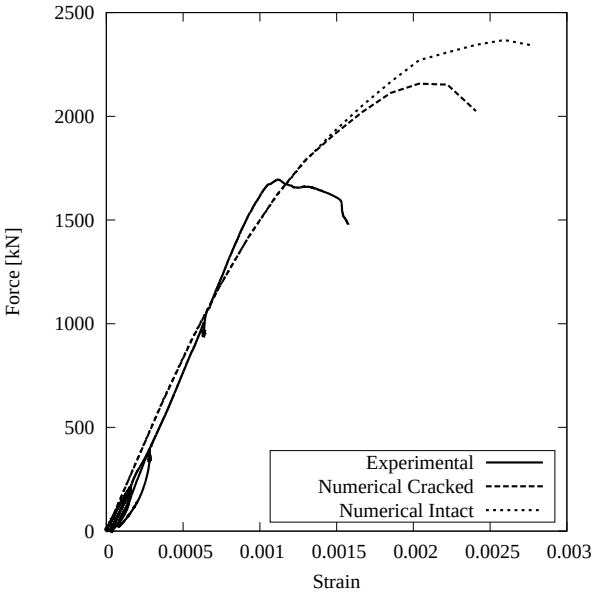

Figure 8.26 Pillar compression force-strain graphs: Comparison between experimental and numerical results.

significant tensile damage was noted in the infill, particularly evident in the interlocking parts with the clay bricks of the outer leaf. At the point of change of stiffness of the force-strain graph the infill, almost in its entirety, has reached its peak compressive stress. This corresponds to the point in which the maximum force was reached in the experiment.

Damage in the outer leaf consisted mainly of tensile damage in the mortar joints. Additionally, limited vertical cracks were formed in the units propagating from the mortar in the head joints. It is reminded that nearly all the visible damage in the outer leaf originated from areas of existing damage or near the load caps.

The obtained damage patterns are illustrated in Figure 8.27. All damage patterns exhibited periodicity along the height of the pillar. A single representative repeating volume of the pillar is used for illustrating this damage in two cross sections of the pillar. The cracks in the infill at the points of interlocking with the units is evident. These are the same locations at which, as shown in Figure 8.24, the vertical compression stress is highest. The limited extent of cracking damage on the external parts is also shown. Cracks in the units originating at the intersection with the head joints are shown. Additionally, the distribution of minimum principal stress at the top of the pillar is shown in the figure. The stress in the head and transversal mortar joints remains high, as in the central part of the units as well. In both of these cases the minimum principal stress is slightly lower than the compressive strength of these materials. The stress over large parts of the infill is close to zero, the material having undergone almost complete softening. The area of the infill near the transversal joint also presents a concentration of stress, which is the opposite of what was noted in the linear elastic results presented in Figure 8.24.

Overall, the compressive strength obtained for the pillar was lower than the compressive strength of any of the material components and the failure appears to be attributable to excessive damage in the infill and limited damage in the outer leaf. The external leaf, especially the area

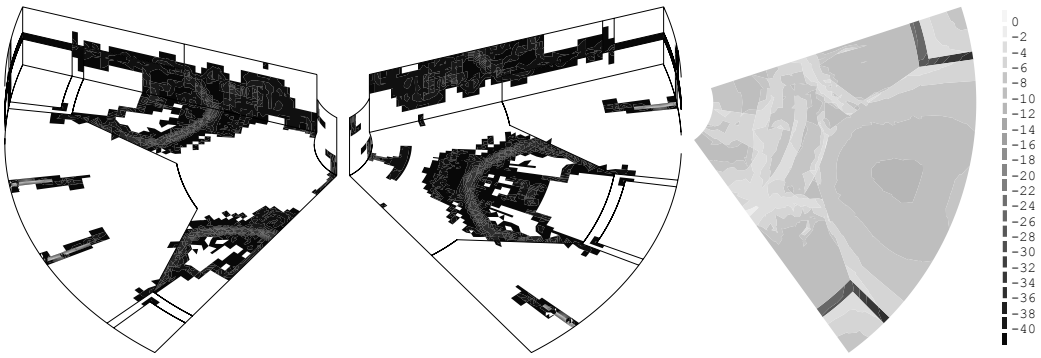

(a) (b) (c)

Figure 8.27 Numerically obtained failure mode at peak vertical stress: (a) & (b) cracking patterns in pillar cross sections and (c) distribution of minimum principal stress at the top of the pillar.

externally visible, exhibited limited damage. This is in general agreement with observations made following the experiment concerning the strength and failure mode of the pillar.

8.13 Conclusions

A masonry pillar extracted from a historical building was tested in concentric compression. Material extracted from the pillar was tested as well in a variety of mechanical tests. Further non-destructive and minor-destructive tests provided valuable information on the construction process and structural behavior of the pillar. A finite element model of the pillar was used for the numerical simulation of the pillar compressive test.

The majority of the material mechanical properties necessary for the execution of a numerical analysis using micro-models was possible to be determined. Clay units, infill and cement mortar were extensively tested using samples extracted through core drilling, while a number of non-destructive and minor-destructive tests were performed as well.

The experimentally derived compressive strength of the pillar is lower than that of any of its constituent materials. This may be attributable to the scatter of the compressive strength and ductility of the materials (especially the infill), size effects and the effect of existing damage.

The finite element micro-model was able to accurately reproduce the experimental value of the Young's modulus of the masonry pillar and to give a fair approximation of its compressive strength. The effect of the difference in the stiffness between the two leaves of the pillar was highlighted: the high stiffness of the infill is detrimental to the global behavior of the pillar in compression. Furthermore, the existing damage on and imperfections of the pillar appear to strongly influence its compressive strength, as shown by altering the boundary conditions of the pillar model and comparing the numerical outcomes.

In addition to the detailed finite element model, a simple analytical model was able to highlight the main structural characteristics of the pillar which affect its behavior in compression. The model is based on the stress-strain curves in compression of the main components of the pillar and not only their peak stress.

The material extraction and testing methodology followed is applicable to a variety of masonry structures and presents a sound basis for the structural evaluation of existing structures and their simulation using micro-models.

Chapter 9

Summary and Conclusions

Detailed Micro-Modeling

A framework for the analysis of masonry walls and pillars using detailed micro-modeling techniques has been presented. The framework has been applied to the simulation of masonry structures subjected to compression and has been shown to provide good estimations of the strength and elastic stiffness of masonry.

A number of practical considerations have been provided for the analyst willing to employ detailed micro-modeling of masonry. Based on a compiled inventory of experimental cases, recommendations are given for the estimation of missing material parameters. The shortcomings of plane stress and plane strain methods have been detailed, as well as the effects of mesh refinement.

The accuracy of the finite element analysis results obtained have been contrasted with results obtained from closed form expressions against the experimental data, indicating a consistently better predictive behavior exhibited by the detailed methods.

Detailed micro-modeling using finite elements may prove to be computationally demanding in the case of the analysis of large structures. The development of alternative/complementary methods of analysis is deemed, for the time being, useful.

Application to Pure Lime Mortar Masonry Tests

An experimental campaign on the compressive strength of pure lime mortar masonry is carried out. The materials used correspond to materials encountered in numerous historic structures. Additionally, the campaign deals with the carrying out of tests for the determination of the material properties needed for micro-modeling analysis. These tests are applicable both to new materials and to materials extracted from existing structures.

The campaign was developed in a controlled laboratory environment. The produced masonry composites were characterized by a high compressive strength, despite the use of very low strength mortars, and a low Young's modulus.

Using the framework developed for detailed micro-modeling, a good prediction of the compressive strength of masonry was achieved. A parametric study of the influence of the properties of the materials was performed. This study highlighted the importance of material properties often seen as secondary in the prediction of the compressive strength: the Young's modulus and the Poisson's ratio of the mortar. The study of the influence of the modeling method was also investigated. The results are strongly in favor of adopting three dimensional modeling for the prediction of the compressive strength of masonry.

Design code specifications failed to provide a good prediction of either the compressive strength or the Young's modulus of the mortar.

Application to Shear Wall Tests

The micro-modeling framework was applied to experimental tests involving shear walls. The prediction of the maximum shear was good, as was the prediction of the failure mode.

The influence of the modeling method in the determination of the maximum shear is investigated. In the case of shear walls, three dimensional modeling was proven to be as accurate as plane strain modeling, while plane stress was not able to produce good results. Computational costs for three dimensional modeling are high. The influence of the behavior of masonry in compression is shown to be critical for the case of shear walls and not just for masonry subjected to pure compression.

Prediction of the Compressive Strength of Masonry

When over-viewing the typical dimensions of a wall or wallette, plane-stress analysis appears conceptually sound due to the small thickness of the full member compared to its total height and length. The confinement of the mortar in the joint, however, is a localized phenomenon, and, therefore, the dimensions to be compared ought to be the thickness of the joint and the transversal thickness of the wall. In this context, the effect of the local out-of-plane stresses becomes significant and plane stress analysis is rendered ineffective. On the other hand, plane-strain modeling appears to overestimate the confinement effect to an unrealistic degree.

Three-dimensional micro-modeling has consistently proven to be the most accurate method to predict the compressive strength of masonry. It results in an intermediate amount of mortar confinement, as produced by the material properties and the geometrical arrangement of the masonry. Plane-stress and plane-strain modeling may provide accurate results under certain conditions: the former when the units do not provide much confinement on the mortar and the latter when the opposite is true.

Concerning the influence of certain material properties on the compressive strength of masonry, a strong connection was found between the predicted strength and some parameters which have not been as deeply investigated as others and/or which are often difficult to determine. A characteristic example of this fact is the Poisson's ratio of the mortar.

Micro-Mechanical Modeling

The accuracy of micro-modeling in simulating the behavior of masonry in compression has been verified. The importance of three-dimensional modeling has been shown to be highly important. This, however, raises the computational cost significantly when employed in finite element analysis. Furthermore, the influence of several material parameters has been demonstrated to be of importance for the numerical determination of the compressive strength of masonry.

For these reasons, a modeling method combining the main features of the detailed micro-modeling approach developed previously has been presented. A three-dimensional micro-mechanical model for the analysis of masonry periodic unit cells is proposed, based on analytical expressions. This model combines the accuracy of the detailed micro-modeling approach with the low computational costs of analytical expressions.

Several different typologies of masonry walls and pillars are modeled, including Flemish bond and three-leaf walls, which have not received significant attention in the literature. The models are able to predict the elastic properties of masonry composites accurately and with a computational cost negligible compared to finite element modeling. These models, especially for the derivation of the elastic properties of masonry, can be implemented without resorting to specialized software.

The compressive strength of masonry is also accurately predicted, as is indicated through comparisons with experiments and finite element benchmark analyses. The behavior of the masonry composite in tension has also been studied. The low computational cost allows for a wide and deep parametric campaign to be performed in order to study the effect of material and geometric properties of the materials on the compressive strength of masonry. Emphasis is placed on the parameters identified in chapter 4, to which the sensitivity of the result appears to be high.

Finally, analytical expressions for the prediction of the compressive strength of masonry are proposed. These expressions are simplifications of the micro-mechanical models presented and are able to provide good results.

Application to a Historical Structure

Detailed micro-modeling requires the determination of numerous material properties of all the components of the masonry composite. The determination of these properties is challenging even in a controlled laboratory environment. This problem is made more difficult in the study of existing structures due to the need to extract material for testing.

Analysis using detailed methods can provide very useful information on the behavior of masonry structural elements. In the context of preservation engineering, it can lead to better evaluation of a structure and more efficient intervention design.

Considering the above, a detailed investigation of a masonry pillar extracted from a historic structure is carried out. The investigation includes testing of the pillar in compression and detailed micro-modeling simulation of the experiment.

Material from the pillar is extracted and subjected to mechanical testing, leading to the determination of the majority of the material properties necessary for a micro-modeling simulation. The missing parameters were determined according to the conclusions of chapter 3. The framework for extraction and testing of materials allows for a comprehensive characterization of masonry materials, especially when coupled with the methods applied in the chapter of pure lime mortar masonry. This framework is applicable for other masonry typologies as well.

Detailed micro-modeling of the compression test on the pillar provided good predictions of the compressive strength, Young's modulus and failure mode of the member. It especially highlighted the influence of the mismatch in the Young's modulus of the masonry leaves on the failure mode.

An analytical model for the determination of the compressive strength of pillars or walls with infill is proposed, based on the behavior of individual leaves in compression. Instead of relying only on the peak stress of the leaves, the influence of the Young's modulus is highlighted. The modeling concept adopted for this analytical model is applicable to pillars with infill and to three-leaf walls.

Suggestions for Future Work

The evolution of the Poisson's ratio of mortar under increasing loads has already been investigated by a number of researchers. In the context of its behavior in joints in masonry more attention needs to be paid by analysts. The development and application of models for the evolution of the Poisson's ratio of lime based and cement based mortars under compressive loads appears to be an important parameter for detailed micro-modeling analyses.

The derived closed form expression for the prediction of the compressive strength of masonry includes a quantification of the amount of confinement afforded on the mortar by the units. This quantification, based on the mismatch of the elastic properties of the two materials, could serve as a guide in electing a plane-stress or plane-strain model instead of a full three-dimensional model in order to benefit from the lower computational cost of plane methods in the cases where they are capable of providing good results. Further development of the model could be attempted in order to include the influence of head and/or transversal mortar joints on the compressive strength of masonry. Additionally, the model could be refined to represent the ratio of lateral to vertical stress beyond the elastic range of masonry more accurately.

A promising field of application for the developed micro-mechanical models is for use in two-scale models of masonry walls and pillars. Their capacity to provide good estimates of the compressive strength of masonry coupled with their low computational cost make them a sound basis for the analysis of large masonry members or even buildings in a method that takes advantage of detailed modeling methods for the analysis of extended systems. Members that can be analyzed in this manner using the models developed here include membrane structures, such as vaults and arches, in addition to pillars and walls.

Further developments are possible for the basic characteristics of the proposed micro-mechanical models. Anisotropic elasticity, as is often exhibited by clay bricks, is easy to implement. In ad-

dition, the models may be applied to further masonry typologies, such as English bond walls. Additional modifications to the model may be used to simulate the existence of reinforcement elements, such as rebars and stirrups. Finally, the models can be used as a basis for the numerical simulations of creep and shrinkage in masonry members.

The sampling/testing methodology based on masonry cores perpendicular to the bed joint can be used for the determination of the properties of the unit/mortar interface properties in existing structures.

Bibliography

[1] J. Aboudi. *Mechanics of Composite Materials: A Unified Micromechanical Approach*. Studies in Applied Mechanics 29, Elsevier, Amsterdam, 1991.

[2] ACI. *ACI 530.1-11. Building Code Requirements and Specification for Masonry Structures and Related Commentaries*. 2011.

[3] J. M. Adam, A. Brencich, T. G. Hughes, and T. Jefferson. Micromodelling of eccentrically loaded brickwork: Study of masonry wallettes. *Engineering Structures*, 32(5):1244–1251, May 2010.

[4] D. Addessi and E. Sacco. A multi-scale enriched model for the analysis of masonry panels. *International Journal of Solids and Structures*, 49(6):865–880, 2012.

[5] M. Ahmadi, M. Izadinia, and H. Bachmann. A discrete crack joint model for nonlinear dynamic analysis of concrete arch dam. *Computers & Structures*, 79(4):403–420, Feb. 2001.

[6] M. A. Aiello, F. Micelli, and L. Valente. Structural upgrading of masonry columns by using composite reinforcements. *Journal of Composites for Construction*, 11:650–658, 2007.

[7] M. A. Aiello, F. Micelli, and L. Valente. FRP confinement of square masonry columns. *Journal of Composites for Construction*, 13(148):148–158, 2009.

[8] A. Akbarzade and A. Tasnimi. Nonlinear Analysis and Modeling of Unreinforced Masonry Shear Walls Based on Plastic Damage Model. *Journal of Seismology and Earthquake Engineering*, 11(4):8–12, 2011.

[9] G. K. Al-Chaar and A. B. Mehrabi. Constitutive Models for Nonlinear Finite Element Analysis of Masonry Prisms and Infill Walls. *ERDC/CERL TR- 08-19*, 2008.

[10] S. S. Ali, I. D. Moore, and A. W. Page. Substructuring technique in nonlinear analysis of brick masonry subjected to concentrated load. *Computers & Structures*, 27(3):417–425, 1987.

[11] S. S. Ali and A. W. Page. Finite Element Model for Masonry Subjected to Concentrated Loads. *Journal of Structural Engineering*, 114(8):1761–1784, 1989.

[12] C. Almeida. Análise do comportamento da igreja do Mosteiro da Serra do Pilar sob a acção dos sismos, 2000.

[13] C. Almeida, C. Q. Costa, J. Guedes, A. Arêde, and A. Costa. Mechanical Behaviour Analyzes of One Leaf Stone Masonry. In *VI Congreso Internacional sobre Patología y Recuperación de Estructuras, 2-4 June 2010, Córdoba, Argentina*, 2010.

[14] C. Almeida, J. P. Guedes, a. Arêde, C. Q. Costa, and a. Costa. Physical characterization and compression tests of one leaf stone masonry walls. *Construction and Building Materials*, 30:188–197, May 2012.

[15] J. C. Almeida, P. B. Lourenço, and J. Barros. Characterization of brick and brick–mortar interface under uniaxial tension. In *Proceedings of 7th Int. Seminar on Structural Masonry, Brazil: CEFET-MG*, number 1997, pages 67–76, 2002.

[16] A. Anthoine. Homogenization of periodic masonry: plane stress, generalized plane strain, or 3D modelling? *Communications in Numerical Methods in Engineering*, 13:319–326, 1997.

[17] A. Aprile, A. Benedetti, and F. Grassucci. Assessment of cracking and collapse for old brick masonry columns. *Journal of Structural Engineering*, 127(12):1427–1435, 2001.

[18] Associação Brasileira de Normas Técnicas. *NBR 8522 - Concreto - Determinação dos módulos estáticos de elasticidade e de deformação e da curva tensão- deformação*. 2004.

[19] ASTM. *ASTM C42 / C42M-13, Standard Test Method for Obtaining and Testing Drilled Cores and Sawed Beams of Concrete*. ASTM International, 2013.

[20] R. Atkinson, D. P. Abrams, and J. L. Noland. Basic Properties of Clay-Unit Masonry Stack-Bond Prisms in Compression. In *8th World Conference on Earthquake Engineering*, San Fransisco, California, 1984.

[21] R. Atkinson, B. Amadei, S. Saeb, and S. Sture. Response of masonry bed joints in direct shear. *Journal of Structural Engineering*, 115(9):2276–2296, 1989.

[22] M. M. Attard, A. Nappi, and F. Tin-Loi. Modeling Fracture in Masonry. *Journal of Structural Engineering*, 133(10):1385–1392, 2008.

[23] C. S. Barbosa, P. B. Lourenço, and J. a. B. Hanai. On the compressive strength prediction for concrete masonry prisms. *Materials and Structures*, 43(3):331–344, Mar. 2010.

[24] R. Berto, L., Saetta, A., Scotta, R., Vitaliani, L. Berto, A. Saetta, R. Scotta, and R. Vitaliani. Failure mechanism of masonry prism loaded in axial compression: computational aspects. *Materials and Structures*, 38(276):249–256, Jan. 2005.

[25] L. Binda, A. Fontana, and G. Frigerio. Mechanical behaviour of brick masonries derived from unit and mortar characteristics. In *8th International Brick and Block Masonry Conference, Vol.1, Dublin, Ireland*, pages 205–216, 1988.

[26] L. Binda, I. Papayianni, E. Toumbakari, and R. van Hees. Mechanical tests on mortars and assemblages. In *Characterisation of Old Mortars with Respect to their Repair - Final Report of RILEM TC 167-COM*, number March, pages 57–76. 2002.

[27] P. Bocca, A. Grazzini, D. Masera, A. Alberto, and S. Valente. Mechanical interaction between historical brick and repair mortar : experimental and numerical tests. In *9th International Conference on Damage Assessment of Structures*, volume 305, 2011.

[28] A. Brencich, C. Corradi, and L. Gambarotta. Compressive strength of solid clay brick masonry under eccentric loading. In *Proceedings British Masonry Society*, pages 37–46, 2002.

[29] A. Brencich and E. Sterpi. Compressive Strength of Solid Clay Brick Masonry: Calibration of Experimental Tests and Theoretical Issues. In *Structural Analysis of Historical Constructions, New Delhi 2006*, number 1995, pages 757–766, 2006.

[30] S. Briccoli Bati, G. Ranocchiai, and L. Rovero. A micromechanical model for linear homogenization of brick masonry. *Materials and Structures*, 32(February):22–30, 1999.

[31] C. Calderini and S. Lagomarsino. A micromechanical inelastic model for historical masonry. *Journal of Earthquake Engineering*, 10(4):453–479, 2008.

[32] K. Callebaut, J. Elsen, K. V. Balen, and W. Viaene. Nineteenth century hydraulic restoration mortars in the Saint Michael's Church (Leuven, Belgium): Natural hydraulic lime or cement? *Cement and Concrete Research*, 31:397–403, 2001.

[33] N. Cavalagli, F. Cluni, and V. Gusella. Strength domain of non-periodic masonry by homogenization in generalized plane state. *European Journal of Mechanics - A/Solids*, 30(2):113–126, Mar. 2011.

[34] CEB-FIP. *Model Code 1990*. Thomas Telford, 1993.

[35] CEB-FIP. *Model Code 2010*. 2012.

[36] A. Cecchi, G. Milani, and A. Tralli. Validation of Analytical Multiparameter Homogenization Models for Out-of-Plane Loaded Masonry Walls by Means of the Finite Element Method. *Journal of Engineering Mechanics*, 131(2):185–198, 2005.

[37] A. Cecchi and K. Sab. A multi-parameter homogenization study for modeling elastic masonry. *European Journal of Mechanics - A/Solids*, 21:249–268, 2002.

[38] CEN. *EN 1052-1 - Methods of test for masonry - Part 1: Determination of compressive strength*. 1999.

[39] CEN. *UNE-EN 772-6 - Métodos de ensayo de piezas para fábrica de albañilería - Parte 6: Determinación de la resistencia a flexotracción de las piezas de hormigón de árido para fábrica de albañileria*. 2002.

[40] CEN. *EN 1996-1-1: Rules for reinforced and unreinforced masonry*. 2005.

[41] CEN. *EN 1015-11 - Methods of test for mortar for masonry - Part 11: Determination of flexural and compressive strength of hardened mortar*. 2007.

[42] CEN. *EN 772-1 - Métodos de ensayo de piezzas para fábrica de albañilería - Parte 2: Determinción de la resistencia a compresión*. 2011.

[43] K. Chaimoon and M. M. Attard. Modeling of unreinforced masonry walls under shear and compression. *Engineering Structures*, 29(9):2056–2068, Sept. 2007.

[44] J. A. Charry Ablanque. *Estudio Experimental del Comportamiento de Paredes de Obra de Fábrica de Ladrillo ante la Acción de Cargas Laterales*. PhD dissertation, Department of Strength of Materials and Structural Engineering, Technical University of Catalonia, Barcelona Spain, 2010.

[45] M. Como. *Statics of Historic Masonry Constructions*. Springer, 2012.

[46] A. Costigan and S. Pavía. Influence of the mechanical properties of lime mortar on the strength of brick masonry. In *2nd Conference on Historic Mortars*, pages 349–360, 2012.

[47] CUR. Structural masonry: a experimental/numerical basis for practical design rules, 1994.

[48] M. E. Dasiou, I. N. Psycharis, and I. Vayas. Verification of numerical models used for the analysis of ancient temples. In *Prohitech Conference*, pages 21–24, 2009.

[49] G. d. F. M. de Vasconcelos, P. B. Lourenço, C. a. S. Alves, and J. Pamplona. Ultrasonic evaluation of the physical and mechanical properties of granites. *Ultrasonics*, 48(5):453–66, Oct. 2008.

[50] P. Degryse, J. Elsen, and M. Waelkens. Study of ancient mortars from Sagalassos (Turkey) in view of their conservation. *Cement and Concrete Research*, 32:1457–1463, 2002.

[51] N. Domède, G. Pons, A. Sellier, and Y. Fritih. Mechanical behaviour of ancient masonry. *Materials and Structures*, 42(1):123–133, Mar. 2009.

[52] M. Drdácký. Non-Standard Testing of Mechanical Characteristics of Historic Mortars. *International Journal of Architectural Heritage*, 5(4-5):383–394, July 2011.

[53] M. Drdácký, D. Masin, M. D. Mekonone, and Z. Slizkova. Compression tests on non-standard historic mortar specimens. In *1st Historical Mortar Conference, 24-26 September 2008, Lisbon*, pages 24–26, 2008.

[54] A. Drougkas, P. Roca, and C. Molins. Micro-Modeling of Stack Bond Masonry in Compression Using a Plasticity Law. In *XII International Conference on Computational Plasticity*, 2013.

[55] A. Drougkas, P. Roca, and C. Molins. Numerical prediction of the behavior, strength and elasticity of masonry in compression. *Engineering Structures*, 90:15–28, 2015.

[56] A. Drougkas, P. Roca, and C. Molins. Strength and elasticity of pure lime mortar masonry. *Materials and Structures*, 2015.

[57] R. Egermann and C. Neuwald-Burg. Assessment of the Load Bearing Capacity of Historic Multiple Leaf Masonry Walls. In *10th International Brick and Block Masonary Conference*, pages 1603–1612, 1994.

[58] A. Eslami, H. Ronagh, S. Mahini, and R. Morshed. Experimental investigation and nonlinear FE analysis of historical masonry buildings – A case study. *Construction and Building Materials*, 35:251–260, Oct. 2012.

[59] B. D. Ewing and M. J. Kowalsky. Compressive Behavior of Unconfined and Confined Clay Brick Masonry. *Journal of Structural Engineering*, 130(4):650–661, 2004.

[60] D. M. Farshchi, M. Motavalli, A. Schumacher, and M. S. Marefat. Numerical modelling of in-plane behaviour of URM walls and an investigation into the aspect ratio , vertical and horizontal post-tensioning and head joint as a parametric study. *Archives of Civil and Mechanical Mechanical Engineering*, IX(1):5–27, 2009.

[61] P. H. Feenstra. *Computational Aspects of Biaxial Stress in Plain and Reinforced Concrete*. PhD dissertation, Delft University of Technology, Delft, The Netherlands, 1993.

[62] T. E. Ford, C. E. Augarde, and S. S. Tuxford. Modelling masonry arch bridges using commercial finite element software. In *9th International Conference on Civil and Structural Engineering Computing*, 2003.

[63] A. Francis, C. Horman, and L. Jerrems. The effect of joint thickness and other factors on the compressive strength of brickwork. In *Proceedings of the 2nd International Brick and Block Masonry Conference*, pages 31–37, 1971.

[64] T. Furtmüller and C. Adam. Numerical modeling of the in-plane behavior of historical brick masonry walls. *Acta Mechanica*, 221(1-2):65–77, Apr. 2011.

[65] L. Gambarotta and S. Lagomarsino. Damage Models for the Seismic Response of Brick Masonry Shear Walls. Part II: The Continuum Model and its Applications. *Earthquake Engineering and Structural Dynamics*, 26(March 1996):423–439, 1997.

[66] H. Ganz and B. Thurlimann. Strength of brick walls under normal force and shear. In *8th Int. Symposium on load bearing brickwork*, pages 27–29, 1983.

[67] D. García, J. T. San-José, L. Garmendia, and R. San-Mateos. Experimental study of traditional stone masonry under compressive load and comparison of results with design codes. *Materials and Structures*, 45(7):995–1006, Jan. 2012.

[68] K. S. Gumaste, K. S. Nanjunda Rao, B. V. V. Reddy, and K. S. Jagadish. Strength and elasticity of brick masonry prisms and wallettes under compression. *Materials and Structures*, 40(2):241–253, July 2007.

[69] V. G. Haach, G. d. F. M. de Vasconcelos, and P. B. Lourenço. Parametrical study of masonry walls subjected to in-plane loading through numerical modeling. *Engineering Structures*, 33(4):1377–1389, Apr. 2011.

[70] P. Haller. *Hochhausbau in Backstein: die technische Eigenschaften von Backstein-Mauerwerk für Hochhäuser*. Verband Schweiz. Ziegelindustrie VSZ, 1959.

[71] A. A. Hamid and A. O. Chukwunenye. Compression behavior of concrete masonry prisms. *Journal of Structural Engineering*, 112(3):605–613, 1986.

[72] B. Haseltine. International Rules for masonry and their effect on the U.K. *Masonry International*, 1(2):41–43, 1987.

[73] A. W. Hendry. *Structural masonry*. Macmillan Education, Limited, 1990.

[74] H. K. Hilsdorf. *Investigation into the failure mechanism of brick masonry loaded in axial compression. Designing, Engineering and Constructing with Masonry Products*. Houston Tex., 1969.

[75] J.-M. Hohberg. *A Joint Element for the Nonlinear Dynamic Analysis of Arch Dams*. Birkhäuser Publishers Basel - Boston - Berlin, 1992.

[76] M. M. Hossain, S. S. Ali, and M. Azadur Rahman. Properties of Masonry Constituents. *Journal of Civil Engineering, The Institution of Engineers, Bangladesh*, CE 28(2):135–155, 1997.

[77] S. Hsieh, E. Ting, and W. F. Chen. A plastic-fracture model for concrete. *International Journal of Solids and Structures*, 18(3):181–197, 1982.

[78] F. Ip. *Compressive Strength and Modulus of Elasticity of Masonry Prisms*. MSc dissertation, Carleton University, Ottawa, Ontario, Canada, 1999.

[79] Italian Ministry of Infrastructure and Transport. Circolare 2 febbraio 2009, n. 617 Istruzioni per l'applicazione delle "Nuove norme tecniche per le costruzioni" di cui al decreto ministeriale 14 gennaio 2008, 2009.

[80] James Instruments. Windsor Pin System WP-2000 - Instruction Manual, 2010.

[81] H. B. Kaushik, D. C. Rai, and S. K. Jain. Stress-Strain Characteristics of Clay Brick Masonry under Uniaxial Compression. *Journal of Materials in Civil Engineering*, (September):728–739, 2007.

[82] C. L. Khoo and A. W. Hendry. *Strength tests on brick and mortar under complex stresses for the development of a failure criterion for brickwork in compression*, volume 21 of *Technical Note*. British Ceramic Research Association, 1973.

[83] H. Köksal and B. Doran. Nonlinear modeling of concentrically loaded reinforced block-work masonry columns. *Canadian Journal of Civil Engineerning*, 3:1012–1023, 2004.

[84] J. Lanas and J. I. Alvarez-Galindo. Masonry repair lime-based mortars: factors affecting the mechanical behavior. *Cement and Concrete Research*, 33(11):1867–1876, Nov. 2003.

[85] J. Lanas, J. Pérez Bernal, M. Bello, and J. I. Alvarez-Galindo. Mechanical properties of natural hydraulic lime-based mortars. *Cement and Concrete Research*, 34(12):2191–2201, Dec. 2004.

[86] J. Lanas, J. Pérez Bernal, M. Bello, and J. I. Alvarez-Galindo. Mechanical properties of masonry repair dolomitic lime-based mortars. *Cement and Concrete Research*, 36(5):951–960, May 2006.

[87] J. V. Lemos. Numerical models for seismic analysis of historical structures. In *Assisi-99 – Workshop on Seismic Performance of Built Heritage in Small Historical Centres, CICOP Italia*, pages K53–K71, 1999.

[88] E. M. Lobato Paz. *Método simple para el análisis de muros de obra de fábrica con aberturas bajo solicitaciones en su plano*. PhD dissertation, Department of Strength of Materials and Structural Engineering, Technical University of Catalonia, Barcelona Spain, 2009.

[89] J. Lopez, S. Oller, E. Oñate, and J. Lubliner. A Homogeneous Constitutive Model for Masonry. *International Journal for Numerical Methods in Engineering*, 46(February):1651–1671, 1999.

[90] H. R. Lotfi and P. Shing. Interface model applied to fracture of masonry structures. *Journal of Structural Engineering*, 120(1):63–80, 1994.

[91] P. B. Lourenço. Analysis of Masonry Structures with Interface Elements. Theory and Applications. *TU-DELFT report no. 03-21-22-0-01, TNO-BOUW report no. 94-NM-R0762*, 1994.

[92] P. B. Lourenço. *Computational strategies for masonry structures*. PhD dissertation, Delft University of Technology, Delft, The Netherlands, 1996.

[93] P. B. Lourenço. Computations on historic masonry structures. *Progress in Structural Engineering and Materials*, 4(3):301–319, July 2002.

[94] P. B. Lourenço, D. V. d. C. Oliveira, P. Roca, and A. Orduña. Dry Joint Stone Masonry Walls Subjected to In-Plane Combined Loading. *Journal of Structural Engineering*, 131(11):1665–1673, 2005.

[95] P. B. Lourenço and J. L. Pina-Henriques. Validation of analytical and continuum numerical methods for estimating the compressive strength of masonry. *Computers & Structures*, 84(29-30):1977–1989, Nov. 2006.

[96] P. B. Lourenço and J. G. Rots. Multisurface interface model for analysis of masonry structures. *Journal of Engineering Mechanics*, 123(7):660, 1997.

[97] P. B. Lourenço, J. G. Rots, and J. Blaauwendraad. Continuum model for masonry: parameter estimation and validation. *Journal of Structural Engineering*, 124(6):642–652, 1998.

[98] L. Macorini and B. A. Izzuddin. A non-linear interface element for 3D mesoscale analysis of brick-masonry structures. *International Journal for Numerical Methods in Engineering*, 85(October 2010):1584–1608, 2011.

[99] G. Magenes and G. M. Calvi. In-plane seismic response of brick masonry walls. *Earthquake Engineering and Structural Dynamics*, 26(February):1091–1112, 1997.

[100] S. Marfia and E. Sacco. Multiscale damage contact-friction model for periodic masonry walls. *Computer Methods in Applied Mechanics and Engineering*, 205-208:189–203, Jan. 2012.

[101] T. J. Massart, R. H. J. Peerlings, and M. G. D. Geers. Mesoscopic modeling of failure and damage-induced anisotropy in brick masonry. *European Journal of Mechanics - A/Solids*, 23(5):719–735, Oct. 2004.

[102] T. J. Massart, R. H. J. Peerlings, and M. G. D. Geers. An enhanced multi-scale approach for masonry wall computations with localization of damage. *International Journal for Numerical Methods in Engineering*, 215089(July 2006):1022–1059, 2007.

[103] T. J. Massart, R. H. J. Peerlings, M. G. D. Geers, and S. Gottcheiner. Mesoscopic modeling of failure in brick masonry accounting for three-dimensional effects. *Engineering Fracture Mechanics*, 72(8):1238–1253, May 2005.

[104] A. Mauro. *Long Term Effects of Masonry Walls*. MSc dissertation, Roma Tre University, Rome, Italy, 2007.

[105] P. Mayorca and K. Meguro. Proposal for an efficient technique for retrofitting unreinforced masonry dwellings. In *13th World conference on earthquake engineering, Vancouver, BC, Canada, August*, number 2431, 2004.

[106] W. S. McNary and D. P. Abrams. Mechanics of Masonry in Compression. *Journal of Structural Engineering*, 111(4):857–870, 1985.

[107] A. B. Mehrabi, P. B. Shing, M. P. Schuller, and J. L. Noland. Performance of masonry-infilled R/C frames under in-plane lateral loads, 1994.

[108] E. Milani. *A FE upper bound limit analysis model for masonry curved and 3D structures, with and without FRP-reinforcement*. PhD dissertation, Department of Engineering, University of Ferrara, Ferrara, Italy, 2010.

[109] G. Milani, P. B. Lourenço, and A. Tralli. Homogenised limit analysis of masonry walls, Part I: Failure surfaces. *Computers & Structures*, 84(3-4):166–180, Jan. 2006.

[110] G. Milani, P. B. Lourenço, and A. Tralli. Homogenised limit analysis of masonry walls, Part II: Structural examples. *Computers & Structures*, 84(3-4):181–195, Jan. 2006.

[111] G. Milani, P. B. Lourenço, and A. Tralli. 3D homogenized limit analysis of masonry buildings under horizontal loads. *Engineering Structures*, 29(11):3134–3148, Nov. 2007.

[112] G. Milani and A. Taliercio. In-plane failure surfaces for masonry with joints of finite thickness estimated by a Method of Cells-type approach. *Computers & Structures*, 150:34–51, Apr. 2015.

[113] J. Milosevic, A. Gago, M. Lopes, and R. Bento. Experimental Tests on Rubble Masonry Specimens–Diagonal Compression, Triplet and Compression Tests. In *15th World Conference on Earthquake Engineering*, 2012.

[114] G. Mohamad, P. B. Lourenço, and H. R. Roman. Mechanics of hollow concrete block masonry prisms under compression: Review and prospects. *Cement and Concrete Composites*, 29(3):181–192, Mar. 2007.

[115] R. Morbiducci. Nonlinear parameter identification of models for masonry. *International Journal of Solids and Structures*, 40(15):4071–4090, July 2003.

[116] K. Naraine and S. Sinha. Cyclic behavior of brick masonry under biaxial compression. *Journal of Structural Engineering*, 117(5):1336–1355, 1991.

[117] A. Ohler. Zur berechnung der druckfestigkeit von mauerwerk unter berücksichtigung der mehrachsigen spannungszustande in stein und mortel. *Bautechnik*, 63(5):163–168, 1986.

[118] D. Oliveira and P. Lourenço. Implementation and validation of a constitutive model for the cyclic behaviour of interface elements. *Computers & Structures*, 82:1451–1461, 2004.

[119] D. V. d. C. Oliveira, P. B. Lourenço, and P. Roca. Cyclic behaviour of stone and brick masonry under uniaxial compressive loading. *Materials and Structures*, 39(2):247–257, Apr. 2006.

[120] A. W. Page. Finite element model for masonry. *Journal of Structural Division, ASCE*, 104(8):1267–1285, 1978.

[121] A. W. Page. The biaxial compressive strength of masonry. In *Proceedings of the Institution of Civil Engineers*, pages 893 –906, 1981.

[122] G. Pande, J. Liang, and J. Middleton. Equivalent elastic moduli for brick masonry. *Computers and Geotechnics*, 8(1989):243–265, 1989.

[123] B. Pandey and K. Meguro. Simulation of brick masonry wall behavior under in-plane lateral loading using applied element method. In *13th World conference on earthquake engineering, Vancouver, BC, Canada, August*, number 1664, pages 1–6, 2004.

[124] M. Panizza, E. Garbin, M. R. Valluzzi, and C. Modena. Experimental investigation on bond of FRP/SRP applied to masonry prisms. In *6th Int. Conf. on FRP Composites in Civil Engineering–CICE 2012*, pages 13–15, 2012.

[125] L. Pelà, A. Benedetti, and D. Marastoni. Interpretation of experimental tests on small specimens of historical mortars. In *8th International Conference on Structural Analysis of Historical Constructions*, 2012.

[126] L. Pelà, M. Cervera, and P. Roca. An orthotropic damage model for the analysis of masonry structures. *Construction and Building Materials*, 41:957–967, Apr. 2013.

[127] A. Penna, P. Morandi, M. Rota, C. F. Manzini, F. da Porto, and G. Magenes. Performance of masonry buildings during the Emilia 2012 earthquake. *Bulletin of Earthquake Engineering*, 12(5):2255–2273, Aug. 2013.

[128] R. B. Petersen, M. J. Masia, and R. Seracino. In-Plane Shear Behavior of Masonry Panels Strengthened with NSM CFRP Strips . II : Finite-Element Model. *Journal of Composites for Construction*, 14(6):764–774, 2010.

[129] F. D. Porto, G. Guidi, E. Garbin, and C. Modena. In-Plane Behavior of Clay Masonry Walls : Experimental Testing and Finite-Element Modeling. *Journal of Structural Engineering*, 136(11):1379–1392, 2010.

[130] B. V. V. Reddy, R. Lal, and K. S. Nanjunda Rao. Influence of Joint Thickness and Mortar-Block Elastic Properties on the Strength and Stresses Developed in Soil-Cement Block Masonry. *Journal of Materials in Civil Engineering*, 21(10):535–542, 2009.

[131] J. R. Riddington and N. F. Naom. Finite element prediction of masonry compressive strength. *Computers & Structures*, 52(1):113–119, 1994.

[132] P. Roca, M. Cervera, G. Gariup, and L. Pelà. Structural Analysis of Masonry Historical Constructions. Classical and Advanced Approaches. *Archives of Computational Methods in Engineering*, 17(3):299–325, July 2010.

[133] C. Rocco, G. V. Guinea, and M. Elices. Size effect and boundary conditions in the Brazilian test : Experimental verification. *Materials and Structures*, 32(April):210–217, 1999.

[134] E. Sacco and J. Toti. Interface Elements for the Analysis of Masonry Structures. *International Journal for Computational Methods in Engineering Science and Mechanics*, 11(6):354–373, Nov. 2010.

[135] S. Sánchez Tizapa. *Étude expérimentale et numérique des murs en maçonnerie confinée chargés dans leur plane: cas: état de Guerrero (Mexique)*. PhD dissertation, University of Paris-Est, Paris, France, 2009.

[136] G. Sarangapani, B. V. V. Reddy, and K. S. Jagadish. Brick-Mortar Bond and Masonry Compressive Strength. *Journal of Materials in Civil Engineering*, (April):229–237, 2005.

[137] R. Schlegel. *Numerische Berechnung von Mauerwerkstrukturen in homogenen und diskreten Modellierungsstrategien*. PhD dissertation, Bauhaus University, Weimar, Germany, 2004.

[138] R. G. Selby and F. J. Vecchio. *Three-dimensional Constitutive Relations for Reinforced Concrete*. University of Toronto, Department of Civil Engineering, 1993.

[139] R. Senthivel, P. B. Lourenço, and G. d. F. M. de Vasconcelos. Analytical Modeling of Dry Stone Masonry Wall Under Monotonic and Reversed Cyclic Loading. In *Structural Analysis of Historical Constructions, New Delhi 2006*, number 2005, pages 1005–1012, 2006.

[140] B. P. Sinha and A. W. Hendry. Splitting failure of brickwork as a function of the deformation properties of bricks and mortar. *British Ceramic Research Association, Technical Note No. 86*, 1966.

[141] A. Stavridis and P. B. Shing. Finite-Element Modeling of Nonlinear Behavior of Masonry-Infilled RC Frames. *Journal of Structural Engineering*, 136(3):285–296, 2010.

[142] C. A. Syrmakezis and P. G. Asteris. Masonry Failure Criterion under Biaxial Stress State. *Journal of Materials in Civil Engineering*, 13(1):58–64, 2001.

[143] A. Taliercio. Closed-form expressions for the macroscopic in-plane elastic and creep coefficients of brick masonry. *International Journal of Solids and Structures*, 51(17):2949–2963, Aug. 2014.

[144] TNO. *DIANA User's Manual*. TNO DIANA BV, Delft, 2012.

[145] M. Tohidi. *Experimental Mechanical Characterization of Historical Mortars by Windsor Pin Penetrometer*. MSc dissertation, Department of Strength of Materials and Structural Engineering, Technical University of Catalonia, Barcelona Spain, 2012.

[146] Y. Totoev, K. Lin, and A. W. Page. Numerical modeling of framed dry stack masonry panels. In *11th North American Masonry Conference*, 2011.

[147] V. Turnšek and F. Cacovic. Some experimental results on the strength of brick masonry walls. In *Proceedings of the 2nd Intern. Brick Masonry Conference*, pages 149–156, 1971.

[148] A. D. Tzamtzis and P. G. Asteris. Finite Element Analysis of Masonry Structures: Proposed 3-D Nonlinear Microscopic Model. In *North American Masonry Conference*, pages 146–155, 2003.

[149] A. D. Tzamtzis and P. G. Asteris. FE Analysis of Complex Discontinuous and Jointed Structural Systems (Part 1: Presentation of the Method - A State-of-the-Art Review). *Electronic Journal of Structural Engineering*, 1:75–92, 2004.

[150] J. Válek and R. Veiga. Characterisation of mechanical properties of historic mortars: testing of irregular samples. *Transactions on the built environment*, 83:365–374, 2005.

[151] M. R. Valluzzi, F. D. Porto, and C. Modena. Behavior and modeling of strengthened three-leaf stone masonry walls. *Materials and Structures*, 37(April):184–192, 2004.

[152] R. Van der Pluijm. Material properties of masonry and its components under tension and shear. In *Canadian Masonry Symposium*, pages 675–686, 1992.

[153] G. van Zijl. *Computational Modeling of Masonry Creep and Shrinkage*. PhD dissertation, Delft University of Technology, Delft, The Netherlands, 2000.

[154] F. J. Vecchio and M. P. Collins. The modified compression-field theory for reinforced concrete elements subjected to shear. *American Concrete Institute Journal*, 83(2):219–231, 1986.

[155] A. T. Vermeltfoort. *Brick-mortar interaction in masonry under compression*. PhD dissertation, Eindhoven University of Technology, Eindhoven, The Netherlands, 2005.

[156] A. T. Vermeltfoort, D. Martens, and G. van Zijl. Brick–mortar interface effects on masonry under compression. *Canadian Journal of Civil Engineering*, 34(11):1475–1485, Nov. 2007.

[157] E. N. Vintzileou. Three-Leaf Masonry in Compression, Before and After Grouting: A Review of Literature. *International Journal of Architectural Heritage*, 5(4-5):513–538, July 2011.

[158] E. N. Vintzileou and A. Miltiadou-Fezans. Mechanical properties of three-leaf stone masonry grouted with ternary or hydraulic lime-based grouts. *Engineering Structures*, 30(8):2265–2276, Aug. 2008.

[159] C. V. U. Vyas and B. V. V. Reddy. Prediction of solid block masonry prism compressive strength using FE model. *Materials and Structures*, 43(5):719–735, July 2010.

[160] C. Wu and H. Hao. Numerical derivation of averaged material properties of hollow concrete block masonry. *Engineering Structures*, 30(3):870–883, Mar. 2008.

[161] F. Y. Yokel and S. G. Fattal. Failure hypothesis for masonry shear walls. *Journal of the Structural Division*, 102(3):515–532, 1976.

[162] A. Zucchini and P. B. Lourenço. A micro-mechanical model for the homogenisation of masonry. *International Journal of Solids and Structures*, 39(12):3233–3255, June 2002.

[163] A. Zucchini and P. B. Lourenço. A micro-mechanical homogenisation model for masonry: Application to shear walls. *International Journal of Solids and Structures*, 46(3-4):871–886, Feb. 2009.